OPTIMIZING THE DESIGN AND ANALYSIS OF CRYOGENIC SEMICONDUCTOR DARK MATTER DETECTORS FOR MAXIMUM SENSITIVITY

A DISSERTATION
SUBMITTED TO THE DEPARTMENT OF PHYSICS
AND THE COMMITTEE ON GRADUATE STUDIES
OF STANFORD UNIVERSITY
IN PARTIAL FULFILLMENT OF THE REQUIREMENTS
FOR THE DEGREE OF
DOCTOR OF PHILOSOPHY

Matt Christopher Pyle
June 2012

Abstract

For the past 15 years, the Cryogenic Dark Matter Search or CDMS has searched for Weekly Interacting Massive Particle dark matter (WIMPs) using Ge and Si semiconductor crystals instrumented with both ionization and athermal phonon sensors so that the much more common electron recoil leakage caused by photons and βs from naturally present radioactive elements can be easily distinguished from elastic WIMP nucleon interactions by looking at the fraction of total recoil energy which ends up as potential energy of e^-/h^+ pairs .

Due to electronic carrier trapping at the surface of our semiconductor crystals, electron recoils which occur near the surface have suppressed ionization measurements and can not be distinguished from WIMP induced nuclear recoils and thus sensitivity to the WIMP nucleon interaction cross section was driven in CDMS II by our ability to define a full 3D fiducial volume in which all events had full collection. To remain background free and maximally sensitive to the WIMP-nucleus interaction cross section, we must improve our 3D fiducial volume definition at the same rate as we scale the mass of the detector, and thus proposed next generation experiments with an order of magnitude increase in active mass were unfortunately not possible with our previous CDMS II detector design, and a new design with significantly improved fiducialization performance is required.

In this thesis, we illustrate how the complex E-field geometry produced by interdigitated electrodes at alternating voltage biases naturally encodes 3D fiducial volume information into the charge and phonon signals and thus is a natural geometry for

our next generation dark matter detectors. Secondly, we will study in depth the physics of import to our devices including transition edge sensor dynamics, quasiparticle dynamics in our Al collection fins, and phonon physics in the crystal itself so that we can both understand the performance of our previous CDMS II device as well as optimize the design of our future devices. Of interest to the broader physics community is the derivation of the ideal athermal phonon detector resolution and it's T_c^3 scaling behavior which suggests that the athermal phonon detector technology developed by CDMS could also be used to discover coherent neutrino scattering and search for non-standard neutrino interaction and sterile neutrinos. These proposed resolution optimized devices can also be used in searches for exotic MeV-GeV dark matter as well as novel background free searches for 8GeV light WIMPs.

Initial performance studies of our first two next generation iZIP detectors at the University of California Berkeley CDMS test facility indicate that electron recoil surface event misidentification is $< 2\text{x}10^{-5} \pm^{2.5\text{x}10^{-5}}_{2\text{x}10^{-5}}$ (90%CL) for a recoil energy range of 8keV$_r$-60keV$_r$ strongly indicating that z fiducial volume performance will not limit our WIMP sensitivity in next generation experiments. Furthermore, phonon only fiducial volume selections were created for nuclear recoil energies >2keV$_r$ suggesting that phonon only background free or background subtracting light WIMP mass experiments are potentially viable.

Preface

As a member of the $\sim$ 40 member large collaboration, CDMS, my work, effort, and knowledge large derives value through the work and knowledge of others. Without Paul, Astrid, Matt Cherry, Larry, Jasmine, and Rudy, the detector designs that I have created over the years would have never been fabricated. Likewise, without the work and effort of the entire UCB crew in building and troubleshooting their dilution fridge, CDMS would pretty much have never tested a signal R&D device during my graduate career. For a final example, without the decade of effort by a huge number of people before my graduate school career began, there simply wouldn't have been the CDMS project to work on.

So since my work doesn't stand independently from those of my collaborators, I believe that it makes the most sense for my thesis to be explicitly constructed to rely heavily on the theses of other CDMS members and internal CDMS documents. Explicitly:

- Introduction: The standard CDMS thesis, for example Sunil's [1], Jeff's [2], and Zeesh's [3], has spent a sizable number of pages summarizing the theoretical and astrophysical motivation for WIMPs. In that there is no reason to reinvent the wheel, this motivation section has been compressed to the smallest possible size!

- Position Correction: A staggering percentage of my graduate career was spent on improving CDMS II analysis, in particular, optimizing the position correction to remove outlier surface events. Zeesh, though, has written a quite amazing thesis chapter on this topic [3] and thus there is no reason to introduce the

algorithm and it's sizable flaws when we use it to develop high energy phonon only fiducial volume cuts for the iZIP.

- Detector Monte Carlo: A year or so of my graduate experience was spent developing the first comprehensive detector monte carlo for the CDMS collaboration. Though incredibly valuable for it's time, it has now been greatly improved upon and superseded by the work of Kevin McCarthy and Steve Leman at MIT. Consequently, only a qualitative outline of the phonon, charge, and sensor dynamics will be discussed here (my largest contribution), and the more quantitative results of the CDMS detector monte carlo can be found [4], [5] and eventually in the not to be missed thesis of Kevin.

- Reliance on CDMS internal notes: Virtually every topic discussed in this thesis has already been documented in internal CDMS collaboration documents (ebooks). These have been symbolically linked whenever possible. It goes without saying, that sometimes these ebooks have greater depth of thought and this thesis is a poor summary. On the otherhand, some of these original ebooks are overly simplistic and blatantly wrong. This is science in action!

  For those of you reading this thesis who do not have access to our internal CDMS documentation, I must say that my thesis is even more awesome when used as a reference guide for CDMS members. One quite reasonable solution to this issue, is that you considering joining as a collaborator.

Acknowledgements

Not only does my work derive value through the work of others, it also wouldn't have been possible without an enormous amount of personalized teaching and insightful comments by my friends and colleagues. I still remember my first week in the collaboration when Clarence took me to the CoHo in Tresidder and setup my CAP, and how over the next 2 years I constantly bothered Walter with all sorts of questions.

In hindsight, the one year I spent in fabrication helping to build CDMS II tower 5, studying the effectiveness of AP-400, converting CDMS to EV-Align photolithography from the UltraTek, and fabricating the first iZIP (along with all of its mask design) was enormously important to the rest of my CDMS career and thus I owe much to Paul, Astrid, Matt C. and Betty. The knowledge I gained from them placed me in the entirely unique position of being able to both analyze data and understand the fabrication process, and thus I was supremely qualified, perhaps even solely qualified, to ask the question, 'How can I redesign our detector to improve performance?'

The method by which I gained this fabrication knowledge is not unique in the slightest; pretty much all of the knowledge I currently possess about CDMS has come through and been developed by conversations with colleagues. Without Kyle, I wouldn't be able to trivially think in fourier space. Without Steve and Richard, my understanding of statistics would be even worse than it is now! It's hard to over emphasize how important conversations with Jeff have been to me personally. One sign of his importance is the fact that the ebook html template which I've used for the past 6 years was shamelessly stolen from him. Even with him now working at Caltech on Spyder,

I still find him on my speed dial. Zeesh, Dave, and Scott have also been incredible colleagues. My understanding of position manifolds was largely developed through conversations with Zeesh and it was Dave who found the error in my background subtracting Optimum Filter algorithm logic at the most recent LTD. With Scott, I will always be impressed with his principle of QET close packing. If this idea can be implemented in next generation devices, our fabrication yield will almost certainly improve.

Though this two year delay between my defense and thesis has been frustrating, I can say with honesty that Blas may have been the absolute perfect advisor for me. Blas gave me an enormous amount of freedom to work on pretty much anything that I found interesting in CDMS and with this freedom I have truly shined. Futhermore, much of the way in which I think and problem solve today is modeled upon Blas.

Last but not least is Bruno. Without question, I've worked more closely with Bruno the past n years than with anyone else within our collaboration and I have found his opinions and advice on virtually all topics (position correction algorithms, noise sources, coding etiquette, increasing meeting efficiency, management) to be invaluable. He has made me both a better scientist and a better person.

To all of my colleagues mentioned directly above, and all the others who are unnamed but helped me along the way, I thank you.

Contents

List of Tables

List of Figures

Chapter 1

Scientific Motivation

1.1 Astrophysical and Cosmological Evidence for Dark Matter

By looking at doppler shifts of various easily distinguishable spectral features, astronomers have been able to measure the rotational velocity of stars in spiral galaxies as a function of distance from the galactic core (Fig. 1.1) and match these observations to our understanding of gravitational dynamics [6]. If we naively assume that the luminosity distributions are an excellent proxy of the matter density distributions (i.e. all the matter of the galaxy is in its stars and in dust/gas near the stars), then using Gauss' law we can calculate the centripetal force on a star as a function of it's orbital radius,

$$\frac{mv^2}{r} = \frac{mGM(r)}{r^2}$$

At high radius, well away from the bright galactic center, the mass within the Gaussian surface should be roughly constant and thus we expect that

$$v(r) \propto r^{-1/2}$$

As you can see in Fig. 1.1 though, spiral galaxies display roughly constant velocity distributions at high radius and, consequently, we are left with the exciting and mysterious conclusion that the vast majority of the matter in a spiral galaxy is at high radius and is **dark**.

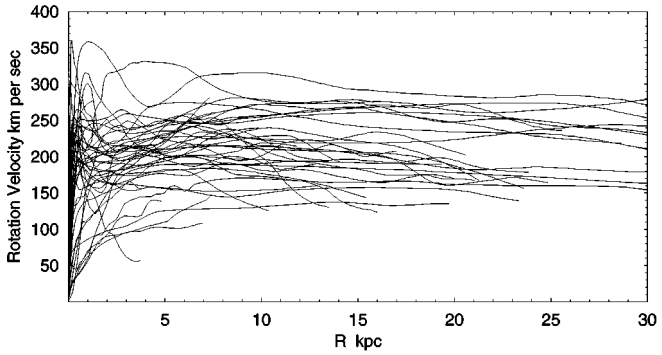

Figure 1.1: Average star rotational velocity versus distance from galactic center for a characteristic sample of spiral galaxies. From [6]

Spiral galaxies are not alone in requiring large amounts of dark matter for their dynamics to be understood. At the same length scales, elliptical galaxy dynamics have been observed through a variety of techniques and the conclusion is identical[32]. Additionally, evidence for dark matter is also found at much larger scales in galaxy clusters [33, 34].

Further properties and characteristics of dark matter can be constrained by studying the dynamics of the universe as whole (cosmology). As the universe cooled after the big bang, the light stable atomic elements of ^{2}H, ^{3}He,^{4}He, and ^{7}Li began to be synthesized from free neutron and protons. As shown in Fig. 1.2, the relative relic abundance of the intermediate products (^{2}H and ^{3}He) is quite sensitive to the baryon/ photon density ratio. Qualitatively, this is due to the fact that the probability of interaction scales as the square of the baryon density and thus the probability of incomplete nucleosynthesis (and thus larger relic amounts of ^{2}H and ^{3}He) is much

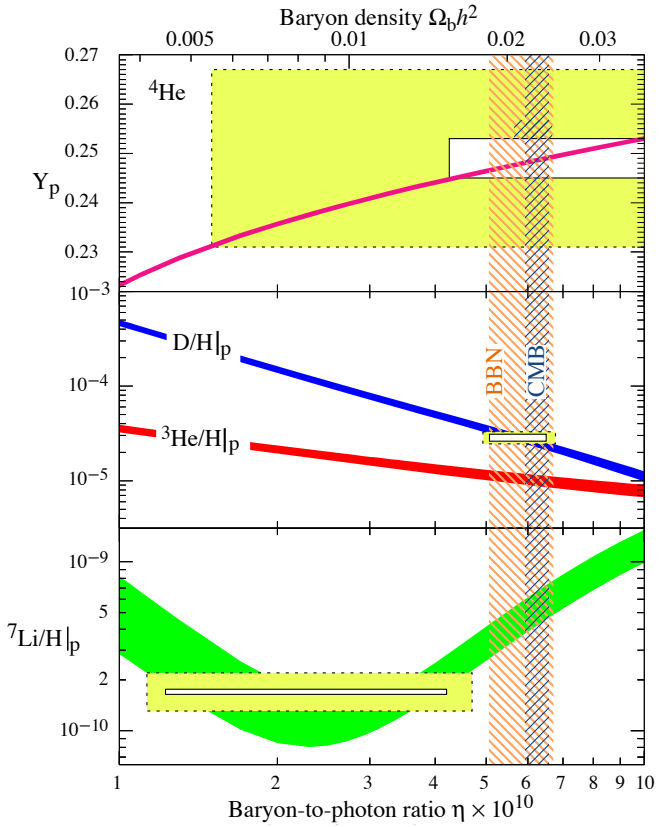

Figure 1.2: Calculated elemental abundances from Big Bang Nucleosynthesis for ^{7}Li (green) ^{3}He (red) and ^{2}H as a ratio to simple ^1H and ^{4}He as a ratio to the total baryonic mass (pink). 90% CL for current observational constraints are shown in yellow (stat+sys) and white (stat only).[7]

more likely for small baryon densities [35]. Unfortunately, observation of the relative relic abundances of ^{4}He and ^{3}He today has been made enormously more complicated by the fact that these elements are also byproducts in stellar nucleosynthesis and thus the only precise measure of the baryon density is the relic abundance of ^{2}H (due to its fragility, it can not be produced in stars). This measurement alone, though, strongly constrains dark matter properties. It suggests that **the majority of dark matter must be non-baryonic** [7].

Further evidence for the mostly non-baryonic nature of dark matter can be can be seen in observations of the cosmic microwave background, or CMB . Before the universe

cooled to the point where e^- and p^+ would coalesce into neutral particles (recombination), photons were strongly coupled to these charged particles. After cooling though, these photons travelled largely unimpeded all the way to our telescopes today giving us a snap shot of the acoustic excitations that existed in this photon-baryon fluid (Fig. 1.3) and consequently an enormous amount of information about the dynamical properties of the fluid itself. Most importantly for us, the dynamics are quite sensitive to the baryon density and the small observed baryon density measured reaffirms the fact that dark matter is largely non-baryonic[8].

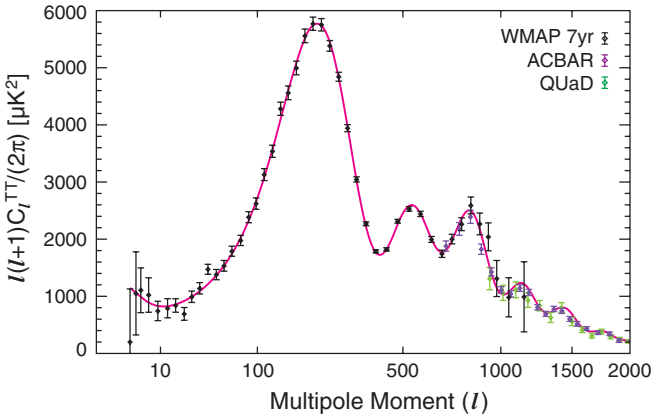

Figure 1.3: Angular power spectrum of the thermal anisotropies found in the CMB [8]

One final piece of evidence which supports the non-baryonic nature of dark matter is that of the enormous amount of structure visible in the universe today [9, 36]. At the time of recombination, fluctuations in the baryonic matter density are directly measured by fluctuations in the CMB spectrum to be $\sim 10^{-5}$. These fluctuations are so small because the strong coupling to photons means that non-linear gravitational collapse is impossible, and thus any fully baryonic matter models of the universe require that the enormous amount of structure visible today develop in the relatively short time after recombination. By contrast, cosmological models with large amounts of non-baryonic, **non-relativisitic** dark matter can begin to clump at times well before recombination and thus the baryonic matter will very quickly collapse into the

pre-existing gravitational wells immediately following photon decoupling. This additional requirement that dark matter be cold prior to recombination seems inviolate. Relativistic or hot dark matter simply has too much kinetic energy to be collected in the initial small density perturbations.

Taking into account all of these observational bounds, the current best estimate on the fractional amount of cold non-baryonic dark matter in the universe is Ω_{CDM}=0.228±0.016 or $\Omega_{CDM}h^2$=0.1126±0.036 [8].

1.2 WIMP Hypothesis

Numerous candidate particles have been proposed which meet the astrophysical/cosmological criteria that the particle be non-baryonic and cold including the broad classes of axions [37], SuperWIMPs [38], and super heavy relics [39, 40]. The general class of the WIMP, or Weekly Interacting Massive Particle, is largely though considered to be the most compelling theory currently and it is the class for which we have optimized our detector.

Let's propose the existence of a massive non-baryonic particle (χ) which is in thermal equilibrium with the universe at early times. As the temperature of the universe drops below the mass of χ, two things occur. First, the particles become non-relativistic and thus the non-relativistic constraint for structure formation is automatically satisfied due to their massive nature. Secondly, the number density begins to scale as $e^{-M_\chi/T}$. Microscopically, this is due to the fact that in equilibrium the creation and annihilation rates must be identical and as the temperature decreases a smaller fraction of lighter particles (photons, electrons, etc...) have the necessary kinetic energy to create a particle with such a large mass. This is the shoulder in Fig. 1.4.

Since the annihilation rate is very dependent upon the particle density, there comes a point in the expansion and cooling of the universe where annihilation rate is slower than the cooling rate and at this point the particle 'freezes out' and the comoving

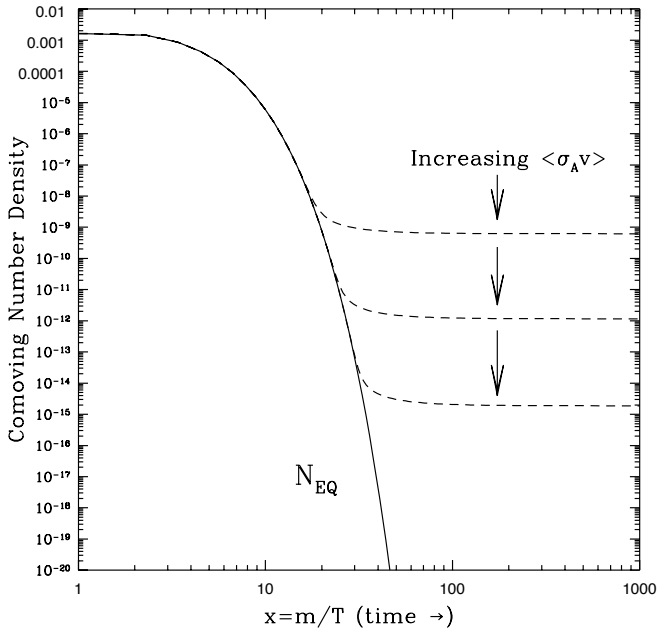

Figure 1.4: WIMP number density as function of 1/T for different annihilation cross sections. [9]

density becomes invariant. For non-relativistic particles, the fractional dark matter density at which freeze out occurs is [41]

$$\Omega_\chi h^2 \simeq \frac{3x10^{-28}}{<\sigma_{\chi\chi} v>} cm^3/s$$

Roughly, larger annihilation cross sections means that the particle remains in thermal equilibrium slightly longer and thus larger cross sections mean smaller relic densities. Interestingly, the mass of the particle is only important insofar as it varies the annihilation cross section.

The WIMP hypothesis is so compelling because the relic dark matter density needed to match cosmological observations places the annihilation cross section, $\sigma_{\chi\chi}$, at roughly the weak scale, and it's exactly at this scale where we expect an enormous amount of new physics and particles to solve the hierarchy problem. Consequently, the

WIMP hypothesis kills two birds with stone. If the hierarchy problem is solved with new physics near the weak scale, then it's enormously reasonable to assume that the lowest energy, most stable particle caused by this new physics explains non-baryonic cold dark matter mystery quite easily. [41]

Chapter 2

Experimental Design Roadmap

2.1 Overall Direct Detection Design

Currently, three broad experimental search techniques are being used to search for WIMPs. At accelerators like the LHC, one can hope to create these massive particles and look for missing momentum / energy signatures. Secondly, one can hope to observe WIMP annihilation products from those locations with a high density of dark matter. Finally, one can hope to directly measure WIMP- matter elastic scattering, our focus in CDMS.

The challenges in the latter derive solely from the required WIMP characteristics. The weak to very weak elastic scattering interaction rates expected from crossing arguments on the annihilation cross section suggests that large instrumented detector masses with very small backgrounds are required to discover WIMPs. Consequently, all direct detection experiments are constructed from radioactively pure materials and are located underground to shield from backgrounds produced by cosmic rays and muons.

Secondly, the WIMPs with which we would hope to interact, are gravitationally bound to our galaxy, and thus their velocity distribution will have a maximum cutoff

of $\sim$2x10^{-3}c [42]. For elastic e$^-$ recoils, this velocity constraint is equivalent to a recoil energy constraint of $\sim$10eV, which is certainly a bit daunting; standard large mass ultra-clean scintillator based experiments like KAMLAND and BOREXCINO have energy thresholds which are 3 orders of magnitude too large.

For elastic nuclear recoils, the kinematic restrictions are less severe. Due to the relatively near mass matching, nuclear recoil energies on the order of 10keV will be produced, suggesting that WIMP-nucleus interactions are the preferred detection technique. A second enormous advantage of WIMP-nuclear scattering is that for these small momentum transfers we expect scattering amplitudes to sum coherently across all nucleons giving us a total nucleus cross section which scales as A^2 ($\sim$ x5000 for Ge).

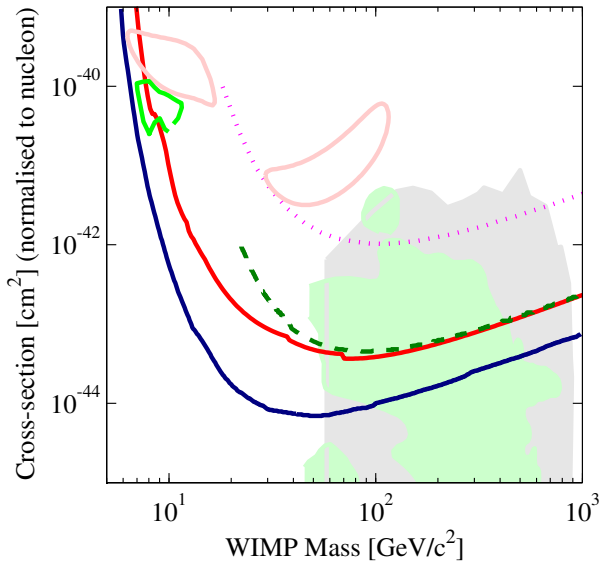

Figure 2.1: Current limits on the WIMP-nucleon cross section as a function of the WIMP mass for Xenon 100 (blue) [10] , CDMS II (red) [11], Edelweiss (dashed green) [12], and WARP (magenta) [13] all of which discriminate between electronic and nuclear recoils. Signal excesses at low energy seen in CoGENT (green) [14] and DAMA (magenta) [15], neither of which can distinguish between nuclear and electronic recoils, could be attributed to WIMPs with masses within the inclusion contours shown. Finally, regions of MSSM parameter space in which WIMPs are are particularly well motivated are shown in grey [16] and green [17].

The elastic nuclear recoil detection channel offers one more enormous advantage. Since the vast majority of radioactive backgrounds interact with matter electronically while WIMPs hypothetically interact through nuclear scattering, a detector which has the ability to distinguish between nuclear and electronic recoils will remove the vast majority of the remaining background. The advantages of this technique can be seen in Fig. 2.1. For large WIMP masses, the top 4 limits are all set by experiments with recoil type discrimination.

In summary, all direct detection WIMP search experiments will share these elements:

- Sensitivity to low energy nuclear recoils
- Large instrumented masses
- Underground
- Composed of radioactively clean materials
- Excellent electron/nuclear recoil discrimination

2.2 General Design of Semiconductor based Dark Matter Experiments

In semiconductors, the recoil energy for both electronic and nuclear interactions is converted into numerous crystal vibrations (phonons) and e^-/h^+ excitations [43]. However, the relative ratio of these products differs drastically depending upon the recoil type [44]. Electonic recoils are near maximally efficient at producing e^-/h^+ pairs. Roughly, phonon creation rate only begins to dominate when the energetic electronic excitations do not have the necessary kinetic energy to create an additional excited pair. Ge is slightly non-ideal in that there is some optical phonon production but still $\sim$25% of the recoil energy is converted into potential energy of e^-/h^+

pairs.

By contrast, non-relativistic nuclear recoils like those produced by hypothetical WIMP interactions are much less efficient at producing charge carrier excitations (Lindhard theory[44]). Qualitatively, the low velocity of the nucleus means that perturbation of the e^- is more akin to a slow, adiabatic perturbation that produces very few excitations. For Ge, in the 10-100keV$_r$ energy range, nuclear recoils produce $\sim 1/3$ the ionization of that for an equivalent energy electron recoil ($\sim 8\%$). This is seen in Fig. 2.2 for a CDMS II dark matter detector where the y-axis is the fractional amount of electronic potential energy normalized to 1 for electronic recoils. So a semiconductor detector which measures both the number of charge carriers produced in an interaction as well as the amount of phonons produced in an interaction will be able to discriminate between nuclear and electronic recoils.

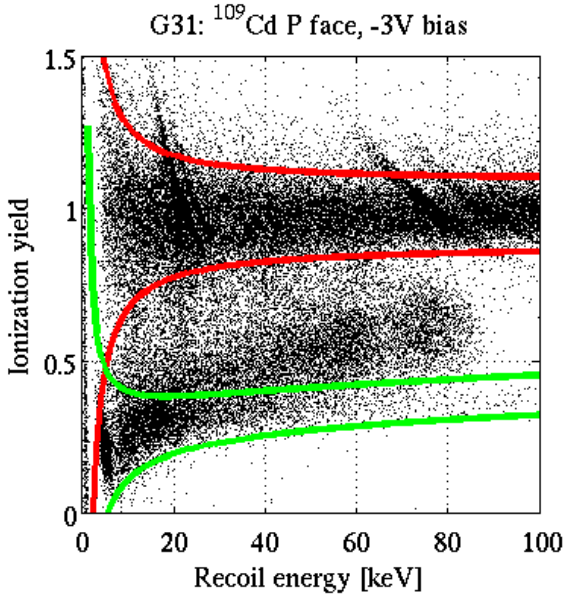

Figure 2.2: Ionization yield as a function of recoil energy for a CDMS II detector with the fully collected $\pm 2\sigma$ electron recoil and nuclear bands shown in red and green. Electron recoil events which occur near the surface of the detector have systematically suppressed charge collection (lower black band) and can thus be misidentified as nuclear recoils (from Jeff).

In a traditional semiconductor ionization device, the number of e^-/h^+ pairs produced

in an interaction is measured by drifting the carriers with an electric field to electrodes instrumented with high impedance charge amplifiers and measuring the image charge collected on those electrodes. As seen in Fig. 2.2, CDMS has found that e^-/h^+ trapping on the surfaces of our detector (both the cylindrical sidewalls and the z faces) significantly suppresses the ionization signal produced for an event and thus in CDMS II near surface electron recoil events had the potential to be mis-identified as nuclear recoils. Consequently, semiconductor dark matter devices must be able to define a 3-D fiducial volume which separates events which occur near a surface from those which occur in the bulk of the detector.

In summary, a semiconductor based dark matter device must have:

- high resolution phonon energy measurement
- high sensitivity charge excitation measurement
- full 3-D fiducial volume control using charge and/or phonon signals.

In the CDMS II device [3] [2] [45], radial fiducial definition was defined by splitting the charge electrode into inner and outer concentric rings, while z fiducial volume was defined through phonon pulse shape parameters. This hybrid fiducial volume met the requirements of performance requirements of CDMS II in that our background rate was < 1 for the entire experimental lifetime. As we attempt to increase our WIMP sensitivity by 2 orders of magnitude in a second generation direct search dark matter experiment though, leakage of electron recoil surface events past this hybrid fiducial volume would be significant, drastically limiting our sensitivity and thus We designed a next generation device, the interleaved ZIP or iZIP, which has significantly improved fiducialization performance.

As in the CDMS II devices, the high impedance charge electrode has been separated into inner and outer electrodes allowing for excellent radial fiducial volume control with charge (Fig. 2.3 left). However, unlike in the CDMS II design, both sides are instrumented with high impedance charge electrodes and thus both the number of electrons and holes produced during the event interaction are measured separately

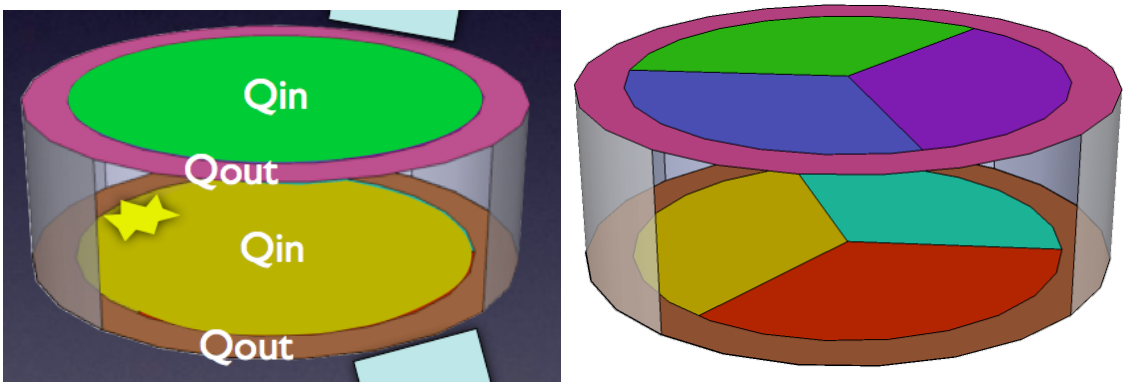

Figure 2.3: Charge (left) and Phonon (right) sensors in the iZIP4/5 design are split into localized channels so that position information can be gathered for each and every event.

which, as we will see in chapter 7, leads to significantly improved radial fiducial volume definition. Secondly, the number of phonon channels has been increased to 8 from 4 (Fig. 2.4) and phonon sensors are now fabricated on both sides of the detector leading to superior z-fiducial volume definition. Finally, the channel geometry was redesigned so that there is now a circular outer phonon channel on both sides of the detector for significantly improved radial fiducial volume control through the partitioning of energy and pulse shape in the phonon channels.

This ability to place high impedance charge and low impedance phonon sensors upon the same face is a beautiful by product of the interleaved electrode geometry (Fig. 2.4). In 1994, Paul Luke was attempting to produce ionization detectors from high Z semiconductors (large stopping power) with large band gaps (no cooling required) [46]. Unfortunately, the crystals studied had poor hole mobility and thus the amount of image charge collected on the instrumented positively biased electrode in a standard coplanar electrode geometry would hugely vary depending upon event location, leading to large position dependence in the signal amplitude. To solve this problem, Luke interleaved two different collection grids and placed one at a higher voltage so as to collect all the mobile e^- on a single electrode. The second electrode was then used for an estimate of the h^+ image charge for subtraction.

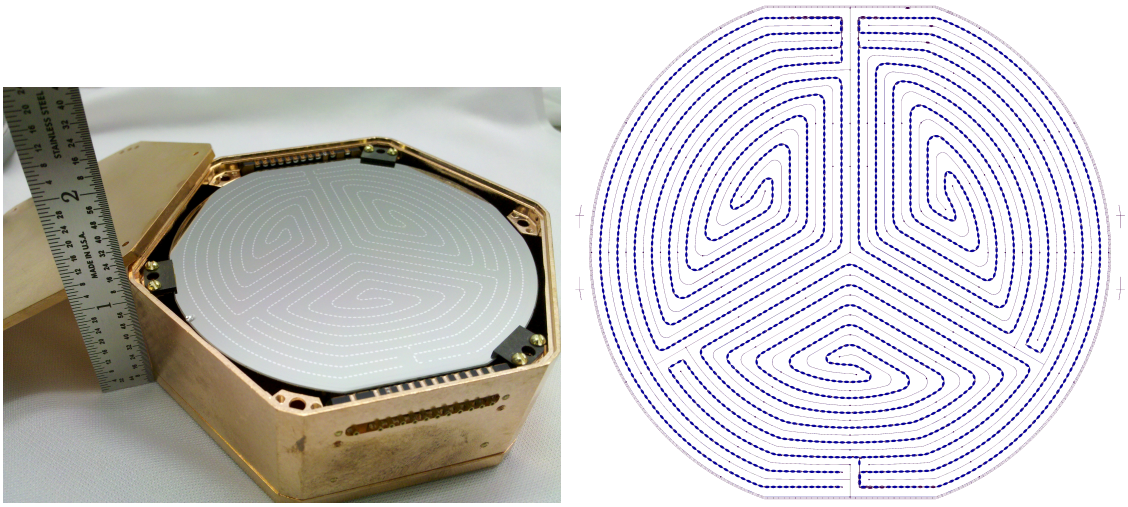

Figure 2.4: Interleaved electrodes with alternating voltages produce complex E-field geometries (Fig. 2.5) that encode z position information into charge collection and luke phonon creation locations.

Blas repurposed this interleaved geometric design by recognizing that complex E-field geometries (Fig. 2.5) produced by complex electrode patterns (Fig. 2.4) at a variety of voltage biases would encode the original event position information upon the carrier transport and thus the high impedance instrumented electrode signals. For the interleaved design, in particular, an event in the bulk uniform field region (Fig. 2.5) left) will have e^- transport to the thin +2V electrode instrumented with charge amplifiers while the h^+ are transported to the identically instrumented -2V electrode on the opposite face, leading to a symmetric signal for bulk events. For surface events by contrast, carriers follow the large E-fields which run between the interleaved electrodes on the same face (Fig.2.5 right) leading to asymmetric charge collection signals, and thus the interleaved design allows one to discriminate surface events from bulk events creating a full 3D fiducial volume using charge signals alone.

After reasonable preliminary results [47], this design geometry languished primarily due to fears that:

1. Complex electrode geometries have low E-field saddle points on which one could trap charge.

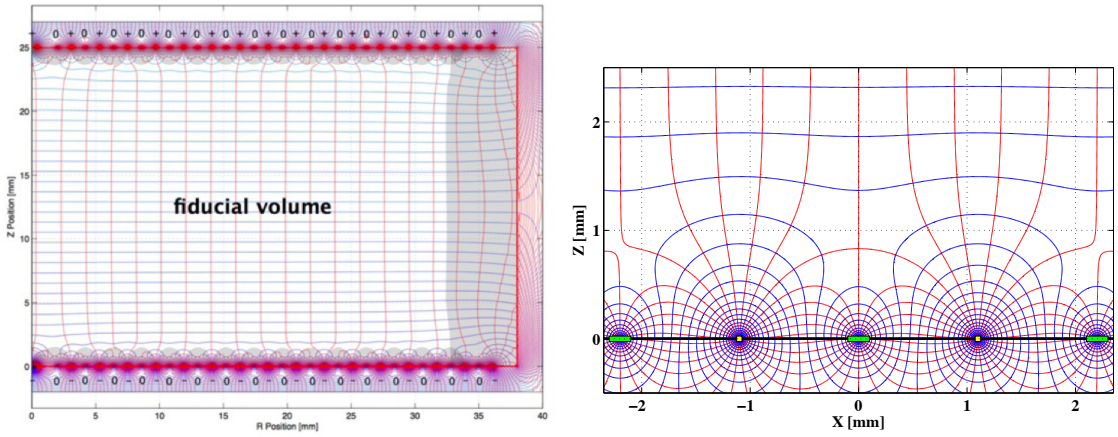

Figure 2.5: With $\pm 2V$ electrodes instrumented with high impedance charge amplifiers (thin 40μ m yellow boxes in the right zoom) alternating with 0V on the low impedance QET instrumented phonon sensors (wide green boxes), excited carriers produced in the bulk of the detector will collect on the top and bottom charge electrodes (producing symmetric charge signals), while carriers excited near the surface will travel along the surface and produce an asymmetric charge signal.

2. The low Al coverage requirements of an interleaved design meant that phonon pulse shape position information would be severely degraded from CDMS II.

With the success of the Edelweiss detector modeled upon the CDMS R&D device [12], the first fear was found to be groundless. Secondly, I realized that through the creation of Luke-Neganov phonons (Ch. 6), additional position information was encoded into phonon pulse shapes and partition as well, potentially offsetting the small Al coverage penalty, and consequently the iZIP design program was restarted and designs 2-5 were produced in relatively short succession.

Over the next 4 chapters, we will delve deeply into the physics and design of the phonon sensors (Ch. 3-5) and phonon dynamics (Ch. 6), leaving the charge transport, charge sensor design and the interplay between optimizing an interleaved charge/phonon detector for charge or phonon sensitivity largely for future theses/papers. Then in Ch. 7, we will present the preliminary device performance of the iZIP at the University of California Berkeley surface test facility.

Chapter 3

Lump Element TES Dynamics

In the ideal world, the device we use to measure the amount of phonon energy absorbed per unit time would neither add any uncertainty or any systematic distortions to the true signal. Alas, this simply isn't possible. Our sensing element, the Transition Edge Sensor (TES) unfortunately degrades the phonon signal in both of these ways and thus it's certainly worth a few chapters to understand the dynamics of TES in general and ours in particular and thereby quantify both the magnitude of uncorrectable noise and understand to what extent we can disentangle the true phonon absorption pulse shape from our measured quantities.

The theory presented in this entire chapter is largely distilled from Kent Irwin's excellent summary/review [48]. Hopefully, the more careful discussion on correlations between joule heating fluctuations and Johnson noise fluctuations, the discussions on dominant noise terms and the emphasis on CDMS specific issues and device drivers will give it relevance to the CDMS reader. For the non-CDMS reader, the derivation of the T_c^3 resolution scaling law for signal bandwidth limited devices like those of a CDMS athermal phonon sensor will almost certainly be the most interesting new result. It strongly suggests that CDMS-like athermal phonon sensors have a compelling role to play in neutrino physics as well as searches for light and ultra-light dark matter.

3.1 TES dynamics

3.1.1 Ideal Scenario: Perfect Voltage Bias and No Inductor

Most basically, a TES is a superconductive material which has been artificially stablized in some way such that it remains in the middle of it's superconducting to normal transition. When in this state, any release of energy into the system will increase the resistance of the film substantially which can then be measured.

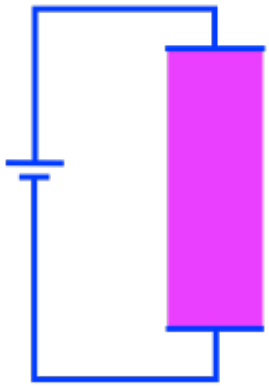

Figure 3.1: Simple Voltage Biased TES

The simplest method (and the one that we use) to keep the TES in the middle of it's transition is to place it in a voltage biased circuit as shown in Fig. 3.1 [49]. Roughly, there will exist some temperature and current in which the joule power being dissipated into the electronic system by the external voltage bias will be exactly offset by the cooling of the system through a thermal resistance. Furthermore, when voltage biased the system is naturally stable. Literally, infinitesimal thermal excursions will be be exponentially damped. Specifically,

1. A temperature excursion increases the R
2. An increase in R decreases the joule heating (i.e. V^2/R)
3. A decrease in joule heating leads to a decrease in the thermal excursion

4. repeat 1-3 indefinitely ... the system returns to equilibrium

Mathematically, we can represent the voltage biased TES circuit as the single non-linear differential equation

$$C\dot{T} = \frac{V_b^2}{R(T)} - P_{bath}(T)$$

where C is the total heat capacity and P_{bath} is the thermal energy flow to the bath. For most systems, the functional dependence of P_{bath} on the temperature can be described as

$$P_{bath} = K\left(T^n - T_{bath}^n\right) = \Sigma\mathcal{V}_{tes}\left(T^n - T_{bath}^n\right) \tag{3.1}$$

where K is an extrinsic physical characteristic that in a CDMS style W TES can be written in terms of Σ, an intrinsic electron/phonon coupling coefficient (measured later), and the total TES volume, $\mathcal{V}_{tes}$. Please note, that in this chapter we are considering the 455 parallel TES found in the iZIP4/5 TES channel design to be a single combined and contiguous TES with a total width and total volume ,$\mathcal{V}_{tes}$, that is simply 455 times of the actual single TES element. This simplification does gloss over some complexities which will be discussed in detail in the next chapter. These and other important measured W TES characteristics for the iZIP4/5 TES design can be found in the quick reference table (Tab. 3.1) below.

As expected for a simple metal, $C \propto T$. However, the proportionality constant when biased within the transition will be a raised slightly by the factor,f_{sc}, from its normal metal values since we also have the latent heat associated with breaking cooper pairs.

With these definitions, let's taylor expand to first order about the equilibrium state

(T_o, R_o) where $P_{bath} = \frac{V_b^2}{R_o}$:

$$\begin{aligned} C\delta\dot{T} &= \left(\frac{-V_b^2}{R_o^2} \left.\frac{\partial R}{\partial T}\right|_{To} - G \right) \delta T \\ &= -G \left(\frac{P_{bath}\alpha}{GT} + 1 \right) \delta T \end{aligned} \tag{3.2}$$

where we've defined both the differential thermal conductance

$$G = \left.\frac{\partial P_{bath}}{\partial T}\right|_{To} = nKT_o^{n-1} \tag{3.3}$$

and also α as

$$\alpha = \left.\frac{\partial R}{\partial T}\right|_{T_o} \frac{T_o}{R_o}$$

α quite intuitively quantifies the idea of sharpness/sensitivity: if I have α=100, then a 1% change in the TES's temperature will give me a 100% in it's resistance.

The dimensionless grouping $\frac{P_{bath}\alpha}{GT}$ seen in Eq. 3.2 will occur so regularly that Irwin has created the low frequency loop gain parameter, $\mathcal{L}$, defined as

$$\mathcal{L} = \frac{P_{bath}\alpha}{GT} = \frac{\alpha \left(1 - \frac{T_{bath}^n}{T_o^n}\right)}{n} \tag{3.4}$$

You can think of $\mathcal{L}$ as a comparative measure of the feedback abilities of the changes in Joule heating and changes in the thermal heat flow to the bath. Specifically, for systems with large $\mathcal{L}$, a temperature excursion will be damped almost exclusively by a changing of R, which will lead to a change in the joule heat flowing into the TES that will eventually suppress the excursion.

Eq. 3.2 is of course the ODE for a simple exponential decay with an electro-thermal feedback falltime,$\tau_{\rm eff}$, of

$$\tau_{\rm eff} = \frac{C}{G}\frac{1}{\mathcal{L}+1} \tag{3.5}$$

All other things being equal, a larger α (a sharper transition) or $\mathcal{L}$ means your TES has a larger sensor bandwidth and is simply more sensitive to power fluctuations. Likewise, notice that your sensor bandwidth decreases as T_{bath} approaches T_c. However, they have to be surprisingly close to have any significant effect. For $T_{bath} = \frac{1}{2}T_c$, the change in sensor bandwidth is only 3%.

For a first very rough estimate of $\tau_{\rm eff}$ for CDMS W films, let's follow an argument first put internally forward by Adam and the MIT group and look at W film resistance curves versus T_{bath} for test wafers which went through the film deposition process with G48 that were taken by Betty Young, Jeff Yen, and Marco Razeti at Stanford with the AST dilution fridge (fig. 3.2).

This data indicates that the intrinsic transition widths for our W films, which we will quantify by estimating the ΔT over which the resistance varies from 10% to 90% of R_n ($\Delta T_{90-10\%}$), are $\sim$ 0.5mK. As with any measurement though, there are some systematics. Most importantly, if the input excitation used to measure the resistance is too large, then the W film will self heat and the transitions will seem unnaturally sharp. This is especially true for 4 terminal measurements in which a current excitation is used ($P_{joule} \propto I^2R$). To minimize this effect, one should:

1. use SQUIDs if possible.
2. use as small of an excitation as possible.
3. measure W films with large volume. This increases both the heat capacity and the thermal conductance to the substrate both of which suppress self heating effects.

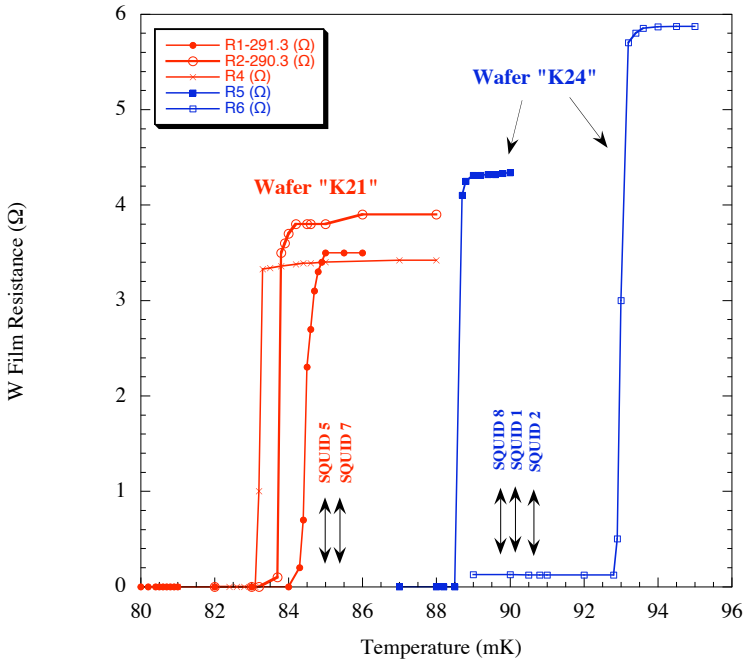

Figure 3.2: W test films Resistance profiles for test wafers which were deposited with G48 (from Betty Young/Jeff Yen/Marco Razeti)

Finally, to bound this systematic, the easiest technique is to look for variations in the measured transition width as one varies the magnitude of the excitation. This systematic check was attempted and found to negligibly effect the results.

The resistance curves in Fig.3.2 also measure the T_c of the films. One of the interesting/annoying facts about our current fabrication process is that the measured T_c values for Si test wafers are usually about 12mK below those values measured for CDMS detectors from the same deposition (occasionally and for unknown reasons this rule breaks). As of this moment, there is no clear understanding of the cause of this offset. Possibilities include:

1. Electronic noise on the AST system is suppressing the T_c
2. aSi/W bilayers deposited on Ge and Si have different stress characteristics which correlate to T_c

3. Si wafers can macroscopically deform to relieve stress which then suppresses Tc

With the knowledge acquired up to this point, we can plug and chug the values found in Tab. 3.1, and end up with an expected/theoretical τ_{eff} vs. T_c shown in Fig. 3.3. This plot and all future calculations assume that $\Delta T_{90-10\%}$ is invariant as one varies T_c through either ion-implantation or through a change of the deposition settings and thus $\alpha \propto T_c$ and $\omega_{\text{eff}} \propto T_c^{n-1}$. We know that this is roughly true for small amounts of ion-implantation (varying the T_c from 110 mK to 80mK for example) [50]. However, the veracity of this assumption is not known for either larger amounts of ion-implantation or for T_c variation through variation of deposition settings (gas pressure, etc.).

To give some sense of scale to these values, the iZIP4/5 has a ballistic phonon collection time scale of 750μs (much slower) and the risetime of a very localized event on the closest channel is about $\sim 7\mu$s. So these expected sensor falltimes (3.0μs @80mK) are very fast!

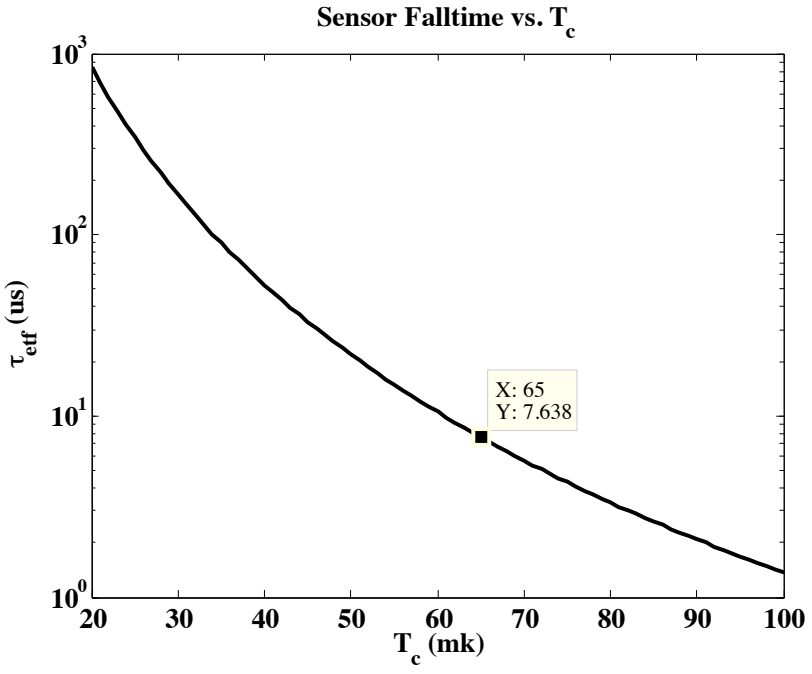

Figure 3.3: Expected CDMS TES decay times (τ_{eff}) as a function of T_c

Now because our phonon collection times are so much slower than τ_{eff}, we can't just experimentally check these expectations by measuring the falltime for a regular CDMS event since it gets confusingly mixed in with short time scale phonon physics. 5 years ago or so though, Walter showed that we can use "glitch" events for this purpose.

We believe that a glitch event is a voltage spike down the bias line whose temporal width is much shorter than all other time scales of the experiment. It's dominate effect is simply to directly heat the TES and we consequently expect that the falltimes of these pulses should be an excellent experimental measure of τ_{eff}. An example glitch event is shown for G51 at UCB, an iZIP4 detector with T_c's measured between 70-80mK and with $T_{bath} \sim 40$mK in Fig. 3.4

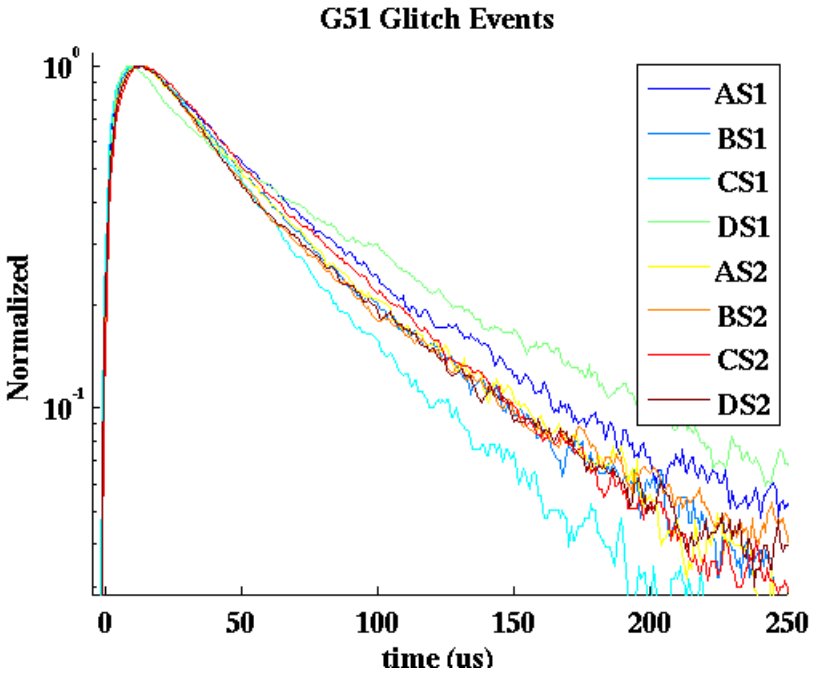

Figure 3.4: Glitch Event for G51

There are clearly lots of problems here! First, the glitch has 2 distinct falltimes rather than simply 1. Secondly, the quickest of these two falltimes is $\sim 40\mu s$ where naively reading from Fig. 3.3, we would expect falltimes between 3-6μs. We are an order of magnitude off our expectations! Reconciling these statements by accounting for more

Component	Value	Comments
Σ	$0.32\pm.02\pm.12$ $\frac{pW}{K^5m^3}$ [51]	Electron/phonon coupling constant: $P_{bath} = \Sigma\mathcal{V}_{TES}\left(T_c^n - T_{bath}^n\right)$
n	5	Thermal conduction power law exponent
$\mathcal{V}_{tes}$	17000 μm^3	Total Volume of W TES per channel in the iZIP4/5: $\mathcal{V}_{tes} = n_{qet}(t_{tes}h_{tes}l_{tes} + \mathcal{V}_{fin})$
ρ_w	1.32x10$^{-7}\Omega$m	W film resistivity: for new SuperCDMS 40nm films ($R_\square \sim 3.3\Omega$).
R_n	$\sim$ 700 mΩ	Normal resistance of single phonon channel
f_{sc}	$\sim$ 2.5	Heat capacity increase due to superconducting/normal phase change
γ_w	108 $\frac{J}{K^2m^3}$ [52]	W heat capacity coefficient: $C = f_{sc}\gamma_w\mathcal{V}_{TES}T_c$
T_c	$\sim$ 80 mK 40-110mK	Nominal value Value range
$\Delta T_{c\,90\%-10\%}$	0.5-1.5mK	Unfortunately, has yet to be well measured
l_{tes}	220nm	Length of TES in the direction of current flow
n_{chan}	8	Number of Phonon Channels in the iZIP4/5.

Table 3.1: Aggregate CDMS iZIP4/5 W TES characteristics

complex TES dynamics will be our primary job for the next two chapters.

3.1.2 Adding additional complexities

Unfortunately, answering the above τ_{eff} mystery and deriving the theoretical noise PSDs, signal green's function, and complex impedance of the circuit,$Z_{tot}(\omega)$, will require a few complicating details. First, we'll have to read out the change in resistance/current with some device. The easiest way is to couple to a SQUID inductively and thus we'll complicate the circuit by adding an inductance, L (FETs aren't ideal due to the difficulty in implementing feedback and impedance mismatch). Secondly, we voltage bias by placing a shunt resistor, R_s, that is much smaller than the TES equilibrium resistance in parallel with the inductor/TES leg of the circuit. This shunt resistor plus the stray parasitic resistances can be combined into a single load resistor, R_l (Fig. 3.5). Values for these components in our current CDMS II electronics can

be found in Tab.3.2. Finally, we will allow the resistance of the TES to also have functional dependence on the current flowing through the device.

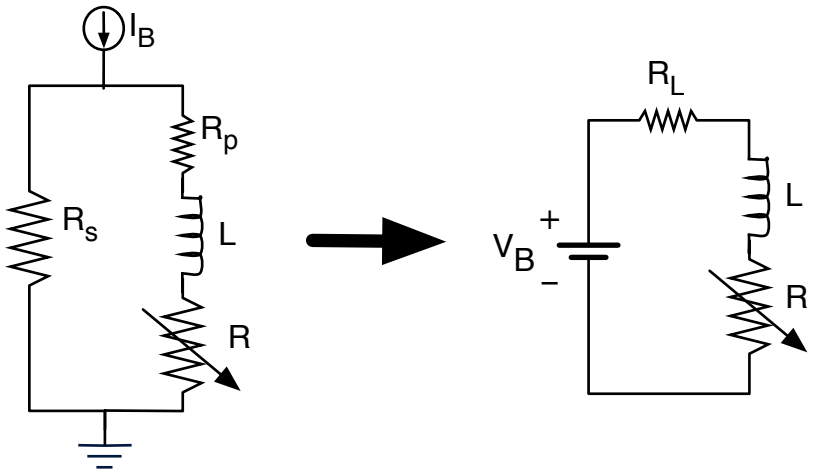

Figure 3.5: Left: Diagram of actual current biased sensor circuit. Right: Thevenin equivalent voltage biased circuit where $V_b = I_b R_s$ and $R_l = R_p + R_s$

With these changes we pick up an additional coupled nonlinear ODE for the current

$$L\frac{dI}{dt} = V_b - I\left(R_l + R(T,I)\right) + \delta V \tag{3.6}$$

and we must also remove the assumption of constant voltage across the TES

$$C\frac{dT}{dt} = I^2 R(T,I) - P_{bath} + \delta P \tag{3.7}$$

In the coupled dynamical equations above, we also introduced δV and δP which will be place holders for pulses, oscillating perturbations, and various noise terms.

Component	Value	Comments
R_{bias}	1.25kΩ	UCB warm electronics
	2.5kΩ	Soudan warm electronics
T_{bias}	∼300K	Except at Soudan :)
$R_{feedback}$	1kΩ	
R_s	20-22mΩ	metal film resistor. With the current cold electronics, this is quite difficult to measure accurately
	+∼4mΩ	If T_{still} >1.2K, a normal Al wirebond is in series with the designed R_s [53]
T_s	∼600mK	In our cold electronics the shunt resistor is located on the still thermal stage
	∼1.2K	At UCB, the still stage runs hot
	∼1.0K	At Soudan, the still stage runs hot for 5 towers because the thermal conductance of the tower graphite is larger than expected
R_p	∼ 4mΩ	4 Mill-max pin/socket interconnections on 10mK stage
	+∼ 2mΩ	2 Mill-max pin/socket interconnections on 4K stage
	+∼ 4mΩ	If T_{still} >1.2K, a normal wirebond is also include in the total R_p [53]
T_p	∼40mK	Approximate temperature of base stage at UCB and Soudan
	1.0-1.2K	Approximate temperature of still stage at UCB and Soudan
	4.2K	4K stage at UCB (2 mill-max pin/sockets)
	∼5.5K	4K stage temperature at Soudan
L	∼100nH	Squid Inductance when feedback locked
	+50-150nH	Parasitic Inductance of wiring and detector with current cold electronics

Table 3.2: Cold Electronics Values

3.1.3 Equilibrium '$I_B I_S$' studies

Before deriving the small signal dynamics and noise about the equilbrium point for the more complex system, let's discuss how the equilibrium itself varies with a change in the voltage biasing [54] and how one can measure R_n and R_p. Experimentally, the simplest method of doing this is simply to voltage bias with a slow triangle wave so that the voltage drop across L is negligible(Fig. 3.6 left). Due to the non-linearity of the dynamical equations (Eq. 3.6 and 3.7), analytical simulations of these curves are impossible and one must therefore resort to computational methods.

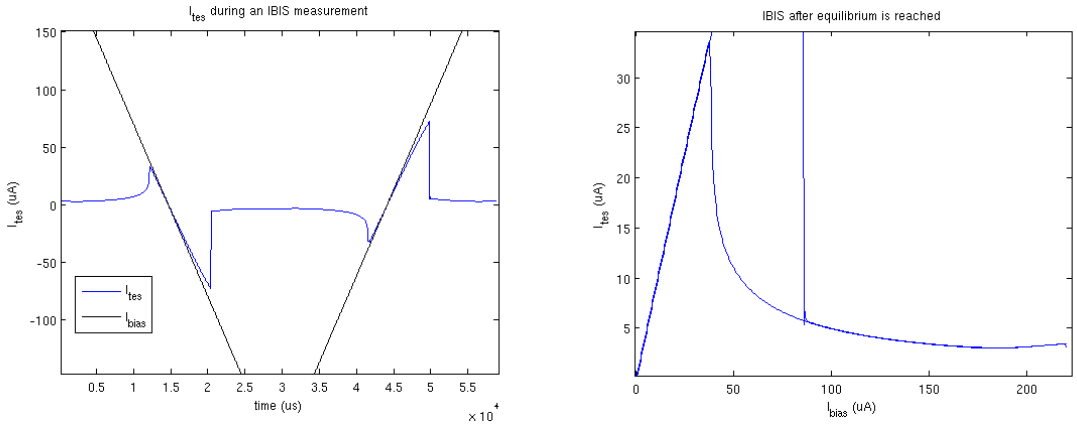

Figure 3.6: left: Simulated equilibrium current through a TES, I, plotted versus time for a triangle wave variation in voltage bias V ($\propto I_b$) right: I plotted directly against I_b

In Fig. 3.6 right , one can roughly pick out 3 distinct dynamical regions. First, at very small I_b, the current flowing through the TES is insufficient to heat the TES and thus the TES itself is entirely superconducting. With only the small parasitic resistance R_p on the TES leg of the circuit (Fig. 3.5 left), almost all the current flowing through the system (I_b) is flowing through the TES:

$$I = \frac{R_s}{R_s + R_p} I_b$$

Therefore, the superconducting region can be used to estimate R_p if R_s is precisely

known.

As the voltage bias is increased, the critical current is eventually reached and the system jumps from being superconducting to having some amount of resistance. Please notice that the 'snapping' point is dependent on past history, it's hysteretic. This follows simply from the fact that the critical current depends significantly on the temperature of the system. If the magnitude of the voltage bias is being decreased, then the temperature of the electronic system is $\sim T_c$ of the film. By contrast, if the magnitude is being increased from zero, then there is no joule heating since the film is superconducting and consequently the electronic tempature is very close to the substrate temperature, $\sim T_{bath}$. Since colder superconducting films have larger critical currents, the snap point occurs at a larger bias current.

At voltages higher than the snap point, the TES is biased with natural negative feedback in the middle of it's transition. As long as the width of the transition, ΔT_{90-10}, is significantly smaller than T_c then the cooling power is roughly fixed as is the joule heating (remember at equilibrium, the joule heating is equal to the cooling power). Assuming that the TES is truly voltage biased ($R_p << R_s << R_o$):

$$I \sim \frac{P_{bath}}{I_b R_s} = \frac{P_{bath}}{V_b}$$

As one can see in Fig. 3.7, the total power isn't exactly constant in this transition region, potentially for a few different reasons.

For single block TES structures, the most likely cause is the finite temperature width of the transition: smaller voltage biases require large current flow, or equivalently small resistances, to remain in equilibrium. Consequently, at low biases the required joule heating is slightly smaller than at large biases leading to the $P(V_b)$ curve being slightly positively sloped. As an masochistic exercise in differential calculus one can calculate that the expected slope is $\frac{dP}{dV_b} = \frac{2+\beta}{1+\beta+\frac{\alpha}{n}} I$ where β, the dimensionless current sensitivity of the TES, is defined later in Eq. 3.8.

In CDMS detectors, the TES is actually a composite object made of a large number of TES in parallel distributed over a large area. Unfortunately, our somewhat archaic film deposition machine has poor film property uniformity over full wafer scales and as such we usually have a 5-10mK gradient in T_c across the detector . This gradient completely swamps the intrinsic width of the transistion and consequently, the slope of the power curve in the transition region should not be used to estimate the intrinsic width.

Finally, as we'll discuss in much greater detail in the next chapter, thermal phase separation along the length of the TES also leads to large perturbations from the idealized constant power curve in the transition region.

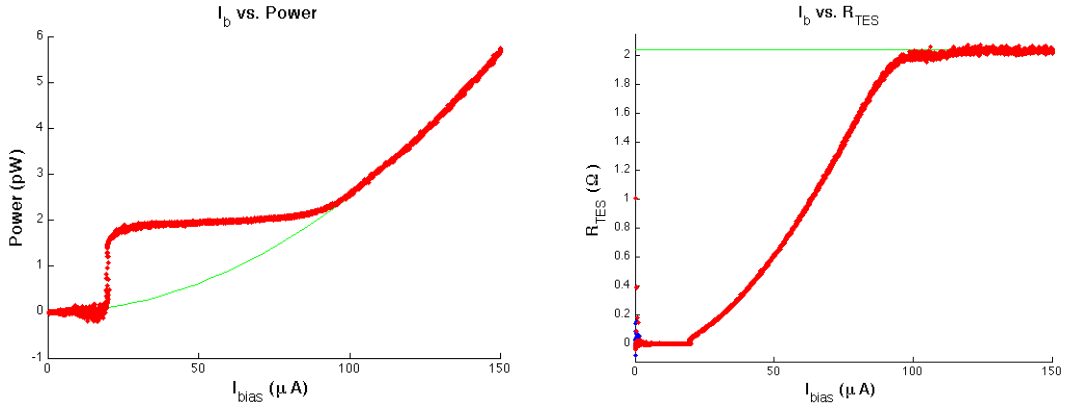

Figure 3.7: left: Measured Joule heating versus I_b for TES test structures. right: Measured TES resistance versus I_b for TES test structures(produced by Sean Hart)

In the final region of the IBIS curve, the voltage bias has been increased to such a level that the TES has been heated out of its transition region and it consequently behaves for all intents and purposes like a simple resistor so that

$$I = \frac{R_s}{R_s + R_p + R_n} I_b$$

Thus, this normal section of the IBIS can be used to estimate R_n given a knowledge of R_s.

Determination of TES cooling coefficients

Primarily, we use IBIS curves to measure R_p and R_n for the device as well as to determine I_b required to bias the TES at the desired equilibrium resistance of the TES, R_o, for best sensitivity and necessary bandwidth. Additionally though, by taking multiple IBIS curves at various bath temperatures, T_{bath}, one can experimentally measure K, n, and Σ by measuring the the joule heating as a function of T_{bath} ($I_o^2 R_o = \Sigma \mathcal{V}_{tes}(T_o^n - T_{bath}^n)$).

Over the years, this study has been made numerous times by our group ([55],[51]) with little internal consistency suggesting that there is an underestimate of various systematics. The most likely culprits are:

- Poor thermal coupling between the Si chip/test device and the bath (negative bias for K)
- Poor thermometer calibration
- Poor thermal coupling between the bath and the thermometer(positve bias on K)
- Large β in W films (next section)

Data from the most recent study by Sean Hart in 2009 on the geometries seen in Fig. 4.4 are shown in Fig. 3.9. In this study, we experimentally measured the thermal conductance of the Stycast epoxy joint connecting the Si test chip to the copper tower and from this estimated the Si chip temperature, T_{Si}, as a function of T_{bath} and P_{joule} to remove the first systematic mentioned above. Unfortunately, we didn't expend significant effort in minimizing the other possible systematic sources.

The experimental heating curves are consistent with the expected n=5 power law, which suggests that the dominant thermal impedance is the coupling between the W electron and phonon systems. When biased, the effective temperature of the quasiparticles is $\sim T_c$ while the W phonon system is well coupled to the thermal bath and as such has a temperature near T_{bath}.

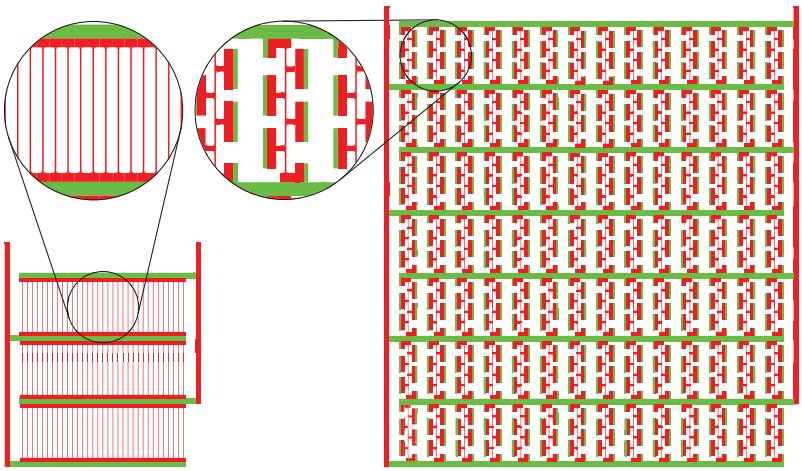

Figure 3.8: A pair of TES structures consisting of 100 100um long W TESs (red) connected in parallel by superconducting Al leads (green). The line width of all TESs is $\sim$1.5 μm. For the device on the right, each W fin connector overlaps a rectangular Al region by 3.5um at its edge. In the region where the W does not overlap the Al, the side connectors each have a volume of 5.6μm^3 and the end connectors have a volume of 3.3 μm^3. The thickness of the W in these devices is $\sim$40nm.

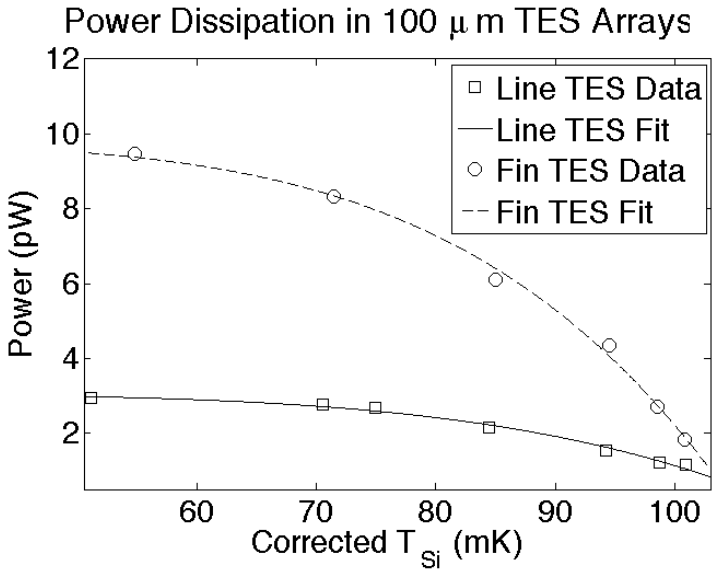

Figure 3.9: Joule heating as a function of the Si wafer temperature for two different TES geometries (produced by Sean Hart).

In alignment with our expectations (studies were also done on 300um long TES structures as well), the electron-phonon coupling coefficient was found to scale linearly with the total W volume of the line only TES devices,$\mathcal{V}_{TES}$, and consequently it's natural to define the phonon coupling per unit volume, $\Sigma = K/\mathcal{V}_{TES}$. Least Squares fitting gives us a best estimate of $\Sigma = 0.32\text{x}10^9 \pm 0.02(\text{stat})\pm 0.12(\text{sys})\frac{W}{m^3K^5}$ where we've estimated the systematic error by assuming a 4mK miscalibration of the thermometer.

The more complex W structures with fin connectors have a physical volume which is ∼x6 larger than the simple line geometry but their electron/phonon coupling coefficients were increased by only ∼x4. This suggests either a large thermal gradient along the W fin connector due to small quasiparticle thermal conductivity along the fin connector, or a change in Σ due to the proximity of Al.

3.1.4 Small Signal Dynamics

As with the simplified analysis, let's taylor expand to first order about the equilibrium and then rewrite $\frac{\partial R}{\partial T}\big|_{I_o,T_o}$ in terms of the dimensionless sharpness parameter α. Let's also define an analagous dimensionless parameter for the current as

$$\beta = \frac{I_o}{R_o}\left.\frac{\partial R}{\partial I}\right|_{I_o,T_o} \tag{3.8}$$

Then,

$$\begin{aligned}\frac{d}{dt}\begin{bmatrix}\delta I\\ \delta T\end{bmatrix} &= -\begin{bmatrix}\frac{R_l+R_o+I_o\frac{\partial R}{\partial I}}{L} & \frac{I_o\frac{\partial R}{\partial T}}{L}\\ -\frac{2I_oR_o+I_o^2\frac{\partial R}{\partial I}}{C} & \frac{-I_o^2\frac{\partial R}{\partial T}+G}{C}\end{bmatrix}\begin{bmatrix}\delta I\\ \delta T\end{bmatrix}+\begin{bmatrix}\frac{\delta V}{L}\\ \frac{\delta P}{C}\end{bmatrix}\\ &= -\begin{bmatrix}\frac{R_l+R_o(1+\beta)}{L} & \frac{G\mathcal{L}}{I_oL}\\ -\frac{I_oR_o(2+\beta)}{C} & \frac{G(1-\mathcal{L})}{C}\end{bmatrix}\begin{bmatrix}\delta I\\ \delta T\end{bmatrix}+\begin{bmatrix}\frac{\delta V}{L}\\ \frac{\delta P}{C}\end{bmatrix}\end{aligned} \tag{3.9}$$

Finally, we can switch to the frequency basis and then invert the impedance matrix (which we'll call M) to find the current and temperature responses to small power or voltage bias excitations.

$$\begin{bmatrix} i\omega + \frac{R_l+R_o(1+\beta)}{L} & +\frac{G\mathcal{L}}{I_o L} \\ -\frac{I_o R_o(2+\beta)}{C} & i\omega + \frac{G(1-\mathcal{L})}{C} \end{bmatrix} \begin{bmatrix} \delta I \\ \delta T \end{bmatrix} = \begin{bmatrix} \frac{\delta V}{L} \\ \frac{\delta P}{C} \end{bmatrix} \tag{3.10}$$

$$\begin{bmatrix} \delta I \\ \delta T \end{bmatrix} = M^{-1} \begin{bmatrix} \frac{\delta V}{L} \\ \frac{\delta P}{C} \end{bmatrix} \tag{3.11}$$

3.1.5 Thermal Power to Current Transfer Function

By disturbing the TES with a small fluctuating thermal power source, δP, we can calculate the transfer function (i.e. green's function) of the current response in frequency space through Eq. 3.11.

$$\begin{aligned} \frac{\partial I}{\partial \delta P} &= \frac{M^{-1}_{(1,2)}}{C} \\ &= \frac{-G\mathcal{L}}{C I_o L} \frac{1}{\left(i\omega + \frac{G(1-\mathcal{L})}{C}\right)\left(i\omega + \frac{R_l+R_o(1+\beta)}{L}\right) + \mathcal{L}\frac{R_o}{L}\frac{G}{C}(2+\beta)} \end{aligned} \tag{3.12}$$

One can simply not overemphasize the importance of this calculation. From this equation we can calculate both the magnitude of the current signal for an input thermal power and the pulse shape distortion caused by the sensing system. Qualitatively, we can see in Fig. 3.10 that above $\frac{1}{\tau_{\text{eff}}}$ the sensitivity of our sensor to thermal power fluctuations starts to diminish substantially. The qualitative reason is that for power fluctuations above this frequency, as soon as the TES starts to heat up, the thermal power has already flipped signs and thus the maximum temperature excursions are quite suppressed.

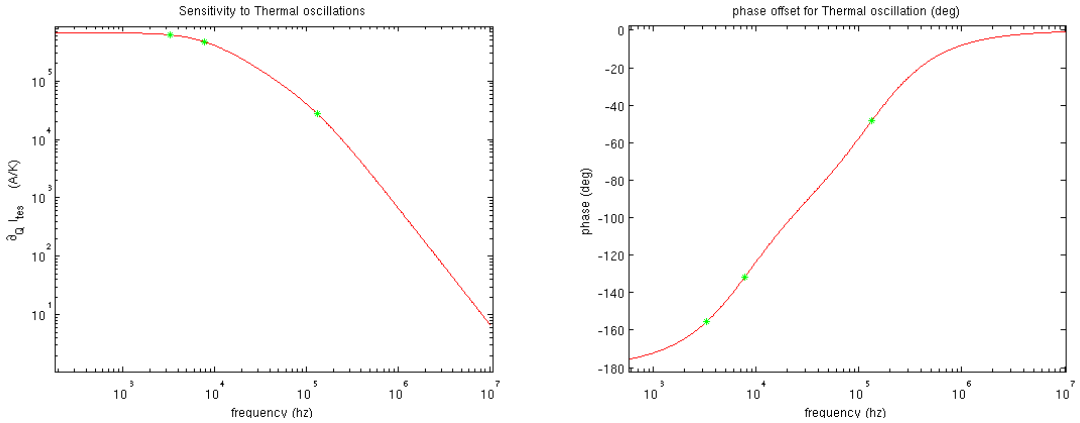

Figure 3.10: Magnitude (left) and phase (right) of the current response for a differential thermal power input.

To gain a little further intuition, let's look at the limiting case where $L \rightarrow 0$. Then,

$$\lim_{L\to 0} \frac{\partial I}{\partial \delta P} = \frac{-1}{I_o\left((R_o - R_l) + \frac{R_l + R_o(1+\beta)}{\mathcal{L}}\right)} \frac{1}{(1 + i\omega/\tau_{\text{eff}})} \tag{3.13}$$

where τ_{eff} is

$$\lim_{L\to 0} \tau_{\text{eff}} = \frac{C}{G\left(1 + \mathcal{L}\frac{(1-\frac{R_l}{R_o})}{1+\beta+\frac{R_l}{R_o}}\right)} \tag{3.14}$$

We've now generalized Eq. 3.5 to account for the effects of both β and R_l on τ_{eff}. This additional dependence of the sensor bandwidth upon $\frac{R_o}{R_l}$ and β is pretty large and both of these effects could be increasing τ_{eff} from the simplistic expression calculated in Fig. 3.3. When running G48 at UCB, $R_l \sim 34\text{m}\Omega$ and $R_o \sim 175\text{m}\Omega$ for a ratio of 5:1 which means that the imperfect nature of our voltage bias dropped our sensor bandwidth by $\sim \frac{1}{3}$. This is a far cry from the needed 90% drop needed to bring all measurements into agreement but it is a start.

A large β could also be the cause for our small measured bandwidth ... but it would have to be pretty large! For this to be the primary culprit for our small τ_{eff} we would need $\beta \sim 4$ (this is pretty big in the world of TES).

Roughly, the DC value comes from the idea that to remain in equilibrium, the addition of a heat source must be offset by a decrease in the joule heating, $\delta P + \delta I V_b = 0$, or $\delta P = -V_b \delta I$ when there is no R_l and $\mathcal{L} >> 1$.

3.1.6 Voltage Bias Excitations: Complex Impedance

To get around the fact that $\frac{\partial I}{\partial P}$ is not directly measurable in our detectors, in the previous section we used voltage bias spikes as a proxy to a thermal heat pulse. In the more complex derivation which included an inductor (Eq. 4.8) that we just completed however, δV and δP excitations are clearly different beasts. This suggests that for high frequencies we need be a lot more careful.

A second reason for us to really spend time studying TES response to voltage fluctuations is that experimentally they are so incredibly easy for us to create in a reproducible manner. All you need to do is just put some type of small signal jitter on top of the DC bias and record with your standard DAQ setup. Furthermore, the sensitivity of this measurement can be increased to an almost arbitrarily high precision by increasing the time of the measurement. It's for this reason that throughout the TES community (even those experiments which can directly measure $\frac{\partial I}{\partial P}$), complex impedance characterization is now the defacto standard.

Bizarrely, even though this revolution was at least partially led by ex-CDMS grad-students, Tali and Tarek, ([56],[57],[58]), CDMS itself has never spent significant resources on these studies. In my opinion, this oversight can be traced to the combination of numerous factors:

- There was a 5 year period in which detector R&D was completely frozen. Thus, improved sensor understanding would not have necessarily lead to a detector

redesign (CDMS had more important problems).

- There was a false belief in the collaboration that T_c gradients limited the usefulness of complex impedance studies.
- All nascent attempts to study these curves led to confusion because shapes did not match theory due to phase separation (next chapter) and difficulties in removing the SQUID transfer function due to the fact that the mutual inductance between feedback and sensor loops on our current SQUID chips lead to a SQUID transfer function which varies with R_o which was studied and understood by Bruce and Kyle [59]
- For the last 4 years, we've been switching to new warm electronics and DAQ. Consequently, there has been negligible desire to write automation codes for IBIS and complex impedance measurements at UCB.

So in this subsection, $\frac{\partial I}{\partial V}$ curves will only be shown for the 100um long line device (Fig. 4.4 left) and even for this device the analysis will be quite limited compared to what is now standard in the TES community. We will though briefly discuss some of these more advanced techniques since they will certainly be used with next generation CDMS detectors that have decreased TES length/lower T_c (no phase seperation) and new squid electronics.

When trying to use $\frac{\partial I}{\partial V}$ to understand $\frac{\partial I}{\partial P}$, the first thing to notice is that the poles for these transfer functions are absolutely identical as long as there is some off diagonal mixing in the M matrix (there is) from Eq. 3.10. So, by carefully measuring the voltage transfer function (i.e the complex impedance) by either placing a small AC voltage oscillation on top of the equilibrium DC bias or by placing a tiny squarewave function on top of the DC bias, we can at minimum gain information upon all of the pole locations in the $\frac{\partial I}{\partial P}$ green's function. Furthermore, this trick is independent of the complexity of the M matrix. Throughout this chapter, our M matrix has been 2 dimensional (1 current and 1 thermal Degree of Freedom, DOF). In the next chapter though, we will vastly complicate the issue by adding additional thermal

DOFs (phase separation and W fin connectors) and our understanding of the actual sensor dynamics will be more qualitative than quantitative. Even in this case though, we can say with certainty that the measured $\frac{\partial I}{\partial V}$ poles are the poles of $\frac{\partial I}{\partial P}$.

Within the simple single thermal DOF TES dynamical model that we have been developing in this chapter, $\frac{\partial I}{\partial P}$ in its entirety (poles and zeros) is fully constrained by $\frac{\partial I}{\partial V}$ or equivalently the complex impedance (quick aside: Lindeman proves in this very nice paper [60] that for a subset of more complex systems $\frac{\partial I}{\partial V}$ still completely defines $\frac{\partial I}{\partial P}$.):

$$\begin{aligned} Z_{tot} &= \frac{\partial I_{tes}}{\partial V_b}^{-1} \\ &= \frac{L}{M^{-1}_{(1,1)}} \\ &= R_l + i\omega L + Z_{tes} \end{aligned} \tag{3.15}$$

where

$$Z_{tes} = R_o\left(1+\beta\right) + \frac{R_o\mathcal{L}}{1-\mathcal{L}}\frac{2+\beta}{1+i\omega\frac{C}{G(1-\mathcal{L})}} \tag{3.16}$$

To obtain some qualitative feel for the complex admittance function, let's look at Fig. 3.11. At high frequencies, the current response is suppressed by the inductor (high frequency black x is the inductive pole). We can also clearly see that below ω_{eff} (low frequency black x), the current response is anti-correlated with the voltage oscillation. This is absolutely expected and can be simply understood by realizing that for small changes in voltage, the system will remain within the superconducting transition and therefore the quasi-equilibrium condition

$$P_{bath} \simeq P_{joule} = V(t)I(t)$$

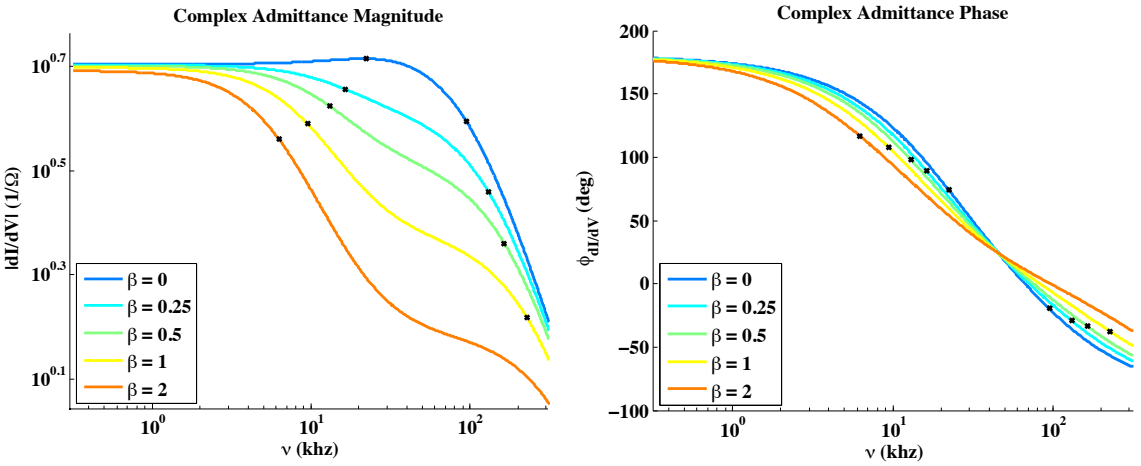

Figure 3.11: Simulated magnitude (left) and phase (right) of the current response for a differential voltage bias oscillation for an iZIP4/5 TES with Tc=65mK for various β

can be differentiated with time to give

$$\frac{dP_{bath}}{dt} \simeq 0 \simeq \frac{d}{dt}\left(V(t)I(t)\right) = V(t)\frac{dI(t)}{dt} + I(t)\frac{dV(t)}{dt}$$

or

$$\frac{dI(t)}{dt} \simeq -\frac{1}{R_o}\frac{dV(t)}{dt} \tag{3.17}$$

The DC approximation above or equivalently a simplification of eqs. 3.15 and 3.16 in the $\mathcal{L} >> 1$ limit for $\omega = 0$, also shows that at low frequency, the magnitude of the impedance of the TES is $\sim R_o$ (precisely $R_o - R_l$) instead of the dynamical impedance $R_o(1+\beta)$ which means that these low frequencies have minimal dependence on β.

On the other hand, above ω_{eff} but below the inductive pole, the TES never has time to heat up and thus the TES current response is roughly in phase with the voltage excitation. It's in this region as well that one is fully sensitive to β. In fact, if the two

poles are well separated, you can simply read β directly off the $\frac{\partial I}{\partial V}$ plot and not resort to least squares fitting by looking at the ratio of the two plateaus. Finally, note that β tends to separate the two poles.

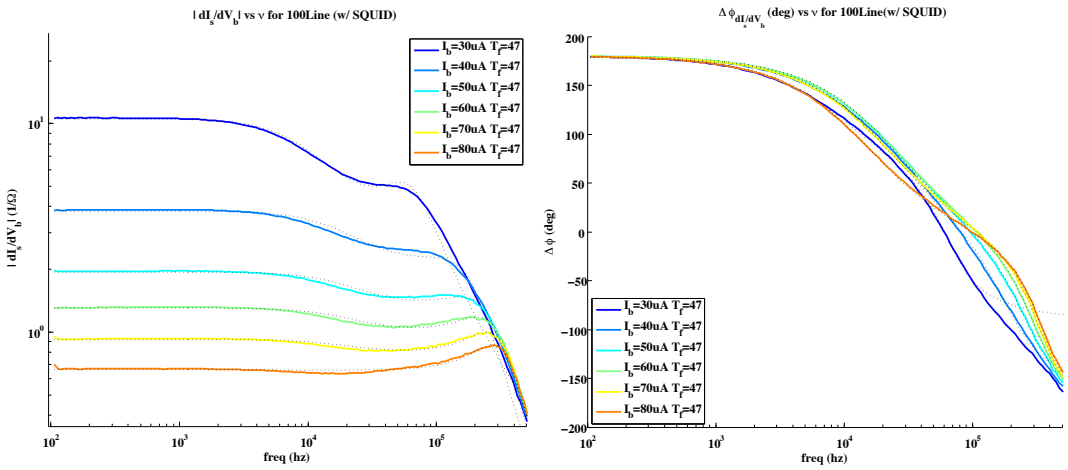

Figure 3.12: Experimental $\frac{\partial I}{\partial V}$ curves for the 100μm line test structure with T_c=110mK and R_n=1.9Ω

Let's apply this knowledge to measured $\frac{\partial I}{\partial V}$ curves for the 100μm line TES W test structure (Fig. 3.12). At low frequencies, the curves are pretty much textbook. There is just a single low frequency pole (in contrast to what was seen in the Glitch pulses) that for bias points with $20\% < R_o/R_n < 50\%$, $\tau_{\rm eff}$ was fit to be 7-10μs (Tab. 3.3). The uncertainties for these bandwidth estimates are completely dominated by systematics. As previously alluded to, the feedback coil in our current cold electronics has significant coupling to the sensor coil which suppresses L when the squid is in feedback mode [59]. Furthermore, this suppression depends upon R_o and thus the squid transfer function varies depending upon the bias point. However, in creating the $\frac{\partial I}{\partial V}$ curves shown in Fig. 3.12 we subtracted the squid transfer function measured at R_n and thus we've induced (no pun intended!) the dominant systematic in these estimates. To bound the scale of this error, $\frac{\partial I}{\partial V}$ pole locations were fit both with and without squid transfer function subtraction.

As with the CDMS detector glitch events, these measured $\tau_{\rm eff}$ are mysteriously quite slow compared to the naive expectations of $\sim$1μs for a W film T_c of 109$\pm$ 2mK

$I_b(\mu\text{A})$	R_o (mΩ)	$\frac{R_o}{R_n}$	τ_{eff}	β	α
30	120 ± 5	0.06 ± 0.006	20 ± 2	$1.2 \pm .1$	111 ± 20
40	250 ± 5	0.13 ± 0.006	11.5 ± 3	$0.55 \pm .05$	111 ± 20
50	400 ± 5	0.21 ± 0.006	8.5 ± 0.5	$0.40 \pm .04$	125 ± 20
60	600 ± 5	0.32 ± 0.006	7.8 ± 0.2	$0.26 \pm .03$	117 ± 20
70	840 ± 5	0.44 ± 0.006	8.3 ± 0.3	$0.15 \pm .02$	125 ± 20
80	1100 ± 5	0.58 ± 0.006	10.9 ± 0.3	$.07 \pm .02$	111 ± 20

Table 3.3: Dynamical Properties of the 100μm line test structure for various I_b ($I_b = V_b/R_s$

from Figs. 3.2 and 3.3. Furthermore, this device had a large $R_n(1.9\Omega)$ and these measurements were taken with $T_{bath} \sim 47$mK, so bandwidth suppression due to these complexities should be minimal (Eq: 3.14).

At very low voltage biases ($\sim 6\%$ R_n: blue curve), we do clearly see a suppression of the response plateau at high frequencies which when fit suggests a $\beta = 1.2 \pm 0.2$ but our more standard bias points of $1/5R_n < R_o < 1/3R_o$ have an acceptable $0.26 < \beta < 0.40$. Basically, we can say that our measured ω_{eff} is being suppressed by $20 - 30\%$ due to β, and our best guess for α is ~ 125 which corresponds to a $\Delta_{T90-10\%}$ >2mK. Clearly, something is amiss!

If we are grasping for straws, one possible systematic in the $\frac{\partial I}{\partial V}$ measurement is that the fridge thermometer used to estimate the T_c of this device was self heating/poorly thermally heat sunk and thus rather than a T_c of ~ 110mK, the real value was actually 100mK (anything more than this would have been really hard to fathom). However, even with this large hypothesized systematic though, the two measurements are still in disagreement and in the future more careful studies will have to be performed. Personally, I have an inclination towards believing this $\frac{\partial I}{\partial V}$ result, but this is in some sense personal judgement.

So far, we've discussed how ω_{eff}, β, R_o, and $\omega_{\sim L/R}$ are all readily estimable from Z_{tot} or $\frac{\partial I}{\partial V}$. We would though really like to estimate α and C individually to quantify the phase separation length scale and unfortunately, in the limit of $\mathcal{L} >> 1$, Z_{tes} only depends on the combination $\mathcal{L}/C$. In a neat trick, to my knowledge first used

by Tarek and the Goddard group [56], complex impedance measurements were done at two vastly different bath temperatures such that $\mathcal{L}$ varied significantly between the two measurements ($\mathcal{L} \propto 1 - \frac{T_{bath}^n}{T_c^n}$). By least squares fitting both measurements together (being careful to allow freedom for β changes), $\mathcal{L}$ and C can be separated. Note that the α estimate shown in fig. 3.2 is the limiting case of this idea where one has attempted to go to $\mathcal{L} \sim 0$ but in this method all of the systematics discussed (i.e. self heating and β) are now explicitly measured.

3.1.7 Electrothermal Oscillation

After deriving Eq. 4.8, we immediately Fourier transformed the equation and calculated both the power/current transfer function and the complex impedances. We could have also traveled down another path and calculated the eigenvectors and eigenvalues. Most interestingly, the phase difference in the off diagonal elements means that there is a possibility that the eigenvectors have imaginary components; physically the system has an oscillation resonance.

The very fact that resonances can be created in a system with nominally only an inductor and a resistance is quite intriguing. Naively, one would like to ask, 'Where's the capacitor?'. Bizarrely, due to the driven nature of the system, the thermal heat capacity of the TES plays this role. To see how this happens, let's displace the system from equilibrium with a thermal heat pulse. This will, of course, immediately increase both the temperature and the resistance. The current on the other hand, decreases with a time delay due to the inductor. Effectively, for a short time period after the pulse, the inductor increases the voltage across the TES to discharge the energy that was housed in the inductor's B-field into the TES causing additional increases in both the temperature and resistance. The TES will eventually begin too cool due to the decreased joule heating. Again though the inductor causes a delay in the current response: while cooling, the voltage across the TES is suppressed because the inductor is siphoning off joule heating to the TES so as to recharge it's B-field. Consequently, the temperature of the TES falls below the equilibrium point; we've

set up an electro-thermal oscillation.

Of course, these oscillations are unwanted and thus let's find the constraint on the operating point's resistance, R_o, such that the dynamics are overdamped (both eigenvalues real) [49] [48]:

$$R_o > \frac{GL\mathcal{L}}{C(3+\beta-2\sqrt{2+\beta})}$$

or

$$\frac{L}{R_o} < \frac{C}{G\mathcal{L}}(3+\beta-2\sqrt{2+\beta})$$

In calculating this constraint we assumed that R_l is negligible and also that the cooling of the system is dominated by electrothermal feedback ($\mathcal{L} >> 1$). Notice that this is the one place where having a large β is an advantage. At $\beta = 0$, $\tau_{\text{eff}} > 6\frac{L}{R_o}$ where for $\beta = 2$, $\tau_{eff} > 3\frac{L}{R_o}$.

3.2 Noise

To quantify the sensitivity of phonon sensors, we must also estimate the intrinsic noise of our sensing circuit. A warning before we begin ... this is a reasonably complex system and thus we have many sources of noise that we must estimate and then sum in quadrature. We will though make a significant effort to determine the dominant noise source so that back of the envelope calculations are possible.

3.2.1 Thermal conductance noise across G_c

As with their electronic brethren, thermal conductors are noisy and infact well designed TES sensors are dominated by thermal fluctuation noise (TFN) across the

thermal link which connects the TES to the cooling bath in the signal region.

We'll reprint the traditional derivation of the thermal power fluctuation spectrum which can be found in many places including [61] with hopefully a tinge of interesting insight.

Deriving PSD of thermal impedance noise

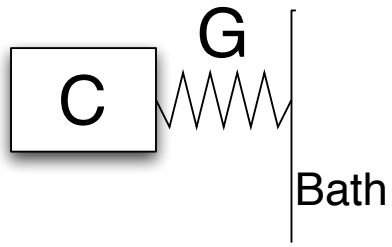

Figure 3.13: simplistic thermal circuit

The derivation precedes with the standard assumptions. First and most importantly, one assumes that the random power fluctuations dynamically evolve in an identical manner as their larger non-stochastic brethen (the Langevin assumption [61]). By this I mean that the very same green's function which determines the dynamic behavior of macroscopic deviations from equilibrium will also match the dynamical evolution of these microscopic stochastic fluctuations.

With this assumption in mind, the first step is clear: let's find the dynamical transfer function for how a heat pulse, $\delta P(t)$, changes the temperature of a simple block with a heat capacity, C, that is coupled to a thermal bath by a thermal conductance ,G, (Fig. 3.13).

$$C\dot{T} = -GT + \delta P(t)$$

To get the green's function, let's just Fourier transform the linear differential equation

and then solve for $T(\omega)$:

$$T(\omega) = \frac{\delta P(\omega)}{G\left(1 + i\frac{C}{G}\omega\right)} \tag{3.18}$$

To help with insight, a graph of the transfer function is shown in Fig. 3.14. Notice that at frequencies well above the inverse of the decay constant, $\tau = \frac{C}{G}$, the magnitude of G doesn't change the thermal response. Physically, the oscillation is so quick that before the system has a chance to respond and heat up, the oscillation has reversed sign and thus cools itself. By contrast, at frequencies well below the decay constant the magnitude of G is extremely important. Physically, the larger the thermal coupling the harder it is to get a significant temperature difference between the system and it's bath with a constant DC power.

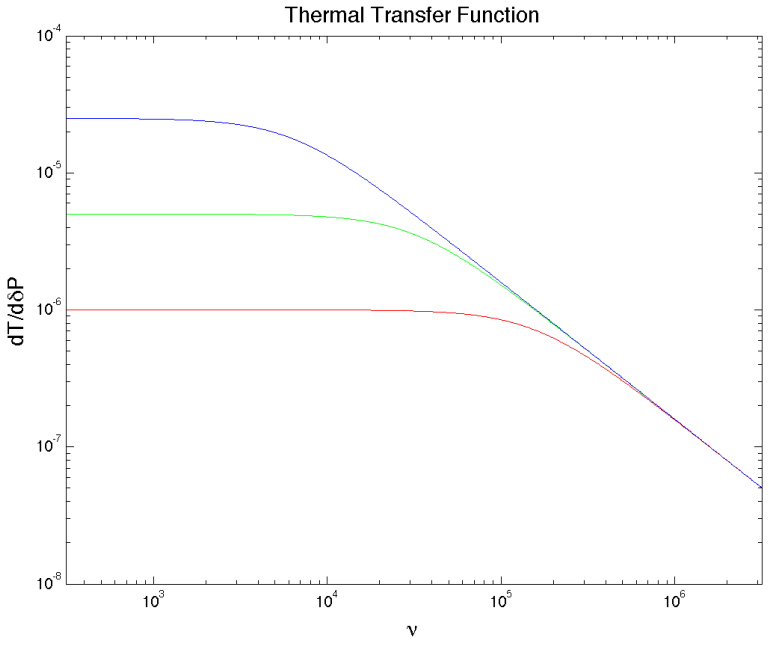

Figure 3.14: Here we graphed the thermal transfer function for various G (blue = small G red= large G). Notice how the high frequency response is totally determined by C, while the low frequency response is completely determined by G

The second assumption in the standard thermal noise derivation is that the frequency

power spectrum for the stochastic thermal noise, $S_{\delta P(\omega)}$, is white. This is also an eminently reasonable assumption. If we assume that the thermal energy is carried into the system in small random bursts that have time lengths which are much smaller than the dynamics of the system (shot noise... imagine an excited electron that traverses some boundary), then we can certainly approximate the spectrum as white.

$$S_T(\omega) = \frac{S_{\delta P}(\omega)}{G^2\left(1 + \left(\frac{C}{G}\right)^2 \omega^2\right)} = \frac{S_{\delta P\, o}}{G^2\left(1 + \left(\frac{C}{G}\right)^2 \omega^2\right)}$$

As an aside, our thermal conductance certainly doesn't physically match this electronic shot noise imagery. In our case, the hot quasi-particle (dressed electron) system in W is very poorly connected to the much colder phonon system of the W and thus our impedance is quantum-mechanical in nature. This isn't a problem though and the above derviation still holds. All that is required is that the system is shot noise like... thus as long as the creation of one phonon doesn't effect the probability of annihilating/producing another phonon over times scales of our sensor (bounded on the highside by L/R $\sim 1\mu s$) then the second assumption is valid.

Statistical mechanics is absolutely useless for calculating anything to do with time scales because at it's very core, one assumes that systems are in absolute equilibrium ... there is no change in the probability functions with time! However, one can calculate the overall statistical fluctuation of the various exstensive properties of a system given a microcanonical coupling and then use this and the knowledge of the noise spectrum shape (the time scale part which is derived from the Langevin assumption and the assumption of white noise in the heat power spectrum) together to calculate power noise spectrum.

Let's start with the partition function (Z) and show how one can calculate both the average energy of the system and the variation in the average energy simply by taking derivatives with respect to β (aside: here we're using β in the thermodynamic sense as $\frac{1}{k_b T}$ rather than as the dimensionless measure of TES resistance dependence on current).

$$< E >= \frac{\sum E_i e^{-\beta E_i}}{\sum e^{-\beta E_i}} = \frac{\frac{-\partial Z}{\partial \beta}}{Z} = -\frac{\partial ln(Z)}{\partial \beta}$$

$$\sigma^2_{<E>} = \frac{\sum E_i^2 e^{-\beta E_i}}{\sum e^{-\beta E_i}} - < E >^2 = -\frac{\partial < E >}{\partial \beta} = \frac{\partial < E >}{\partial T} k_b T^2 = C k_b T^2 \tag{3.19}$$

At the end of Eq. 3.19 we've explicitly related the energy variance of an equilibrium system with it's heat capacity, C. Taking a step back, not even considering the very clean derivation shown, the answer seems to be reasonable. First, one would expect the energy variation to scale linearly with the number of elements in the system and thereby C just because of brute $\sqrt{N}$ statistics: if I have n statistically independent processes then the variance of summed properties will scale linearly with the number of processes. Secondly, as absolutely required there is no mention of G anywhere because again the magnitude of G will only change the time scales over which a system gets to equilibrium.

To couple these two pieces of information, we must only realize the the integral over all frequencies of the energy noise power spectrum,$S_E(\omega) = C^2 S_T(\omega)$, is equal to the variance.

$$C k_b T^2 = \sigma^2_{<E>} = \int \frac{d\omega}{2\pi} S_{<E>}(\omega) = \int \frac{d\omega}{2\pi} \frac{C^2 S_{\delta P o}}{G^2 \left(1 + \left(\frac{C}{G}\right)^2 \omega^2\right)}$$

or

$$S_{Ptfn} = 4 k_b T^2 G \tag{3.20}$$

where the power spectrum, $S(\omega)$, has been defined implicitly through

$$< f^2 >= \int_0^\infty \frac{d\omega}{2\pi} S_f(\omega)$$

For those of you really following along, please notice that the integral only covers positive coefffients (certainly an easy way to pick up an extra factor of 2).

Again, at first glance this answer passes the smell test. Let's say I have a system coupled to a bath by a thermal link G and then add a second identical thermal link in parallel. This second thermal link is completely independent of the first and thus one would expect the two thermal fluctuation spectrums to add in quadrature (i.e. the power spectrums simply sum) which the equation clearly shows since G scales linearly with the number of links added. Secondly, the power spectrum doesn't depend on the heat capacity of the connected system! Again, this is what one would expect.... randomly fluctuations at some boundary shouldn't depend on variables which are completely non-local unless there's some really interesting and weird physics occuring.

On a second glance though, these equations deserve a little more attention. In particular, I'll highlight the strangeness of this result by looking at two systems with identical C but wildly different thermal conductances, G_1 and G_2 where $G_2 >> G_1$. From Eq. 3.20, we know that raw amount of fluctuating heat flowing through G_2 is significantly larger in size than the amount of stocastic heat flux in G_1. Naively, one would then expect that the thermal/energy variance should also then be greater for G_2. However, this is not the case. We derived in Eq. 3.19, that the energy variance is independent of the size of the thermal conductance. Thus, we have a slight quandry; clearly our intuition is letting us down. In fact it is. We must also take into account how the thermal conductance effects the transfer function. Explicitly, the increased stochastic thermal noise through high G couplings, is offset by the fact that the larger thermal conductance also helps to dissipate random fluctuations quicker (Eq. 3.18).

The above argument fundamentally relies upon the fact that all elements are in equilibrium. During operation however, this certainly isn't the case: there's a large temperature difference between the TES and the bath. In the limit of ballistic phonon transport between the two temperatures, Eq.3.20 is suppressed linearly by the factor

[62] [63]:

$$F_{tfn}(T, T_{bath}, \text{ballistic}) = \frac{(T_{bath}/T)^{n+1} + 1}{2}$$

which for $T_{bath} \to 0$ (where we would like to be) gives us $F_{tfn} = 1/2$ which seems reasonable since we should naively be able to associate the thermal fluctuations in the equilibrium case as being 1/2 from fluctuations in the number of phonons produced in the bath and absorbed in the heat capacity, while the other 1/2 would be fluctuations in the number of phonons produced in the heat capacity and absorbed by the bath.

The other limiting case is the diffusive limit [64] in which F_{tfn} takes the form:

$$F_{tfn}(T, T_{bath}, \text{diffusive}) = \frac{n}{2n+1} \frac{(T_{bath}/T)^{2n+1} - 1}{(T_{bath}/T)^{n} - 1}$$

Calculating Thermal Fluctuation Noise

Now that we know the thermal power fluctuation spectrum, we need only to see how it couples through to the current signal that we measure. Once again, positing the Langevin assumption, we'll just use the macroscopic transfer function (Eq. 3.12) and consequently the current noise caused by thermal fluctuations is simply

$$S_{ITFN} = \frac{\partial I}{\partial P}^2 4k_b T^2 G F_{tfn}$$

To make comparisons between the various Johnson noises and TFN noise more straightforward, let's substitute in the low frequency limit of the transfer function

(Eq.3.13) as well as rewriting G in terms of P_{bath} (Eq. 3.3)

$$\lim_{L\to 0} S_{I\,TFN}(\omega) = \frac{4k_bT}{R_o}\frac{nF_{tfn}}{\left(1-\frac{T_{bath}^n}{T_o^n}\right)}\frac{R_o^2}{(R_o-R_l)^2}\frac{1}{1+\omega^2/\tau_{\rm eff}^2} \tag{3.21}$$

So, at low frequencies and with $R_l = 0$, **the TFN is just the naively calculated Johnson noise boosted by** $\frac{F_{tfn}n}{1-\frac{T_{bath}^n}{T_o^n}}$.

3.2.2 Johnson load noise

To keep our $\frac{\partial I}{\partial P}$ bandwidth high, we found that we needed R_l, or equivalently R_s and R_p, to be much smaller than R_o. This at minimum necessitated the use of superconducting wiring (Al films on the detector itself, NbTi on the vacuum coax, flyover) throughout the cold electronics.

We did though choose to have 6 millmax normal metal pin connectors (small black circles in Fig. 3.15) each with $\sim$ 1mΩ in series with the TES for our CDMS II electronics. The decision to accept this amount of R_p was definitely an optimization of two directly competing design goals. On the one hand, we want highly sensitive detectors. On the other hand, we would like to make designs which are easy to assemble and disassemble multiple times which is definitely an issue with wirebonding or soldering. At Stanford back in the 90's, we attempted to get the best of both worlds by using tinned millmax connectors and depressingly found that after the first few assembly cycles they would become normal because the Sn film would just flake off. So, we decided to accept and design around the R_p associated with normal metal connectors.

There is one other design compromise in our current CDMSII cold electronics which should be discussed. Sensor wiring goes from the detector (on the mixing chamber thermal stage), up through the still stage (nominally 600mK), to the 4K stage, then back down to the still stage to connect with the SQUIDs. This is clearly not optimal

design! A much simpler design would have 4 millmax pin connectors and go directly from the base thermal stage to the 600mK stage. Even better, one could place R_s on the base stage again with 4 millmax pins. Both of these would have less R_p (good), be simpler (good), and have less thermal conductance between the 4K and the 600mK stages and thus be easier on the fridge (good).

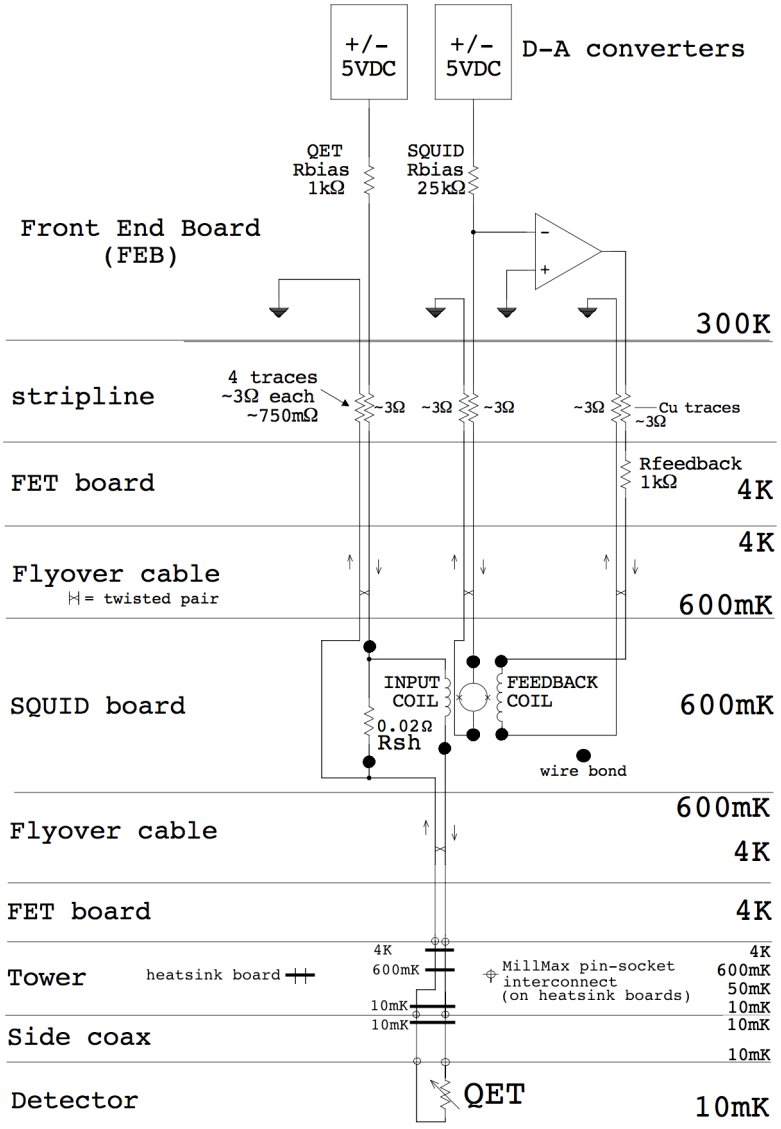

Figure 3.15: CDMS II Cold Electronics Layout (From Dennis) [18]

The reason why the electronics weren't originally designed in this manner is purely

historical. The cold electronics were originally designed for high impedance NTD BLIP detectors which had their phonon signals read out by FETs on the 4K stage just like charge channels. When our collaboration switched over to low impedance SQUID readout and TESs, we didn't completely redesign the cold hardware but rather made this setup to save having to remanufacture the vacuum side coaxes and rigid thermal assembly (tower).

Furthermore, both the UCB and Soudan dilution fridges have still stages which operate abnormally hot. Instead of having the stage around 600mK (as shown in the drawing), for both fridges the temperature is around 1.1mK. The problem is that the 4K and 600mK stages of the CDMS tower are separated by a graphite tube whose thermal conductivity is much larger than originally expected and thus the thermal isolation is insufficient. Therefore, the Al wirebonds (black solid dots) on the still stage are normal rather than superconducting leading to an additional $\sim$4mΩ of R_p (10mΩ total) and also an additional $\sim$4mΩ on R_s (24 mΩ total).

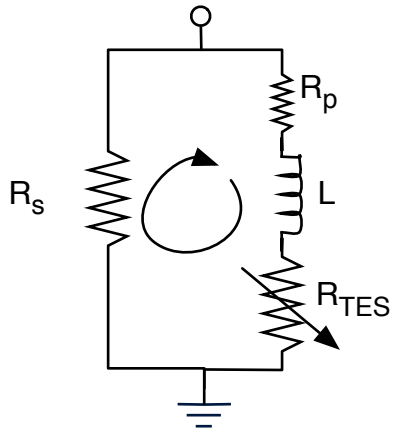

Figure 3.16: Electronic diagram of TES circuit splitting R_l into it's physical components. Due to the large impedance of the bias line, circular Johnson currents around this low impedance loop dominate.

Let's sum the Johnson voltage noise from all these sources in quadrature

$$S_{I\,L}(\omega) = \frac{4k_b\left(\sum_j T_{s\,j}R_{s\,j} + \sum_i T_{p\,i}R_{p\,i}\right)}{|Z_{tot}(\omega)|^2} \tag{3.22}$$

and then we can find the current noise power, $S_I(\omega)$ by dividing by the magnitude of the total complex impedance of the circuit (Eq. 3.15)

To set the scale, for frequencies below $\omega_{L/R}$, think of $|Z_{tot}|$ to be $\sim R_o$ or

$$S_{I\,L}(\omega < \omega_{\text{eff}}) \sim \frac{4k_b}{R_o}\frac{\left(\sum_j T_{s\,j}R_{s\,j} + \sum_i T_{p\,i}R_{p\,i}\right)}{R_o} = \frac{4k_b}{R_o}T_\star \tag{3.23}$$

This last simplification is pretty cool! We were able to rewrite all of the unecessary load resistor Johnson noise in terms of a simplistic standard TES Johnson noise term and an effective temperature just like we were able to do earlier with TFN noise. Unfortunately, as we lower the T_c of our TES in future designs our shunt and parasitic noise will remain constant while all intrinsic noise sources decrease and thus our sensitivity will eventually will be needlessly dominated by cold electronics Johnson noise. This is shown explicitly in Fig. 3.17. Around a T_c of 82mK, the two noise sources are of equal magnitude and thus our total noise is roughly $\sqrt{2}$ higher than ideal. At 20mK it's even more appalling! Using our current electronics would result in a $\sim$x2 sensitivity loss at low frequencies.

In the long term, the only solution is to drop R_s to the base stage and if single stage SQUIDs on the 600mK stage are still used, one must take care that the R_p from any normal connector is minimized. Most likely this means that if we still use normal connectors, we must find ones with smaller R_p than a standard millmax connector provides. Personally, this doesn't seem like a huge issue to me. At a minimum, we can just place 4 millmax connectors in parallel.

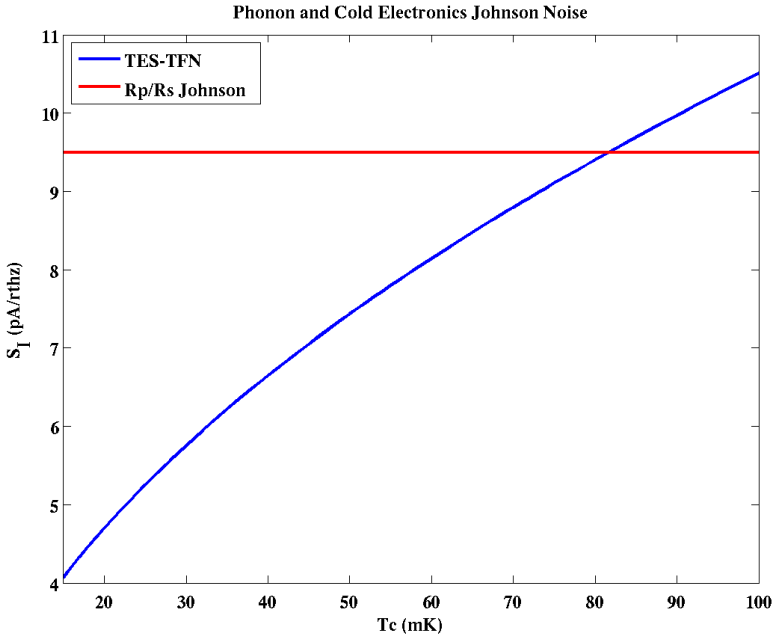

Figure 3.17: Relative magnitudes of TFN and load resistor Johnson noise for CDMS II electronics as a function of TES T_c

3.2.3 TES Johnson noise

When calculating how the Johnson noise across the shunt resistor translates into the measured current noise, we implicitly kept track of how ETF interacted with the noise source because we used the complex impedance,$Z_{tes}(\omega)$ (it's part of Z_{tot}), and not simply R_o in Eq. 3.22. (As an utter aside, at low frequencies $|Z_{tot}| \sim |Z_{tes}| \sim R_o$ even though the phase is totally different ... thus the PSD wouldn't change that significantly at lower frequencies).

Unfortunately, we can't simply use the same method for calculating the current noise contribution from the the TES itself for a rather subtle reason which was first discussed in a paper by [64].

I find that the most intuitive way to think about Johnson noise is to explicit recognize that ohm's law is only valid in the aggregate sense because the dissipative process

that it characterizes is absolutely stochastic. Thus in an ideal world, one would really always write $< V >=< I >< R >$ rather than $V = IR$ to explicitly make this clear. The concept of Johnson noise is now seen to be absolutely vital. It is the statistical measure of the variation one can expect at any random time away from ohm's law.

Continuing down this path, one sees that the joule heating law, $P = I^2R$ is also only valid in the mean sense and, most importantly for us, that the voltage fluctuations and joule heating fluctuations about the equilibrium conditions are strongly correlated! To determine the correlation let's take kirchoff's voltage laws about the simplified electrical diagram seen in Fig. 3.18

$$V_b + \delta V_{TES} = IR_l + L\dot{I} + IR_{TES}$$

and multiply both sides by the current. Please notice that for simplicity we have dropped the Johnson fluctuations across the load resistor and the voltage fluctuations across the power source. Though both of these are certainly important (we've already calculated the current noise contribution from the load resistor and we'll calculate what is effectively the source voltage noise below), these noise sources absolutely have no correlations with the joule heating of the TES (Johnson noise across the load resistor correlates to the joule heating of the load resistor not to the joule heating of the TES!) and thus for the purposes of this calculation they can be dropped.

$$IV_B = I^2R_l + \frac{d}{dt}\frac{1}{2}LI^2 + \left(I^2R_{TES} - I\delta V_{TES}\right)$$

We can now simply read off the terms. On the left we have the average amount of power which is being supplied to the circuit by the input power from the voltage source. The first term on the right is the average amount of power being dissipated in the load resistor while the second term corresponds to the amount of power which is being stored magnetically in the inductor.

The final term (everything in the parantheses) are all of the joule heating terms for the TES. I^2R_{TES} is of course the mean power which is dissipated into the TES and thus $-I\delta V_{TES}$ must correspond to the stochastic joule heating fluctuation. In words, one finds that with this sign convention, a positive voltage noise fluctuation has less power dissipation in the resistor. This certainly makes sense... An electron which easily passes through the resistor will lose less energy to the TES system (less Joule heating) and consequently will have more potential energy ($\delta V_{TES} > 0$) than usual.

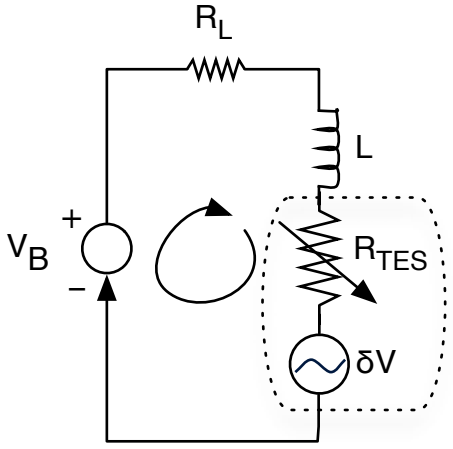

Figure 3.18: Dominant current noise loop superimposed on a simplified TES circuit diagram

To take into account this correlation is quite easy. We must replace the heat pulse place holder in Eq. 3.11 with $-I_o\delta V$

$$\begin{bmatrix} \delta I \\ \delta T \end{bmatrix} = M^{-1} \begin{bmatrix} \frac{\delta V}{L} \\ \frac{-I_o \delta V}{C} \end{bmatrix}$$

or in non-matrix form the current through the TES is related to the random fluctuations of voltage across the TES by

$$\delta I = \frac{dI}{dV}_{tes} \delta V = \left(\frac{M^{-1}_{1,1}(\omega)}{L} - \frac{I_o M^{-1}_{1,2}(\omega)}{C} \right) \delta V$$

which in the important limit of of $L \to 0$ and $\mathcal{L} >> 1$ gives us

$$lim_{L\to 0\,\&\,\mathcal{L}>>1}\frac{dI}{dV}_{tes} = \frac{1}{R_l + R_o(1+\beta)}\frac{i\omega}{i\omega + \mathcal{L}\frac{G}{C}\left(1+\beta-(2+\beta)\frac{R_l+R_o\beta}{R_l+R_o(1+\beta)}\right)}$$

Basically, at frequencies below $\sim \omega_{\text{eff}}$, Johnson noise from the TES is largely suppressed by feedback. Physically, on the one hand a positive Johnson noise voltage fluctuation means smaller than average joule heating in the TES, which cools the sensor, decreases the resistance, and increases the current. On the otherhand, at frequencies below ω_{eff} the positive voltage fluctuation leads directly to a smaller current (Eq. 3.17). These two effects largely cancel each other.

The calculation of the current noise due to the Johnson noise of the TES noise follows seamlessly

$$S_{ITES} = \frac{dI}{dV}^2_{tes} 4k_bT_oR_o$$

All of the noise derivations above assume that the voltage and current fluctuations of the system when biased (and thus not at equilibrium) are identical to those of a similar system at proper equilibrium. When this assumption is carefully studied [48] using non-linear non-equilibrium fluctuation dissipation techniques [65] [66], an increase in the noise magnitude for the case of $\beta \neq 0$ is found

$$S_{ITES} = \frac{dI}{dV}^2_{tes} 4k_bT_oR_o((1+\beta)^2 + \dots)$$

Note also that the noise is now not strictly gaussian.

In the $L \to 0$ and $\mathcal{L} >> 1$ limit, the above simplifies to

$$S_{ITES} \sim \frac{4k_bT_o}{R_o}\frac{R_o^2\left((1+\beta)^2+\dots\right)}{\left(R_l+R_o(1+\beta)\right)^2}\frac{\omega^2}{\omega^2+\omega^2_{\sim eff}} \tag{3.24}$$

where as one would expect, $\omega_{\sim eff} \sim \omega_{\text{eff}}$. Again, with the exception of the low frequency rolloff, this looks incredibly similar to plain old Johnson noise!

3.2.4 Johnson noise from the hot bias resistor

We've now accounted for all the noise sources in the cold electronics. We must still estimate the current jitter induced by the warm electronics. Naively, this could be enormous, since all the warm electronic are at 300K compared with 80mK for the TES itself.

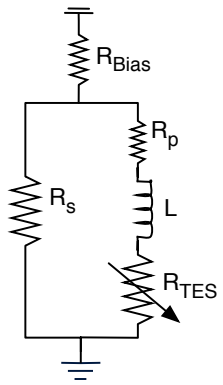

Figure 3.19: Simplified electronic circuit including R_{bias} which due to it's large size switches a voltage source to a current source. It's Johnson noise is insignificant.

As seen in Fig. 3.19, CDMS creates the constant current going to the TES circuit by placing a relatively huge resistor,R_{bias} $\sim$1kΩ, below a standard voltage source. Since $R_{bias} >> R_s$ and R_o we can estimate the current jitter going through the entire circuit as

$$S_{I\,bias} = \frac{4k_bT_{warm}}{R_{bias}}$$

Now the vast majority of δI_{bias} will be channeled through the shunt resistor because of it's lower resistance and thus the current noise which effects our measurement is

attentuated even further. Explicitly,

$$S_{I_{tes}\,bias} = \frac{4k_bT_{warm}}{R_{bias}}\left(\frac{R_s}{Rs+R_o}\right)^2$$

A quick glance at Tab. 3.2 will show that current noise from R_{bias} is suppressed by two orders of magnitude with respect to the other sources of noise and thus we'll forget about it from this point on [45]. The moral of the story is that as long as one is not worried about energy loss in the bias resistor, one can always minimize the warm electronics current noise by simply increasing the size of R_{bias}. Even if one is concerned about dumping power, since we aren't trying to read out any signal on this line we can just put a huge capacitor in parallel in R_{bias} and filter this Johnson noise (or more importantly non-intrinsic stray electronic noise) down to any arbitrary level.

3.2.5 Squid noise

For the sake of brevity, I'll gloss over many interesting issues involving our SQUID based current readout electronics (mutual inductances resonances between the feedback inductance loop and the TES circuit inductance loop [59], possibilities for multiplexing) and simply just give you the rough noise contribution of a decent CDMS II SQUID array when referenced to the TES current, I: $\sqrt{S_{I\,Squid}} \sim$ 2-4$\frac{pA}{\sqrt{hz}}$.

Of course, we would hope that our system is designed and operated in a manner such that the intrinsic sensor noise dominates.

3.2.6 Total Noise Spectrums & NEP

Since the noise sources mentioned above are certainly not correlated, we can simply sum them in quadrature to find the overall current noise for our detector. In Fig.3.20, I've shown both the simulated current noise spectrum for a large iZIP channel with

T_c = 70mK with an operating equilibrium point of R_o =150mΩ and a measured CDMS II noise spectrum from Soudan.

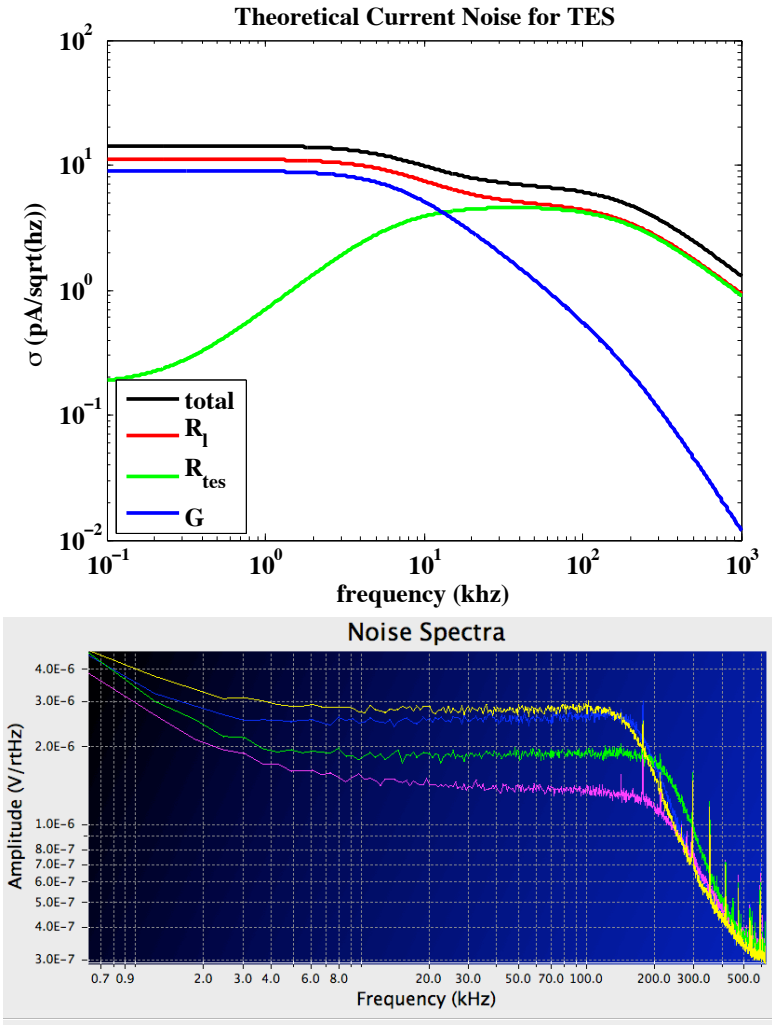

Figure 3.20: Total Current Noise Spectrums for a simulated iZIP4/5 with T_c =65mK, β=1 (right) and a measured noise Spectrum for the CDMSII detector T3Z2 at Soudan (left)

One quite surprising feature of the Soudan spectrum is the complete lack of a noise shoulder around ω_{eff} where the TFN noise starts to fall off and where the load resistor Johnson noise begins to be suppressed by β ($\beta = 1$ in simulation). For sensors with higher T_c's, this shoulder should be even more clearly visible per Fig. 3.17, and the

$\beta = 1$ assumption certainly isn't absurdly large. So this is a bit of mystery.

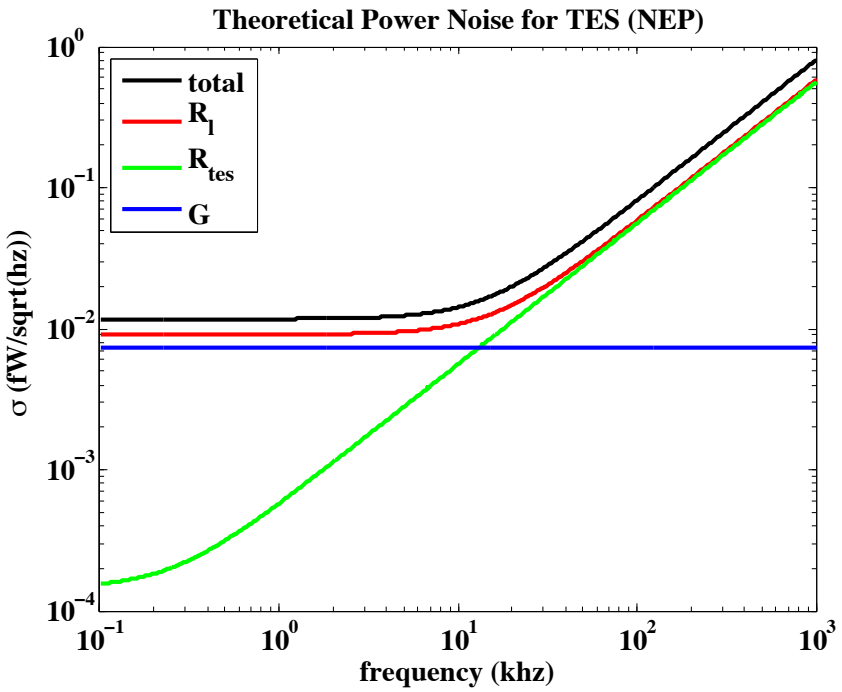

Figure 3.21: Noise Equivalent Power split by source at various frequencies

To truly understand our sensitivity, let's further reference our noise in units of thermal power by dividing S_I by $\frac{\partial I}{\partial P}^2$ (Fig.3.21). This "Noise Equivalent Power" is definitely the most natural units in which to study our sensitivity because at the end of the day, we are fundamentally trying to measure a thermal power signal being dropped into the TES.

Just as we found that the current referenced noise sources were easily written in terms of simple Johnson in the limits of $L \to 0$ (eqs. 3.21, 3.23,& 3.24), we find that here

everything can be easily referenced to the thermal fluctuation noise (TFN):

$$\begin{aligned} S_{pTFN} &= 4k_bT_c^2GF_{tfn} \\ S_{p\,R_l} &= 4k_bT_c^2G\frac{T_\star\left(1-\frac{T_{bath}^n}{T_o^n}\right)}{T_cn}\left(1+\omega^2\left(\frac{C}{G(1-\mathcal{L})}\right)^2\right) \\ S_{p\,R_{tes}} &= 4k_bT_c^2G\frac{\left(1-\frac{T_{bath}^n}{T_o^n}\right)(1+\beta)^2}{n\mathcal{L}^2}\left(1+\omega^2\left(\frac{C}{G}\right)^2\right) \\ &\sim 4k_bT_c^2G\frac{\left(1-\frac{T_{bath}^n}{T_o^n}\right)(1+\beta)^2}{n\mathcal{L}^2}\frac{C^2}{G^2}\omega^2 \end{aligned} \tag{3.25}$$

With this new basis (Fig. 3.21), it's immediately apparent that above ω_{eff}, our thermal power noise is increasing rapidly! Physically this occurs because our power transfer function, $\frac{\partial I}{\partial P}$, is dropping exponentially above ω_{eff} where the Johnson noise terms don't really begin to drop off until the inductor cut-off.

From a CDMS design perspective, this fact seems pretty constraining! If we want our sensitivity to high frequency pulse shape information to be similar to our sensitivity to low frequency total phonon information, then we must design ω_{eff} to be at the same rough frequency as ω_{shape}. This translates into a lower limit on the T_c of the sensors since ω_{eff} scales as T_c^{n-1}.

Though reasonable, the above is a bit simplistic. In CDMS, we don't need our high frequency pulse shape sensitivity to be identical to our low frequency pulse shape information. Rather, we would like both our high frequency and low frequency sensitivities to be as large as possible! If DC sensitivity grows faster than our sensitivity at 20khz with lowering the T_c, that's okay. They're still both getting bigger.

So we need to find out how sensitivity scales for $\omega > \omega_{\text{eff}}$ with T_c. Luckily, we already have all the tools to do this estimation. If $S_p(\omega = 0)$ is dominated by TFN noise (here we are explicitly assuming that in the future Johnson noise on load resistors

won't be an issue), then

$$\sqrt{S_p(0)} \propto \sqrt{T_c^2 G} \propto T_c^{\frac{n+1}{2}} \propto T_c^3$$

This plus the additional fact that $\omega_{\text{eff}} \propto T_c^4$ leads to

$$\sqrt{S_p(\omega > \omega_{\text{eff}})} \propto T^{-1}$$

Our previous argument, fortuitously turns out to be correct. If $\omega_{\text{eff}} > \omega_{shape}$, then lowering the T_c of the sensor decreases our noise as T_c^3. Continuing to lower the T_c such that $\omega_{\text{eff}} < \omega_{shape}$ though then increases our noise as T_c^{-1}. The absolute optimum is $\omega_{\text{eff}} = \omega_{shape}$.

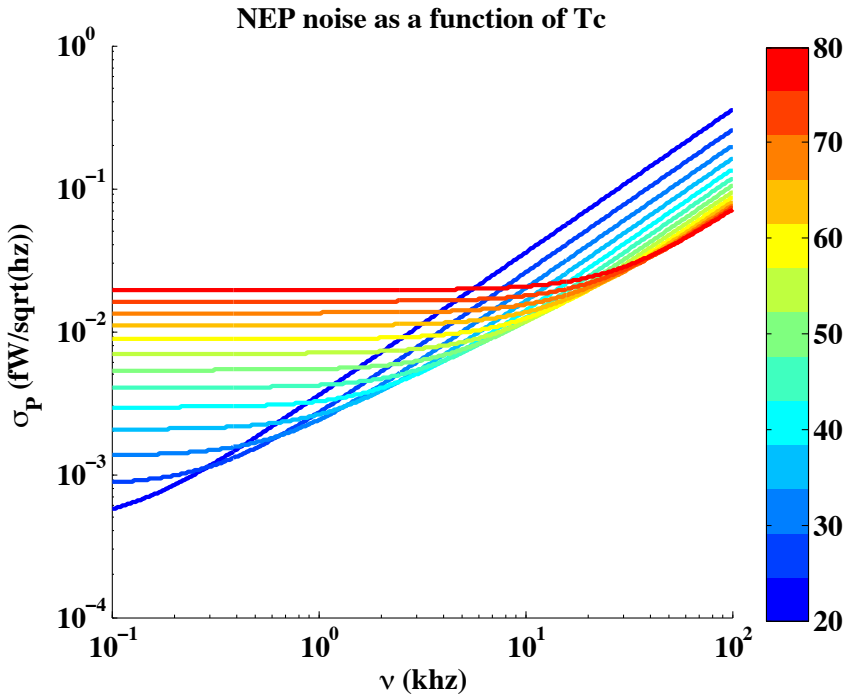

Figure 3.22: Simulated total Noise Equivalent Power for the iZIP4/5 as a function of sensor T_c

Fig. 3.22 clearly shows these scaling laws **for low** T_c. For $T_c >\sim$ 55mK, however,

the above derivation doesn't hold. The high frequency sensitivity seems to remain invariant, while the low frequency information scales as expected. The issue is that $\omega_{\text{eff}} \propto T_c^4$ doesn't account for any variation of β with T_c, which in the full simulation used for Fig. 3.22 varied roughly linearly as shown in Fig. 3.23. So, at high frequencies ω_{eff} ended up scaling with T_c^3 rather than T_c^4 which leads to an invariant high frequency sensitivity.

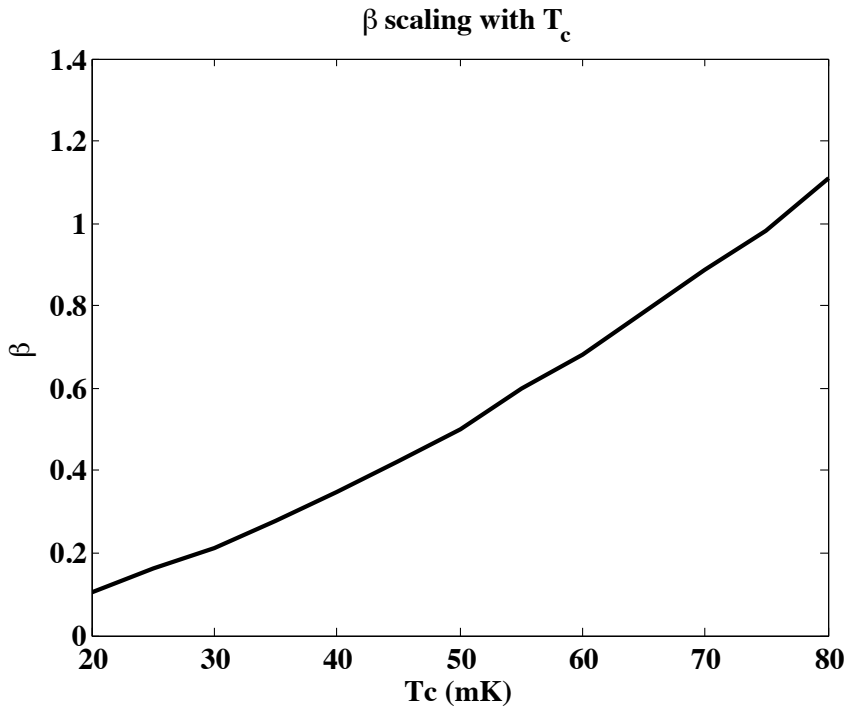

Figure 3.23: β variation with T_c in the NEP simulation

The moral of the story is that to optimize our detector, we really need to carefully experimentally measure ω_{eff}, α, and β as function of T_c for our W films. Once this is done, we can then choose a T_c which correctly balances low and high frequency information.

3.2.7 Optimum Filter Energy/Amplitude Estimation Sensitivity

Just as when we take the mean of multiple indentical and independent measurements to get an estimate with less variation, we would like to optimally combine the phonon flux information on all the various time scales for the best resolution on the magnitude of the pulse. Derivations can be found in [1], [63], and even on wikipedia for least-squares fitting (discrete case only) so I won't attempt to remake the calculation here.

Our best possible energy sensitivity to the recoil energy, E, given that the heat flux into the TES, $Q(t)$, has a known shape, $p(t)$,

$$Q(t) = Ep(t)$$

is

$$\sigma_E^2 = \frac{1}{\int_0^\infty \frac{d\omega}{2\pi} \frac{4|p(\omega)|^2}{S_{p\,tot}(\omega)}} \tag{3.26}$$

This equation can be easily analytically integrated ([48],[63]) in the limit that

1. All of the thermal energy is collected in the TES (ϵ =100%)
2. The signal bandwidth, ω_{pulse} is much greater than the bandwidth of the sensing system, ω_{eff}
3. Noise PSDs are dominated by TFN and TES Johnson noise (i.e. SQUID noise and R_l Johnson noise is negligible)
4. $L \to 0$
5. $\mathcal{L} >> 1$

which all hold for the vast majority of TES devices (infared/optical/x-ray/gamma). For this case:

$$\begin{aligned}\sigma_E^2 &= \frac{4k_bT_c^2G}{\omega_{\text{eff}}}\sqrt{\frac{F_{tfn}\left(1-\frac{T_{bath}^n}{T_o^n}\right)}{n}} \\ &= \frac{4k_bT_c^2C(1+\beta)}{\alpha}\sqrt{\frac{F_{tfn}n}{1-\frac{T_{bath}^n}{T_o^n}}}\end{aligned} \tag{3.27}$$

Conspicuous in its absence in the second line is the lack of dependence upon the thermal conductance, G. Physically, as one increases G, the change in the sensor bandwidth(ω_{eff}) precisely cancels out the increased TES noise.

Unfortunately, the standard CDMS detector breaks assumptions 1-3. Specifically:

1. In the iZIP4/5 design only $10-14\%$ of the total phonon energy that is released into the crystal actually collects and is dissipated through electro-thermal feedback in the TES ($10\% < \epsilon < 14\%$).

2. Phonons rattle around in the Ge crystal for $\tau_{\text{pulse}} \sim 750\mu s$ before being collected in the TES. Consequently, $\omega_{\text{eff}} >> \omega_{\text{pulse}}$ except for very small temperatures.

3. Load resistor Johnson noise is at least a significant component of the total noise for our current electronics.

So to estimate the Optimum filter sensitivity of a CDMS detector, we are forced to generalize Eq. 3.27. Luckily for us, this is still a pretty easy integral. The sum of all 3 noise sources in Eq. 3.25 gives you an S_p with only a single zero

$$S_p = 4k_bT_c^2G\left(F_{tfn}+\frac{T_\star\left(1-\frac{T_{bath}^n}{T_o^n}\right)}{T_cn}\right)\left(1+\frac{\omega^2}{\omega_\star^2}\right)$$

where

$$\omega_\star = \frac{G\mathcal{L}}{C(1+\beta)}\sqrt{\frac{\frac{nF_{tfn}}{1-\frac{T_{bath}^n}{T_o^n}}+\frac{T_\star}{T_c}}{1+\frac{T_\star}{T_c(1+\beta)^2}}}$$

and we can write the total athermal phonon pulse shape as a single exponential

$$P(\omega) = \frac{\epsilon}{1+i\omega/\omega_{\rm pulse}}$$

Thus, for the case in which $L \to 0$ and $sL >> 1$, the OF sensitivity (Eq. 3.26) is

$$\sigma_E^2 = \frac{4k_bT_c^2G}{\epsilon^2}\left(F_{tfn}+\frac{T_\star\left(1-\frac{T_{bath}^n}{T_o^n}\right)}{T_cn}\right)\frac{\omega_\star+\omega_{\rm pulse}}{\omega_\star\omega_{\rm pulse}} \tag{3.28}$$

which in the CDMS iZIP limit of $\omega_{\rm pulse} << \omega_{\rm eff}$ reduces to

$$\sigma_E^2 \sim \frac{4k_bT_c^2G}{\epsilon^2\omega_{\rm pulse}}\left(F_{tfn}+\frac{T_\star\left(1-\frac{T_{bath}^n}{T_o^n}\right)}{T_cn}\right) \tag{3.29}$$

Bizarrely, this suggests that we can very slightly increase our baseline energy resolution by increasing T_{bath} since we are dominated by R_l Johnson noise with the old electronics.

Assuming that with next generation CDMS electronics R_l Johnson noise is negligible,

Eq: 3.28 simplifies to:

$$\begin{aligned}\sigma_E^2 &= \frac{4k_bT_c^2G}{\epsilon^2}F_{tfn}\frac{\omega_{\text{eff}}\sqrt{\frac{nF_{tfn}}{\frac{T_c^n}{1-\frac{T_{bath}^n}{T_o^n}}}}+\omega_{\text{pulse}}}{\omega_{\text{eff}}\sqrt{\frac{nF_{tfn}}{\frac{T_c^n}{1-\frac{T_{bath}^n}{T_o^n}}}}\omega_{\text{pulse}}} \\ &\sim \frac{4k_bT_c^2G}{\epsilon^2}\frac{F_{tfn}}{\min(\omega_{\text{eff}}\sqrt{\frac{nF_{tfn}}{\frac{T_c^n}{1-\frac{T_{bath}^n}{T_o^n}}}},\omega_{\text{pulse}})}\end{aligned} \tag{3.30}$$

So, the standard CDMS iZIP4/5 detector with $\omega_{\text{eff}} >> \omega_{\text{pulse}}$ is completely unoptimized for total phonon resolution. Basically, to get the large ω_{eff}, we needed a huge G for which we paid a huge TFN noise penalty but we get no bandwidth benefit for the total phonon estimate because our signal itself is bandwidth limited! This is a severe issue! On the one hand, we want a larger sensor bandwidth for phonon pulse shape information. On the other hand this large sensor bandwidth severely degrades our total phonon estimates and also our low frequency partition estimates. Both can not be optimized at the same time!

Assuming that we don't care about high frequency pulse information, how would we go about optimizing our total phonon resolution? Well, a standard CMB experiment would simply fabricate a detector with smaller G by decreasing the width or increasing the length of the SiN legs. We though don't have this freedom! Our limiting G is the electron/phonon coupling in the W itself and we can't control this independently of the heat capacity, C, in fabrication. By dropping the T_c of our films on the other hand, we can drastically reduce G and ω_{eff} (Fig. 3.24). In fact, since G scales with T_c^{n-1}, $\sigma_{pt} \propto T_c^{\frac{n+1}{2}}$ which for us is T_c^3. Please note that these scaling laws are relatively independent of any α and β uncertainties since these characteristics only change the sensor bandwidth edge which just doesn't matter until one goes to quite low T_c. Thus this scaling law should be quite robust!

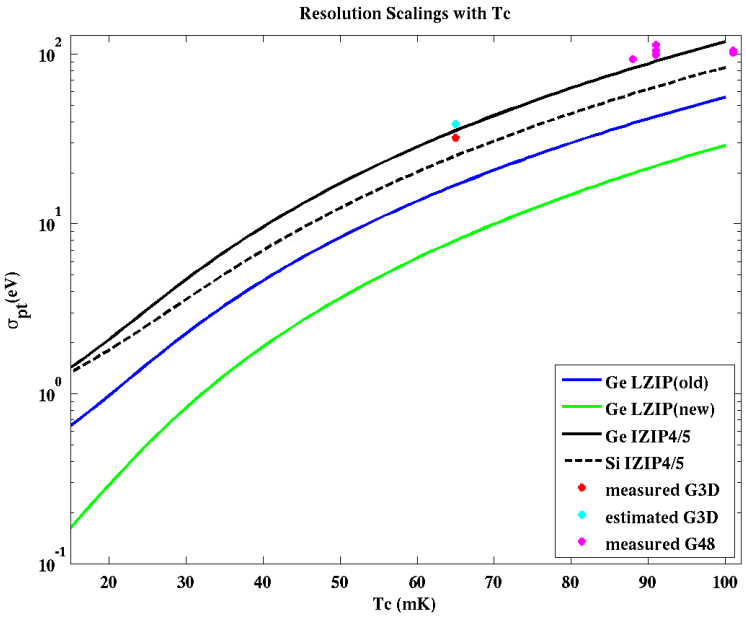

Figure 3.24: Ultimate Baseline Resolution Scaling with T_c

Inexplicably, the measured resolution for G48 after 1/f background subtraction is better for some channels than the ultimate expected sensitivity calculated with Eq.3.30, which of course is impossible. One can always do worse than fundamental noise, but one can never do better! So immediately, after claiming that our T_c scalings are systematically robust, I must unfortunately invoke an unexplained systematic as the culprit for these better than expected sensitivities on the high T_c side. The most likely culprits are:

- Our T_c estimates are preferentially positively biased for distributed TES systems with T_c position gradients. Thus, the 'average' T_c is probably less than the measured T_c and the experimental points should be pushed to the left.
- the electron phonon coupling constant, Σ, could be overestimated for the iZIP4/5 TES design
- R_s could be poorly measured.

This though is a genuinely good problem to have.

In summary, T_c^3 resolution scaling is simply enormous! As shown in Fig. 3.24, if we can get 90eV for a T_c=90mK, then we should be able to get $\sim$ 2eV for the same size detector ($\sim$ 1kg) with the same detector geometry for a T_c=20mK. This is impressive! To my knowledge, no other detector technology currently in existence has the ability to combine such large masses with such high sensitivity to nuclear recoils. The CoGENT ultra low capacitance Ge ionization detectors are limited by 1/f noise and have a $\sigma_{ee} \sim$ 70eV, or an equivalent nuclear recoil threshold of 2keV [14]. In principle, the ionization only signal of a 2-phase Xenon detector is more competitive ($\sigma_{ne} =\sim$ 200eV-400eV [67]), but this is hugely dependent upon the nuclear recoil electron yield factor in Xe which isn't well measured and is still almost 2 orders of magnitude lower in sensitivity than a T_c optimized athermal detector.

3.3 T_{bath} Sensitivity

So far, we've not discussed brute engineering limitations upon our T_c choice and instead have focused upon understanding low and high frequency sensitivity scalings/optimizations with T_c. This is definitely reasonable when thinking about future experiments since Leiden Cryogenics has just tested a new dilution fridge with 2mW cooling power at 100mK and a base temperature of 5.5mK [68]. So 10-20mK base temperatures at the detector itself for 100kg-1000kg detector masses is reasonable. Unfortunately, our current cryogenic installation in Soudan does not meet these lofty goals: T_{bath} is somewhere between 40-55mK with five towers installed. This depressing fact is caused by a combination of poor fridge performance, less than stellar thermal conductance between the mixing chamber and the detector tower, and larger than expected thermal conductivity between still and base temperature stages in the detector tower.

To quantify how this high bath temperature effects device performance, let's return to Eqs. 3.5 and 3.4 and plot how ω_{eff} scales with $\frac{T_{bath}}{T_c}$ (Fig. 3.25). Basically, for T_{bath}=50mK, we could drop our T_c all the way down to 70mK and only have a $\sim$

20% bandwidth degradation, which is completely reasonable, particularly since we have bandwidth to spare. At 60mK, we have a 40% suppression which is liveable but things are starting to get scary. Please note that here we are not taking into account any ω_{eff} suppression due to β which should lessen as we increase T_{bath}, so these scalings are conservative.

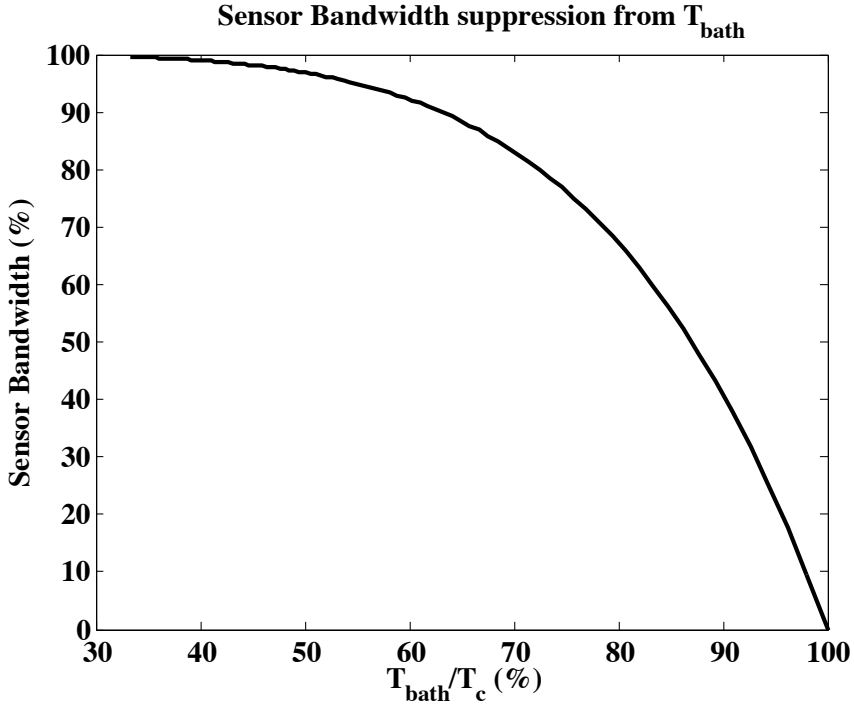

Figure 3.25: Sensor Bandwidth suppression due to T_{bath}

Secondly, Blas always argues that one of the largest and unsung advantages of an athermal sensor design is the lack of sensitivity to T_{bath} fluctuations in $\frac{\partial I}{\partial P}$. At high frequencies, this statement is quite difficult to assess since it depends so heavily upon α and β scalings as one changes the bias point, but for low frequencies which are of incredible importance to the CDMS iZIP because of its slow phonon collection times, we can simply look at the normalized DC gain shift for small T_{bath} fluctuations.

To do this let's rewrite Eq. 3.13 in terms of the constant V_b (if the bath temperature

fluctuates during an experiment we will not change V_b to compensate):

$$\lim_{L\to 0\&\mathcal{L}>>1} \frac{\partial I}{\partial P} = \frac{-1}{(V_b - 2I_o R_l)} \frac{1}{(1 + i\omega/\tau_{\text{eff}})} \tag{3.31}$$

then

$$\begin{aligned}
\frac{\Delta \frac{\partial I}{\partial P}(0)}{\frac{\partial I}{\partial P}(0)} &= \frac{\frac{\partial}{\partial T_{bath}} \frac{\partial I}{\partial P} \Delta T_{bath}}{\frac{\partial I}{\partial P}} \\
&= \frac{\frac{\partial}{\partial I_o} \frac{\partial I}{\partial P} \frac{\partial I}{\partial P} \frac{\partial P}{\partial T_{bath}} \Delta T_{bath}}{\frac{\partial I}{\partial P}} \\
&= \frac{\partial}{\partial I_o} \frac{\partial I}{\partial P} \frac{\partial P}{\partial T_{bath}} \Delta T_{bath} \\
&= \frac{-2nR_l}{\left(1 - \frac{T_{bath}^n}{T_o^n}\right)\left(1 - \frac{R_l}{R_o}\right)^2 R_o} \frac{T_{bath}^{n-1} \Delta T_{bath}}{T_c^n}
\end{aligned}$$

which is shown in Fig. 3.26 for a ΔT_{bath}=1mK and T_{bath} =50 mK for various T_c. The 3% DC gain fluctuation for a T_c=60mK is relatively modest and of roughly the same order as the residual position dependence in our non-stationary Optimum Filter total phonon estimator and also the temporal variation in e/h trapping. Consequently, if our maximum T_{bath} fluctuations throughout a Soudan run are ∼1mK, then we should be able to run detectors with 60mK T_c quite reasonably from a stability perspective. Furthermore, by carefully measuring the complex impedance on a regular basis, this gain shift could be removed on a run by run basis.

3.4 Saturation Energy

In detectors optimized for total phonon resolution ($\omega_{\text{eff}} < \omega_{\text{pulse}}$), saturation energy can be roughly and easily estimated as the energy required to change the resistance of the TES from the operating point ($\sim 30\%R_n$) to $\sim 90\%R_n$ **under constant voltage**

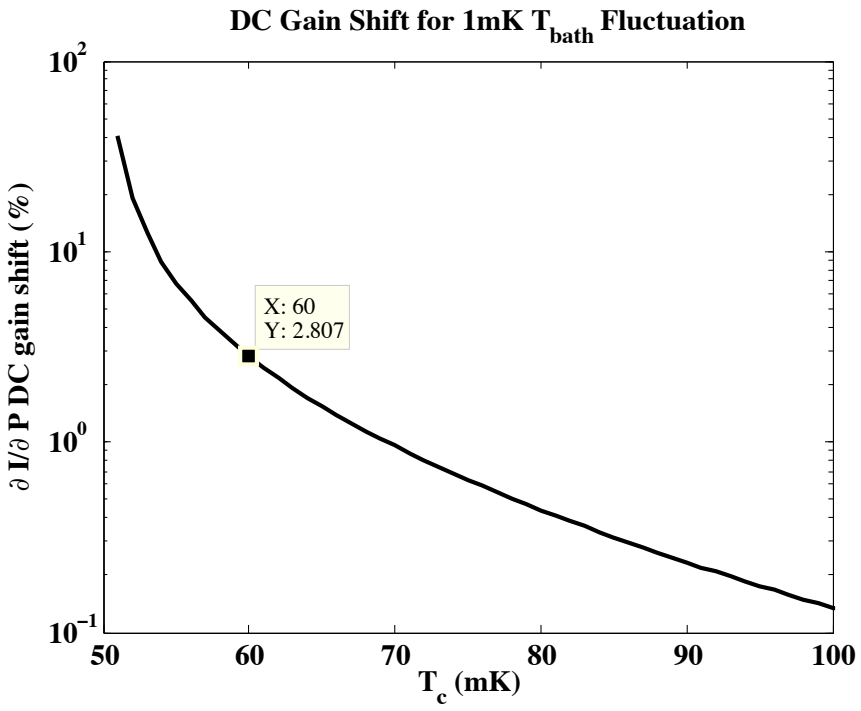

Figure 3.26: DC Sensitivity of $\frac{\partial I}{\partial P}$ to T_{bath} fluctuations

bias:

$$E_{sat} = C(T)\Delta T_{90-30\%V_b}$$

For devices with small β, one can then write E_{sat} in terms of α [69] as

$$E_{sat\,\beta=0} \sim \frac{C(T_c)T_c}{\alpha}$$

For large β devices though, the temperature transition is effectively broadened under voltage bias. To see this let's simply calculate $\frac{\partial R}{\partial T}\big|_V$ for $R(I,T)$:

$$\left.\frac{\partial R}{\partial T}\right|_V = \left.\frac{\partial R}{\partial T}\right|_I + \left.\frac{\partial R}{\partial I}\right|_T \left.\frac{\partial I}{\partial T}\right|_V$$

where you can calculate $\frac{\partial I}{\partial T}\big|_V$ from $V = IR$ as

$$\left.\frac{\partial I}{\partial T}\right|_V = \frac{-I}{R}\left.\frac{\partial R}{\partial T}\right|_V$$

or subbing in one finds that

$$\left.\frac{\partial R}{\partial T}\right|_V = \frac{\frac{\partial R}{\partial T}\big|_I}{1+\beta} = \frac{\frac{R}{T}\alpha}{1+\beta}$$

and consequently, a more general estimate of E_{sat} for the $\omega_{\text{pulse}} >> \omega_{\text{eff}}$ limit is

$$E_{sat} \sim \frac{C(T_c)T_c(1+\beta)}{\alpha} \tag{3.32}$$

If one naively plugs the iZIP TES characteristics into Eq. 3.32, one finds a saturation energy of 74keV for a $T_c = 80$mK which completely underestimates our actual saturation energies. To obtain a better E_{sat} estimate in the $\omega_{\text{eff}} >> \omega_{\text{pulse}}$ limit, let's require that the maximum phonon power into the TES is less than the Joule heating for a saturated TES:

$$P_{sat} = \omega_{\text{pulse}} E_{sat} = P_{bath} - \frac{V_b^2}{R_n} = P_{bath}\left(1 - \frac{R_o}{R_n}\right)$$

or

$$E_{sat} \sim \frac{P_{bath}\left(1 - \frac{R_o}{R_n}\right)}{\omega_{\text{pulse}}} \sim \frac{P_{bath}\frac{2}{3}}{\omega_{\text{pulse}}}$$

Finally, for an E_{sat} estimate which is acceptable for all ω_{eff}, let's just directly sum the

two limits (this isn't perfect by any means but ...)

$$E_{sat} \sim \frac{C(T_c)T_c(1+\beta)}{\alpha} + \frac{P_{bath}\frac{2}{3}}{\omega_{\text{pulse}}} \tag{3.33}$$

which can be seen in Fig. 3.27. Please beware, that this just an estimate! For the distributed TES systems that we use in CDMS, the position dependent phonon signal can locally saturate some TES at energies scales below those estimated by Eq. 3.33 leading to non-linearities in pulse shape rather than a sharp saturation cutoff.

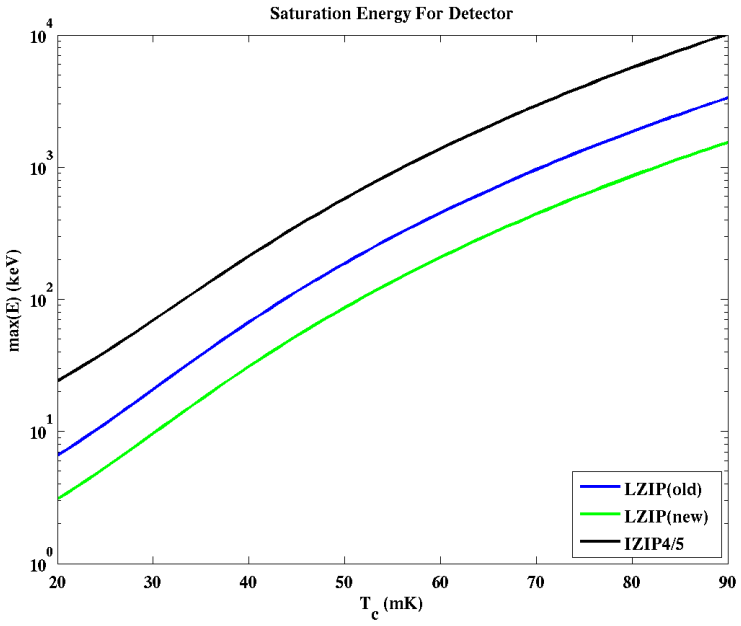

Figure 3.27: Approximate saturation energies for the iZIP4/5 and for two proposed ultra low threshold designs as a function of T_c

3.5 Detector Design Driver Summary

- $R_o/20 < R_s + R_p < R_o/5$: To keep large sensor bandwidth, we need $R_l << R_o$. On the other hand, as we increase the ratio between R_o and R_l, the thermal

power dumped onto the fridge stage which holds R_s increases linearly. Thus, decreasing $R_l < R_o/20$ doesn't make much sense either.

- R_p on the still stage or higher needs to be minimized so that unnecessary Johnson noise doesn't dominate intrinsic TES noise
- T_{bath} should absolutely be kept below $\sim 80\%$ of T_c to minimize sensor bandwidth fluctuation and DC gain shift. For the Soudan fridge, this suggests that 63mK is probably the lowest T_c that we really want to try. Of course, further suppression of T_{bath} only improves device performance and thus $T_{bath} \sim 1/2T_c$ is desired.
- Low frequency signal sensitivity used for total phonon estimators as well as DC phonon partition scales as T_c^{-3}. The lower one can go, the better!
- High frequency pulse shape information is optimized when $\omega_{\text{eff}} \lesssim \omega_{shape}$. Matching this condition by variation of TES T_c, depends intimately on $\beta(T_c)$

Competition between these last two design drivers makes precise T_c optimization difficult and dependent upon the WIMP mass for which one wants ultimate sensitivity. High WIMP mass searches are limited by charge noise in electron recoil/ nuclear recoil discrimination and thus better total phonon resolution isn't a large advantage. By contrast, pulse shape information for fiducial volume definition is incredibly important so T_c should be chosen so that sensitivity at 10khz is **near** optimum. Specifically, we should lower the T_c until 10khz noise scales with T_c^{-1}. By contrast, low WIMP mass optimized detectors would be designed to absolutely minimize threshold energy and thus lower T_c's are favored.

3.6 Future Studies

- Determine T_c ranges for which W films can be produced dependably, using both ion-implantation or deposition parameter variation as the dependent variable
- Understand the mechanism by which W films on Si test wafers have suppressed

T_c for the Balzers deposition system

- Experimental characterize α, β, ω_{eff} for the feasible temperature range(which hopefully goes all the way to 20mK)

Chapter 4

Advanced TES Dynamics

4.1 Motivation

Unfotunately, CDMS detector channels have never perfectly followed simplistic TES dynamical theory presented in the previous chapter. Many of these idiosyncracies can be explained away by the fact that we gang together 500-1000 spatially separated TESs in parallel across, what at times is, a sizeable temperature gradient. Thus, as mentioned in the previous channel, we don't expect the slope of the equilibrium power curve vs bias potential to be related to the intrinsic temperature width or α.

However, there are discrepancies which can't be so easily explained away. In fig. 4.1, I've plotted the responsivity curves for 4 of the 120 phonon channels from the CDMS II experiment which span the spectrum of various shapes. With the exception of T1-Z5B (blue) which seems to at least qualitatively match a simple TES with $\beta \sim 0.3$ all the other devices have much more complex transfer functions. T2Z5-A (cyan) and T3Z4-B (red), both display quite broad resonance features in the 10-100khz range which can't be produced without an additional pole zero pair, so they definitely don't match standard theory. At first glance, one could argue that T3Z2-C (yellow) corresponds to a channel which has been biased too low in its transition and

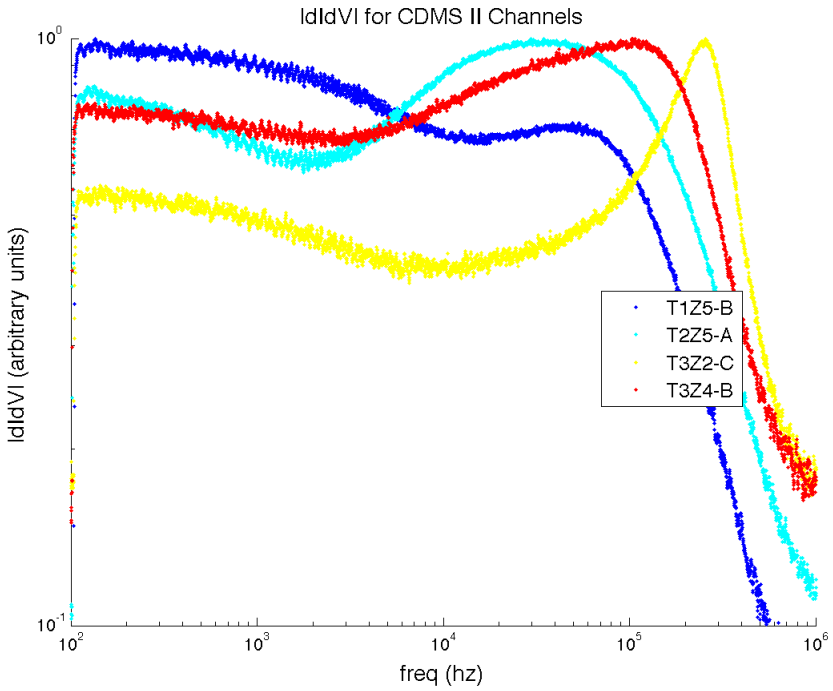

Figure 4.1: Wide range of current responses to bias voltage fluctuations found in CDMS II detectors.

is thus starting to display Electro-thermal oscillation. However, this argument doesn't explain the sensitivity dip between 2-20khz. Taking one more stab at matching T3Z2-C, we could say that perhaps this dip is caused by β. Under closer scrutiny though, this theory also fails. β suppresses ETO, and thus if there is enough β to create a dip, then there is also enough β to suppress ETO. Likewise, if there is ETO, one can't see the characteristic β dip. So, in summary, we can say that the admittance curves in Fig. 4.1 are too complex to be described by simple TES theory with 1 thermal DOF ... we simply need more poles and zeros.

Aside: Historically, we also hypothesized that perhaps the long pulse falltimes seen in CDMS II were also due to exotic TES dynamics but the iZIP R&D runs (pulses with 750-850μs falltimes and no dependence on T_c [G3D had a 40mK difference in T_c between it's two sides]) are clearly inconsistent with these theories.

4.2 Complications due to Absorbers

For applications in which the TES is not only the sensing element but also the incident energy absorber (optical devices), the physical devices closely resemble the dynamical equations produced in the previous chapter. In devices that are optimized to study higher energy gamma and x-ray radiation on the other hand, almost always an additional absorber is used to account for the smaller interaction cross sections. Hoevers et al [70], one of the first groups to study the noise and the dynamical changes created through additional heat capacity couplings, constructed x-ray devices with thick Au absorbers for example. A modern day example, dear to many of my fellow CDMS collaborators, is the μ-X focal plane shown in fig. 4.2 [58, 71].

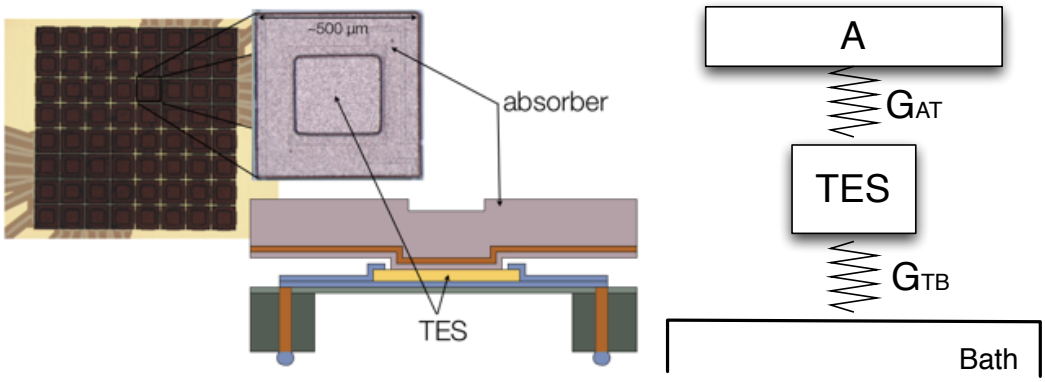

Figure 4.2: left: Photo of a preliminary μ-X TES array. Right: Thermal Conductance diagram for TES devices with coupled absorbers.

Since CDMS detectors are, in essence, just high energy gamma detectors (albeit measuring energy in 2 ways), Kyle Sundquist [72] suggested that one would naively expect us to roughly share the same thermal diagrams and perhaps even some of the dynamical complications of μ-X.

Though, in essence correct, there are a few modifications. As discussed in much greater detail in the next chapter, CDMS detectors concentrate phonon energy in the TES through athermal phonon collection in Al fins which are then connected to the W TES via a W/Al fin connector(fig. 4.3). Due to the large bandgap of the Al films

(∼2K), there are virtually no thermally excitable electronic states and consequently, there is virtually no **thermal** conductance between the TES and the Al. By contrast the W only part of the fin connector, has approximately the same T_c as the W TES and consequently there are electronic states which are thermally accessible. Thus, a physically accurate thermal diagram of a CDMS QET structure would include the heat capacity of the W only fin connector,C_F, separated from the TES by a thermal conductance, G_{TF}.

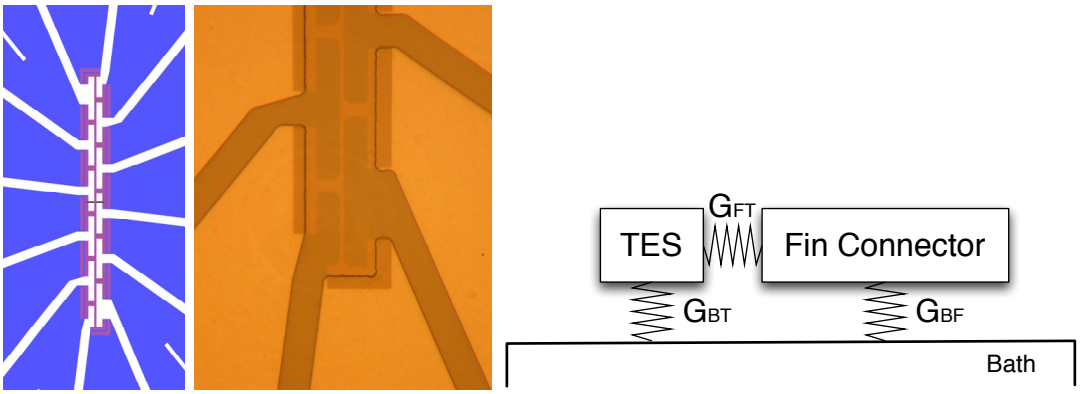

Figure 4.3: left: A superCDMS TES (magenta line) is connected to the Al phonon absorption fins (blue) through 10-12 W connectors (depending on the design). The physical volume of the W is completely dominated by the connectors Center: For CDMS II and mZIP devices, nominally 1/2 the width of the W connector overlaps the Al fin ($\sim 3.5\mu m$) Right: Thermal Diagram for a CDMS TES.

To understand if the anomalies in the complex admittance plots are due to this additional thermally connected heat capacity, let's first estimate the values for G_{TF} and C_F and then derive the small signal dynamics for this 2 thermal body system.

4.2.1 Estimating thermal properties

In CDMS II QETs, the W only part of the fin connectors has a physical volume per TES, $\mathcal{V}_f$, of $\sim$ $70\mu m^3$ (12 x 40 μm x 3.5μm x 40nm) while the TES volume varies depending on the line width thickness from 10-25 μm^3(1- 2.5 μm line width). Thus, in the limit of small thermal gradient and little lateral proximity effect, both

the heat capacity and the electron/phonon coupling should be totally dominated by contributions from the fin connector.

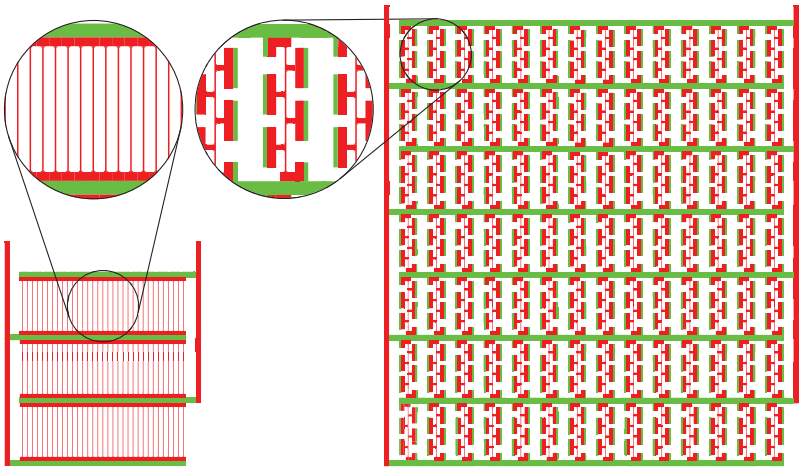

Figure 4.4: A pair of TES structures consisting of 100 100um long W TESs (red) connected in parallel by superconducting Al leads (green). The line width of all TESs is ∼1.5 μm. For the device on the right, each W fin connector overlaps a rectangular Al region by 3.5um at its edge. In the region where the W does not overlap the Al, the side connectors each have a volume of 5.6μm^3 and the end connectors have a volume of 3.3 μm^3. The thickness of the W in these devices is ∼40nm.

This was indeed found to be the case when we (Sean Hart et al. [51]) measured pairs of TES devices with and without fin connectors (fig. 4.4) for TES lengths of 100μm and 300μm. As shown in table 4.1, the joule heating required to keep the TES with fin connectors was approximately 4 times larger than for the same size TES without attachments. The simplest quantification of these results is to define an efficiency factor,$\mathcal{E}_{fc}$, by which we scale the W-only fin connector volume when we calculate the total thermal conductance:

$$P_{bath} = \Sigma(\mathcal{V}_{tes} + \mathcal{E}_{fc}\mathcal{V}_f)(T^5 - T_{bath}^5) \tag{4.1}$$

Combining information from both 100μm and 300μm devices, our best estimate for $\mathcal{E}_{fc}$ is $70 \pm 10\%(stat)$. In the chapter on simplistic TES dynamics we discussed the systematics for this measurement in some depth. Most of these systematics effect

both devices equally and thus we believe that our estimate of $\mathcal{E}_{fc}$ is quite robust from a **measurement perspective**. The physical mechanism for this phonon electron coupling suppression though is quite complex and thus $\mathcal{E}_{fc}(T_c, T_{bath})$ where we've only measured one point in the total parameter space. If we model the cause of $\mathcal{E}_{fc}$ as being a simple thermal gradient along the fin connector, then $\mathcal{E}_{fc} \sim 70\%$ corresponds to a thermal gradient of $\sim 12\%$, which is certainly reasonable. With this model, we would expect that as one decreases T_c, the thermal gradient across the fin connector would decrease and thus in the low T_c limit we would expect $\mathcal{E}_{fc} \to 1$. On the other hand if $\mathcal{E}_{fc}$ is primarily caused by a suppression in density of free carriers due to a proximity effect (the superconducting Al fin is physically connected to the W fin, then $\mathcal{E}_{fc}$ would largely be independent of T_c.

	$R_s(\mathrm{m}\Omega)$	$R_p(\mathrm{m}\Omega)$	$R_n(\Omega)$	$\mathcal{V}_{tf}(\mu\mathrm{m}^3)$	K (W/K^5)	T_c (mK)
100μm Line TES	23	12	1.94	594	1.9$\pm$0.2x10^{-7}	109.8 ± 2.0
100μm Fin TES	20	13	1.58	3430	7.5$\pm$0.7x10^{-7}	105.3 ± 1.2
300μm Line TES	25	13	1.85	5400	18.2$\pm$1.7x10^{-7}	108.9 ± 1.4
300μm Fin TES	24	12	1.64	27600	75.2$\pm$8.6x10^{-7}	105.6 ± 1.4

Table 4.1: TES test structure measured characteristics

In principle, combining these equilibrium measurements with $\frac{\partial I}{\partial V}$ at multiple T_{bath} and T_c could allow one to measure the suppression in both the electron-phonon coupling and the heat capacity of the system separately. However, for the purposes of the small signal calculations in this chapter though, we will assume (with little/no justification) that the heat capacity suppression is identical to $\mathcal{E}_{fc}$.

For an initial rough estimate of the thermal conductance between the fin connector and the TES, we'll estimate the electronic thermal conductivity (g_w) from the normal resistivity ($\rho_W = 1.32\text{x}10^{-7}\Omega m$ for SuperCDMS films) using the law of Wiederman-Franz ($g_w = \frac{\beta_{wf} T}{\rho_w} \sim 1.3\text{x}10^{-2} \frac{W}{Km}$). Of course, the true dynamical problem is a continuous material with both a specific heat and a thermal conductivity rather than the block model above, so we must guess a length scale. The most reasonable guess would probably be $\sim 1/2$ the distance between the TES and the farthest point of the fin connector because the energy is evenly distributed along the length of fin

connector. Since we expect larger deviations from simplistic TES dynamics for weaker couplings though (in the limit of infinite conductivities the connector and the TES have identical temperatures and behave like a single block element with the total heat capacity), let's be conservative though and use the full length of 30μm. Thus,

$$G_{TF} \sim g_W(12\text{x}40\text{nmx}3.5\mu\text{m})/30\mu\text{m} \sim 600\frac{pW}{K} \tag{4.2}$$

where the 12 accounts for the fact that each mZIP TES has 12 fin connectors in parallel(10 for CDMS II or iZIP). Please note, that this number is per TES. When simulating multiple TES in parallel, one must of course multiply by the number of TES.

4.2.2 Small signal derivations for multiple thermal block systems

Of course, the primary change we will introduce to the simplistic TES dynamics is the addition of another thermal degree of freedom, T_F, so that the fin connector temperature can fluctuate independently from the TES temperature (now T_T instead of simply T). For ease of understanding though, let's also define the fin connector and TES heat capacities in terms of the total heat capacity, C, as

$$C_F = \zeta_F C$$
$$C_T = \zeta_T C$$

where

$$\begin{aligned}\zeta_F &= \frac{\mathcal{E}\mathcal{V}_f}{\mathcal{V}_{tes} + \mathcal{E}\mathcal{V}_f} \\ \zeta_T &= 1 - \zeta_F\end{aligned} \tag{4.3}$$

With these definitions the full non-linear dynamical equations are

$$\begin{aligned}L\frac{dI}{dt} &= V - I\left(R_L + R(T_T, I)\right) + \delta V \\ C\zeta_T\frac{dT_T}{dt} &= I^2 R(T_T, I) - P_{BT}(T_T, T_{bath}) - P_{TF}(T_T, T_F) + \delta P_T \\ C\zeta_F\frac{dT_F}{dt} &= -P_{BF}(T_F, T_{bath}) + P_{TF}(T_T, T_A) + \delta P_F\end{aligned} \tag{4.4}$$

As always, let's linearize about equilibrium to distill the all important small signal ODE and noise PSDs, rewriting the resistance derivatives in terms of α and β. Let's also assume here that $T_{Fo} \sim T_{To}$ and thus the differential conductance between the fin connector and the bath is symmetric: $G_{BF} \simeq \frac{\partial P_{TF}}{\partial T_T} \simeq -\frac{\partial P_{TF}}{\partial T_F}$. Finally, let's assume that the differential thermal conductances to the bath from the TES, $G_{BT} = \frac{\partial P_{BT}}{\partial T_T}$, and from the fin connector, $G_{BF} = \frac{\partial P_{BF}}{\partial T_F}$, scale with fractional volumes so that we can rewrite them in terms of a total bath coupling, G_B. With all of these simplifications we end up with

$$\frac{d}{dt}\begin{bmatrix} L\delta I \\ C\zeta_T\delta T_T \\ C\zeta_F\delta T_F \end{bmatrix} = -\begin{bmatrix} R_o(1+\beta) + R_l & \frac{P_o\alpha}{I_o T_{To}} & 0 \\ -\frac{P_o(2+\beta)}{I_o} & G_{TF} + \zeta_T G_B - \frac{P_o\alpha}{T_{To}} & -G_{TF} \\ 0 & -G_{TF} & G_{TF} + \zeta_F G_B \end{bmatrix}\begin{bmatrix} \delta I \\ \delta T_T \\ \delta T_F \end{bmatrix} + \begin{bmatrix} \delta V \\ \delta P_T \\ \delta P_F \end{bmatrix} \tag{4.5}$$

To match Irwin's 1D equations even more closely, let's use his DC loop gain quantity,

$\mathcal{L} = \frac{P_o \alpha}{T_o G_B}$. With this

$$\frac{d}{dt}\begin{bmatrix} \delta I \\ \delta T_T \\ \delta T_F \end{bmatrix} = -\begin{bmatrix} \frac{R_o(1+\beta)+R_l}{L} & \frac{\mathcal{L}G_B}{LI_o} & 0 \\ -\frac{P_o(2+\beta)}{I_o C \zeta_T} & \frac{G_{TF}+\zeta_T G_B - \mathcal{L}G_B}{C\zeta_T} & -\frac{G_{TF}}{C\zeta_T} \\ 0 & -\frac{G_{TF}}{C\zeta_F} & \frac{G_{TF}+\zeta_F G_B}{C\zeta_F} \end{bmatrix}\begin{bmatrix} \delta I \\ \delta T_T \\ \delta T_F \end{bmatrix} + \begin{bmatrix} \frac{\delta V}{L} \\ \frac{\delta P_T}{C\zeta_T} \\ \frac{\delta P_F}{C\zeta_F} \end{bmatrix} \tag{4.6}$$

Furthermore, since we are really attempting to understand the dynamical differences caused by the additional thermal DOF, let's simplify the above system by taking the limit as $L \to 0$. With this simplification, we kill off one degree of freedom and from the first row of Eq: 4.6, we can write δI in terms of δT_T and δV as:

$$\delta I = -\frac{\mathcal{L}G_B}{R_l + R_o(1+\beta)}\delta T_T + \frac{1}{R_l + R_o(1+\beta)}\delta V \tag{4.7}$$

In fourier space, this simplified 2D ODE,M_{2D}, is just

$$\begin{bmatrix} i\omega + \frac{G_B}{C\zeta_T}\left(\mathcal{L}\frac{R_o - R_l}{R_o(1-\beta)+R_l} + \zeta_T\right) + \frac{G_{TF}}{C\zeta_T} & -\frac{G_{TF}}{\zeta_T C} \\ -\frac{G_{TF}}{\zeta_F C} & i\omega + \frac{G}{C} + \frac{G_{TF}}{\zeta_F C} \end{bmatrix}\begin{bmatrix} \delta T_T \\ \delta T_F \end{bmatrix} = \begin{bmatrix} \frac{\delta P_T + I_o(2+\beta)\frac{R_o}{R_o(1+\beta)+R_l}\delta V}{\zeta_T C} \\ \frac{\delta P_F}{\zeta_F C} \end{bmatrix} \tag{4.8}$$

In the limit of $G_{TF} >> G_B$, we can taylor expand the dynamical eigenvalues about $G_B = 0$ and we find

$$\begin{aligned} \frac{1}{\tau_{\text{eff}}} &= \frac{G_B}{C}\left(\mathcal{L}\frac{R_o - R_l}{R_o(1+\beta)+R_l} + 1\right) - \zeta_F^2 \frac{C}{G_{TF}}\left(\frac{G_B}{C}\mathcal{L}\frac{R_o - R_l}{R_o(1+\beta)+R_l}\right)^2 + ... \\ \frac{1}{\tau_{TF}} &= \frac{G_{TF}}{\zeta_F \zeta_T C} + \frac{G_B}{C}\left(\mathcal{L}\frac{\zeta_F}{\zeta_T}\frac{R_o - R_l}{R_o(1+\beta)+R_l} + 1\right) + \zeta_F^2 \frac{C}{G_{TF}}\left(\frac{G_B}{C}\mathcal{L}\frac{R_o - R_l}{R_o(1+\beta)+R_l}\right)^2 + ... \end{aligned} \tag{4.9}$$

As expected, in this limit τ_{eff} is exactly what one would expect from an idealized TES with the heat capacity of the entire system as we guessed earlier. The next term though is a bit scary. As $G_{TF} \rightarrow \mathcal{L}G_B$, the sensor bandwidth will start to be suppressed.

The fast decay eigenvalue is associated with an assymetric eigenvector. This sets the times scale for which energy fluctuations become shared between both the TES and the fin connection.

In Fig. 4.5, $\frac{\partial I}{\partial V}$ and $\frac{\partial I}{\partial P_F}$ curves for a variety of different G_{TF} multiples for both the full equations with L=250nH, and for the simplified M_{2D} ODE are shown. For our base conservative case with G_{TF}=600pW/K (black), the characteristic fluctuating response seen in many CDMS II channels is absent (Fig. 4.1). If we drop G_{TF} by an additional factor of x3-x10 though, we do start to see features which are reminiscent of our response. So, is it possible (albeit very unlikely) that we've overestimated our minimum super conservative G_{TF}? If yes, then we've potentially found the culprit for the non-ideal TES dynamics.

We can though immediately disregard this hypothesis though by realizing that dropping G_{TF} by these large factors also suppresses the time scale at which energy absorbed in the fin connector is transferred to the TES, τ_{TF}. By itself, a $G_{TF} = 60$ pW/K ($G_{TF}/10$) gives us a $\tau_{TF} \sim 6\mu$s which is roughly the size of the phonon pulse risetimes seen in both the CDMS II oZIP and iZIP detectors for quick surface events in the primary channel. Once we account for additional delays due to phonon physics and quasi-particle diffusion in the fins, these small G_{TF} can be ruled out experimentally.

It would be nice to develop a little bit of intuition into how a small G_{TF} creates bumps in $\frac{\partial I}{\partial V}$ because it may give us insight into how other physical mechanisms also produce similar features, so let's try to understand the simplified 2D dynamical response (red dotted). At high frequencies ($\omega > \omega_{\text{eff}}$), neither the TES nor the fin connector shows significant thermal fluctuations. Consequently, the TES behaves like a regular resistor with resistance, $R_o(1+\beta)$. At very low frequencies, the TES and the

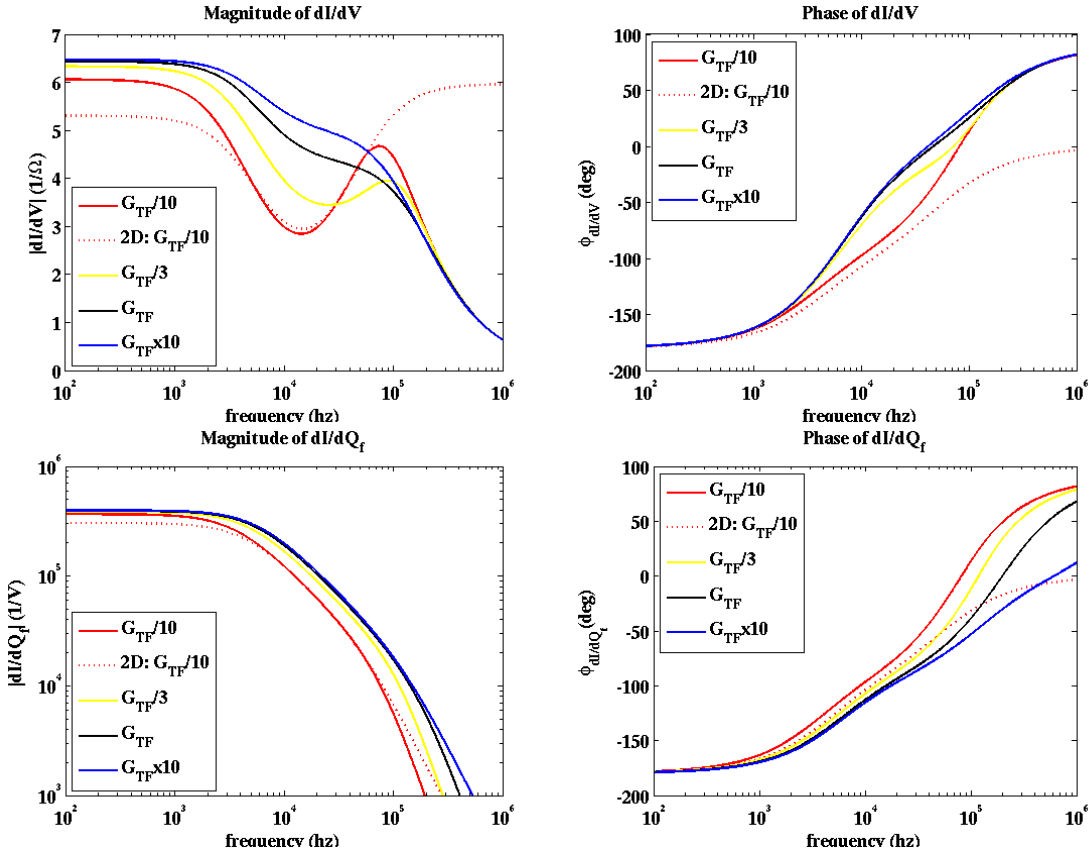

Figure 4.5: Simulated current transfer functions for bias voltage fluctuations, $\frac{dI}{dV}$, and power fluctuations into the fin connector, $\frac{dI}{dP_f}$, for the wiederman-franz estimated thermal conductance between the fin connector and the TES in black and for a variety of multiples. To grossly approximate experimental CDMS II $\frac{dI}{dV}$ curves seems to require an unphysically small G_{tf}. In dotted red are shown curves for the simplified 2 DOF system ($R_l = 0$, $\beta = 0$ and $L = 0$). Below what would have been the L/R cutoff, the simplified equations match quite well.

fin connector always remain in quasi-equilibrium and thus the thermal power flowing from the TES into the fin connector,P_{TF} is equal to the thermal power flowing from the fin connector to the bath, P_{BF}, which is very slowly varying with temperature and thus effectively constant. Thus, $\frac{dP_{TF}}{dt} \sim 0$ and the system can effectively be considered a single composite object which follows 1D TES dynamics or $\frac{\partial I}{\partial V}(\omega = 0) = \frac{-1}{R_o - R_l}$. In between, these two limits though things get a bit tricky. There exists a frequency region, $\omega_{\text{eff}} < \omega < \omega_{TF}$, in which a significant portion of the joule heating caused

by the δV fluctuation is traveling through P_{TF} and heating/cooling the fin connector ($\delta P_{TF} \neq 0$). If this joule heat is heating the fin, it's not heating the TES and thus the 180^o current response seen at DC is muted.

4.2.3 Additional noise due to finite G_{TF}

Since we've gone through all the hassles of deriving the small signal dynamics, we might as well go the one additional step and calculate the noise induced into our measurement by thermal power fluctuations across G_{TF}. In our block model, the heat capacity of the conductance is infinitesimal and consequently by energy conservation any random power fluctuation into the TES (δP_t) is offset by an opposite power fluctuation in the fin connector ($\delta P_f = -\delta P_t$). Of course, this was also true for power fluctuations from the bath and the TES in the last chapter. However, there we weren't sensitive to the energy changes in the bath and thus we didn't explicitly keep track of the anticorrelation. By contrast, here the TES is sensitive to energy fluctuations in both the bath and the fin connector.

As derived previously, the PSD spectrum is white (shot noise assumption) and the magnitude is

$$S_{P_{TF}\,G_{TF}}(\omega) = 4k_b T^2 G_{tf} \tag{4.10}$$

Taking into account the anticorrelation between δP_T and δP_F, we find the current transfer function for these fluctuations is

$$\frac{\partial I}{\partial P_{tf}} = \left(\frac{M_{3D}^{-1}(1,2)}{C\zeta_T} - \frac{M_{3D}^{-1}(1,3)}{C\zeta_F} \right) \tag{4.11}$$

or

$$\begin{aligned}\frac{\partial I}{\partial P_{tf}} &= \frac{-\mathcal{L}G_B}{I_o(R_l + R_o(1+\beta))}\left(\frac{M_{2D}^{-1}(1,1)}{C\zeta_T} - \frac{M_{2D}^{-1}(1,2)}{C\zeta_F}\right) \\ &= \frac{-\mathcal{L}G_B}{I_o(R_l + R_o(1+\beta))}\frac{1}{C\zeta_T}\frac{\left(i\omega + \frac{G_B}{C}\right)}{(i\omega + \omega_{\text{eff}})(i\omega + \omega_{TF})}\end{aligned} \tag{4.12}$$

and consequently the noise spectrum referenced to current (fig. 4.6 left) is

$$S_{I\,Gtf} = \frac{\partial I}{\partial P_{tf}}^2 S_{P_{TF}\,Gtf} = \frac{\partial I}{\partial P_{tf}}^2 4k_b T^2 G_{TF} \tag{4.13}$$

The shape of the TFN across G_{TF} (solid magenta) is quite similar to the feedback suppressed Johnson noise of the TES. To gain physical intuition, let's discard the inductor and look at the simplified noise spectrum (dotted magenta) for which $\delta I \propto \delta T_T$. Without feedback, we would expect the temperature fluctuations of the TES due to G_{TF} power fluctuations to be flat until they roll off at $\omega_{TF} = \frac{G_{TF}}{C\zeta_F\zeta_T}$, so the high frequency roll off is expected. Physically, this is simply because low frequency power fluctuations from the fin connector into the TES lead to an increase in δT_T and a decrease in δT_F until the random power fluctuation is canceled out by heat flow due to the thermal gradient. With feedback though, matching joule heating fluctuations suppress δT_T but at the expense of exacerbating the δT_F fluctuation ($\delta P_{TF} \propto \delta T_T - \delta T_F$ ...so if $\delta T_T \sim 0$ due to feedback then δT_F increases to compensate). Thus, we are only sensitive to TFN noise from G_{TF} at low frequencies insofar as the large fluctuations in δT_F lead to fluctuations in the thermal power leaving the fin connector and going into the bath, P_{BF}. Since this varies quite slowly compared to the resistivity changes ($\mathcal{L} >> 1$), $S_{I\,Gtf}$ is quite feedback suppressed at low frequencies.

Unfortunately, these simulations suggest that in the frequency range $\omega_{\text{eff}} < \omega < \omega_{L/R}$, TFN noise across G_{TF} dominates all other noise sources in the case that $G_{TF} = 600$ pW/K. This is a bit depressing! In the previous chapter we learned that we'd like to

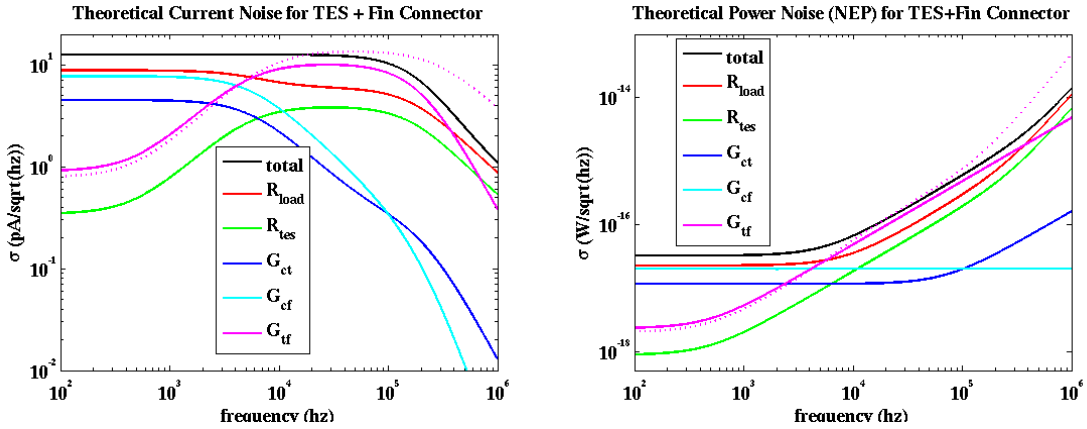

Figure 4.6: Fundamental total noise spectrums (black) and component partitions for a simulated large iZIP (550 TES in parallel) with an operating T_c of 80mK. TFN across a Wiederman-Franz estimated G_{tf} was calculated for the full matrix with L=250nH (solid magenta) and for the simplified ODE with L=0, $\beta = 0$ and $R_l = 0$ (dotted magenta)

place ω_{eff} near but below the frequencies where the pulse shape information which is super important for fiducial volume definition is located. Thus, our lack of attention to G_{TF} may have contributed to sub-optimal fiducial volume definition in CDMS II devices. To make sure that in future devices we are limited by this unnecessary noise, let's develop some design constraints such that TES johnson noise dominates in this frequency range.

Using Eq. 4.12,

$$\frac{\partial I}{\partial P_{tf}}(\omega > \omega_{\text{eff}}) \sim \frac{-1}{I_o(R_l + R_o(1+\beta))}\zeta_F \frac{\mathcal{L}G_B}{G_{TF}} \frac{1}{(1 + i\omega/\omega_{TF})}$$

or dropping β and R_l we find that

$$S_{IGtf}(\omega > \omega_{\text{eff}}) \sim \frac{4k_bT}{R_o} \frac{1}{1+\omega^2/\omega_{TF}^2}\zeta_F^2 \frac{\mathcal{L}G_B}{G_{TF}} \tag{4.14}$$

So to keep G_{TF} noise subdominant at all frequency ranges we need that G_{TF} >>

$\mathcal{L}G_B$ or equivalently that $\omega_{TF} >> \omega_{\text{eff}}$. For low T_c, this is a trivial constraint since $G_{TF} \propto T_c$ while $\mathcal{L}G_B \propto T_c^n$. For higher T_c devices (Fig. 4.6), we must be vigilant. In the worst case scenario, we can decrease G_{TF} by increasing the number of fins and/or decreasing the percentage of the fin edge which is overlapped with W (as long as QuasiParticle collection isn't adversely effected (next chapter), the latter is especially beneficial since it also decreases ζ_F. Additionally, it even decreases the magnitude of G_B so even regular TFN noise is suppressed. Infact, the QETs used in the iZIP4/5 series have been designed with only 1/2 the fin edge being covered with W (best conservative guess for $G_{TF} \sim 1200$pW/K).

4.3 Internal TES inhomogeneities

In the noise derivations which treat the TES as a single block object, we never looked at internal TES power fluctuations. Specifically, what about the stochastic power fluctuation shown in fig. 4.7, where half the TES is randomly heated while the other half is randomly cooled.

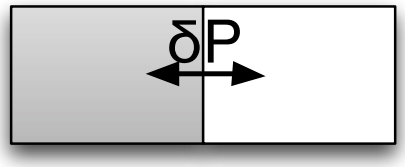

Figure 4.7: Diagram of an internal stochastic noise fluctuation in which energy is taken from the right half of the TES and placed into the left half

To see if this fluctuation couples to the current flowing through the TES, we just need to calculate if the total resistance of the TES, which is the sum of the resistance of

the left and right halves (R_l,R_r), fluctuates:

$$\begin{aligned}\delta R &= \delta R_l + \delta R_r \\ &= \left(\frac{\frac{\partial R_l}{\partial T_l}}{C_l} - \frac{\frac{\partial R_r}{\partial T_r}}{C_r}\right)\delta P \\ &= \left(\frac{\frac{\partial \rho_l}{\partial T_l}}{A_l^2 c_l} - \frac{\frac{\partial \rho_r}{\partial T_r}}{A_r^2 c_r}\right)\delta P\end{aligned} \tag{4.15}$$

So we can now see the implicit assumptions in all of our previous noise derivations. Internal TES fluctuations will not couple to the current as long as:

1. $\frac{\partial \rho_l}{\partial T_l} = \frac{\partial \rho_r}{\partial T_r}$
2. the cross sectional area doesn't vary along the TES ($A_l = A_r$)
3. the specific heat of the W, c, doesn't vary along the TES

Occasionally, violations of these conditions are done on purpose [73]! The most likely non-advertant cause for location dependent variations in resistivity though is almost certainly thermal variations across the TES such that different regions of the TES are in different parts of the superconductivity transition. In devices fabricated on SiNx membranes with diffusive phonon propagation for instance, a spatial thermal gradient is a necessary byproduct of the radial thermal cooling link of the SiNx. A second method, which we will discuss in much greater depth below due to its pertinence in our own devices is the spontaneous thermal symmerty break or 'thermal phase separation' in TES which are too long.

As we will see the good news is that, in both cases, the minimization/elimination of these spatial inhomogeneities is straightforward: design the TES such that internal thermal impedance of the TES is much smaller than the cooling impedance to the bath.

4.3.1 Understanding Thermal Phase Separation

The easiest way to intuitively see why thermal variation across a TES is the rule rather than the exception is to study the seemingly different problem of thermal stability for a thermally uniform TES.

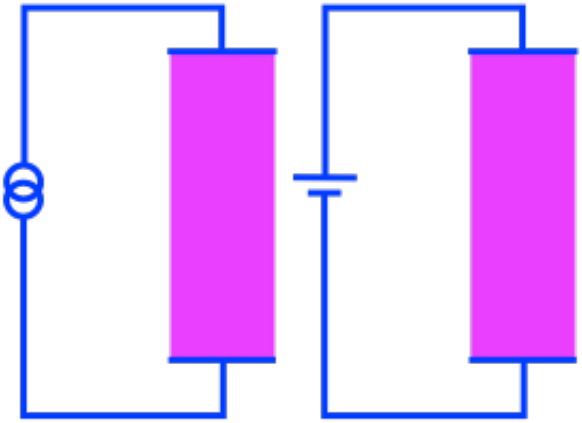

Figure 4.8: left: A TES biased with constant current right: A TES biased with voltage

Fig. 4.8 left shows a TES operating under constant current bias. Assuming a single temperature for the entire TES, one ends up with the rather simple energy dynamics equation of:

$$C\dot{T} = I^2 R(T) - P_{bath}(T)$$

where we've used the same variable definitions as found in the previous chapter. To test the stability of the equilibrium, we'll just taylor expand to 1st order about the equilibrium point and see if thermal excursions (physically usually caused by thermal noise) grow unabatted or if they exponentially diminish with time. The result is

$$C\delta\dot{T} = \left(I_o^2 \frac{\partial R}{\partial T} - G\right)\delta T$$

As you can see, as long as the derivative of the Joule heating is larger than the derivative of the substrate cooling (almost always the case since the resistance changes very quickly with temperature whereas the substrate cooling power changes much more slowly), any thermal excursion is exponentially amplified... the equilibrium is unstable.

Contrast this to voltage biasing scenario (Fig. 4.8 right), whose dynamical equation and it's 1st order taylor exspansion are reprinted below.

$$C\dot{T} = \frac{V^2}{R(T)} - P_{cool}(T)$$
$$C\delta\dot{T} = \left(-I_o^2\frac{\partial R}{\partial T} - G\right)\delta T$$

In this situation, the joule heating term has now been flipped to supply negative feedback and the circuit is completely stable.

Now that we understand thermal stability for TESs under voltage and current bias, let's throw a curve ball. Let's take the TES in Fig. 4.8 and split him into 2 TES that are in series as shown below

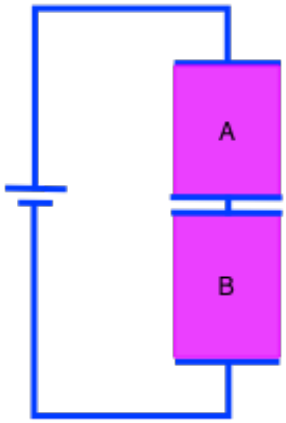

Figure 4.9: 2 TES in series

The 1st order taylor expanded differential equation is slightly more complex due

to the increased dimensionality and is shown below in the limit that variations in the substrate cooling power are inconsequential with respect to the huge changes in resistivity ($\mathcal{L} >> 1$ limit)

$$C \begin{bmatrix} \Delta\dot{T}_A \\ \Delta\dot{T}_B \end{bmatrix} = \frac{V^2}{(R_A + R_B)^3} \begin{bmatrix} (R_B - R_A)\frac{\partial R_A}{\partial T_A} & -2R_B\frac{\partial R_B}{\partial T_B} \\ -2R_B\frac{\partial R_A}{\partial T_A} & (R_A - R_B)\frac{\partial R_B}{\partial T_B} \end{bmatrix} \begin{bmatrix} \Delta T_A \\ \Delta T_B \end{bmatrix} \quad (4.16)$$

Unfortunately, the differential matrix is still rather daunting... ideally it should be diagonalized so that we can find the dynamical eigenvalues. To get an idea of the stability we can take just look at the scenario where R_A and R_B are of equal size. In this case, the diagonal terms cancel exactly and we are left with just the off diagonal terms. A matrix of this type has both a positive and a negative eigenvector: THE EQUILBRIUM IS UNSTABLE!

To give a more intuitive understanding we'll state what happens in words for the case that $R_A = R_B$:

1. A thermal excursion in A increases R_A

2. An increase an R_A decreases I

3. (a) The decrease in I and increase in R_A cancel and there's no change to the Joule Heating in A (the diagonal term is 0)

   (b) A decrease in I leads to a decrease in the Joule Heating of B

4. B cools. A's temperature remains constant

5. B cooling decreases R_B

6. A decrease in R_B increases I

7. (a) An increase in I increases the Joule Heating in A

   (b) An increase in I and the decrease in R_B cancel so that there's no change to the Joule Heating in B (the diagonal term is 0)

8. A warms further. B Remains at the temperature at step 4

9. Repeat above indefinitely ... A goes normal and B goes superconducting.

The conclusion that two resistors in series will always tend to separate temperatures seems to damn our assumption that there is no variation within a TES since I can always think of any resistor of length l as simply two resistors butted together with length $l/2$. Don't get too upset though.... there must be someway to reconcile the instability of the 2 resistor scenario and the assumption made by everyone in our field that a correctly operating TES has thermal homogeneity.

The answer to this false paradox is that in the 2 resistance scenario mentioned above, I physically seperated the 2 TES and as such didn't allow for any thermal conduction between R_A and R_B which would try to keep the two resistors at the same temperature.

In summary, we can say that significant thermal variation along a TES ('thermal phase separation') will occur unless the thermal conduction along the TES overcomes the destabilizing influence of the joule heating. Thus, if I make a TES too long and effectively decrease the thermal conductance along the TES it will phase separate.

Likewise, by increasing the sharpness of the resistance transition I am increasing the destablizing influence of the voltage bias and thus will eventually overcome the stablizing influence of the internal thermal conductivity of the TES. Finally, if I increase the coupling to the substrate too much (by adding fins in a very pertinent example), I will also increase the destablizing influence of the voltage bias and again force the system to spontaneously symmetry break.

4.3.2 Quantitative Phase Separation Criteria

Let's flush out the statements made above. Particularly, I would like to estimate the exact length when phase separation occurs for a TES with certain properties [74].

First, we must modify the equations for the system in Fig. 4.8 right to allow for internal thermal variation by letting the temperature vary with both time and **position along the TES**:

$$\begin{aligned} L\dot{I}(t) &= V_b + I(R + R_l) \\ cA_{TF}\dot{T}(x,t) &= \frac{I^2\rho(T(x,t))}{A_T} - p_{bath}(T(x,t))A_{TF} + g_w A_T \nabla_x^2 T(x,t) \end{aligned} \tag{4.17}$$

where we are now using volume normalized quantities of c (specific heat $\left[\frac{J}{m^3K}\right]$) and p_{bath} (volume normalized power which cools the TES $\left[\frac{W}{m^3}\right]$) instead of C and P_{bath}. g_w is the internal conductivity coefficient which tends to keep the TES at a uniform temperature($\left[\frac{W}{mK}\right]$). This problem has two distinctly different and important cross-sectional areas for CDMS QETs. As discussed earlier, the W fin connectors significantly increase both the coupling between the phonon bath and W electron system and also the total heat capacity (assuming $G_{TF} >> \mathcal{L}G_B$). Thus, the pertinent cross-sectional area for these terms in Eq. 4.17 is the average cross sectional area of the total fin connector + TES system, A_{TF}. Both the thermal and electrical

conductances along the TES however depend only on the cross sectional area of the TES, A_T, though since the fins connectors are disconnected appendages. These two are related by the previously defined ζ_T, $A_T = \zeta_T A_{TF}$ (Eq. 4.3).

The TES resistance, R, in Eq. 4.17 is now an integral quantity

$$R = \int_0^l dx \frac{\rho(I, T(x,t))}{A_T}$$

where l is just the length of the TES in the direction of current flow.

So, not only is this PDE totally nonlinear, but it's also nonlocal. This is the true definition of nasty!

To find if the homogenous equilibrium point is stable let's taylor expand all of the nonlinear terms in both equations to 1st order around the thermally homogenous equilibrium point (**potentially an unstable equilbrium**). In this 1st order limit, δR simplifies to

$$\begin{aligned}\delta R(t) &= \int_0^l dx \frac{1}{A_T} \left(\left.\frac{\partial \rho}{\partial I}\right|_{I_o,T_o} \delta I(t) + \left.\frac{\partial \rho}{\partial T}\right|_{I_o,T_o} \delta T(x,t) \right) \\ &= \frac{R_o \beta}{I_o} \delta I + \frac{R_o \alpha}{T_o} \int_0^l dx\, \delta T(x,t)\end{aligned}$$

and then in the limit of $L \to 0$, Kirchoff's voltage equation can be solved to give

$$\delta I(t) = \frac{-I_o R_o \alpha}{T_o (R_l + R_o(1+\beta))} \int_0^l dx\, \delta T(x,t)$$

and the set of nasty nonlinear coupled equations can be written as the single PDE:

$$cA_{TF}\delta\dot{T}(x,t) = \frac{P_o\alpha}{lT_o}\left(\delta T(x,t) - \frac{(2+\beta)R_o}{R_o(1+\beta)+R_l}\frac{1}{l}\int_0^l dx\,\delta T(x,t)\right) - g_b A_{TF}\delta T(x,t) + g_w A_T \nabla_x^2 \delta T(x,t) \tag{4.18}$$

In keeping with defining volume normalized properties, g_b, is just the volume independent version of G_b.

To get rid of the spatial derivatives, we can easily switch to fourier space since we have dropped what would be the horrid many-body terms. There's one subltely here though. We must choose our fourier modes to satisfy the boundary conditions. In particular, the spatial derivative must be zero at both x=0 and $x = l$ because there is no heat flow out either of the ends of the TES (thermal flux $\propto \nabla T$). This condition corresponds to cosine waves with $k = \frac{m\pi}{l}$:

$$T(x,t) = \mathcal{T}_k'(t)\cos(kx) \qquad k = \frac{m\pi}{l} \qquad m \subset I : [0,\infty) \tag{4.19}$$

where implicit summation over k indices is assumed. This set of fourier modes is certainly non-standard and it's worth a little time to go into it's properties. First and foremost, this set of fourier modes is complete: every possible function within the range $(0, l)$ can be made simply by varying the coefficients. This is a tinge surprising since the standard fourier set has both sine and cosine terms (or equivalently complex coefficients).

$$T(x) = A_k\cos(kx) + B_k sin(kx) \qquad k = \frac{2\pi m}{l} \qquad m \subset I : [0,\infty) \tag{4.20}$$

A qualitative and certainly non-rigorous way to see the equivalence of these two spaces

is to simply look at the number of degrees of freedom per unit of k space. In the cosine space there is 1 degree of freedom for every $\frac{\pi}{l}$. In the standard basis there are 2 degrees of freedom for every $\frac{2\pi}{l}$, the exact same number. This basis set is also orthogonal, $\int_0^l dx \cos(qx)\cos(kx) = \frac{l}{2}\delta(k-q)$, so deconstructing a complex function into its components is easy.

With this said, working in cos(kx) basis is definitely more challenging from a brute calculation perspective (switching back and forth between sine and cosine with derivatives, etc) and thus throughout the rest of the chapter we will write these modes as the sum of exponentials,

$$T(x,t) = \mathcal{T}(k,t)^{'}\cos(kx) = \mathcal{T}(k,t)e^{ikx} \qquad k = \frac{m\pi}{\mathcal{L}} \qquad m \subset I : (-\infty, \infty) \tag{4.21}$$

where $\mathcal{T}(k)$ is always real and $\mathcal{T}(k) = \mathcal{T}(-k)$. There are only two properties which don't totally match the rules for the standard basis. First, with the coefficient constraints this basis is overcomplete and thus not orthogonal. Resolving $T(q)$ is though still easily possible. It's now just the real component of the convolution:

$$\mathcal{T}(q,t) = \Re\left(\frac{1}{l}\int_0^l dx e^{-iqx}T(x,t)\right)$$

Secondly the definition of white noise is slightly off. The noise is of course called white because all frequencies have the exact same magnitude in the standard basis. By contrast, in the cosine basis all of the frequency modes have random phases like usual, but the zeroth harmonic is twice as big as all others:

$$< \delta f(k \neq 0)\delta f(k \neq 0) >= \frac{1}{2} < \delta f(k=0)\delta f(k=0) > \tag{4.22}$$

The same qualitative reasoning we used to understand completeness can also be used here. In the standard basis with complex coefficients we can decompose the coefficient

variance into two terms: an imaginary variance and a real variance. Since the phase is absolutely random, we further know that both of these terms on average contribute 1/2 of the total variance. In the cosine basis by contrast, we have only the real component; the imaginary components have effectively been spread out over all of the cosine terms made from odd values of m ($k_{odd} = \frac{m_{odd}\pi}{l}$).

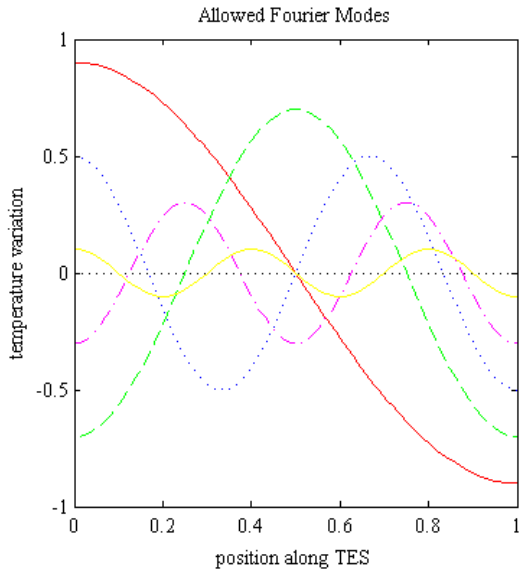

Figure 4.10: Allowable lowest order thermal modes in the TES

With this aside finished, one simplification which was unexpected is that only the zeroth harmonic has a non-zero integral over the TES and thus the joule heating term simplifies significantly and Eq: 4.18 becomes

$$\begin{aligned}\dot{\mathcal{T}}(k,t) &= \frac{P_o\alpha}{cA_{TF}lT_o}\Big(\mathcal{T}(k,t) - \frac{(2+\beta)R_o}{R_o(1+\beta)+R_l}\mathcal{T}(0,t)\delta(k-0)\Big) - \frac{g_b}{c}\mathcal{T}(k,t) - k^2\frac{g_w\zeta_T}{c}\mathcal{T}(k,t) \\ &= \frac{g_b}{c}\Big((\mathcal{L}-1)\mathcal{T}(k,t) - \mathcal{L}\frac{(2+\beta)R_o}{R_o(1+\beta)+R_l}\mathcal{T}(0,t)\delta(k-0)\Big) - k^2\frac{g_w\zeta_T}{c}\mathcal{T}(k,t)\end{aligned} \tag{4.23}$$

At this point, we can see how voltage biasing effects the various fourier modes. For the zeroth harmonic (mean temperature of the TES), voltage biasing certainly makes

the system more stable... there's 'electrothermal feedback'. However, this is not true for the higher modes. In fact, **voltage biasing destablizes all modes except the first**. Only internal thermal diffusion (with a little help from substrate cooling) keeps the higher modes from exploding. Secondly, notice that β only effects the dynamics of the k=0 mode! As we've seen time and again, β pretty much only hurts our performance! We want a large sensor bandwidth for the 0^{th} mode and β suppresses it. We want to have higher mode fluctuations suppressed and β is no where to be found!

The maximum length condition at which a TES is thermally uniform is then simply the length at which the first harmonic mode ($k = \frac{\pi}{l}$) stops being suppressed or

$$l_{max} = \sqrt{\frac{g_w \pi^2 \zeta_T}{g_b(\mathcal{L} - 1)}} \tag{4.24}$$

which we can simplify further by rewriting g_w in terms of ρ_w using the Weidermann-Franz law, g_b in terms of Σ, and we can decompose $\mathcal{L}$ into it's components:

$$l_{max} = \sqrt{\frac{\pi^2 \beta_{wf} \zeta_T}{n \Sigma T_c^{n-2} \rho_w \left(\frac{\alpha}{n}\left(1 - \frac{T_{bath}^n}{T_c^n}\right) - 1\right)}} \tag{4.25}$$

where β_{wf} is the Weidermann-Franz coefficient. This final formulation of the phase separation limit, illustrates one of the tricks for diagnosing phase separation problems in your sensor. If you believe that your TES is operating in a phase separated regime, you can drop $\mathcal{L}$ and eventually homogenize the TES performance by increasing T_{bath} (This is another trick which I should have used to a much greater extent)!

The prominence of the TES fractional volume coefficient, ζ_T, highlights another strong feature of the phase separation hypothesis. In our current fabrication process we have significant variation in the width of the TES both across the detector face and between fabrication batches, which consequently means that we have significant variation in both ζ_T and in the amount and magnitude of phase separation in the TES. Basically,

the dynamical response depends significantly upon physical variables over which we have minimal control. The inverse argument is also quite powerful. If we want to make detectors which behave identically and don't have 'personalities', we must design the TES (decrease the T_c/ decrease the length of the TES/decrease the fin connector volume) so that the system isn't phase separated.

A History of CDMS & Phase Separation

In the next section we will properly show that operating a TES when phase separated results in suboptimal performance, but we can guess this would be the case since the vast majority of a phase separated TES is either completely super-conducting or normal and thus has no sensitivity to thermal changes (smaller signal sensitivity), Additionally, the noise on the measurement has increased since thermal noise fluctuations across the boundary between the two modes couple to the current. So we can be pretty confident that phase separation is evil and should be avoided in devices at all costs. Furthermore, this understanding is not new. Our collaboration has always attempted to design thermally uniform devices (Blas and Kent originally developed a slightly simplified Eq. 4.25 and thus it's not like our collaboration didn't understand these concepts).

Unfortunately though, we have yet to achieve this goal. When designing the CDMS II oZIP QET [75], we unfortunately did not account for the increased electron-phonon coupling due to the huge fin connectors ($\zeta_T \sim 1/7$). Consequently, the CDMS II oZIP TES is actually phase separated for all $T_c >\sim 65mK$ (α assumed to be 80) when we thought it had been conservatively designed for operation at 80mK as seen by the black curve in Fig. 4.11.

Over the following years, phase separation continued to float around as possible culprit for a variety of ills in the Cabrera group at Stanford even though we falsely believed that the CDMS II detector was immune to these issues. Most notably, Steve correctly and smartly hypothesized that phase separation could be the cause of strange pulse shape behavior in his x-ray detector [76] and I attempted to explain non-intuitive

pulse shape behavior in quasi-particle diffusion experiments by allowing for thermal variation along the TES [77]. Eventually, while attempting to analyze the CDMS II $\left|\frac{\partial I}{\partial V}\right|$ (Fig. 4.1 [78]), Jeff and I came to the conclusion that phase separation was the most likely culprit for the non-simplistic transfer functions and we understood the CDMS II design mistake of not accounting for ζ_T.

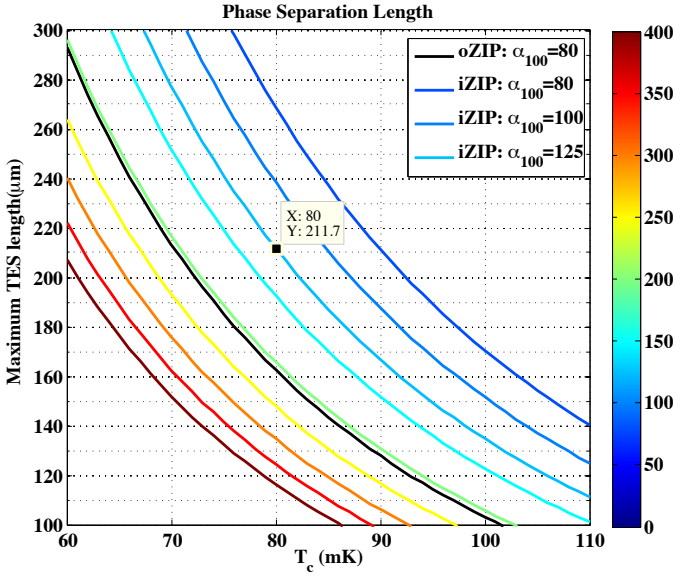

Figure 4.11: Maximum Length for which a TES remains thermally uniform as a function of T_c for ζ_T corresponding to oZIP (black) and iZIP (all colors) QET designs

In the hope that this issue would never again plague CDMS, the iZIP TES design was significantly altered. First, we decreased the iZIP QET length to 220μm from the 250μm of the CDMSII oZIP. Secondly, we substantially decreased the volume of the W fin connectors and because we switched to full-wafer contact photo-lithography on the EV-Align from optical stepper photolithography on the Ultratek our W TES line widths increased from $\sim$1μm to $\sim$2.4μm which though horrid from the perspective of maximizing the Al surface coverage (next chapter) also helped to increase ζ_T from $\sim$1/7 to $\sim$1/2. Due to these changes, we estimated that the iZIP TES with an $\alpha = 80$ would phase separate at 88 mK and thus we thought that we had built in a little safety margin since we planned on operating the devices at a T_c of 80mK.

Unfortunately, the vast majority of the iZIP4/5 detectors which were fabricated for

β_{wf}	2.22x10$^{-8}\frac{W\Omega}{K^2}$
Electron/Phonon Coupling Coefficient (Σ)	0.32±.02±.12 $\frac{pW}{K^5m^3}$ [51]
Thermal Conduction Power Law Exponent (n)	5
TES length (l)	220μm for iZIP 250μm for oZIP
TES volume fraction (ζ_T)	0.5 for iZIP 0.14for oZIP
α	125 - 300
ρ_w	1.32x10$^{-7}\Omega$m

Table 4.2: Phase Separation Characteristics for CDMS TES

SuperCDMS Soudan have T_c which are within the range 95mK-105mK since we stopped ion-implanting detectors after implanting the first batch resulted in detectors with unexpected T_c (To this day we still don't have a full understanding as to what happened. A significant possibility is human error). Thus, we fully expected these high T_c detectors to be phase separated.

To my utter dismay though, even G51 with $71mK < T_c < 82mK$ seems to display some features in their $\frac{\partial I}{\partial V}$ curves that Adam, Steve, and Tali have quite persuasively argued are still quite indicative of phase separation. Basically, their argument is that I massively overestimated the phase separation length for a given T_c when designing the iZIP4/5 QET by using an α=80, since the Stanford measured R vs T curves indicated an α >300 . As we discussed in the previous chapter though, this α estimate is inconsistent with that from $\frac{\partial I}{\partial V}$ curves for the W TES test structures which seem to indicate an $\alpha \sim 125$. So, we know that my original estimate was too low but not how low. Without more careful and consistent measurements of $\alpha(T_c)$ in the future, there will remain significant uncertainty on the phase separation length scale.

To help guide this discussion in the future, the curves shown in Fig. 4.11 show the maximum TES length for thermally uniform dynamics as a function of T_c for a wide variety of α.

4.3.3 Phase Separation Dynamics and Noise

Problems with 1st Order Approximations

In the derivation to find the point at which a TES phase separates, we truncated all of the taylor exspansions at first order so that we could make the system easily solveable.

To see how much information we lost in making this huge simplifying assumption one only needs to look at the plot of R(T). Notice, that the first order taylor exspansion is completely unphysical. At temperatures far below T_c, the first order taylor exspansion gives negative resistances... likewise at high temperatures the resistance continues to grow indefinitely!

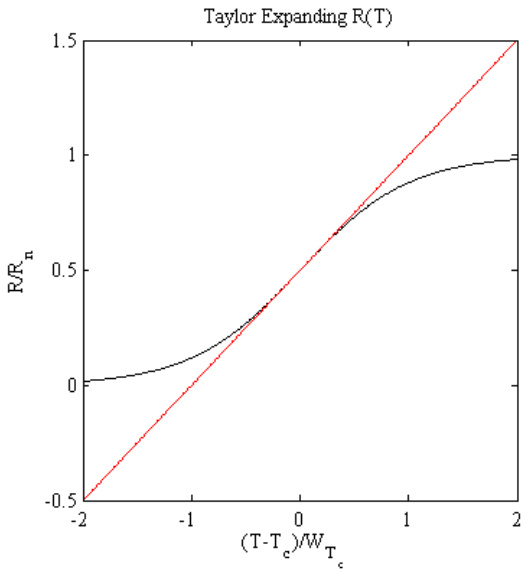

Figure 4.12: default

This unphysicality is implicitly found in our simplified dynamical equations for $\mathcal{T}(k)$. In particular, let's say I have a system in which I can magically manipulate only the thermal conduction along the TES and not change any of the other electrical/thermal properties of the system. With this power, I can take a system which is stable and exhibits no phase separation and change the thermal connection slightly and force

the system into an unstable regime. Then any small/random thermal fluctuation in the first harmonic mode,$\delta\mathcal{T}(1)$, will cause an exponential growth of the 1st thermal harmonic:

$$\mathcal{T}(1,t) = \delta\mathcal{T}(1)e^{\gamma t} \tag{4.26}$$

Literally, the linearized equations say that the first harmonic will never stop growing. On one side of the TES, we'll have infinite positive resistance and on the other side we'll have infinite negative resistance. Furthermore, the system will never be in equilibrium... there will never be a situation where all time derivatives go to zero.

Truly, we must accept the added computational hassles and keep higher order terms if we want to say anything about a phase separated equilibrium point!

nonlinear PDE in the x basis

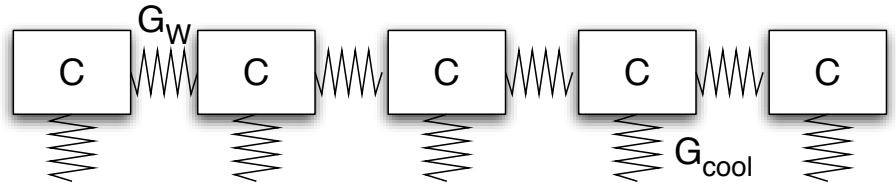

Figure 4.13: Discretized TES approximation to the full PDE

To solve the full non-linear dynamics computational, the most obvious solution is to discretize the TES into n components connected both thermally and electrically in series as shown in Fig. 4.13. With this simplification Eq. 4.17 becomes

$$\begin{aligned} L\dot{I} &= V_b + I(R + R_l) + \delta V \\ C_i\dot{T}_i &= I^2 R_i(I,\vec{T}) - P_{i\,bath}(T_i) + G_w\left(T_i - T_{i-1}\right) - G_w\left(T_{i+1} - T_i\right) + \delta P_i \end{aligned} \tag{4.27}$$

Up to this point, we've been able to get away with only defining $R(I,T)$ locally

in terms of R_o, $\frac{\partial R}{\partial I}$, and $\frac{\partial R}{\partial T}$. When operating a TES in a phase separated regime though, the entire resistance curve is expressed and thus we need to use some reasonable functional form for the resistance. Historically, the CDMS Cabrera group has used

$$\rho(J,T) = \frac{\rho_n}{2}\left(1 + \tanh\left(\frac{T - T_c - \left(\frac{\eta}{1.76}\sqrt{\frac{\hbar\rho_n T_c}{k_b c}}J\right)^{\frac{2}{3}}}{\Delta}\right)\right) \tag{4.28}$$

where Δ characterizes the width of the transition ($\Delta = \Delta T_{90-10}/\log(9)$) and the dimensionless η characterizes the sensitivity of your film to current.

One should consider the absolute blind use of this formula throughout the rest of this chapter to be a significant systematic since the functional form is certainly not well theoretically motivated. However, it also was not arbitrarily generated. As discussed in Jenn Burney's thesis [79], the dependence of ρ on the current density, J, was generated from the BCS critical current equation. Hopefully, the qualitative features of phase separated dynamics and noise will be independent of this precise functional form.

After propagating in time for scales long with respect to τ_{eff}, equilibrium current and temperature distributions along the TES can be obtained. As expected, TES with $l < l_{max}$ have uniform thermal distributions. Interestingly, for devices with physical properties such that $l_{max} < l < 2l_{max}$, the length scale over which thermal variation occurs is substantial compared to the length of the TES itself as shown in (Fig. 4.14). Intuitively, this makes sense: internal thermal conduction along the TES may not be large enough to suppress thermal fluctuations completely but it can at least keep the thermal gradient from growing too large. Eq. 4.23, though not completely valid since it drops all non-linear terms, also hints at this result since in the region of $l_{max} < l < 2l_{max}$, only the first harmonic term grows exponentially.

To computationally estimate both $\frac{\partial I}{\partial V}$ and $\frac{\partial I}{\partial P}$, we must just ping the simulation with

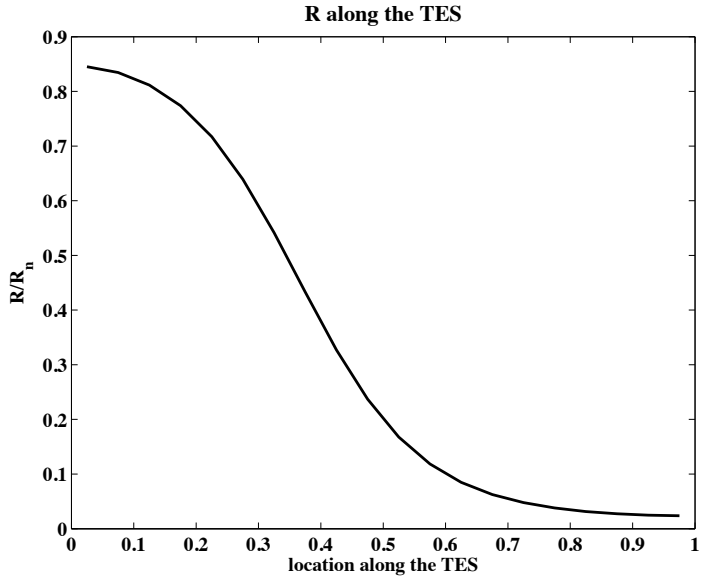

Figure 4.14: Simulated equilibrium resistivity along a phase separated iZIP4/5 TES with T_c=75mK and ΔT_c=1mK for which l_{max}=169μm

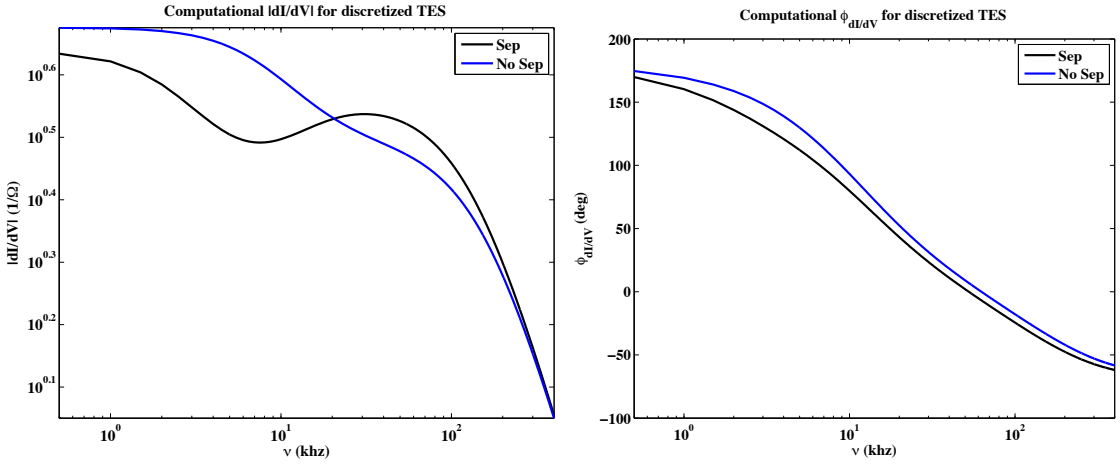

Figure 4.15: Simulated $\frac{\partial I}{\partial V}$ curves for phase separated (black) and non-phase separated (blue) iZIP4/5 TES with T_c=75mK and ΔT_c=1mK

a dirac delta δV or δP (note: this is simply equivalent to starting the simulation with a small current or temperature offset). Results are shown in Figs. 4.15 & 4.17. To emphasize the differences caused by phase separation, these plots also all display the greens function for a TES with absolutely identical physical characteristics except for

G_w which was increased by x4 so that a thermally uniform state was stable.

The fact that the telltale dip and bump seen in $\left|\frac{\partial I}{\partial V}\right|$ for many of the CDMS II detectors(Fig. 4.1) was naturally and easily replicated for the phase separated simulation (black) definitely suggests that we have found the cause of our complexities!

Fortuitously, we can experimentally strengthen this argument further by looking at the TES test structures. Due to the large T_c(105-110mK) on all the devices we fabricated and studied, Eq. 4.25 indicates that all but the 100μm line device are phase separated for the entire domain of expected α. This means that by looking at the 300μm line only device, we can precisely separate all dynamical effects which are caused by non-infinite G_{TF} from the effects caused by phase separation.

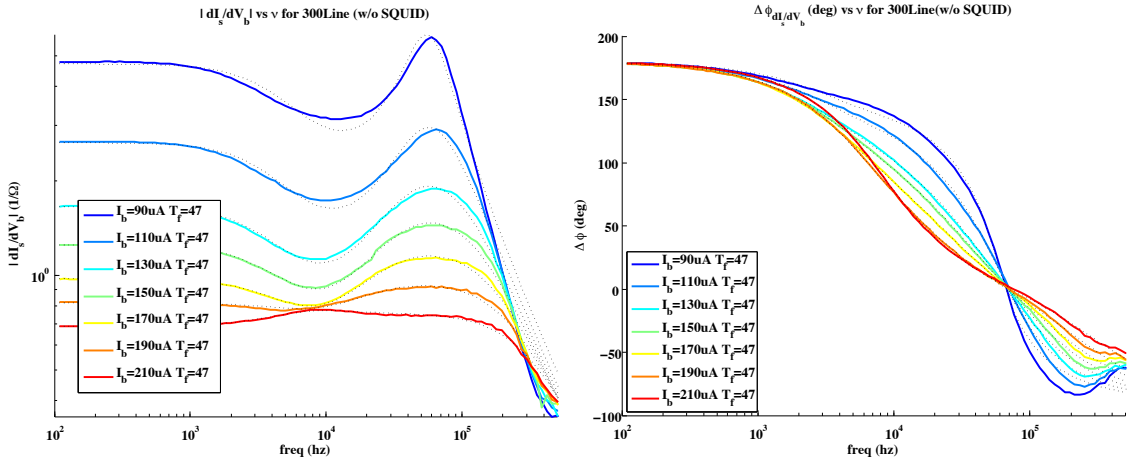

Figure 4.16: Experimental $\frac{\partial I}{\partial V}$ curves for 300μm line only test structure

When biased low in the transition(blue curves), the measured $\frac{\partial I}{\partial V}$ (Fig. 4.16) certainly qualitatively matches both the simulation and the CDMS II detectors. The disappearance of the dip and bump when biased higher in transition (red) is also consistent with phase separation hypothesis because a smaller $\mathcal{L}$ should increase l_{max}.

The $\frac{\partial I}{\partial P}$ curves shown in Fig. 4.17 display an enormous number of interesting features. First and foremost, operating in a phase separated state (black) substantially decreases your power sensitivity over the same TES which has been artificially homogenized. Secondly, two falltime poles are clearly distinguishable in the time domain

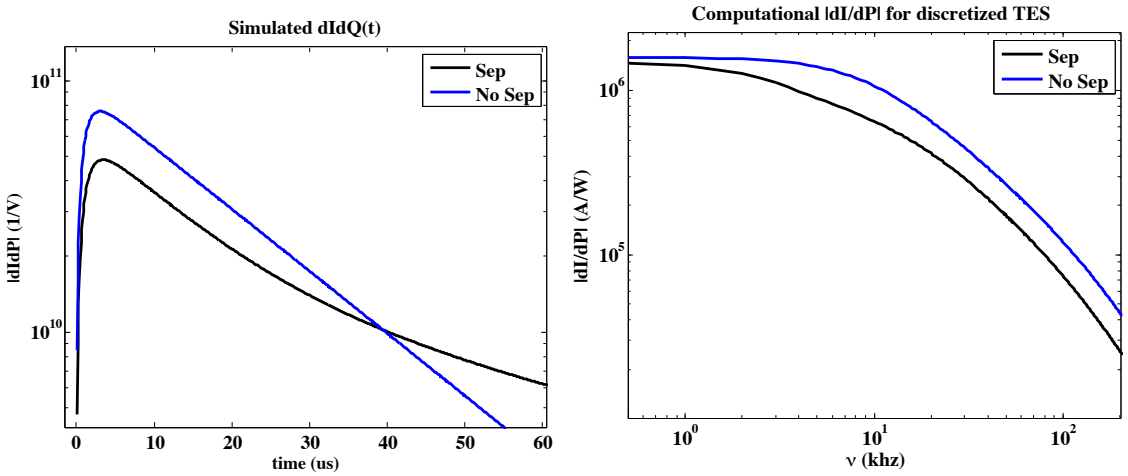

Figure 4.17: Simulated $\frac{\partial I}{\partial V}$ curves for phase separated (black) and non-phase separated (blue) iZIP4/5 TES with T_c=75mK and ΔT_c=1mK in time and fourier domain

just like for iZIP glitch events. Basically, a uniform thermal power spike dominately couples to only 2 thermal eigenvectors of the system. Even more interestingly, the highest frequency falltime pole, $\omega_{fall\,1}$, for the phase separated case is very similar to the $\omega_{\rm eff}$ pole for the thermally uniform simulation. If this result is general and not hugely dependent upon the precise functional form used for $\rho(I,T)$, then we already have an excellent understanding of our actual $\omega_{\rm eff}(T_c)$ just by looking at phase separated glitch events and other $\frac{\partial I}{\partial V}$ curves. Channel A1 of G51(T_c=71±2mK), for example, has pole frequencies of 5.0±0.7 khz which under the assumption of β=0.3 give us an α estimate of 110±20. Making our standard assumption of linear dependence of α on T_c (transition width invariant), this gives us an α_{100mK}= 160±30 which roughly matches that device characteristics found for the TES test structures.

One confusing detail in the G51 glitch analysis, is that since side 1 channels are 71-75mK while side 2 channels are at 77-82mK we should expect a clear correlation between the quick falling edge pole and channel side. Being more precise, we naively would expect $\omega_{fall\,1\,A1}$ ∼x1.7$\omega_{fall\,1\,A2}$. This is not seen.

In a test to study the feasibility of taking $\frac{\partial I}{\partial V}$ curves for all devices at the bias point only, we measured the response of G12G (Side 1: 73mK< T_c <78mK & Side 2:

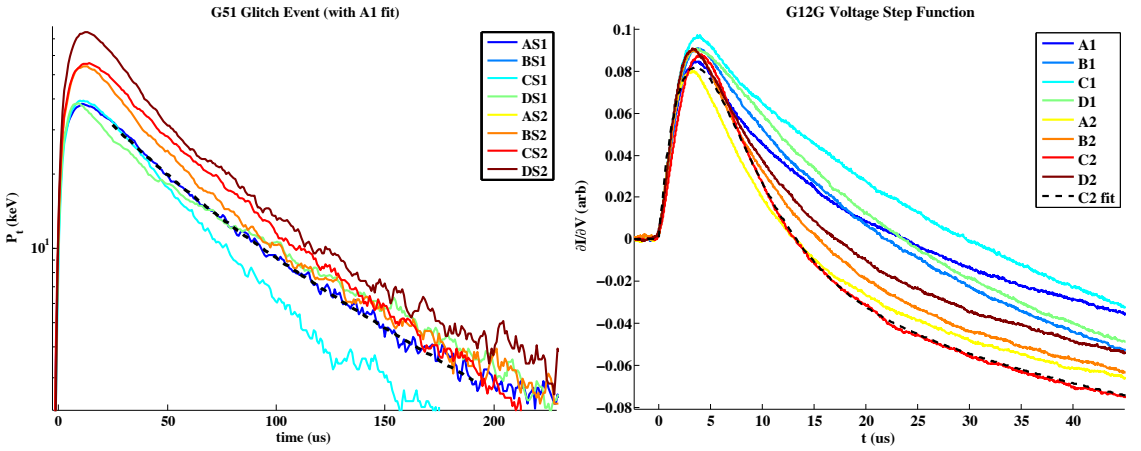

Figure 4.18: G51 glitch event with falling edge fit A1 and G12G response to voltage square wave excitation (channels names correspond to DIB addressing)

59mK$< T_c < 65mK$) to a small square wave function and the results are seen in Fig. 4.18 right. Though not trivially visible, Adam found transfer functions with 3 poles plus an offset (an additional pole at ω=0) were required to fit all channels, which means that all channels had 2 excitable thermal degrees of freedom and were thus phase separated even though the side 2 channels were quite low in T_c [80]. Even more confusing is the enormous size of the primary falltime pole. For C2, $\omega_{fall\,1}$= 40 $\pm$ 13 khz ($\tau_{fall\,1} \sim 4\ \mu$s), which is x8 faster than the quick falltime pole seen for G51 glitch events even though G51 had larger T_c. This falltime is so quick that it suggests an $\alpha >$400.

Trying to reconcile these two measurements is certainly difficult. One possibility is that the electronic glitches aren't tantamount to dirac-delta functions but are actually slower than the sensor response. Another possibility is that α has wild fluctuations between different depositions. Finally, this pole is so quick that it could just barely be caused by poor thermal connectivity between the fin connectors and the TES (remember we experimentally argued that G_{tf} was absolutely too large to cause 6μs response, so 4μs is on the edge). Under this hypothesis though, we would expect 3 thermal poles for a truly phase separated device like G48 rather than just 2. So this hypothesis certainly seems disfavored. To conclusively disprove this hypothesis

though, we would really like to study a 100μm fin connected device which we know to be phase uniform (T_c <80mK).

Additional Noise Sources in the X basis

In splitting up the TES into n_x independent pieces, we added a significant number of degrees of freedom to the system and we should certainly expect stochastic fluctuations between these degrees of freedom. Luckily, in the x-basis this is quite simplistic. For the johnson noise across the TES, we must only assume that the voltage drop across each component TES is independent of all others and thus we can use simple noise theory for the magnitudes:

$$S_{v\,tes\,i} = 4k_bTR_i(T_i) \tag{4.29}$$

Of course, the voltage johnson noise is still anti-correlated with power noise for each individual TES segment as we derived in the previous chapter.

Likewise, if we assume that the thermal fluctuations across each of the thermal conductances to the bath are also non-correlated, then we end up with

$$S_{p\,G_b} = 4k_bT_i^2G_b(T_i(t)) \tag{4.30}$$

The fluctuations across the thermal conductance between two series TES (Internal Thermal Fluctuation Noise [ITFN]) are of course more tricky because by definition they take energy from one TES and move it to another and thus by energy conservation we have $\delta P_{ITFN\,i}(t) = -\delta P_{ITFN\,i-1}(t)$ for the thermal power fluctuations across the conductance between the i^{th} and $i+1^{th}$ elements.

The magnitude of these fluctuations is simply

$$S_{pG_w,i+1} = 4k_b \left(\frac{T_i + T_{i+1}}{2}\right)^2 G_{W\,i,i+1} \tag{4.31}$$

Please note that unlike in the basic TES chapter, I haven't explicitly calculated the first order transfer functions from the various noise sources to current. Conceptually, I could explicitly linearize the nD+1 dynamical equations to find the rather large and daunting M_{nD+1} dynamical matrix but at the end of the day you, the reader, would have gained very little from this experience that we didn't already know from just looking at the computationally calculated Fig. 4.19.

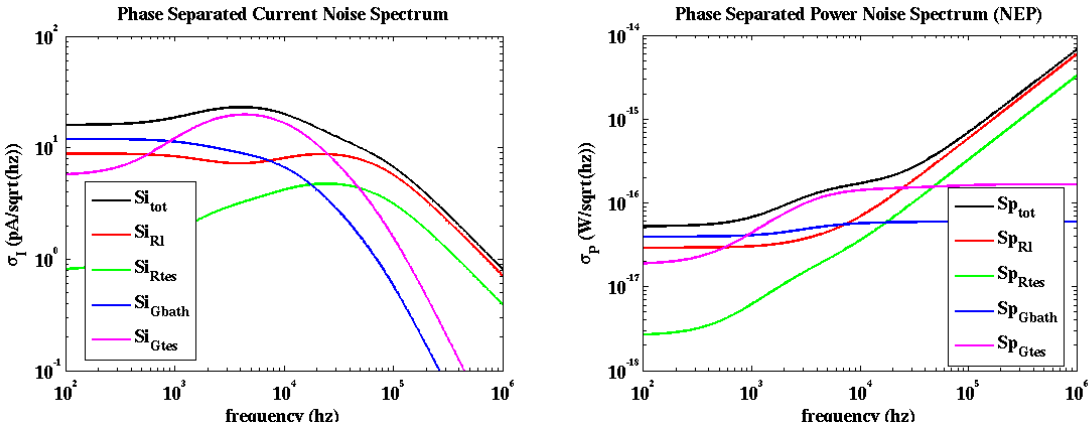

Figure 4.19: Simulated current (left) and power (right) noise.

In a phase separated device, ITFN along the TES (magenta) couples quite strongly to current and dominates all other noise sources around ω_{eff}. For CDMS II, this is particularly problematic since this is the precise frequency range which contains all of our fiducial volume information (i.e. the electron recoil/nuclear recoil timing cuts). Being a bit bolder, one could quite reasonably argue that the CDMS II standard analysis threshold could have been set at 5keV rather than 10keV if only our devices hadn't been phase separated. Clearly, the design requirement of no phase separation is valid.

4.3.4 Many body vector ODE in fourier space

During the ending days of the CDMS II experiment, we were quite interested in the second low frequency pole seen in the phase separated green's function. The hope was that we could understand the long position dependent pulse times seen in the CDMS II experiment as being caused by phase separation in the TES. This hypothesis hinged on finding physical TES characteristics which both decreased the frequency of this slow pole and increased it's efficacy with respect to the $\omega_{fall\,1}$ pole, something we found incredibly hard to reproduce in the simulation by just randomly trying different $\rho(I,T)$ curves.

Of course we now understand that our issue in simulating this performance was that these long collection times were actually due to phonon physics and the fact that it was hard to reproduce the desired characteristics was a sign that we were barking up the wrong tree, but at the time I was convinced that with just a little more effort and understanding these long falltimes could be matched. So the rest of this chapter, though intrinsically interesting and beautiful doesn't significantly add to our understanding of the CDMS detector and thus definitely it can be skipped with impunity.

Our basic plan was to gain more intuitive understanding of the system by finding some small dimensional basis in which to expand both the perturbations and the equilibrium thermal shape. This seemed quite reasonable since the simulated current response to a dirac-delta voltage or uniform power input (Fig. 4.15) was dominated by 2 eigenvectors. This is a bit surprising. For a TES split into n_x bins, there are n_x+1 degrees of freedom, or equivalently, the linear pertubation matrix, $M(\omega)$ has dimensions n_x+1 x n_x+1. Consequently, the transfer function for this model, nominally has n_x+1 poles! Since, these poles aren't seen in the current response it means that the vast majority of the dynamical eigenvectors aren't excited by the homogenous pertubations (the only ones we really care about) and thus we can totally drop them without loss of information.

The cosine basis which diagonalizes $\dot{T} = -D\nabla^2 T$ would seem to be an excellent

basis in which to expand our system for two reasons. First for large k pertubations, thermal diffusion dominates all other terms in the dynamical equations due to the k^2 (Eq. 4.23). Secondly, a nice approximation to the equilibrium $\rho(x)$ seen in fig. 4.14 (and more generally all weakly phase separated systems) can be built with only the smallest few 3-4 degrees of freedom.

Handling Convolutions

This basis though has one huge problem: nonlinear x basis operators aren't easily represented. Thus we'll need to figure out how to relate the fourier components of $T(x,t)^n$ to $\mathcal{T}(k)$. For simplicity, let's play with $T(x,t)^2$ and then generalize:

$$\begin{aligned} T(x,t)^2 &= \mathcal{T}(k_1,t)e^{ik_1x}\mathcal{T}(k_2,t)e^{ik_2x} \\ &= \mathcal{T}(k_1,t)\mathcal{T}(k_2,t)e^{i(k_1+k_2)x} \\ &= \mathcal{T}(k_1,t)\mathcal{T}(k_2,t)\delta(k_1+k_2-p)e^{ipx} \\ &\equiv \mathcal{T}_2(p,\vec{\mathcal{T}}(t))e^{ipx} \end{aligned}$$

where in the second to last line we summed over a delta function and then in the final line we defined $\mathcal{T}_2(p,t)$ as the fourier coefficient for $T(x,t)^2$ (nothing we just did is earth shattering by any means... we simply just derived the convolution formula). Next, we can generalize the procedure and find the fourier coefficient for $T(x,t)^m$:

$$\mathcal{T}_m\big(p,\vec{\mathcal{T}}\big) = \mathcal{T}(k_1,t)\mathcal{T}(k_2,t)...\mathcal{T}(k_m,t)\delta(k_1+k_2+...k_m-p) \tag{4.32}$$

One can think of these formulas diagramtically as well. Fundamentally, $\mathcal{T}_m(p)$ is simply the sum of all feynman vertices which conserve momentum (Fig. 4.20 illustrates all the diagrams for T^3).

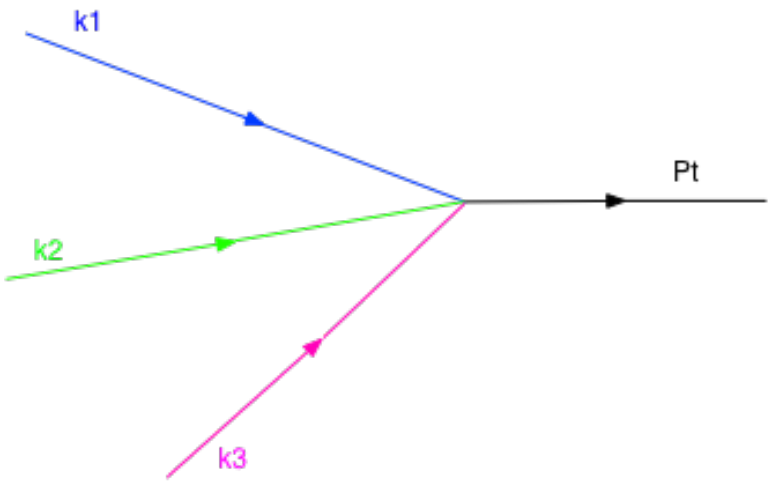

Figure 4.20: Graphical schematic for convoluting a $T(x)^3$ operator

In the definition above, $\mathcal{T}_0$, is ambiguous. Since we plan on always summing our many-body expansions about the homogenous equilbrium point though, it simplifies the calculations tremendously if we define $\mathcal{T}_0$ as

$$\mathcal{T}_0(p) = \delta(p - 0) \tag{4.33}$$

Using these definitions, we can now expand the ρ fourier modes in terms of $\vec{\mathcal{T}}$.

$$\begin{aligned} \rho(x,t) &= \frac{1}{m!}\frac{\partial^m \rho}{\partial T^m} T^m(x,t) \\ &= \frac{1}{m!}\frac{\partial^m \rho}{\partial T^m} \mathcal{T}_m(k, \vec{\mathcal{T}}(t)) e^{ikx} \\ &\equiv \rho(k, \vec{\mathcal{T}}(t)) e^{ikx} \end{aligned} \tag{4.34}$$

As an aside, you can now see the price of keeping the non-linear terms ($T(x,t)^2$, $T(x,t)^3$, ...) in our calculation. In fourier space, these terms are correspond to many body couplings (yikes!).

4.3.5 Pertubatively Calculating the Resistance

In the first order calculation above, we found quite unexpectedly that working in the fourier domain simplified tremendously the nonlocal Resistance term. Luckily, a similar simplification is seen even when we keep all perturbative orders. Explicitly:

$$\begin{aligned} R(t) &= \int_0^l dx \frac{\rho(T(x,t))}{A_t} \\ &= \rho(k, \vec{\mathcal{T}}) \int_0^l dx \frac{e^{ikx}}{A_t} \\ &= \frac{\rho(0, \vec{\mathcal{T}})l}{A_t} \end{aligned} \tag{4.35}$$

Just as warning... the equation for R(t) looks quite simple. $\rho(0, \vec{\mathcal{T}})$ though, does include all of the many body feynman diagrams implicitly!

4.3.6 Putting it all together: the many-body differential equation

Let's take eq. 4.17 and taylor expand to all orders about thermally homogenous equilibrium temperature,T_u (if $l > l_{max}$ this is an unstable equilibrium point!). Then let's fourier transform all of the resulting terms. Finally, we can use the orthogonality of the fourier components to split the partial differential equation into a vector

ODE:

$$L\frac{d}{dt}I(t) = V_b - I(t)\left(R_l + \frac{\rho(0,\vec{\mathcal{T}}(t))l}{A_t}\right) + \delta V(t)$$
$$cA_{tf}\frac{d}{dt}\mathcal{T}(k,t) = \frac{I^2(t)\rho(k,\vec{\mathcal{T}}(t))}{A_t} - p_{bath}(k,\vec{\mathcal{T}}(t))A_{tf} - g_w A_t k^2 \mathcal{T}(k,t) + \delta P(k,t) \tag{4.36}$$

Notice that for simplicity, we constrain R to only vary with T and not I ($\beta = 0$). This allows us to drop all the higher order partials which combine T and I.

4.3.7 Small Signal Taylor Exspansions about points near T_u

Just as in the x-basis, eqs. 4.36 can be tossed into a numerical ODE solver and we can find the stable equilbrium points as well as current pulse shapes. The whole purpose of switching to the fourier basis though, was to develop smaller (and thus more comprehensible) formulations for $\frac{dI}{dV}$ and $\frac{dI}{dP(0)}$ as well as gain understanding into the nature of the phase separated equilbrium, neither of which we have yet accomplished. For the later, let's look at the taylor expansion about an arbitrary point, $\vec{\mathcal{T}}_\star$, which is between the stable equilibrium phase space point,$\vec{\mathcal{T}}_{eq}$, and the unstable equilbrium. Afterwards, we can then obtain the important transfer functions by simply setting $\vec{\mathcal{T}}_\star$ to $\vec{\mathcal{T}}_{eq}$.

The first order taylor expansions are

$$\begin{aligned} L\frac{d}{dt}\delta I(t) &= -\left(R_l + \frac{\rho(0,\vec{\mathcal{T}}_\star)l}{A_t}\right)\delta I(t) - \frac{I_u l}{A_t}\left.\frac{\partial\rho(0)}{\partial\mathcal{T}(q)}\right|_{\vec{\mathcal{T}}_\star}\delta\mathcal{T}(q,t) + \delta V(t) \\ c_v A_{tf}\frac{d}{dt}\delta\mathcal{T}(k,t) &= \frac{2I_u\rho(k,\vec{\mathcal{T}}_\star)}{A_t}\delta I(t) + \frac{I_u^2}{A_t}\left.\frac{\partial\rho(k)}{\partial\mathcal{T}(q)}\right|_{\vec{\mathcal{T}}_\star}\delta\mathcal{T}_q - g_{b\,q}(k)\delta\mathcal{T}_q - g_w k^2\delta\mathcal{T}_k(t) + \delta P(k,t) \end{aligned} \tag{4.37}$$

Just like in the basic TES dynamics chapter, we've added the possibility of voltage and power perturbations so that we can eventually calculate all the external transfer functions. Due to the constraint that $\mathcal{T}(-k) = \mathcal{T}(k)$, we can shrink the phase space vector to only $I(t)$ and $\mathcal{T}_k(t)|k \geq 0$ without any loss of generality if we redefine partial derivatives to be

$$\frac{\partial\mathcal{T}_m(k)}{\partial\mathcal{T}(q)}(\vec{\mathcal{T}}) = \begin{cases} m\mathcal{T}_{m-1}(|k-q|) & \text{if } q = 0 \\ m\big(\mathcal{T}_{m-1}(|k-q|) + \mathcal{T}_{m-1}(|k+q|)\big) & \text{if } q \neq 0 \end{cases} \tag{4.38}$$

With this in mind, the thermal conductance to the substrate, g_b, and $\frac{\partial\rho(k)}{\partial\mathcal{T}(q)}$ are now both matrices defined as

$$g_{b\,q}(k) = \frac{1}{m!}\Sigma\left.\frac{\partial^m T^n}{\partial T^m}\right|_{T_u}\left.\frac{\partial\mathcal{T}_m(k,\vec{\mathcal{T}})}{\partial\mathcal{T}(q)}\right|_{\vec{\mathcal{T}}_\star} \tag{4.39}$$

$$\frac{\partial\rho(k)}{\partial\mathcal{T}_q} = \frac{1}{m!}\left.\frac{\partial^m\rho}{\partial T^m}\right|_{T_u}\left.\frac{\partial\mathcal{T}_m(k,\vec{\mathcal{T}}))}{\partial\mathcal{T}(q)}\right|_{\vec{\mathcal{T}}_\star} \tag{4.40}$$

Phase Separated Equilibrium and Higher Order Suppression

Since the inductor only changes the behavior of the system on short times, we can remove him if we are only trying to understand properties of the equilibrium state. Secondly, since we aren't trying to be exact in this section let's also remove R_l ($R_0 >> R_l$ if in strong electro-thermal feedback regime) and $g_{bq}(k)$ ($\mathcal{L} >> 1$). With these simplifications δI is now a function of $\delta\vec{\mathcal{T}}$

$$\delta I(t) = \frac{-I_\star \left.\frac{\partial\rho(0)}{\partial\mathcal{T}_q}\right|_\star}{\rho(0)_\star}\delta\mathcal{T}_q + \frac{A_t}{\rho(0)_\star l}\delta V \tag{4.41}$$

and thus eq. 4.37 can be written only in terms of temperature changes:

$$cA_{tf}\frac{d}{dt}\delta\mathcal{T}(k) = \frac{I_\star^2}{A_t}\left[\left.\frac{\partial\rho(k)}{\partial\mathcal{T}(q)}\right|_\star - \frac{2\rho(k)_\star}{\rho(0)_\star}\left.\frac{\partial\rho(0)}{\partial\mathcal{T}(q)}\right|_\star\right]\delta\mathcal{T}(q) - g_w A_t k^2\delta\mathcal{T}(k) + \frac{2I_\star\rho(k)_\star}{l\rho(0)_\star}\delta V + \delta P(k) \tag{4.42}$$

The dynamical regime that we are interested in for CDMS II / SuperCDMS devices is $l_{max} < l < 2l_{max}$. Consequently, the diffusion term ($-g_w k^2$) dominates joule heating terms in eq. 4.42 for all thermal modes $k > \frac{\pi}{l}$ and thus we would expect that the true equilibrium state,$\vec{\mathcal{T}_{eq}}$, would have small contributions from these higher order modes (as seen in fig. 4.14).

Bizarrely, the smallness of these modes also tends to suppress the importance of the higher order many body couplings. To see this, note the presence of $m!$ in the denominator of eq. 4.34 means that for large m, each individual many body term has an extremely minute size. So for these terms to be non-negligible, a huge number of them must sum coherently. In the case of $l > 5l_{max}$ for instance, 5 different thermal modes could have significant deviations from zero. Thus, the phase space for an m-order coupling is 5^m which which is much larger than $m!$ for $m < 5$. and consequently the 5th order many body coupling will almost certainly dominate the $m = 1$ or $m = 2$ many body contributions. In our case, the suppression of higher order modes due to

diffusion allows us to cut off our many order couplings as well.

With this in mind, let's write eq. 4.42 in matrix format, keeping only the $m < 2$ many body terms and only the $k = 0, \frac{\pi}{l}$ thermal modes

$$cA_{tf}\frac{d}{dt}\begin{bmatrix}\delta\mathcal{T}(0)\\ \delta\mathcal{T}(1)\end{bmatrix}=\begin{bmatrix}-\frac{I_\star^2}{A_t}\left(\frac{\partial\rho}{\partial T}+\frac{\partial^2\rho}{\partial T^2}\mathcal{T}(0)\right) & -2\frac{I_\star^2}{A_t}\frac{\partial^2\rho}{\partial T^2}\mathcal{T}(1)\\ \frac{I_\star^2}{A_t^2}\left(2\frac{\partial^2\rho}{\partial T^2}-\frac{\left(\frac{\partial\rho}{\partial T}\right)^2}{\rho(0)}-\frac{\frac{\partial^2\rho}{\partial T^2}\frac{\partial\rho}{\partial T}}{\rho(0)}\mathcal{T}(0)\right)\mathcal{T}(1) & \frac{I_\star^2}{A_t^2}\left(\frac{\partial\rho}{\partial T}+2\frac{\partial^2\rho}{\partial T^2}\mathcal{T}(0)-4\frac{\frac{\partial^2\rho}{\partial T^2}\frac{\partial\rho}{\partial T}}{\rho(0)}\mathcal{T}(1)^2\right)-g_w\end{bmatrix}\begin{bmatrix}\delta\mathcal{T}(0)\\ \delta\mathcal{T}(1)\end{bmatrix} \tag{4.43}$$

The validity of eq. 4.43 critically depends on $\frac{\partial^2\rho}{\partial T^2}$ at the unstable equilibrium. If negative, the presence of $|T(1)|$ tends to accelerate the phase separation process. Physically, the transfer of energy from one part of the TES to the other will result in a decrease in the overall resistance, which leads to an increased current and thus faster growth of $|T(1)|$. Eventually, $|T(1)|$ becomes so large that higher order many body terms become dominant (and eventually cut off the growth). **By contrast, a positive $\frac{\partial^2\rho}{\partial T^2}$ decreases the current traveling through the TES which tends to suppress the exponential growth of $|T(1)|$ and thus the two equilibrium are relatively near each other.**

The dependence of $\frac{dI}{dP(0)}$ transfer function on the amount of phase separation(fig. 4.21) can also be readily read off the matrix. First and foremost, the amount of mixing between $T(0)$ and $T(1)$ depends upon the magnitude of the off diagonal elements (elements [1,2] and [2,1] in eq. 4.43) which are proportional to the amount of phase separation at equilibrium. Consequently, a TES with just a tinge of phase separation will have $\frac{dI}{dP(0)}$ that is dominated by a single exponential with a time constant slightly longer than τ_{etf} for the homogenous system. The other assymetric eigenstate (mostly $\delta T(1)$) which is barely excited by homogenous power inputs will then have incredibly long time constants(element [2,2])!

By contrast, TES with larger amounts of phase separation will show two exponential decays of similar magnitude and similar time constants. So our hope of explaining

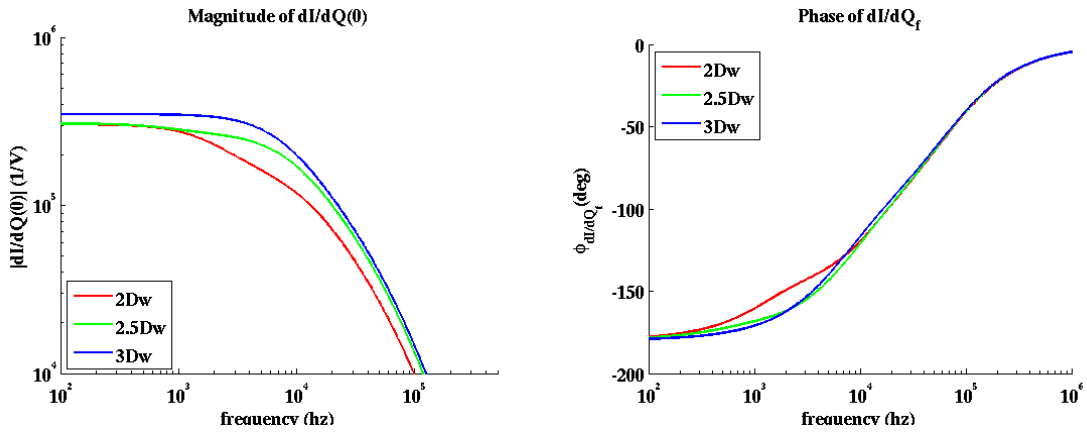

Figure 4.21: Current response to uniform thermal power fluctuations for differing levels of phase separation

the long time constants ($\sim 350\mu s$) seen in CDMS II devices through phase separation certainly doesn't hold in the slightly phase separated limit. Of course, this derivation is limited to the small $T(1)$ regime. Consequently, we have not proven that $\frac{dI}{dP(0)}$ with dominant long fall time exponentials are impossible to create with stronger phase separation. Blas and I, though, simulated a variety of different largely phase separated systems with different $\rho(T)$ curves and found the above ideas to always hold true. Thus, we are very confident that dominant falltimes $> 200\mu s$ are very difficult to generate through a phase separated mechanism (Plus, we now know they are caused by phonon physics).

4.3.8 Additional Noise Sources in the k basis

When deriving the noise frequency distribution functions in the basic TES chapter, we took as fact the statement that a shot noise source which is totally random in time has a white frequency spectrum (random and absolutely constant at all frequencies). Ideally, we' d like to transfer all of this reasoning over to k-space when deriving the noise power at different wavelengths but unfortunately we can't.

The reason is that in a phase separated state, we know that the resistivity may

vary hugely across the TES. Consequently, we can't claim that the voltage noise fluctuations are absolutely random in space. Rather, in the parts of the TES with larger resistivities, the noise will be larger and in areas where the resistivity is small, the voltage noise will also be tiny. This means that at least the johnson noise spectrum for a TES won't be white.

To calculate and understand the frequency spectrum for this non-stationary noise source it actually helps to have first looked at how one calculates noise spectrums under the more standard "ergodic" assumption (noise is statistically similar at all times). To keep from having to use gated functions in the definition of the S we'll make this derivation using a discrete fourier basis or equivalently a finite time range from [0,T) and in the standard fourier basis ($\delta\omega = \frac{2\pi}{T}$) with complex coefficients.

To calculate $< z(t)z^\star(t+\tau) >$, the absolutely first thing we'll do is use the assumption that the statistical properties are equivalent at all times by switching the average over an ensemble to an integration over time. Thus,

$$\sigma_z^2(\tau) =< z(t)z^\star(t+\tau) >= \frac{1}{T}\int_0^T z(t)z^\star(t+\tau) = \sum_{\omega_1}\sum_{\omega 2} z(\omega_1)z^\star(\omega_2)e^{i\omega_2\tau}\frac{1}{T}\int_0^T e^{-i(\omega_1-\omega_2)t} \tag{4.44}$$

The integral, is simply a delta function which forces $\omega_2 = \omega_1$ and thus we are left with

$$\sigma_z^2(\tau) = \sum_{\omega} z(\omega)z^\star(\omega)e^{i\omega\tau} \tag{4.45}$$

Eq. 4.45 looks like a fourier transform in the variable τ, so let's just simply invert it to isolate $z(\omega)z^\star(\omega)$.

$$z(\omega)z^\star(\omega) = \frac{1}{T}\int_0^T d\tau\sigma_z^2(\tau)e^{-i\omega\tau} \tag{4.46}$$

Now if we take the assumption that σ_z^2 is non-zero only for $\tau = 0$ (i.e. uncorrelated in time), we immediately see that the right side of eq. 4.46 does not vary with ω and consquently $|z(\omega)|^2$ is a constant.

Let's look at eq. 4.44 in another way. In the derivation we rationalized the averaging over t because of the assumption of uniformity. However, we can also look at this as simply the 0^{th} harmonic mode in a fourier exspansion of t. Thus, if we want to allow the noise to vary at different times/locations or be "non-stationary" we must not take the average of t/x and instead keep all of the higher order terms. In this vein let's fourier expand $< z(x)z^\star(x+\lambda) >$ in momentum space (unlike usual we are using the standard fourier basis!).

$$\begin{aligned}\sigma_z^2(q,\lambda) &= \frac{1}{l}\int_0^l dx < z(x)z^\star(x+\lambda) > e^{-iqx} \\ &= \sum_{k1,k2} < z(k_1)z^\star(k_2) > e^{-ik_2\lambda}\frac{1}{l}\int_0^l dx e^{i(k_1-k_2-q)x} \\ &= \sum_k < z(k+q)z^\star(k) > e^{-ik\lambda}\end{aligned} \tag{4.47}$$

Generalizing the previous case, we can determine all elements of the covariance matrix in frequency space just by inverting with respect to λ/τ. In particular, the off diagonal elements of the frequency space covariance matrix are zero for stationary noise sources since $\sigma_z^2(q,\lambda) = 0$ for all $q \neq 0$. For non-stationary noise sources, nonzero q modes of $\sigma_z^2(q,\lambda)$ exist and consequently correlations exist between the various k modes!

Thermal Fluctuation Noise

Even though we just spent a page deriving the non-stationary noise fourier transforms, let's assume that the variation in temperature across a phase separated TES is small relative to mean temperature and thus can safely be ignored when calculating the power fluctuations across the coupling to the bath (G_b). With this assumption, the

noise per unit length is then white and thus in our cosine basis

$$\begin{aligned} S_{\frac{d\delta Q}{dx}\,TFN}(q=0,\omega) &= \frac{4k_bT^2G_b}{l^2} = \frac{4k_bn\Sigma\bar{T}^{n+1}A_{tf}}{l} \\ S_{\frac{d\delta Q}{dx}\,TFN}(q\ \neq 0,\omega) &= \frac{2k_bT^2G_b}{l^2} = \frac{2k_bn\Sigma\bar{T}^{n+1}A_{tf}}{l} \end{aligned} \tag{4.48}$$

where q are discrete fourier modes and the ω are continuous. The magnitude of all the terms were automatically set by the zeroth term.

Internal Thermal Fluctuation Noise

For the thermal power fluctuations within the TES, let's again assume that the variation in temperature is small so that we don't have to keep track of the non-diagonal correlations just as we did in eq. 4.48. This calculation has one significant complication though. The boundary conditions of the TES require that these internal power fluctuations be expanded in the sine basis (at $x = 0$ and $x = l$ the heat transfer is always zero). If so, then the differential heating per length, $-\nabla\delta Q_{ITFN}$, will be in the cosine basis as we derived earlier. As with the cosine basis, the sine basis is complete from $(0, l)$.

However, we can't simply find the coefficients of all higher order terms through calculating the zeroth harmonic and then declare the system to have no spatial correlations, because by definition there is no zeroth harmonic; the Al bias lines have a superconducting band gap and thus the thermal conduction out the two ends is exponentially suppressed!

Consequently, to set the magnitudes of the fluctuations, let's follow the previous calculations in spirit and calculate the magnitude of power fluctuations necessary so that σ_E^2 of the left 1/2 of a TES matches the value from statistical mechanics (fig. 4.22). We could follow Voss [61] and integrate energy variation over 1/2 the volume

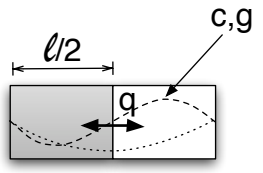

Figure 4.22: default

or we can simply track the power fluctuations through the $l/2$ surface. Following the second method, we find that

$$< \sigma^2_{E\,l/2} >= \sum_{\omega=\frac{2\pi m}{l}} \sum_{k=\frac{m\pi}{l}} \frac{< \delta P(k,\omega)\delta P^{\star}(k,\omega) >}{\omega^2 + \frac{g^2k^4}{c^2}} e^{ikl} + \frac{< \delta P(k,\omega)\delta P^{\star}(-k,\omega) >}{\omega^2 + \frac{g^2k^4}{c^2}} \tag{4.49}$$

Using the fact that $\delta P(-k,\omega) = -\delta P(k,\omega)$ (this is a sine basis), we find that only the k_{odd} terms are non zero and consequently

$$< \sigma^2_{E\,l/2} >= c\frac{lA_{cs}}{2} k_b \bar{T}^2 = \sum_{\omega=\frac{2\pi m}{l}} \sum_{k_{odd}=\frac{m_{odd}\pi}{l}} \frac{2 < |\delta Q(k,\omega)|^2 >}{\omega^2 + \frac{g^2k^4}{c^2}} \tag{4.50}$$

Since we are in the large T limit, we can switch the ω summation to an integral and consequently the power fluctuations have a magnitude of

$$S_{\delta Q\,ITFN}(k,\omega) = 4k_b\bar{T}^2 \frac{g_w A_{cs}}{l} \tag{4.51}$$

Correlated Johnson Noise

Due to the large variation of the resistivity when phase separated, we must keep track of the correlations between different noise spatial frequencies. Again setting the magnitudes based upon the 0^{th} mode, we find that the differential voltage fluctuation

covariance matrix has values:

$$S_{\delta\frac{dV}{dx}}(k, k+q, \omega) = 4k_b\bar{T}\frac{\rho(q)}{A_{cs}} \tag{4.52}$$

where we've simply generalized from the standard definition of the power spectrum:

$$< z(k)z^{\star}(q) >= \int_0^{\infty} \frac{d\omega}{2\pi} S_z(k, q, \omega) \tag{4.53}$$

Of course, if a simulated noise spectrum is required then one can diagonalize the covariance matrix to find the uncorrelated eigenvectors, randomize in both magnitude and phase along these dimensions and then rotate back into the experimental basis.

Total Current Noise Calculations

The relative magnitude of these additional noise sources can again be seen in fig. 4.19 and we now have the ability to understand the low frequency suppression of ITFN power fluctuations as a consequence of the $|T(1)|$, $T(0)$ anticorrelation found in the slightly phase separated state (Eq. 4.43). Due to a positive $\frac{\partial^2\rho}{\partial T^2}$, an increase in $|T(1)|$ increases the total resistance which then due to joule heating decreases $T(0)$. Thus, at long time scales, there are two competing effects on the current. These effects have different time constants though, so once we go to frequencies above the lowest rolloff, the noise will begin to increase.

4.4 Detector Driver Summary

- Our fin connectors should be designed so that $G_{tf} >> \mathcal{L}G_b$ to minimize unnecessary thermal fluctuation noise.

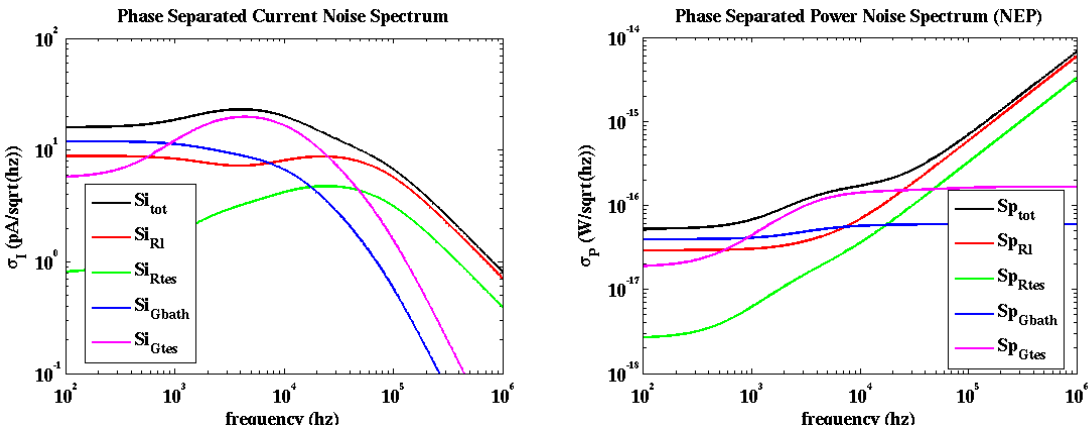

Figure 4.23: Fig. 4.19 reprinted for convenience of reader

- T_c, ζ_T and l should be chosen so that our devices are not phase separated (Eq. 4.25).

4.5 Future Studies

- 2D finite element simulation of complex W TES structures with fin connectors. Can one account for the smaller effective electron/phonon coupling with a simple wiederman franz thermal impedance or must one also take into account variations in gap energy?

- Carefully measure $\alpha(T_c)$, so that phase separation lengths can be accurately estimated.

- By varying the fridge temperature and/or bias point and measuring the onset of phase separation, β and ω_{eff} with $\frac{\partial I}{\partial V}$ curves, one can precisely and experimentally determine the required changes necessary so that the phase separated TES operates in a thermally uniform manner. It's a shame that this study wasn't completed before the iZIP4/5 design.

- Measure and understand $\frac{\partial I}{\partial V}$ curves for 100μm line device with T_c <70mK so that we can be certain that the device is not phase separated.

Chapter 5

QET design and Optimization

5.1 Using Bandgaps to concentrate and separate energy

If one strips away all the cumbersome details which we delved into in the TES chapters, the estimate for energy noise in any well designed (bandwidth matched intrinsic noise limited) bolometric device boils down to the fact that stochastic thermal fluctuations scale with the specific heat, C, and the temperature, T, of the system:

$$\sigma_E^2 \propto CT^2 \tag{5.1}$$

With this understanding, optimizing for maximum sensitivity is quite simplistic: Operate at low temperatures and concentrate the signal in as small of an effective volume as possible . A CDMS detector is a perfect example of taking both of these rules to extremes. First, the sensing element is operated at a temperature around 80mK, about 4000 times colder than a standard Palo Alto day.

Concentrating the energy into a small region is less straightforward, largely because

we require a huge volume if we are to have any hope of seeing a single wimp interaction due to the incredibly small theoretical wimp/nucleon cross section. Consequently, we can't simply use mirrors to concentrate the signal into a small sensing area as is done with visual wavelength light in telescopes, for example. Instead, we collect and concentrate the particles produced in the interaction through the manipulation of both semiconductor and superconductor bandgaps. To set the scale at how well we do this: the ratio of the active sensor volume (TES volume) to volume of the wimp interaction volume is 10^9.

5.1.1 Electronic bandgap and freeze out

The lions' share of this factor comes from using a large bandgap material as the absorber (Ge). At 80mK, the thermal excitations have an energy on the order of 10μeV. By contrast, the energy required to raise an electron from the valence band to the conduction band is $\sim$0.7eV and the energy required to raise an electron from a donor impurity state to the valence band is $\sim$100meV. Therefore, it's statistically impossible to thermally excite the electrons in the crystal; they're "frozen out". How does this effect the heat capacity? if I vary the temperature slightly (say by a $\sim$1 mK), the total electronic state and consequently the total electronic energy hasn't changed at all; the electronic heat capacity is negligible.

In summary, at these small temperatures Ge phonons will never interact with the electronic system of the Ge. Their energy will always remain concentrated in the phonon system.

One can certainly make a high quality thermal sensor with just this level of concentration. Cuore, for example, is a neutrinoless double beta decay experiment that attaches a small thermal sensor (NTD) to a 125cm^3 crystal of TeO_2. Edelweiss, another direct detection dark matter experiment is also designed in this way.

5.1.2 Creation and Collection of Non-Thermal Excitations through Superconducting bandgaps

As discussed previously, a CDMS detector also measures the number of electron-hole pairs produced in an interaction. This is done by drifting the charge particles to electrodes at differing voltages on the surface of the crystal of which at least one is instrumented with a FET.

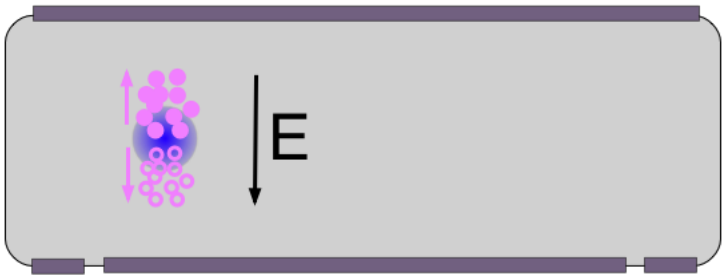

Figure 5.1: Detector Schematic showing electrons and holes drifting across the detector under the influence of an E field

For the measured charge signal to be both reproducible and independent of the exact interaction point, the excitations must reach the electrodes. This requires that the electron-hole recombination time and the mobility,μ, are both very large. Also, the rate of trapping for excitations in a localized state must also be small (at 77K, the drifting E field must be large enough ($\sim 500 V/cm$) so that neither the electrons nor holes can get stuck in unfilled local impurity state).

In some sense this measurement is the exact complement to the thermal phonon measurement we discussed in the previous section. There we used the large band gap in semi-conductors to decouple all the electronic degrees of freedom from the low energy phonons that we were attempting to measure. By contrast, here we are using the semi-conductor bandgap to conserve the number of high energy excitations (potential energy of the excitation >> thermal energy) and their quasi-stable nature to concentrate them at the electrodes through physical drift.

In CDMS, We've simply stolen all of these charge measurement ideas that have

been around for the last 50 years and directly applied them to our phonon sensor where we've simply switched from an electronic bandgap to the superconducting bandgap.

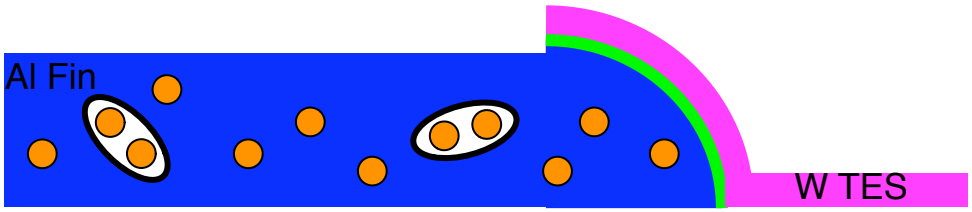

Figure 5.2: QET cross section

The basic design can be seen in the cross section schematic of a phonon sensor (Fig.5.2) [81]. Phonons with energy greater than double the superconducting bandgap of Al (T_c ~1K therefore $2\Delta E_{Al} \sim 300\mu$eV) split Al cooper pairs into quasi-particles. In the ideal scenario, the excitations randomly diffuse until they get trapped in an area with suppressed Tc due to an overcoating of W (~40nm thick) along one edge. Eventually these quasi-particles cross into the W and are pulled into the W TES due to the spatial Tc gradient (fig. 5.3). Hopefully, the T_c variation is sharp enough so that a large percentage of the Al quasi-particles' potential energy is converted into kinetic and potential energy of much higher number of W excitations.

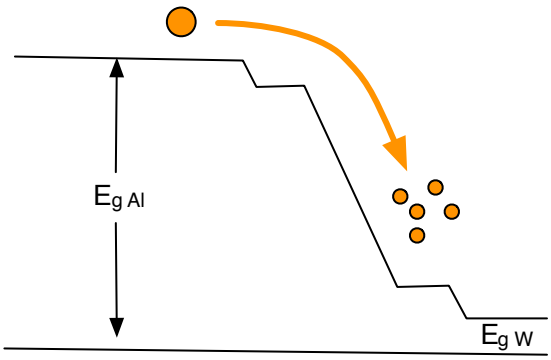

Figure 5.3: Superconducting Bandgap Energy Variation within QET

In direct analogy with the more standard semi-conductor charge measurement, the Al superconducting film has 3 property requirements for this mechanism to effectively

collect energy.

1. the quasi-particle recombination rate must be small
2. the quasi-particle trapping rate must be small
3. the diffusion(D_{Al})/mobility(μ_{Al}) of the Al quasi-particles should be as large as possible

There are some differences however. In the semi-conductor, the excitations are forcibly drifted by the electric potential. Unfortunately, a similar forcing mechanism is not as easily engineered into the system and consequently for the vast majority of the Al 'fin', the propagation is completely random. Qualitatively, this means that the length of the fin shouldn't be too much greater than a few diffusion length, $l_{fin} \lesssim \sqrt{D_{Al}\tau_{trap\,Al}}$, whereas for the semiconductor $l_{drift} \lesssim \mu|E|\tau_{trap\,Ge}$ where $|E|$ is the magnitude of the E field.

In summary, with the above sensor design principle, we collect the energy from athermal phonons which were located throughout the entire crystal volume and condense the energy into the volume of the W TES! Naively, this huge additional decrease ($\sim$ 7x10^4) in active sensor heat capacity with respect to an Edelweiss style Ge dark-matter device with NTD readout (the original prototypes of this style were also made by CDMS) should lead to a 2 order of magnitude sensitivity increase and this doesn't even account for the fact that the intrinsic temperature sensitivity of a TES ($\alpha \sim$ 100-300) is significantly greater than for an NTD ($\alpha \sim$ -10) [1]. Unfortunately, the 'as built' energy resolution improvements over an NTD style readout were significantly more modest ($\sim$x3) than this for CDMS II. Much of this discrepancy we can already understand through this and earlier chapters:

- Edelweiss NTD sensors operate at $\sim$20mK rather than our $\sim$100mK
- poor matching of TES bandwidth to phonon signal bandwidth
- non-intrinsic 1/f noise at low frequencies and unnecessary johnson noise from high temperature R_s and R_p due to archaic cold electronic design

- TES sensor bandwidth suppression due to phase separation (this would only effect the energy sensitivity in the limit of large phonon signal bandwidth)

The final, yet to be discussed, culprit which leads to poor sensitivity in our current designs is poor energy collection efficiency. This was first brought to light in a study by Walter Ogburn in the r118-r119 analysis (fig.5.4), where he found that only 1-4% of the total phonon energy produced in an event interaction and subsequent electron/hole drift actually ends up in the TES electronic system! All the rest of the energy somehow gets lost.

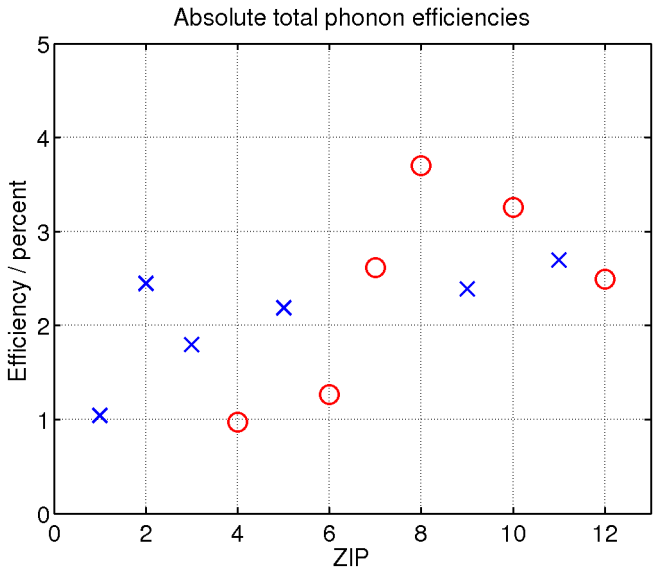

Figure 5.4: Total Phonon Collection in CDMS II devices. Red circles are Si substrates while blue crosses are Ge.

On the brightside, such huge collection inefficiencies mean that sizeable gains in phonon sensitivities can be produced in future experiments, if we can only isolate and fix those parts of our collection process which are most problematic. This is the essence of this chapter. Within, we'll attempt to estimate and simulate the losses in each of the stages mentioned above, discuss potential fabrication improvements, and optimize the QET geometry for both position sensitivity and optimum filter energy resolution.

5.2 Allocation of Phonon Losses

Any attempt to further optimize the energy sensitivity of our devices requires that we either experimentally or theoretically allocate losses to the individual stages:

1. $\epsilon_{crystal}$: In order for phonons created by particle interaction to reach the Al film on the surface, they must first undergo downconversion processes so as to reach energies at which they travel ballistically, E_b (they must reach the surface to interact afterall). In the bulk of the crystal, it's believed that higher (i.e. non-harmonic) terms in the phonon hamiltonian are responsible for the decay. While at the surface, down conversion could potentially occur through any number of different processes (surfaces are messy!). For the purposes of estimating the efficiency of the cascade, $\epsilon_{crystal}$, we'll separate the phonons into 3 categories based on energy:

   (a) $E_p > E_b$: Phonons with energy greater than the ballistic cutofff energy will wander around the crystal until they split into multiple lower energy phonons.

   (b) $E_b > E_p > 2\Delta E_{gap} = 2 \cdot 1.76\, k_b T_c$ (in BCS theory): These phonons are now ballistic and thus interactions with the Al film on the surface of the detector will totally dominate further phonon downconversion processes. Effectively, E_b sets the lower edge of the cascade.

   (c) $2\Delta E_{gap} > E_p$: subgap phonons which comprise the lost energy. Our sensing system will never see these phonons since they can't be concentrated into our W TES through quasiparticle creation. They will simply wander around in the crystal until full thermalization occurs.

   To set a rough scale on the magnitude of these losses, let's make the assumption that after the cascade has completed, all phonon states below E_b are equally populated. This 'ideal' approximation was used to great effect in Klein's work on calculating the average ionization energy for semiconductor cascades [43].

The basic idea is that after going through so many levels of downscattering, the energies of all the produced particles have very little dependence upon the actual down conversion cross sections. Effectively,we hope that any small bumps/variations are smoothed through numerous convolutions with the energy particle density.

With the additional assumption of an isotropic phonon model with the dispersion relation, $\omega = v|k|$ ($n(E) \propto E^2$) we have

$$\epsilon_{crystal} \sim \frac{\int_{2\Delta E_{gap}}^{E_b} En(E)dE}{\int_0^{E_b} En(E)dE} = 1 - \frac{\int_0^{2\Delta E_{gap}} En(E)dE}{\int_0^{E_b} En(E)dE} = 1 - \frac{(2\Delta E_{gap})^4}{E_b^4} \quad (5.2)$$

Using the ballistic cutoff frequencies (∼16K Ge / ∼31K Si) found in [21], this line of reasoning gives estimates of 98% for Si and 94% for Ge.

The difference in the efficiency loss magnitude between Si and Ge seen in the above estimate is largely due to fact that the phase velocity is roughly a factor of two smaller in Ge: all the phonon states are simply lower in energy and thus a larger percentage of states are subgap. Thus, even if one of the many assumptions in the above estimate is wrong and we have completely underestimated the losses in both Si and Ge, we would still expect that $\epsilon_{crystal\,Ge} < \epsilon_{crystal\,Si}$.

Since this loss mechanism is a function of fundamental crystal characteristics, future improvement of $\epsilon_{crystal}$ through various engineering tricks is quite unlikely . . . we have what we have.

2. $\epsilon_{passive\,Al}$: The face of a CDMS device has many elements other than the concentration fins which are composed of Al (with a bilayer of Al/W on one edge) including alignment marks (CDMS II oZIP), stitching pads (CDMS II oZIP), large DIB bonding pads (all), electrode grid (CDMS II oZIP and mZIP), small safety bonding pads (iZIP), and finally phonon bias rails (all). All of these structures unfortunately concentrate and sink athermal phonons as well, leading to

	% Active	% Passive(top/bottom)	$\epsilon_{passive}$ (Area/Volume)
CDMS II oZIP	19.6% / 0%	12.5% / 10.0%	41% / 59%
SuperCDMS mZIP	37% / 0%	6.1% / 10.0%	71% / 85%
SuperCDMS iZIP	4.8% / 4.8%	1.5% / 1.5%	78% / 78%

Table 5.1: Percentage active and passive Al coverage as well as the collection efficiency for various CDMS detector designs

a potentially quite severe drop in energy collection efficiency.

On the brightside, the calculation of $\epsilon_{passive}$ is by far the most straightforward. It's simply the amount of Al found in the active Al fins divided by the total amount of Al on the surface of the detector (Tab. 5.1)

There is one slight subtlety. In both the CDMS II ZIP and SuperCDMS Mercedes designs, the thickness of the Al on the phonon face is ∼350nm while the Al film on the charge side is ∼ 20nm. Estimates of the phonon/cooper pair cross section [82], indicate that high energy athermal phonons ($> 15K$) largely interact and begin their quasiparticle cascades within the first 20nm. Thus, for high energy phonons the efficiency losses should be based upon the active and passive Al surface areas. By contrast, phonons with energies near the cooper pair interaction threshold have interaction rates on the scale of 1mm and consequently the volume ratio should be used. Ideally, we would convolute the Al thicknesses with a phonon monte carlo for an average event to get an better estimate. but for right now the table above at least gives an upper and lower bound on the true $\epsilon_{passive}$ (notice that for our newer symmetric designs, this only effects the phonon absorption bandwidth, ω_{pulse}, and not the absolute phonon efficiency).

This table also clearly illustrates the huge strides we've made in minimizing the amount of passive Al on the device face since CDMS II.

3. $\epsilon_{Al\,cascade}$: Athermal phonons initialize a cascade production of quasiparticles in the Al. As discussed in [82], the actual cascade dynamics are totally different

from those found in an electronic cascade of a semiconductor. In a good semiconductor, the electron-electron scattering cross section largely dominates the electron-phonon production process and thus phonons are only generated mostly in the case that the kinetic energy of the electrons and holes are insufficient to create another electron-hole pair.

By contrast, in the superconducting cascade the electron-phonon and phonon-electron processes totally dominate the direct electron-electron interaction. As long as the generated phonon though has energy above $2\Delta E_{gap}$, it will eventually break another cooper pair. Consequently, if all the electronic kinetic energy at each step is converted into a single phonon then the cascade will be very efficient at producing quasiparticles. On the otherhand, if the cascade produces large numbers of subgap phonons when the production of above gap phonons is energetically possible then the process is horridly inefficient.

To set a maximum efficiency for the Al cascade, let's for the moment assume the former (since the phonon density of states goes as E^2 this probably isn't that bad of an assumption) and use Klein's equally populated momentum state approximation [43] but with the BCS quasiparticle density of states:

$$n_{qp}(E) \propto \frac{E}{\sqrt{E^2 - \Delta E_{gap}^2}} \tag{5.3}$$

With these approximations, $\epsilon_{Al\,cascade} = 55\%$. More complex simulations by Paul [19] match this number incredibly well in the high energy limit (fig. 5.5).

4. $\epsilon_{collect\,Al}$: Once all the Al quasiparticles relax to the superconducting band edge, they diffuse randomly until they either recombine into cooper pairs, trap in a localized region with lower Tc, or eventually make their way into the W of the W/Al overlap region through what could be a sizeable surface impedance. The first two possibilities mentioned are direct signal sinks.

   Theoretical calculations of the trapping rate are impossible because the trapping

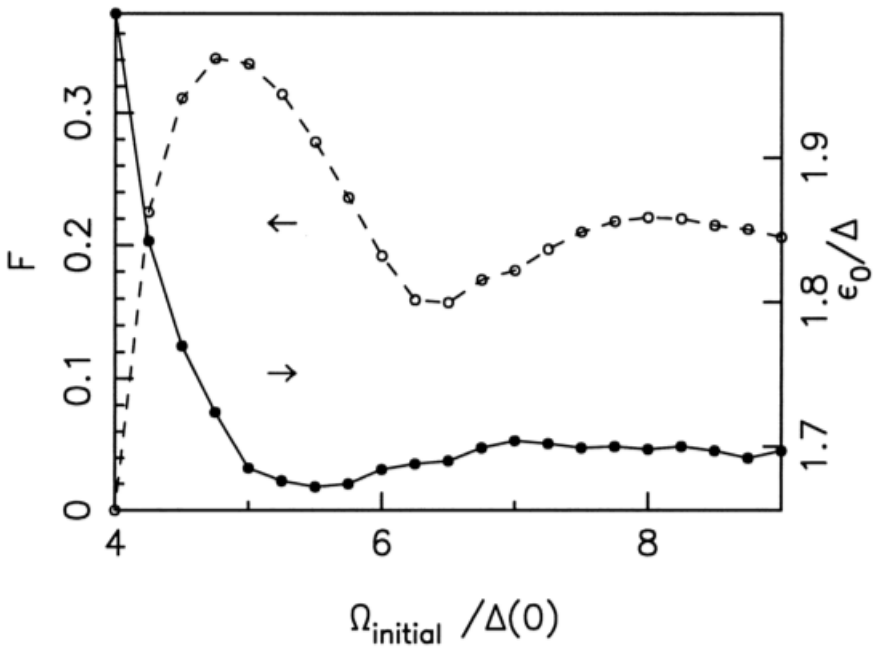

Figure 5.5: Average phonon energy per quasiparticle ($1/\epsilon_{Al\,cascade}$) produced versus incident phonon energy (solid line). Produced by Paul Brink. [19]

rate depends almost exclusively on the film quality and thus experimental data is vital. Unfortunately, setting up and maintaining a process to directly measure $\epsilon_{collect\,Al}$, D_{Al}, and $\tau_{trap\,Al}$ with test structures is quite resource intensive and thus has never fully been incorporated into the fabrication. An initial preliminary measurement was done by the Cabrera group in 1998 which will be discussed in great detail in a subsequent section and in the very near future, Jeff Yen and the rest of the Cabrera group will finally begin a long awaited and much, much improved measurement.

Due to it's ease of measurement, we have mostly relied upon the Residual Resistance Ratio (RRR) as a very rough proxy for film quality. The basic principle behind the RRR measurement is the assumption that at room temperature, electron scattering with equilibrium thermal phonons totally dominates ρ for metals and thus there is no machine or film quality dependence. Consequently, we can

Sample ID	Thickness (nm)	RRR	mfp (nm)	method	Dep Rate (nm/s)
DH1	225.0	6.5	96.9	sputtered	0.2
DH2	227.5	5.53	82.4	sputtered	13.4
DH3	170.0	5.19	77.3	sputtered	11.4
DH4	211.5	3.61	53.8	sputtered	1.1
DH5	203.0	3.63	54.1	sputtered	0.7
DH6	200.0	2.72	40.5	sputtered	0.2
DH7	200.0	2.73	40.7	sputtered	0.2
DH8	205.5	8.22	122.5	sputtered	0.2
DH9	95.0	7.1	105.8	sputtered	0.2
DH10	229.0	12	179.0	sputtered	22.2
DH11	139.0	9.41	140.2	sputtered	20.0
Balzers	250.0	4.19	62.4	sputtered	
Gryphon	800.0	42	625.8	sputtered	1.7
SL1	1400.0	9.4	140.0	sputtered	0.4
SL2	972.4	9.9	147.5	sputtered	0.4
SL3	216.7	4.7	70.0	sputtered	0.4
SL4	219.7	4.5	67.1	sputtered	1.5
SL5	1140.0	28.8	429.1	e-beam	57.2
SL6	1100.0	19.2	286.1	e-beam	54.8
SL7	280.0	18.1	269.7	e-beam	56.0
SL8	270.0	12.3	183.3	e-beam	53.2

Table 5.2: RRR measurements for a variety of different Al deposition machines.

remove the the geometry systematics (changes is thickness, non-simplistic current densities) in the calculation of ρ from R by simply taking the ratio of the resistances at 300K and 4K. In some incredibly time intensive studies by Betty Young which are preserved in Tab. 5.2, the RRR was found to vary wildly with deposition machine. Unfortunately, the deposition machine which we have used for the past 10 years, the 'Balzers', is certainly not the best on the list. It was chosen not for its high quality Al films but rather for it's ability to produce W with a T_c around $\sim$ 100mK. Thus, any improvements in Al film quality in next generation deposition machines would almost certainly lead to improved $\epsilon_{collect\ Al}$.

A quick glance at the table also immediately suggests that e-beam deposition

systems generally produce significantly higher quality films than sputterers and thus the question of redesigning our fabrication process so that the W and Al are deposited and patterned in different steps is certainly reasonable (mixed α/β phase W has only been produced in sputter deposition machines). The primary disadvantage to this change is that a more complex liftoff process must be used for the Al (the second processing layer). This change though would also allow us to increase the thickness of the Al films until D_{Al} was thickness limited.

5. $\epsilon_{collect\,W/Al}$: The existence of traps in the W/Al means that some of the quasi-particles will never leave the W/Al region. This loss mechanism can be studied by varying W/Al overlap lengths in the banana style test device. Conceptually, this physical mechanism is quite similar to that for $\epsilon_{collect\,Al}$.

6. $\epsilon_{W\,cascade}$ The efficiency of the cascade process from Al quasi-particles each with a potential energy of $\sim$2K into measureable kinetic and potential energy of the W quasi-particles depends on a huge number of variables and thus at first glance is non-simplistic to estimate theoretically. In particular, $\epsilon_{W\,cascade}$, depends on the exact location of the intermediate band gap in the proximitized W/Al region. If the interface impedance between the W and Al is large, then T_c varies quite sharply with position and thus a high energy quasi-particle can easily transfer it's kinetic energy to other electronic excitations. By contrast, if the metals are very well connected, then T_c will vary slowly with position and during the quasi-particle relaxation a significant percentage of the total Al quasi-particle potential energy will end up as sub-gap phonons which immediately migrate back to the Ge/Si crystal instead of electronic excitations which are measureable.

   So we would ideally like to precisely engineer the coupling between the W/Al to be large enough so that transmission of quasi-particles to the W is large ($\epsilon_{Al\,collect}$ improves as the W/Al surface impedance decreases), but small enough such that W cascade is efficient ($\epsilon_{W\,cascade}$ decreases with increased coupling).

Historically, the quality of the Balzers's RF etch which removes the oxide layer between the first W film (last layer of the 'trilayer' deposition) and the active W film deposition has had significant temporal variation and thus it's quite possible that the large variation in the total efficiency found between detectors in CDMS II (Fig. 5.4) is due to variation of the interface quality. This though is not the only possible explanation. Since we did not measure Al RRR religously during the CDMS II fabrication process, it's certainly possible that our Al film quality had significant temporal variability. This hypothesis also seems quite reasonable: if we see such huge variation in film quality between machines, then it's certainly reasonable that quality fluctuations over time exist with the same machine.

5.3 1997 Banana Experiment for Measuring Quasi-Particle Transport Properties

In 1997, the Stanford CDMS group designed, fabricated and tested the device in Fig. 5.6 to isolate and quantify the efficiency losses due to poor QP propagation.

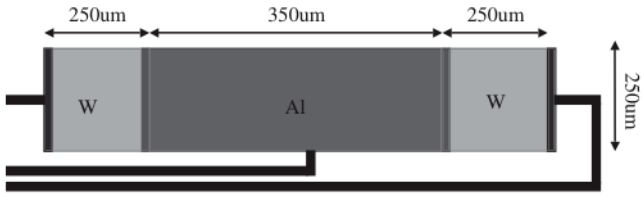

Figure 5.6: Schematic of the 1997 device to quantify the trapping length of QP in balzers Al

5.3.1 Device Design and Qualitative Results

The design concept is as follows. A collimated ∼1.75 keV xray source (flourescence off Si from ^{55}Fe) would uniformly illuminate a 150nm thick sputtered Al fin which is

jointly shared between 2 TES. Quasi-Particles generated due to an x-ray interaction within the Al film would randomly diffuse and the ratio of energy absorbed in the two TES could be simply related to the location of the interaction origin. For example, an event which occurs at the very center of the Al fin would have symmetric energy absorption by both TES, while an event very near one TES would have the vast majority of energy absorbed in a single TES.

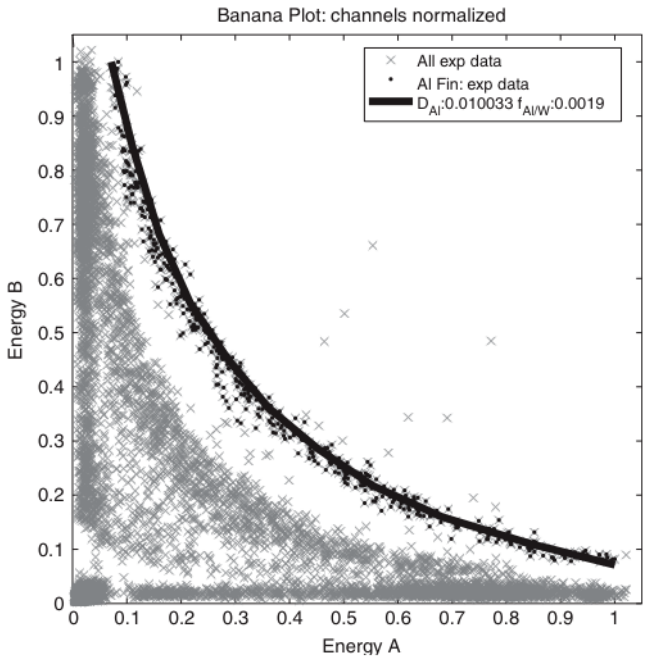

Figure 5.7: 1997 banana

If no quasiparticle trapping occurred in the film then the sum of the energy absorbed by the 2 TES should be completely independent of the interaction location ($E_1 + E_2$ is constant). By contrast, if trapping is significant then interactions occurring near the center of the device should have a suppressed total signal (the event contour should be 'banana' shaped). Unfortunately, the results (Fig. 5.7) clearly indicate that for the Al films produced in the Balzers, quasi-particle trapping is significant.

Notice also, that the banana contour from x-rays interacting with the Al film never reach either axis. Effectively, even events which occur very near one TES have energy

sharing. This suggests that Quasiparticle transmission across the W/Al interface is quite difficult; there's a sizeable interface impedance.

5.3.2 quantitative simulations

The above results can be quite well modeled with a basic 1D diffusive partial differential equation with a linear loss term, $\tau_{trap\,Al}$.

$$\frac{\partial n}{\partial t} = D_{Al}\nabla_x^2 n - \frac{n}{\tau_{trap\,Al}} \tag{5.4}$$

To match the data, we'll choose the boundary conditions which correspond to the fact that the transmission probability for the quasi-particle across the W/Al boundary, $f_{W/Al}$, is small and thus the particle flow across the interface is

$$-A_i D_{Al}\nabla n(x_{end})\cdot\hat{s} = n(x_{end})/R_{i\,Al/W} = \frac{n(x_{end})f_{W/Al}A_i < v_{qp} >}{2} \tag{5.5}$$

where $R_{i\,Al/W}$ is the interface impedance for the QuasiParticles (units of $\left[\frac{\text{time}}{\text{length}^3}\right]$), A_i is the cross-sectional area of the interface, and $\hat{s}$ is the unit vector at the surface pointing in the outward direction.

The equivalence of these three follows from the continuity equation. Let's draw a box with infinitesimal width,Δx, in which one edge is the resistive boundary and the other edge is within the bulk of the diffusive media (Fig. 5.8).

Since the volume of the box is infinitesimal, for the density to remain finite, the flux into the box on the left side ($-A_i D_{Al}\nabla n(x_{end})\cdot\hat{s}$) must be equal to the flux leaving the box through the surface impedance ($n(x_{end})/R_{i\,Al/W}$). Equivalently, we can look at the outgoing flux as the number of particles incident on the surface per unit time $\frac{n\cdot A_i\cdot <v_{qp}>}{2}$ times by the dimensionless transmission probability, $f_{Al/W}$. Notice that in this derivation we're being incredibly cavalier with all the geometric factors of order

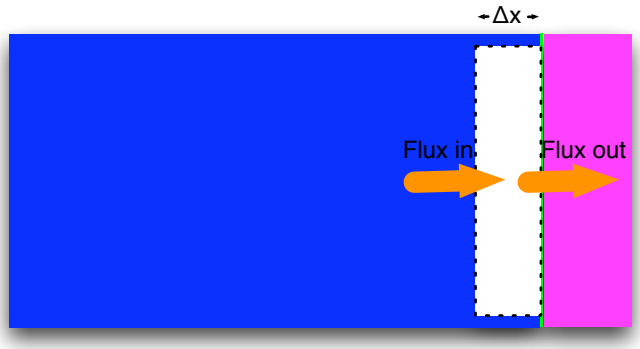

Figure 5.8: schematic for deriving fin boundary conditions

1 associated with calculating the true number of particles that diffusively hit the boundary by just assuming that half the particles are moving to the right with a velocity $< v_{qp} >$. Truthfully, we're just burying them into $f_{Al/W}$.

5.3.3 Quasi-Analytical Solution

To solve this PDE or it's well defined brother where there is a TES at $x = l_{fin}$ and a perfectly reflective boundary at x=0 (a rectangular Al fin on our actual device), we'll travel down the well trodden path of separation by parts, which before application of boundary conditions gives us:

$$n(x,t) = \sum_k e^{-(Dk^2+1/\tau_{trap})t}(T_{-k}e^{ikx} + T_{+k}e^{-ikx})$$

where k is still an arbitrary all real or all imaginary number. Applying the fact that the x=0 boundary condition is completely reflecting, we find that

$$n(x,t) = \sum_k T_k e^{-(Dk^2+1/\tau_{trap})t}\cos(kx)$$

Next we can enforce the impedance constraint at x=l_{fin} and find that k is quantized

by the non-simplistically solvable equation (but easily analytically computed with any number of zero finding routines)

$$k = \frac{\pi}{2l_{fin}}\left(2m + \frac{i}{\pi}\log\left(\frac{ik + K_{surf}}{ik - K_{surf}}\right)\right)$$

with m being integers within the domain $[0, \infty)$ and with the surface wave vector, K_{surf}, being defined as

$$K_{surf} = \frac{f_{Al/W}|v_{Al}|}{2D_{Al}} = \frac{3}{2}\frac{f_{Al/W}}{l_{Al\,scat}}$$

where $|v_{Al}|$ is the average quasi-particle velocity in Al and $l_{Al\,scat}$ is the average distance between scatters for quasi-particles in the Al. Since $\frac{ik+K_{surf}}{ik-K_{surf}}$ has constant unit magnitude for real k but not for imaginary k, only real k satisfy the boundary condition.

Unfortunately, this k basis set isn't orthogonal like those for perfectly transmissive and reflective boundaries and thus the more standard fourier decomposition techniques to find T_k aren't viable. However, a simple linear least squares fit can be used to find the T_k to match any t=0 density distribution with almost as much ease.

To precisely estimate ϵ_{Al}, I find that the easiest technique is to analytically calculate the total percentage of quasi-particles which trap for an uniform distribution

$$\epsilon_{trap\,Al} = \frac{\frac{1}{\tau_{trap}}\int_0^\infty dt \int_0^{l_{fin}} dx\, n_{uniform}(x,t)}{\int_0^{l_{fin}} dx\, n_{uniform}(x,0)} = \sum_k T_{k\,uniform}\frac{\sin(kl_{fin})}{kl_{fin}}\frac{1}{1+k^2l_{trap}^2} \quad (5.6)$$

and then the efficiency to collect quasi-particles would simply be

$$\epsilon_{collect\,Al} = 1 - \epsilon_{trap\,Al} = 1 - \sum_k T_{k\,uniform}\frac{\sin(kl_{fin})}{kl_{fin}}\frac{1}{1+k^2l_{trap}^2} \quad (5.7)$$

The diffusion length, l_{trap} ($\sqrt{D\tau_{trap}}$), shows up as a natural quantity/grouping in virtually all diffusive PDEs. For example, an initial dirac-delta particle distribution that has diffused for a time τ_{trap} will have a gaussian particle distribution with $\sigma = \sqrt{2D\tau_{trap}}$, or $\sigma = \sqrt{2}l_{trap}$. K_{surf}, the other physically important parameter grouping for systems with impedance boundary conditions, is much less common. Looking at it's definition, we see that a given interface impedance effects QP collection much more severely for fins with a large diffusion constant or QP scattering length. Intuitively, one can think of this behavior in two ways. Macroscopically, a system with a small D_{Al} has a large internal impedance and thus a surface impedance has to be pretty large to be physically limiting (we'll develop this idea significantly in the future). Microscopically, we can say that in a system with small D_{Al}, a particle that reflects off the W/Al interface will be much more likely to hang around and make many more attempts at getting through the barrier.

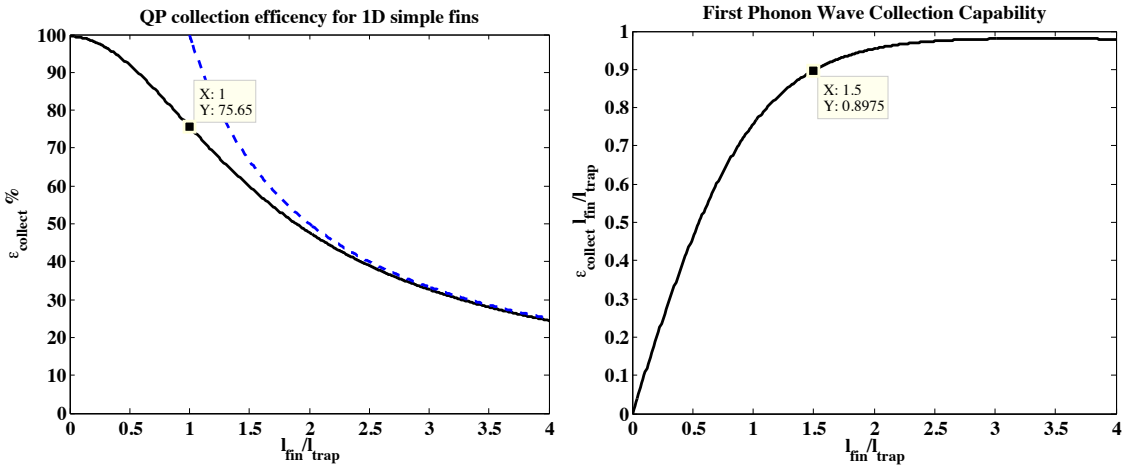

Figure 5.9: Quasi-particle collection efficiency (left) and first pass ballistic phonon collection efficiency (right) for a rectangular fin with perfect transmission collection at the TES/Fin boundary

In the hopes of building intuition, Fig. 5.9-left (solid black) displays the quasi-particle collection efficiency as a function of the fin length in units of l_{trap} for a rectangular fin with perfect transmission at the TES boundary. Basically, for us to keep our collection efficiency as high as possible, any rectangular fin should never really go beyond 1.5 diffusion lengths and we should probably try to keep the fin length less

than a diffusion length. A second interesting feature seen in these curves is that for very long fin lengths, the collection efficiency scales as $1/l_{fin}$(dashed blue). This idea is fleshed out in greater detail in Fig. 5.9-right where I've plotted $\epsilon_{collect} l_{fin}$. To understand this, let's think about a toy detector model where: 1) all phonons are ballistic 2) once a phonon interacts with an uninstrumented surface all position information is lost. If we are solely interested in collecting position information, then only first wave phonons matter (who cares if we collect the phonon in the TES after it's 8th bounce) and the number of first wave phonons which are collected in the TES scales as $\epsilon_{collect} l_{fin}$, the y-axis in Fig. 5.9-right. Here we see that the number of first wave phonons is assymptotically limited for high l_{fin}. Infact, a fin with length 1.5 l_{trap} collects only 10% less position information than one with much larger length but it has a significantly higher collection of multi-bounce phonons which though they contain no position information in this staggeringly simplistic toy model they still contain total energy information. So we've reconfirmed our design constraint of never allowing a rectangular fin to grow beyond 1.5 diffusion lengths.

For the banana device, all qualitative features are similar to the calculation above (non-orthogonal basis, non-simplistic k quantization) except that one needs to calculate T_k for approximate dirac delta functions at a variety of x instead of just for the uniform distribution. Secondly, to separately calculate the collection percentages for the two TES separately, one needs to integrate the flux directly.

5.3.4 Experimental Results

Our best fit to the 1997 banana plot was $l_{trap} = 180 \pm 10um$ and $f_{Al/W} = .0025 \pm .0005$ (In hindsight, we should have quoted l_{trap} and K in the paper since $f_{Al/W}$ is dependent upon the D_{Al} estimate which has more systematics). Unfortunately, direct application of these numbers to our current devices and to designs for future devices is quite difficult because of the many changes that have occurred in our fabrication process. Of greatest importance is the fact that we now deposit Al films with a thickness of $\sim$ 300nm instead of 150nm. Consequently, if the 1997 banana device had quasi-particle

diffusion which was limited by the film thickness, then increasing the film thickness by x2 would increase l_{trap} by $\sqrt{2}$. By contrast, if the diffusion constant for the film was already intrinsically limited in 1997, then l_{trap} is more likely to be invariant. We always hoped to remove this systematic with measurements on a modern banana device eventually (it will happen soon), but in hindsight we could also have just ripped out a simple measurement of the RRR for 2 Balzers Al films with thicknesses of 300nm and 150nm to determine a scale factor.

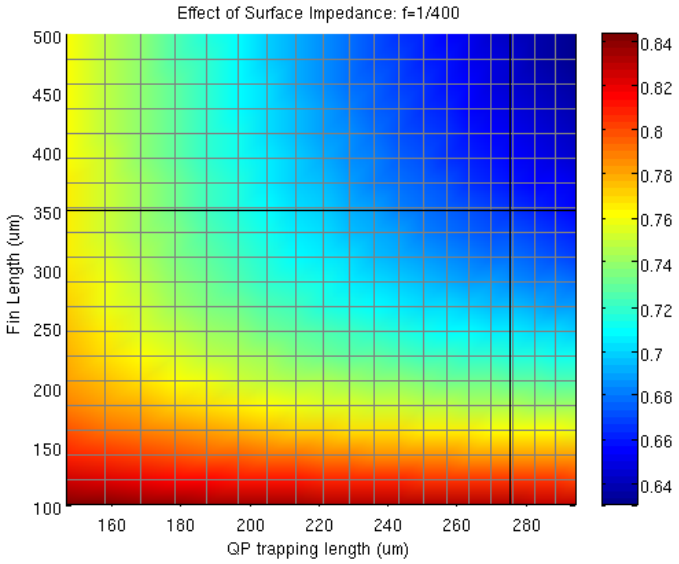

Figure 5.10: Ratio of quasi-particle collection efficiency for QETs with an interface impedance of f=1/400 to those with perfect transmission for various X_{fin} and $l_{trap\,Al}$

To help you grasp the importance of the interface impedance, I've contoured the ratio of QP collection for a rectangular fin with f=1/400 and for one with perfect transmission. As you can see, for large fins with large $l_{trap\,Al}$, $\sim 30\%$ of quasi-particle losses can be contributed to poor interface properties. As mentioned previously, the magnitude of this loss term also suggests that the large variability in overall phonon collection efficiency in CDMS II (Fig. 5.4) could be caused by poor control of the interface impedance in fabrication. On the optimistic side, this experiment was performed in 1997 when the Balzers deposition machine was still a multi-user machine and before Paul and Betty spent significant time optimizing the RF etch

between CDMS II and SuperCDMS. Consequently, it's certainly possible that in the future our surface impedances will be both lower and have significant smaller variability (Of course, confirmation of this requires future banana study).

For quick future design studies, Fig. 5.11 display QP collection efficiencies for various fin and trapping lengths for the rectangular fin geometry used in oZIP/iZIP.

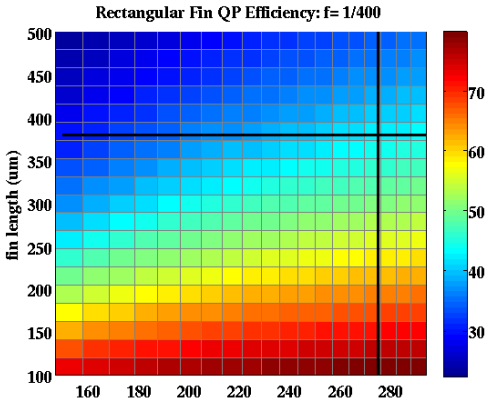

Figure 5.11: Quasi-particle collection efficiency for a rectangular QET with an interface impedance of f=1/400 versus various fin lengths and quasi-particle trapping lengths.

5.3.5 Pulse Shapes and the diffusion coefficient

Conceptually, the TES sensor system used should also have the necessary bandwidth (Squids tuned to say 300khz) to estimate D_{Al} from the relative delay between channels' leading edges as long as one understands the green's functions of the individual TES. Unfortunately, this later constraint proved to be challenging.

As seen in fig. 5.12, the pulse shapes for events which originated in the fins have complex morphologies and are quite different for the two TES. The second is quite surprising since the TES have identical geometries and almost certainly have very similar superconducting properties (T_c , ΔT_{90-10}) since we've historically found our films to have relatively homogenous properties over short length scales.

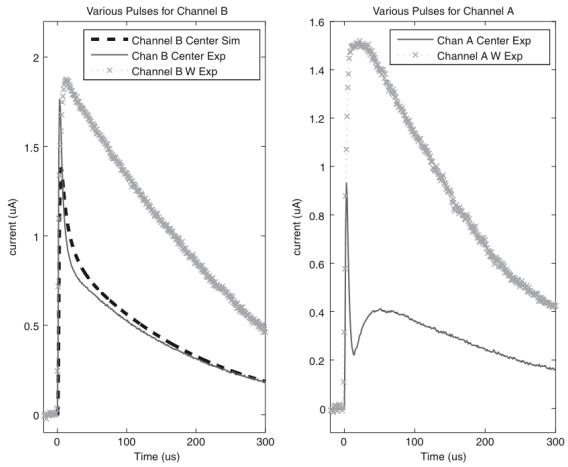

Figure 5.12: Representative pulse shapes for various event types

The easiest way to generate behavioral differences in the TES is to inadvertantly voltage bias them to different equilibrium resistance locations. Under standard linear 0D TES theory though, changes of this type should simply lead to fall time differences in the TES green function and thus the non-exponential behavior can't be explained. Furthermore, we believe that the bias conditions were close to symmetric. Unfortunately, due to the great number of years between the actual experimental run and the analysis of the data in 2004, this can't be guaranteed.

Again due to the numerous years before analysis and poor documentation, it's unknown if both TES were biased with the same sign. Any assymetry in the biasing would lead to a non-symmetric supercurrent flow in the Al. However, any coupling of this supercurrent flow to either the quasiparticle diffusion in the Al or the measured resistance for that channel would be quite complex and thus we would very much like to look for a simpler reason.

When studying phase separation in the Advanced TES Dynamics chapter, we never concerned ourselves with deriving green's functions for non uniform pulse shapes because CDMS devices have large numbers of fins (10-12) which do a reasonable job of spreading the phonon energy evenly over the entire TES. For this banana device though, all of the energy is clearly incident on the side of the TES connected

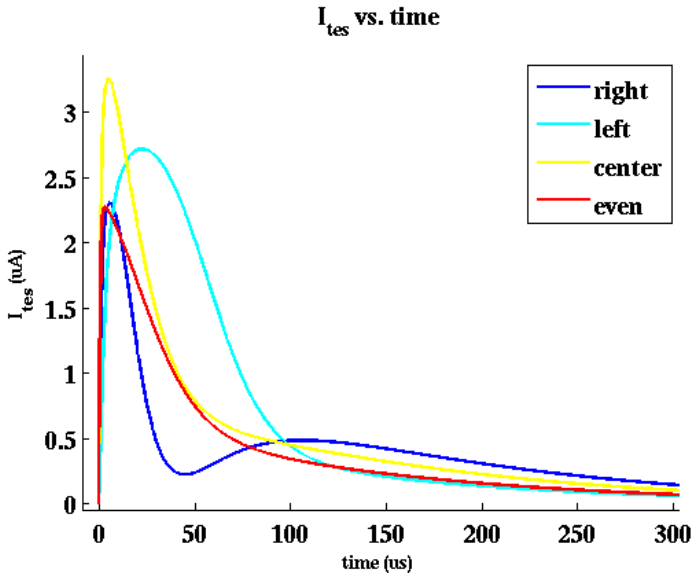

Figure 5.13: thermal phase separation of TES can generate the pulse shape assymetry seen between the channels

to the fin and, as shown in fig. 5.13, the pulse shapes vary hugely depending on if the side receiving the pulse is the high or low resistance edge of the the phase separated TES. Consequently, it seems that hypothesizing phase separation trivially explains both the assymetry in pulse shapes between the two channels and their complexity. Unfortunately, we have had difficulty matching the very long dominant falltimes ($\tau \sim 200\mu s$).

We can think of a few possible reasons for this. One possibility is that we have an abnormally high heat capacitance by ∼x5. If true for this device, then one would expect it to be true for all CDMS devices and thus all the various α estimates made in previous chapters would have to be revised upwards by the same factor of x5. Also, the phase separation length scale would be suppressed by $\sqrt{5}$. Finally, this suggests that the heat capacitance of our W films in their transition are x10 larger than the normal heat capacitance measured by CRESST (quite unlikely) [52].

Secondly, the bath temperature for this run could just be quite near the T_c of the 1997 banana device. This hypothesis is also disfavored, since we would then need

a mechanism other than phase separation to produce complex pulse shape features which are so naturally made with phase separation.

Finally, there is the possibility that a significant percentage of the recoil energy is converted into phonons which diffuse very slowly in the Si substrate. This theory could potentially explain the long falltimes but that is a lot of tightly confined diffusion. The little experience we have with Si iZIPs ($\tau_{p\,absb} \sim 140\mu$s) definitely disfavors this hypothesis. Understanding these issues will simply have to wait until we have banana devices with non-phase separated TES (lower T_c and smaller l_{tes}).

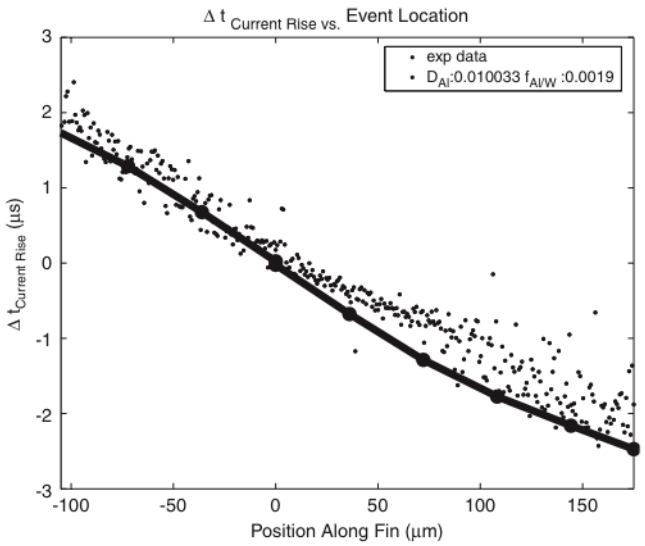

,

Figure 5.14: Relative delay between channels vs. event location

If we do disregard these pulse shape problems and focus only upon the very sharp rising edge (fig. 5.14), we can estimate that $D_{Al} = 100 \pm 10\frac{cm^2}{s}$ for this device. Combining with the estimate of $l_{trap\,Al}$ from the banana, we can then estimate the free lifetime as $\tau_{trap\,Al} = 3.2 \pm 1\mu s$. These quasi-particle free lifetimes are extraordinarily small compared to those measured by other groups in Al. Cresst measured $\tau_{trap\,Al} \sim 100\mu s$ for pure e-beam Al films on sapphire [83]. Furthermore, David Moore found $\tau_{trap\,Al} = 130 \pm 4\mu s$ [84] and Barends found $100\mu s < \tau_{trap\,Al} < 2000\mu s$ [85] (dependent upon lattice damage caused by ion-implantation) for Al sputtered on Si in

MKIDs devices. These two later experiments, though, have two significant unmeasured systematics which make direct comparison difficult. **First, they assume that the spatial dimensions of the Al traps are << than the thickness of the films** (60nm and 100nm respectively) If not, then there exists the possibility that quasi-particles, which are locally stuck in traps and haven't recombined into cooper pairs, can still physically fluctuate with the E-fields even though they aren't completely free to diffuse. **Secondly, they assume that any stray RF fields found in the Al absorber don't artificially keep the quasi-particles from relaxing into localized states (unlike in their MKIDS studies, we certainly won't have these oscillating fields)**.

Consequently, we are left with a few explanations:

1. The Blazers makes incredibly poor quality sputtered Al.
2. The overlaying W film is not completely removed in the etching process leading to large traps.
3. Al films produced on aSi are significantly worse than those produced upon either Sapphire or Si.
4. The Blazers makes sputtered Al of the same quality as other sputterers and all sputtered Al films tend to have quasi-particle traps with large spatial dimensions.

5.3.6 Unexpected Information

Well separated from and beneath the higher energy banana is a second event continuum. We believe that these events can be associated with x-rays that interacted in the Si substrate below the Al fin. The suppressed energy absorption into the two primary TES is then directly attributable to the efficiency of the phonon cascade in the Si for producing above bandgap phonons ($\epsilon_{crystal}$) and also the simple phonon transmission within the substrate away from the TES (Si substrate dimentsions: 1cm x

1cm). With this interpretation then, $\epsilon_{crystal}$ can be bounded as being greater than 0.6 (theoretically we expect it to be ∼95 %, so this is consistent with expectations).

5.4 Al Fin Geometry and Length Optimization

5.4.1 2D Fin Geometries

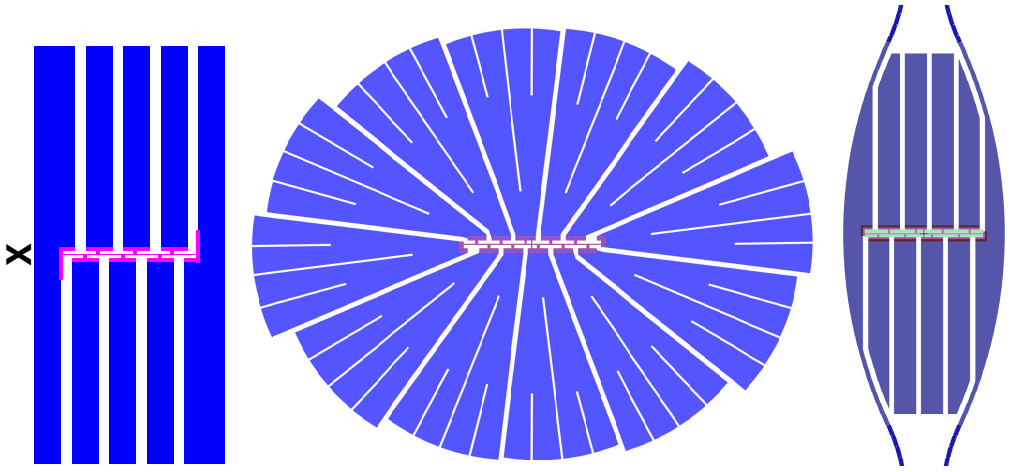

(a) CDMSII QET ('oZIP')

(b) SuperCDMS Maximized Al QET,('mZIP')

(c) 2^{nd} inter-digitated QET ('iZIP')

Figure 5.15: Last 3 QET designs of the CDMS collaboration to scale

So far, we've only discussed 1D quasi-particle propagation models which have the advantages of being mathematically simplistic and were physically motivated by the rectangular Al fin geometries found in the banana quasi-particle test structure and in the CDMS II QET design (Fig. 5.15a). Unfortunately though, these simplistic fin geometries aren't optimal for quasi-particle collection: as typified by the 'X' in Fig. 5.15a, rectangular fin geometries have noninstrumented area which is in very close proximity to the TES. This area is tantamount to beachfront property since quasi-particles created in this area need to travel such minimal distances in the Al to be absorbed by the TES and are thus much less likely to trap.

This suggests that 'coliseum' geometries like that of the mZIP design (Fig. 5.15b) would have far superior quasi-particle collection efficiencies for a given Al fin area, and this is indeed shown in Fig. 5.16.

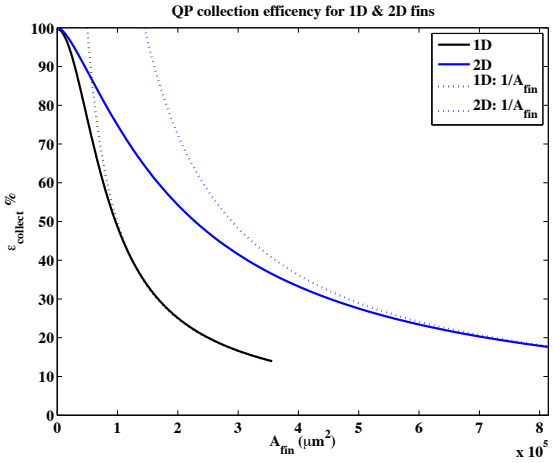

Figure 5.16: left: Quasi-particle collection efficiency for 1D rectangular (black) and 2D coliseum(blue) QETs with perfect transmission at the W/Al interface, a tes length, l_{tes}= 100 μm and $l_{trap\,Al}$= $180\sqrt{2}\mu$m.

To create this efficiency estimate, we followed the same general procedure that was laid out for the 1D fin with an impedance boundary. Of course, there are differences. Most importantly, rather than simple exponential solutions, the eigenvectors are now linear combinations of the zeroth order Bessel, $J_0(kr)$, and Neuman,$Y_0(kr)$, functions:

$$n_{2D}(r,t) = \sum_k T_k e^{-(Dk^2+1/\tau_{trap})t} \left(Y_1(kr_o)J_0(kr) - J_1(kr_o)Y_0(kr)\right)$$

in which the wave vector values, k, are self consistently defined by the equation

$$J_1(kr_o)Y_0(kr_i) - J_0(kr_i)Y_1(kr_o) = 0$$

for a perfect transmission boundary condition at r_i and a perfectly reflecting boundary condition at r_o (to derive this equation, it's necessary to realize that $\frac{\partial J_0(z)}{\partial z} = -J_1(z)$

and $\frac{\partial Y_0(z)}{\partial z} = -Y_1(z)$). As shown in Fig. 5.17, the k solutions to this equation very closely coincide with the the wave solutions to a 1D rectangular fin with length, $r_o - r_i$:

$$k_{guess} = \frac{\pi}{r_o - r_i}(m + 1/2)$$

where m is an integer [0,∞).

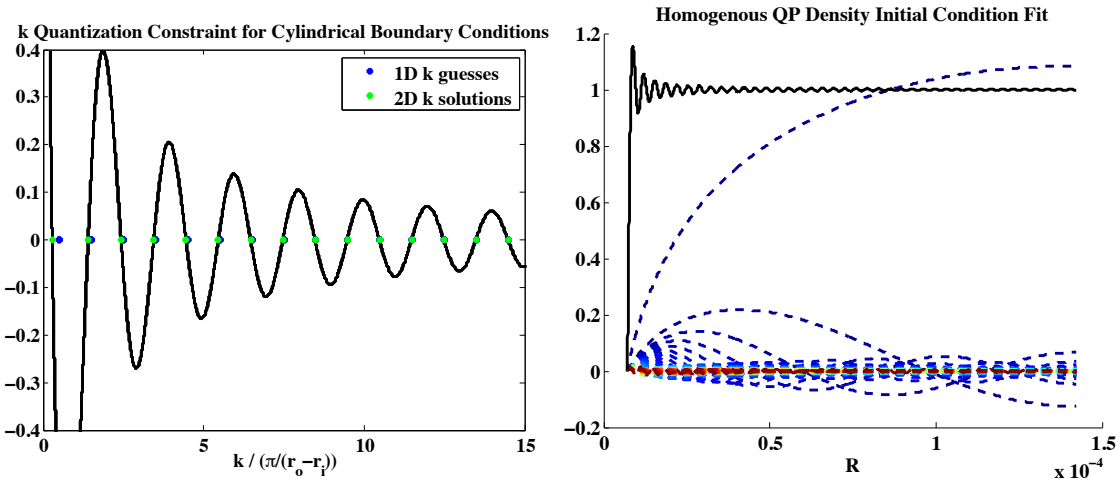

Figure 5.17: left: k quantization constraint for cylindrical diffusion geometries right: Quasi-Particle initial condition fit

Due to the lack of simple orthogonality relations, it's once again simplest to least squares fit the T_k to a homogenous initial quasi-particle state. Then, continuing to follow the outline of the 1D derviation (Eq. 5.6-5.7), one finds that

$$\epsilon_{collect\,Al} = 1 - \epsilon_{trap\,Al} = 1 - \frac{\frac{1}{\tau_{trap}} \int_0^\infty dt \int_{r_i}^{r_o} r dr\, n_{2D}(r,t)}{\int_{r_i}^{r_o} r dr\, n_{2D}(r,0)}$$
$$= \frac{\sum_k \left(\frac{k^2 l_{trap}^2}{k^2 l_{trap}^2 + 1}\right) \frac{T_k}{k^2} \left| kr Y_1(kr_o) J_1(kr) - kr J_1(kr_o) Y_1(kr) \right|_{r_i}^{r_o}}{\sum_k \frac{T_k}{k^2} \left| kr Y_1(kr_o) J_1(kr) - kr J_1(kr_o) Y_1(kr) \right|_{r_i}^{r_o}}$$

5.4.2 Fin Length Optimization for 1D and 2D geometries

Up to now, we've given some broad qualitative design boundaries on l_{fin}: basically keep l_{fin} of the same order as l_{trap}. Now, that we've developed quantitative estimates of quasi-particle collection efficiency in both 1D and 2D fin geometries though, we can go a step further and attempt to find the precise optimum fin lengths as a function of design drivers.

In the TES dynamics chapter, we derived that the optimum filter total phonon energy resolution was approximately

$$\sigma_E^2 \simeq \frac{4k_b T_c^2 G F_{tfn}}{\epsilon_{tot}^2 \omega_{pulse}}$$

in the standard athermal phonon detector limit where the sensor bandwidth, ω_{eff}, is much larger than the ballistic phonon absorption bandwidth, ω_{pulse}. Physically, ω_{pulse} is simply the inverse of the average amount of time in takes to collect a ballistic phonon in an Al fin on the surface of the detector which we can write as the average time between surface bounces, $\frac{<l_{puck}>}{<|v_p|>}$ divided by the probability that the surface interaction location is covered by the Al film, $\frac{A_{Al}}{A_{puck}}$. Even then, the phonon can reflect off the Al/crystal interface or travel into the Al film and then leave without interacting, so we'll multiply by an additional absorption probability, $f_{p\,Al}$. Putting it all together, we find

$$\omega_{pulse} = 1/\tau_{p\,absb} = \frac{<|v_p|>}{<l_{puck}>}\frac{A_{Al}}{A_{puck}} f_{p\,Al}$$

Of great importance to this derivation, $f_{p\,Al}$ is assumed to depend only upon the thickness of the Al film and the crystal type. As an informative aside, we find that Si iZIP4/5 detectors have a τ_{pulse}=140 μs which is ∼x5 faster than the phonon absorption time seen in Ge iZIP4/5 detectors (absolutely identical sensor layout and design). Since the ballistic phonon velocity,$v_{p\,Si}$, is only ∼ x2 faster than is found for Ge, our

experimental results suggest that $f_{p\,Al}$ is ∼x2.5 larger for Si than Ge.

All that is left is to rewrite A_{Al} as the number of QETs on a face of the detector , n_{qet}, multiplied by the total Al fin area for each QET, A_{fin}. Please note, that with this approximation we are incorrectly assuming that the passive Al fraction is negligible. Secondly, we'll also decompose the volume dependence of the W electron-phonon thermal coupling as $G = n\Sigma n_{qet}\mathcal{V}_{tes}T_c^{n-1}$. With these simplifications,

$$\sigma_E \propto \frac{T_c^{\frac{n+1}{2}}}{\epsilon_{tot}}\sqrt{\frac{\mathcal{V}_{tes}}{A_{fin}}} \tag{5.8}$$

Notice, the complete lack of explicit dependence upon n_{qet}. Basically, the derived linear scaling of the phonon collection bandwidth with n_{qet} is exactly offset by the linear scaling of G with n_{qet}. Of course, this is a slight simplification. If we continue to decrease n_{qet}, then eventually the athermal phonon collection bandwidth will be dominated by non-metal phonon thermalization in the crystal and ϵ_{tot}(the total phonon collection efficiency) will start to scale with the total Al area coverage (VERY BAD!).

For Ge crystals, we've experimentally confirmed linear scaling of ω_{pulse} with A_{Al} for all $\nu_{pulse} > 175$hz ($\tau_{pulse} < 900\mu$s phonon absorption time scale) and this is only an experimental limit. It's certainly conceivable that all other phonon thermalization mechanisms are on the 10hz scale and thus we may very well be able to decrease ν_{pulse} by x4 and still be fine.

Fig.5.18-left illustrates that the 2D fin geometry has a reasonably sharp energy signal optimization at around $l_{fin\,2D} \sim 0.6 - 0.90 l_{trap}$. By contrast, 1D rectangular fin geometries optimize at larger lengths, $l_{fin\,1D} \sim 1.1 l_{trap}$. This plot suggests that the SuperCDMS maximal Al design, the 'mZIP', had Al fins which were significantly too long (380μm) for energy sensitivity since our current best guess of l_{trap} is 180μm $< l_{trap} < 180\sqrt{2}\mu$m.

Interestingly, as seen in Fig. 5.18-right, the precise optimization point varies as a

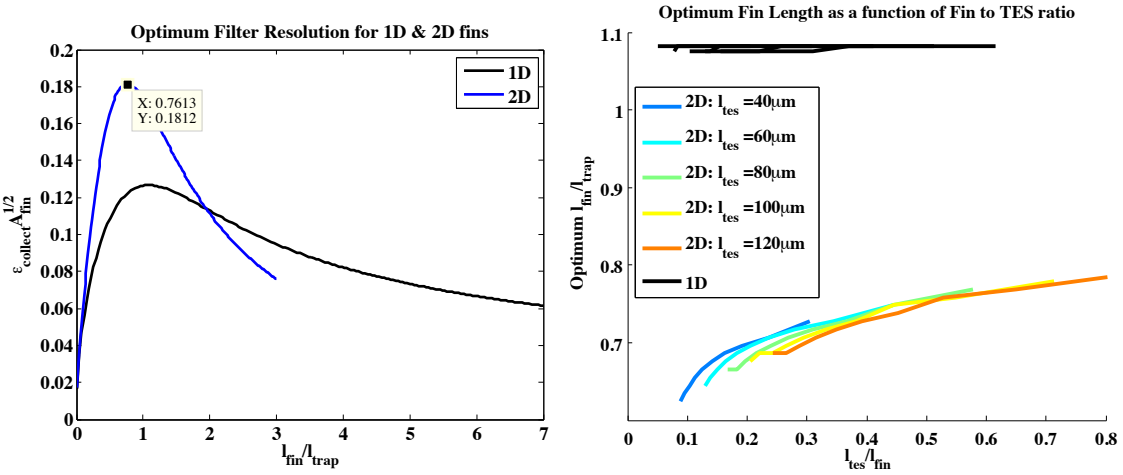

Figure 5.18: left: $1/\sigma_E$ for both 1D and 2D fin geometries as a function of l_{fin}/l_{trap} for l_{trap}=180$\sqrt{2}\mu$m and l_{tes}=100μm
right: Energy Optimized fin length in units of l_{trap} as a function of l_{tes}/l_{fin}

function of l_{tes}/l_{fin} or equivalently the l_{tes}/l_{trap} for 2D geometries. This makes some intuitive sense. In the limit of $l_{tes} >> l_{fin}$, the cylindrical fin geometry should scale as a 1D geometry.

Furthermore, this line of reasoning suggests that to truly take advantage of the increased quasi-particle collection efficiency of 2D fin geometries, one needs to design devices such that $l_{tes} << l_{fin}$ and l_{trap}. This is shown quite clearly in Fig. 5.19 where device designs with $l_{tes} = l_{fin}$ show quite marginal improvement in energy sensitivity. By contrast, devices with $l_{tes} = 1/5\, l_{fin}$ show of x2 sensitivity improvement by switching to 2D fin geometries. This again makes intuitive sense. Looking at Eq.5.8, the collection bandwidth (more is better) scales with the QET area while the thermal fluctuation noise (more is worse) scales with G or equivalently the W volume of the TES. Now, in the limit of 1D fin geometries, the ratio $\frac{\mathcal{V}_{tes}}{A_{fin}}$ is invariant with TES length. In the limit of perfect 2D fin geometries though, A_{fin} is independent of l_{tes}, and thus from an energy sensitivity perspective, it makes sense to design devices with small $\frac{l_{tes}}{l_{fin}}$ ratios.

Secondly, our detectors produce position information by collecting phonons in the Al

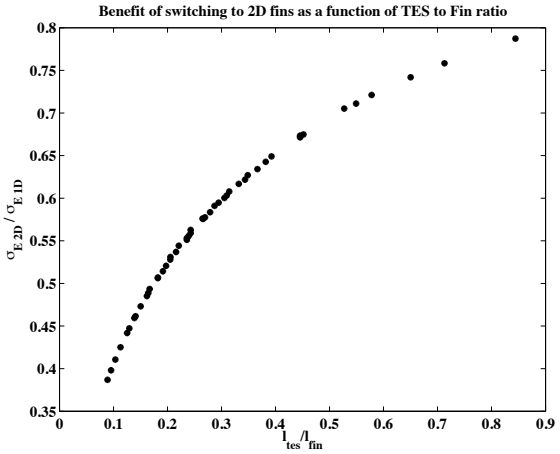

Figure 5.19: Ratio of estimated OF energy resolution for 1D and 2D fin geometries as a function of l_{tes}/l_{fin}

fin before the first ballistic bounce. As we've already discussed, the signal scales as $\epsilon_{tot}A_{Al}$ while the noise is dominated by thermal conductance TFN noise as always. Consequently, the position information signal-to-noise scales as

$$\begin{aligned} \frac{S}{N}_{xyz} &\propto \frac{\epsilon_{tot}A_{Al}}{\sqrt{4k_bT_c^2GF_{tfn}}} \\ &\propto \epsilon_{tot}A_{fin}\sqrt{\frac{n_{qet}}{\mathcal{V}_{tes}}} \end{aligned} \tag{5.9}$$

We'll discuss the n_{qet} scaling in greater depth in the next chapter. For the purposes of right now though, the scaling of fiducial volume information goes as $\epsilon_{tot}A_{fin}$. The difference in A_{fin} scaling between these two optimized signal metrics (energy resolution / position resolution) suggests that both metrics can't be optimized concurrently. We need to choose if we are going to optimize our detector for energy resolution, position information, or some complex combination of the two at the beginning of the design process.

Fig. 5.20, illustrates this choice. A device designed solely for OF baseline resolution would have the l_{fin} which corresponds to the farthest point to the right of the curve.

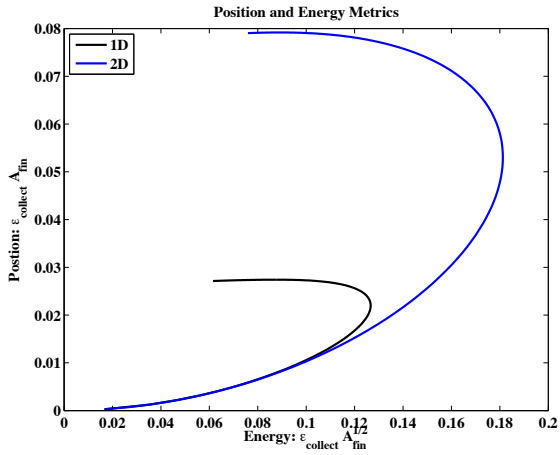

Figure 5.20: Energy sensitivity (x-axis) and postion sensitivity (y-axis) as a functions of l_{fin} for 1D and 2D fin geometries

By contrast, detectors which were designed with an emphasis on fiducial volume sensitivity would have slightly larger fins (for the case shown, a 10% decrease in OF sensitivity gives one a 30% improvement in phonon fiducial volume which is definitely a reasonable tradeoff for a high mass dark matter device.

One final comment. The fin length optimization rules for optimum filter energy resolution presented in this chapter depend upon the assumption that our noise is flat to very low frequencies. Unfortunately, the CDMS II electronics seem to have 1/f noise which tends to dominate TFN noise somewhere between 200hz and 1khz depending on the detector. This noise increases the relative importance of higher signal frequencies and would almost certainly lead us to larger optimized fin lengths and to larger power scalings with n_{qet}.

5.5 Optimizing W/Al interface

5.5.1 Historical Devices

First devices are never expected to be perfect, and the first ever QuasiParticle assisted TES device shown in Fig. 5.21a is no exception. In particular, the 'meandering' W TES has a length of 800μm (Tab. 5.3), a length which we now know to be unequivocally phase separated. Thus, it's no surprise that their sensitivity was significantly lower than found in our present devices which are only partially phase separated.

The second significant flaw in this first device is the "meander" style TES geometry (full disclosure: to my utter shame, the first QET that I proposed for the iZIP 1 detector 7 years ago wasn't a completely straight line either ... Blas correctly had me on a tight leash back then!). The stated original reason to do this was to minimize the T_c differential along the TES (If there is a T_c gradient, then a scrunched up TES will be more uniform) [81]. However, any minimal advantage gained was absolutely and completely dominated by the simple fact that by folding the TES upon itself one loses the ability to optimally surround the TES with Al collection fins. Just think about how much more Al one could place around the TES (or equivalently how much shorter the fins could be made), if one stretched out the TES in Fig. 5.21a.

Removal of these two mistakes, completely dominated the historical evolution of the CDMS QET.

A second evolutionary theme though is also visible in these devices. Over time, the W/Al fin connection shape became significantly less drawn out and it's quite reasonable to ask in hindsight, if this was the correct decision. By constantly tweaking two completely independent variables at every step, could we have confused ourselves and been incorrectly optimizing the W/Al fin connector geometry? Should our W/Al fin connector look more like the design in Fig. 5.21a then in Fig. 5.21g?

Luckily, from a measurement perspective the TES changes largely effect sensitivity (signal-to-noise ratio) and shouldn't significantly effect the amount of phonon energy

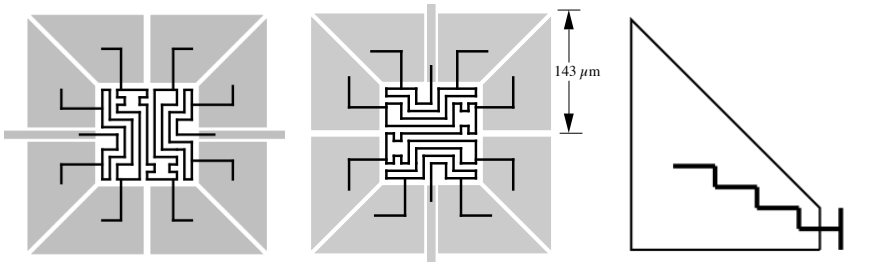

(a) 1^{st} QET: runs 9-15 (b) 2^{nd} QET: runs 22,24,26,28 (c) 3^{rd} Fin Design for run 23

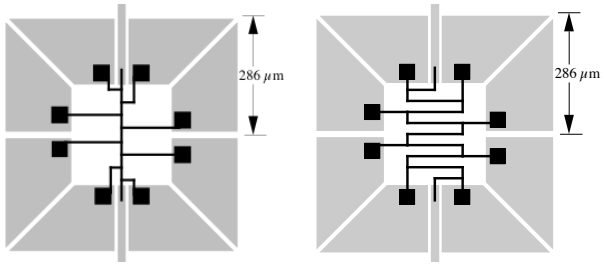

(d) 4^{th} QET: runs 31-34 (e) 5^{th} QET: runs 35-39

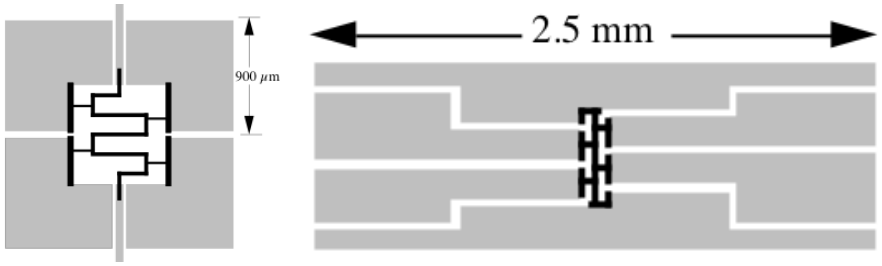

(f) 6^{th} QET: runs 40-46 (g) 7^{nd} QET: run 55

Figure 5.21: Historical R&D devices

removed from the system by electro-thermal feedback. To see this, just note that over timescales much larger than the pulse length, the total amount of energy which has left through the thermal conductance to the crystal, G, is roughly equal to the sum of the joule heating energy and the thermal pulse. Consequently, we should always be able to equate the joule heating decreases to the magnitude of energy which reaches the TES no matter if the TES is phase separated or not. Thus, our ability to measure both the absolute phonon collection efficiency and the sensitivity (2 measurements), should have given us the ability to tweak two parameters at each design step.

Runs	Fin Style	l_{fin} (μm)	t_{fin} (nm)	l_{tes} (μm)	Connector Type	% Absorption (w/o Ti-Au)	% Absorption (w/ Ti-Au)
9-15	triangle	100	60	800	meander	12 %	8 %
16-22,24,26,28	triangle	146	100	800	meander	7 %	
23	triangle	286	100	100	meander	2.0 %	
31-34	triangle	286	100	100	boxed	5.8 %	
35-39	triangle	286	100	400	boxed		2 %
40-46	triangle	900	100	200	line	2.1 %	0.3 %
55 (Alex)	rectangle	1250	150	250	line		

Table 5.3: Geometries and Absolute Phonon Absorption efficiencies for QET R&D devices from 1995-2000

A careful reanalysis of these seminal runs and the design changes they engendered, would certainly be reasonable but it has not been done largely due to the complete hassle of reanalyzing data from over a decade ago. Thus, the veracity of the phonon absorption efficiency numbers quoted in Tab. 5.3 are up for debate. In particular, please notice the huge variability in how the addition of a Ti-Au electrode on the backside of the device changes the % phonon absorption (Depending on the structure, the measured drop varies anywhere from 33% - 85%!). The log books and summaries from this era detail difficulties that the CDMS group had in minimizing ^{4}He exchange gas plate out onto the surface of the devices which is an additional phonon sink in parallel with the Al fins in some of the runs which were considered failures. In all probability, this problem was incredibly prevasive and randomly negatively biased the efficiency calculations even in "good" runs.

As an aside, He films have rarely been the dominant problem during the past 6 years in CDMS (Of course, the exception is the gigantic vacuum leak in the ebox at Soudan which ended R125). We've learned that if we decrease the liquid He rate during the cooldown from 77K, we can stabilize the fridge around 10K for a few hours and remove the vast majority of the He exchange gas through pumping on the IVC. The Goldharber-Gordon group uses ^{3}He as an exchange gas in their dilution fridge cooldowns to minimize this problem. With the increase in the cost of ^{3}He over the past decade, it's reasonable to ask if the additional experimental cost is merited.

Historically though, the dominant concern of our group has been tritium plateout (a beta emitter) on the surfaces of our detectors since commercial ^{3}He comes from the decay of tritium in nuclear weapon stockpiles. Personally, this line of argument never made much sense to me. I would think that we could easily separate any tritium contamination from the ^{3}He by a few distillation cycles at a point somewhere between liquid and pumped ^{4}He temperatures.

So with this known experimental systematic and with the fact that for these original very unoptimized designs the W/Al interface geometry was a second order effect (they were looking for factors of 10 S/N improvement not factors of 2), it's certainly possible that every aspect of our current W/Al interface geometry is completely unoptimized and thus the conservative thing to do would be to start from absolute scratch in designing the W/Al interface. If we are feeling a little bit more bold and frisky, we can compare R23 and R31-34 where the Al fin geometries are identical (R16-22,24,26,28 vs. R31-34 is slightly more messy comparison which also leads to the same conclusion), and draw the conclusion that fin connectors which meander into the Al fin as seen in fig. 5.21b have worse collection properties than fin connector geometries which are more compact as typified by fig. 5.21d and thus there does seem to be some quasi-particle trapping in the overlap region. At the same time, we shouldn't overly exaggerate the magnitude of this trapping. Between these two design iterations, we changed the overlap length by over 200μm and only saw a change in the collection efficiency of $\sim$x3. Thus, for the purposes of total phonon collection estimates in the chapter, let's say that the trapping length in the W/Al overlap region, $l_{trap\,Al/W} > 25\mu$m. This is an extremely conservative estimate (i.e. with this trapping length we should have seen x16 decrease for R23 with respect to R31-R34!)

With this one very poor limit upon $l_{trap\,W/Al}$ and our measurement of $f_{W/Al}$ in the banana device, we've exhausted all the experimental information that CDMS has ever collected on our W/Al interface and we are left with the task of choosing the many devices parameters shown in Fig. 5.22 and listed for the primary CDMS devices in Tab. 5.4.

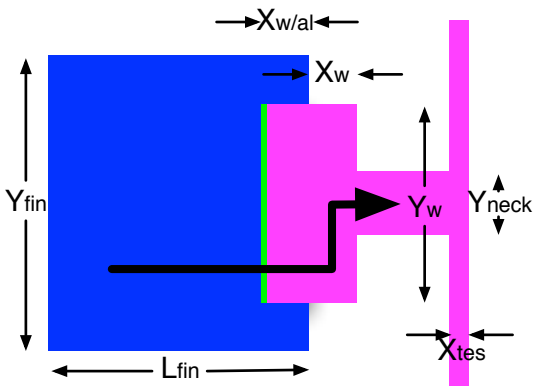

Figure 5.22: Definitions of W/Al interface parameters as well as an assumed quasi-particle collection path.

	oZIP	mZIP	iZIP
fin geometry	rectangular	trapezoidal	rectangular
$l_{fin}(\mu m)$	380	380	325
$Y_{fin}(\mu m)$	50	42	55
$X_{W/Al}(\mu m)$	3.5	3.5	4.5
$X_W(\mu m)$	3.5	3.5	2.5
$Y_W(\mu m)$	50	42	27
$Y_{neck}(\mu m)$	6	6	4
$X_{TES}(\mu m)$	0.8-1.5	1.4-2.4	1.4-2.4

Table 5.4: Geometric Characteristics for as built CDMS QETs

Below is a qualitative and certainly non-exhaustive list of the many ways in which ϵ_{tot} could depend on these design parameters. Both this qualitative discussion and the latter back of the envelope optimization assume a QP transport path illustrated by the black arrow in fig. 5.22. Specifically, a quasi-particle which is absorbed in the W/Al overlap region far from the W stub first travels horizontally down the band gap gradient until it's in the W only portion of the fin connector and then travels vertically towards the W stub.

1. width of W/Al overlap region ($X_{W/Al}$):

   (a) $f_{Al/W}$: Small Al/W transmission coefficient necessitates a large interface area (and thus large $X_{W/Al}$) to maximize transmission of quasiparticles to

the TES.

(b) $l_{trapW/Al}$: A sizeable trapping rate in W/Al means that we should absolutely minimize the time required for quasiparticles to diffuse across the W/Al interface and consequently shorter overlaps are preferable

(c) $\epsilon_{W\,cascade}$: The locations of the superconducting bandgap edges in the staircase (Fig. 5.3) depend intimately on the magnitude of the W/Al surface impedance. Very small surface impedances mean that the W and Al strongly couple and thus there is a single shared bandgap between the Al only and W only bandgaps. In the worst case scenario, this intermediate step is placed so that the high energy Al quasiparticles shed all of the potential energy difference between ΔE_{Al} and $\Delta E_{W/Al}$ as subgap phonons rather than through a process in which the net electronic energy is conserved through cooper pair breaking in the W/Al. To minimize this loss mechanism, we should tend towards smaller overlaps.

2. Fin edge overlap coverage (Y_W/Y_{fin})

(a) ϵW : If Y_W is too large, then W sections of the fin connector which are farthest from the TES thermal connection could develop a bandgap which increases the percentage of energy released in subgap phonons. To see this, just note that in the limit where the bandgap smoothly varies from that of Al to W over very large distances, their is no gain in the number of quasi-particle excitations as one goes from Al to W; the lionshare of the quasi-particle potential energy (1-$\frac{\Delta E_w}{\Delta E_{Al}}$) ends up as subgap phonons.

(b) Minimizing TES C_f and G_{fb}: For a given W/Al overlap area, larger aspect ratios means less W only fin connector material and thus less sensor noise.

(c) Physical durability: the difficulty of fabricating $\sim$ 350nm vertical step off the Al fin suggests that we don't decrease Y_W below 5 μm

(d) By decreasing the W/Al overlap we are effectively increasing the interface

impedance. If the surface impedance is already decreasing qp transport then this could be a severe negative.

3. Width of W only region in the fin connector (X_W):

   (a) C_f and G_{fb}: The stochastic noise in our phonon measurement directly scales with the the fin connector heat capacity / thermal conductance to the substrate. This suggests minimizing the area of all W only portions of the fin connector.

   (b) fabrication constraints: On the EVAlign, there is $\sim 0.5\mu m$ alignment error. Thus, the W only width must be at least this large so as to guarantee some non-vertically proximitized W.

   (c) $\epsilon_{W\,cascade}$: As discussed above, we want quick transmission of quasi-particles to W with minimal bandgap. If X_W is too small, then the large amount of nearby Al will proximitize the W-only section of the fin connector.

5.5.2 Back of the envelope Optimizations

In a first attempt to optimize, We'd like to leverage our understanding of basic electronic circuits (resistances, etc.) to find an order of magnitude estimate for the optimum design. There's nothing too revolutionary about this. Afterall, everytime we talk about thermal impedances in the context of heat transfer we are doing exactly this. There are though two subtleties to our quasi-particle density circuit (Fig. 5.23) which must be correctly modeled for our answers to be even remotely correct.

First, due to the large bandgap difference between Al and W, any quasiparticle which gains entrance into the W will somewhat quickly interact with and lose energy to either the phonon or electron system making diffusion back into the Al impossible. Consequently, the density of quasiparticles,n_{qp} (analogous to voltage), in the W will not effect the quasi-particle current(I_{qp}) flowing into the TES. This goes against our standard electronic intuition; the current flowing through a resistor is proportional

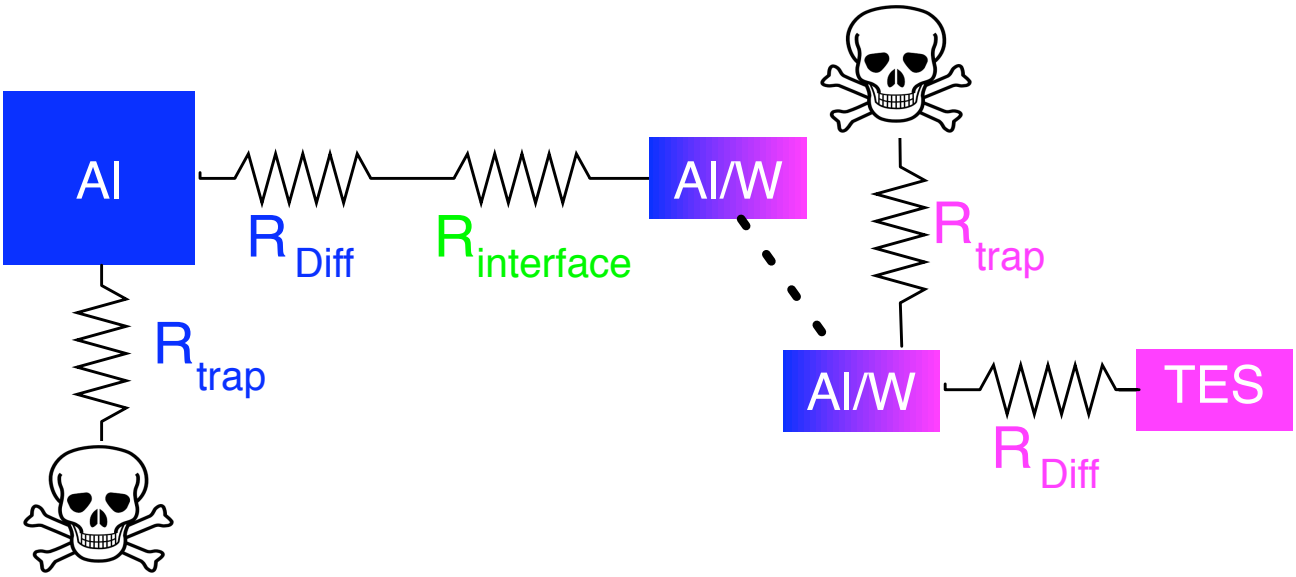

Figure 5.23: Simple Resistance Model of QP absorption

to the voltage drop. Effectively, we have two separate circuits which have current conservation at the interface rather than one large circuit (diagramatically represented as a dotted line).

Secondly, standard circuit theory assumes charge conservation (thermal circuit theory assumes energy conservation). However, in our case there is not conservation of quasi particles. For instance, a significant percentage of them are trapped and eventually recombine in the Al. So for us to use Kirchoff's current law, we must rewrite these loss mechanisms as other possible parallel paths through which quasiparticle current can flow that are connected to our circuit by a trapping impedance, $R_{trap\,Al}$ as seen in Fig. 5.23. To derive an expression of $R_{trap\,Al}$, we must only write the quasiparticle trapping rate in terms of n_{qp}:

$$I_{qp} = n_{qp}/R_{trap\,Al} = n_{qp}\frac{X_{fin}A_{cs\,fin}}{2\tau_{trap\,Al}}$$

where $A_{cs\,fin}$ is the cross sectional area of the fin. The 2 was added to very roughly convert our continuous Al fin into a uniform block (i.e. if quasi-particles are injected

at the end of the Al, the spatially averaged n_{qp} is similar to half the maximum). Thus,

$$R_{trap\,Al} = \frac{2\tau_{trap\,Al}}{X_{fin}A_{cs\,fin}} = \frac{2l^2_{trap\,Al}}{D_{Al}X_{fin}A_{cs\,fin}} \tag{5.10}$$

The Diffusive Impedance of the Al fin, is naturally defined from the diffusive flux relation

$$I_{qp} = A_{cs\,fin}D_{Al}\frac{\partial n_{qp}}{\partial x} \sim \frac{2D_{Al}A_{cs\,fin}}{X_{fin}}\Delta n_{qp} \tag{5.11}$$

or

$$R_{D\,Al} = \frac{X_{fin}}{2D_{al}A_{cs\,fin}} \tag{5.12}$$

where we again added a 2, this time to account for the fact that in real life the Al quasi-particles are uniformly distributed over the fin rather than injected at the end.

Finally the interface impedance was already derived once in Eq. 5.5 . In that derivation, we were highlighting the single dimensionality of the system at the exspense of the true physical setup. We really should have defined the area of W/Al overlap region ($X_{W/Al}Y_W$) rather than the cross sectional area. With this change the true physical $f'_{W/Al}$ is 1/9000.

$$R_{i\,Al/W} = \frac{2l_{scat\,Al}}{f'_{Al/W}X_{W/Al}Y_W D_{Al}} \tag{5.13}$$

where $l_{scat\,Al}$ is the average scattering length in Al (quite possible thickness limited).

Combining the impedances as displayed in Fig. 5.23, we find that the quasi-particle

collection efficiency is

$$\epsilon_{trap\,Al}\epsilon_{trap\,W/Al} = \frac{R_{trap\,Al}}{R_{trap\,Al} + R_{i\,Al/W} + R_{d\,Al}} \frac{R_{trap\,Al/W}}{R_{trap\,Al/W} + R_{d\,Al/W}} \tag{5.14}$$

Fig. 5.24 shows these efficiency contours as a function of the interface geometry for an iZIP-like sensor (fig. 5.15c) with an $f_{Al/W} = 1/100$ (1/4 of that measured in the banana experiments). Surprisingly, for all but the absurdly short overlap trapping length of $5\mu m$ in the leftmost figure, $X_{W/Al} > 10\mu m$ are preferred. Furthermore, as one increases the interface impedance to the values measured in the 1997 banana experiment the optimized $X_{W/Al}$ become even longer. Seemingly, all of our recent devices (Tab. 5.4) have $X_{W/Al}$ which are substantially too short.

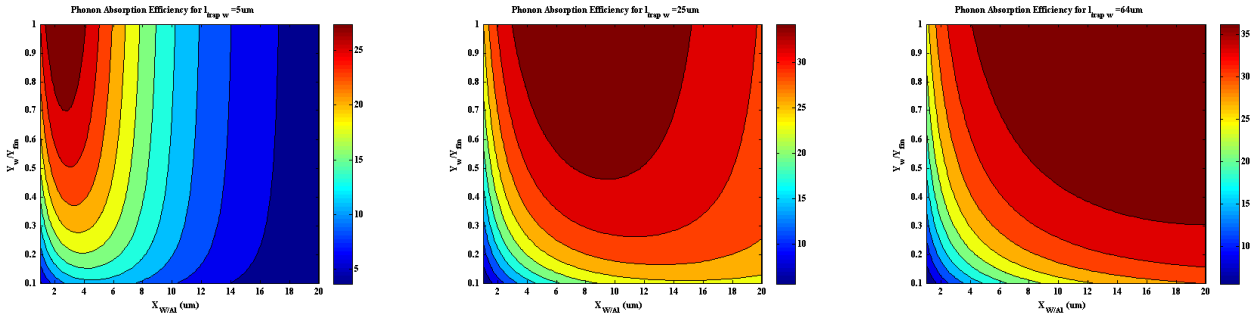

(a) $l_{trap\,Al/W} = 5\mu m$ (b) $l_{trap\,Al/W} = 25\mu m$ (c) $l_{trap\,Al/W} = 64\mu m$

Figure 5.24: QuasiParticle Collection Efficiency Contours as a function of the Al/W interface geometry

Additionally, we can account for the increased stochastic noise due to the increased TES heat capacity and thermal coupling to the bath (issue 2b/3a which is quantitatively shown in Eq.5.8) by dividing the quasi-particle collection efficiency by $\sqrt{\frac{Y_{fin}X_{tes}}{2} + X_W Y_W}$ as shown in Fig. 5.25.

Again, these figures strongly suggest that for all but the smallest $l_{trap\,Al/W}$ (left), overlap structures which travel into the fin rather than along the edge as in the oZIP and mZIP designs (Tab. 5.4) are preferable.

For trapezoidal fin geometries (mZIP Fig. 5.15b), diffusive propagation is inherently

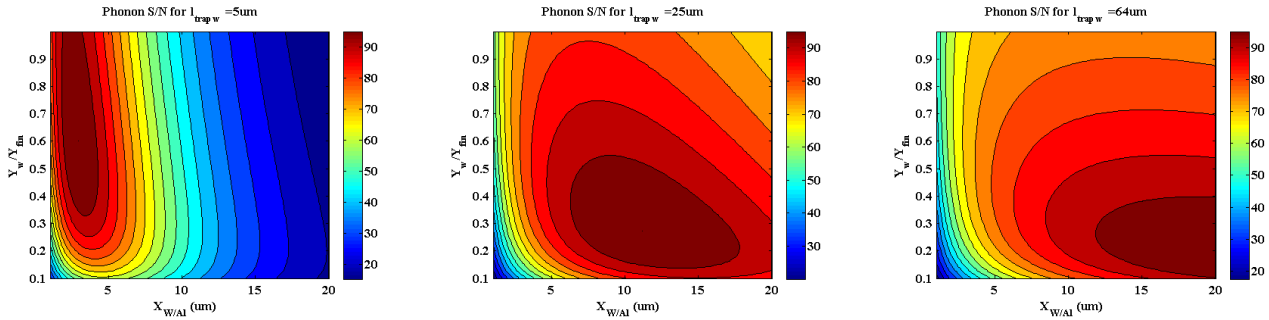

(a) $l_{trap\,Al/W} = 5\mu m$ (b) $l_{trap\,Al/W} = 25\mu m$ (c) $l_{trap\,Al/W} = 64\mu m$

Figure 5.25: Normalized total phonon sensitivity contours as a function of the Al/W interface geometry

2D and thus the simplistic impedance formulations are less accurate but still qualitatively true. This is also true for inherently 2D overlap geometries as seen in Fig. 5.26. Potentially, designs such as these will more effectively minimize both the lengths over which quasi-particles travel in the overlap region and the sensor heat capacity for a given overlap area.

Figure 5.26: An elliptical overlap geometry minimizes the length over which quasi-particles must diffuse in the Al/W overlap region for a given area.

5.5.3 ϵ_{tot} for recent QET geometries

For all three recent device designs (CDMS II oZIP,SuperCDMS mZIP, SuperCDMS iZIP), we can convolute the efficiency estimates for each stage and then compare to the measured absolute phonon efficiencies. Results can be seen in Tab. 5.5. These estimates assume an $l_{trap\,Al} = 255\mu m$, $f_{Al/W} = 1/400$, and $l_{trap\,W/Al} = 25\mu m$ and as stated earlier all of these numbers have sizable systematics. So Beware! Furthermore,

since we have absolutely no handle on $\epsilon_{W\,cascade}$, it was identically chosen for all 3 detectors to match the measured ϵ_{total} for G48 [86].

	oZIP	mZIP	iZIP
estimated $\epsilon_{crystal}$	95 %	95%	95 %
estimated $\epsilon_{passive\,Al}$	50 %	78%	78%
estimated $\epsilon_{Al\,cascade}$	55%	55%	55 %
estimated $\epsilon_{trap\,Al}$	41 %(?)	18%(?)	40%(?)
estimated $\epsilon_{trap\,W/Al}$	95%(?)	95%(?)	95%(?)
estimated $\epsilon_{W\,cascade}$	92%(?)	92%(?)	92%(?)
estimated ϵ_{total}	9.3%	6.5%	14%
measured ϵ_{total}	1-4% [87]	3.5±1% [88]	14±3 % [86] [89]

Table 5.5: Estimated and Measured Phonon Collection Efficiencies for as built CDMS QETs for the film model indicated in the text. '?' indicate numbers which have large systematics due to the use of film properties which may be out of date and should thus be considered as estimates only

Interestingly, this set of values significantly overestimates the phonon collection efficiencies of both the mZIP and the oZIP compared to measured values. To understand if this systemic overestimate is due to poorly chosen film properties, in Fig. 5.27, I've plotted ϵ_{tot} as a function $l_{trap\,Al}$ for both $f_{Al/W} = 1/400$ (solid) and $f_{Al/W} = 1/40$ (dashed). For all possible cases, we find it impossible to create a x3 difference in collection between the iZIP and the other 2 devices.

The most likely hypothesis is that some film or interface property has recently improved significantly with time (the mZIP/oZIP collection efficiency discrepancy would also suggest this as well). Some other hypotheses have been thrown around the collaboration including:

- $\epsilon_{W\,cascade}$ (Me) and fin connector geometry: As mentioned above (3a), decreasing Y_W/Y_{fin} in the iZIP design improved the internal thermal conductance of the W only section of the fin connector and consequently superconducting bandgap formation on the ends of the connector would be substantially suppressed. In all of the efficiency estimates above, we never attempted to estimate changes in ϵ_{trapW} due to variations in bandgaps and thus it's possible that for the oZIP and mZIP

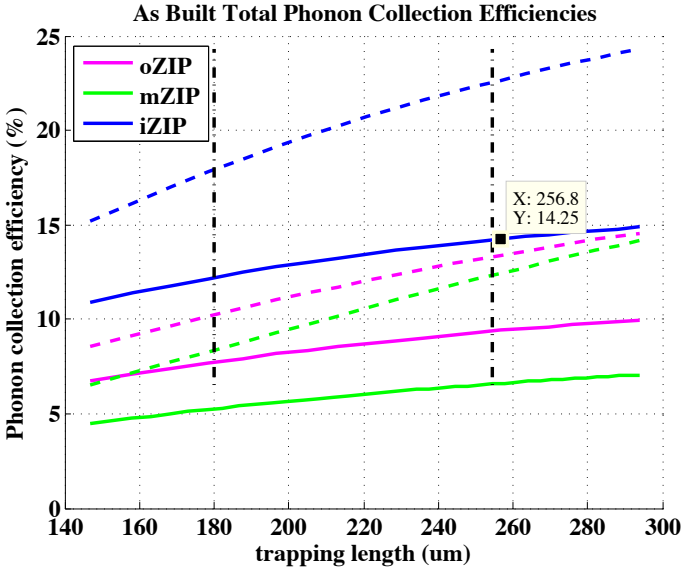

Figure 5.27: Estimates of Phonon Collection Efficiencies for recent CDMS QETs. Solid lines have an interface impedance of $f_{Al/W} = 1/400$ while dashed lines are for $f_{Al/W} = 1/40$

designs, a large percentage of energy is being lost in the fin connector. Unfortunately, this theory has some flaws as well. It doesn't explain the oZIP/mZIP collection efficiency ratio discrepancy. Furthermore, if large bandgaps exist on the outer edges of the oZIP fin design, then one would expect significant decreases in the electron-phonon coupling coefficient. We though only found a 30% decrease in the electron-phonon coupling constant (Chap. 4).

- $\epsilon_{crystal}$ and aSi (Paul Brink): In both the mZIP and oZIP designs both detector faces are 100% covered with aSi. In the iZIP design however, the aSi has been dry etched away. Thus, if the aSi has a strong propensity to downconvert with athermal phonons, it could explain all measured efficiencies. Such a large change in the phonon downconversion rate though should also effect drastically affect the falltimes. In fact, one would expect the phonon lifetime to be $\sim$ x12 larger in the iZIP than the mZIP for this theory to be correct (x3 for Al coverage decrease, x4 for aSi decrease) where experimentally we only see a x3 change. Thus, the theory seems disfavored.

- $\epsilon_{crystal}$ and heavy etching of the outer cylindrical surfaces (Blas): Just recently, we began to heavily etch the outer cylindrical before fabrication in the hopes of removing radon daughter contamination from the surface (the bare detector faces were already free from contamination due to crystal polishing.) Following the same theory as for the aSi, if athermal phonons interacted with this surface and downconverted, then a sizeable efficiency improvement would be seen in the iZIP. The same timing argument disfavors this hypothesis as well.

5.6 Chapter Summary

- Quasiparticle diffusion lengths measured by CDMS seem to be x5 smaller than those of other experimental groups suggesting that improvements in quasiparticle transport could lead to a significant improvement in phonon sensitivity.
- By substantially decreasing the amount of instrumented Al on the surface of the detectors and the Al fin length, we expected the absolute phonon collection efficiency to be x1.6-x2.0 better than found in CDMS II. Experimentally though, our improvement was >x3 suggesting improved transport characteristics in the Al films or more efficient energy transfer in the Al-W quasi-particle cascade due to the different connector geometry.
- For rectangular 1D Al fin geometries, total phonon sensitivity is optimized when $l_{fin} \sim 1.1 l_{trap\,Al}$.
- 2D Al fin geometries have substantially improved quasi-particle collection efficiencies over 1D geometries, particularly in the limit that $l_{fin} >> l_{tes}$. Maximum total phonon optimum filter sensitivity for 2D geomtries occurs when $0.6 l_{trap\,Al} < l_{fin} < 0.8 l_{trap\,Al}$(Fig.5.18 right).
- the large W/Al interface impedance experimentally seen in the first quasiparticle propagation devices suggests that our W/Al interface area could be too small in current W/Al overlap geometries.

5.7 Future Studies

1. Run the already fabricated next generation banana device to obtain more recent estimates of $l_{trap\,Al}$ and $f_{Al/W}$.

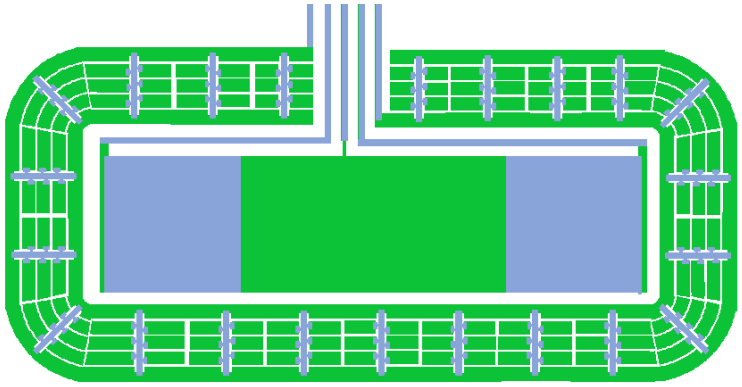

Figure 5.28: New Quasi-Particle collection structure which will be tested in early 2012

2. Design, produce and study devices which specifically measure $l_{trap\,Al/W}$. Almost certainly, the easiest design would be an 1cm x 1cm 4 channel x-ray device in which the 4 channels have $X_{W/Al}$ which span an order of magnitude.

3. Determine if the abnormally quick quasi-particle trapping rates in the Al could be caused by small amounts of residual W not removed in the etching process. As a first step, measuring the amount of W left on the Al fin surface on an unpatterned trilayer wafer after our standard etching process is quite important.

   As a second step, develop an Al liftoff fabrication process and fabricate banana structures for the new process which would keep this W contamination from ever occurring.

4. Produce quasi-analytical estimates for QP quasi-particle collection efficiency for 2D fin geometries with a surface impedance boundary condition (the plots shown were done with incredibly slow finite element code).

Chapter 6

Phonon Physics and Detector Design

It's time for us to take the leap! Now that we have a rough understanding of both the TES and the individual QET elements that dot the surface of our athermal phonon detectors from previous chapters, we just need to add an understanding of phonon dynamics in a semiconductor and then turn the cranks of a giant detector monte carlo to quantitatively estimate the signal pulse shape engendered from a particle interaction at a given location, with a given recoil energy and type (was it a nuclear or electron recoil). If that is too trivial, we could even go a step further and develop algorithms which invert this precision understanding: take pulse shapes and estimate the recoil energy, position and type.

Alas, that will not be the outline of this chapter. The primary reason is that, as of this writing, the detector monte carlo is not quite to the development stage where reproduction of physical phonon and charge signals has been shown to be physically consistent with experiment (but it is really close!). Secondly, even if this was possible currently, my thesis would only briefly discuss these issues, because I stopped personally contributing to the monte carlo effort 4 years ago and thus under the spirit of complementarity of theses, a reader would be much better served by reading about

these efforts and successes in Kevin McCarthy's soon to be written thesis and in papers by Steve Leman [90] and Daniel Brandt [4].

So with recognition that this chapter will be utterly obsolete in a few years time (or at minimum greatly expanded upon), our goal will be to illustrate how measured SuperCDMS iZIP pulse shapes directly constrain the possible phonon dynamics in cold Ge/Si crystals, sometimes at a level which is more precise than experiments which were specially designed for these studies. Hopefully, the current and future members of the CDMS detector monte carlo group will find these ideas particularly useful in this final stage of physical consistency checks. Secondly, we'd like to continue the process of optimizing our phonon sensors for maximum position and energy sensitivity.

6.1 Phonon Dynamics

Since both germanium and silicon have a diamond crystal lattice structure (diatomic basis with FCC bravais lattice), the phonon vibrational modes naturally split up into two branches: acoustic (vibrations in which the two atoms in the primitive cell largely move as one) and optical phonons (sizeable relative atomic displacement between atoms in the same primitive cell). Due to the triviality of 4 momentum conservation, optical phonons have quite short lifetimes and split into multiple relatively long-lived accoustic phonons quite quickly and thus for the purposes of understanding our phonon pulse shapes (μs and longer time scales) we can assume that all phonons are acoustic.

As described by Steve [90] and Daniel [4] but also by a plethora of more primary documents ([20],...) and books (Ashcroft and Mermin), the anisotropy of the FCC lattice hamiltonian leads to complex $\omega(\vec{k})$ relations. In particular, $\omega \neq f(|k|)$ and consequently the group velocity or $\frac{\partial\omega}{\partial k}$ (the velocity vector which characterizes the transport of a localized excitation like a phonon) is not in the same direction as the wave vector, $\vec{k}$. One physically relevant manifestation of this can be seen in work by Northrop and Wolfe (Fig. 6.1), where they laser excite a metal film on the surface

of a Ge crystal and measure the phonon energy collected as a function of direction. Basically, the vast majority of phonon energy is transported along directions with high crystalline symmetry.

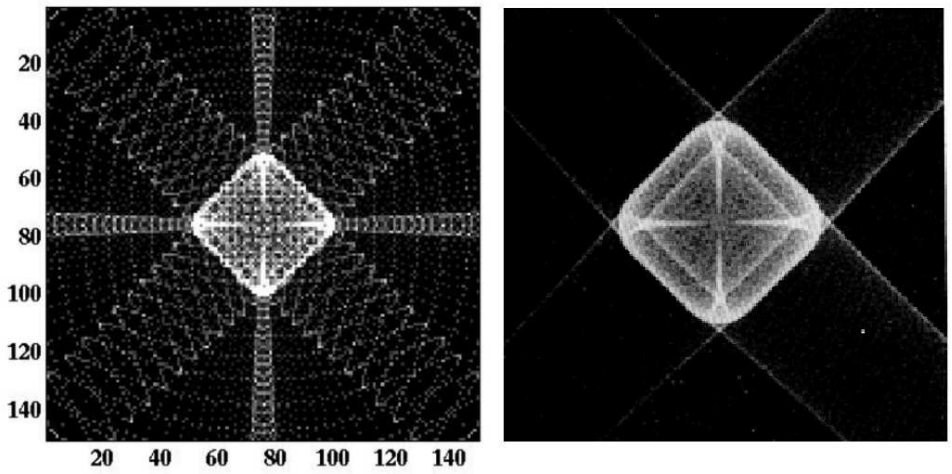

Figure 6.1: Ballistic phonon flux intensity as a function of direction as simulated by Daniel for CDMS [4] (left) and experimentally measured by Nothrop and Wolfe [20] (right)

.

Secondly, these vibrational excitations have three distinct polarization modes: slow transverse (ST), fast transverse (FT) and logitudinal (L). As seen in Fig. 6.2, the longitudinal phonon speed is significantly larger than those of both the slow and fast transverse phonons. If averaged over all directions, the average wave velocities are $[3249\frac{m}{s}$,$3509\frac{m}{s}$,$5324\frac{m}{s}$] for Ge.

Isotopic variation of the constituent atoms destroy crystal symmetry and leads to phonon scattering for which crystal momentum is not conserved. Specifically, Tamura [91] calculated that for non-dispersive acoustic phonons of all polarities (i.e low energy), the total isotopic scattering rate is

$$\Gamma_{\text{isotope Ge}} = \text{A}\nu^4 = 3.67\text{x}10^{-41}\frac{1}{\text{s hz}^4}\nu^4 \tag{6.1}$$

This process also quite efficiently mixes the three different polarization states ([90],[91],[92]),

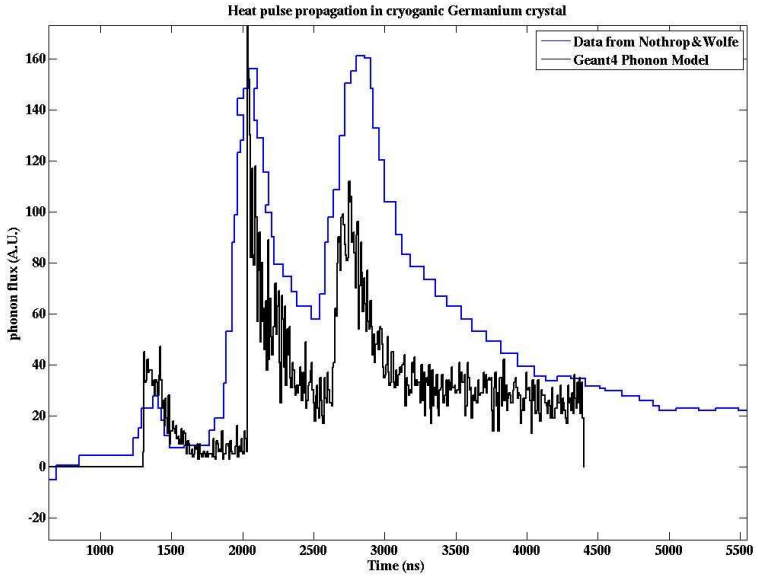

Figure 6.2: Ballistic phonon flux in the [1,1,0] direction as function of time in Ge measured by Nothrop and Wolfe (blue)[20] and matched in the CDMS simulation by Daniel (black) [4]

.

and consequently we can determine the polarization probabilities for a diffusing phonon by using the statistical mechanics principle that all quantum states which satisfy the interaction conservation rules (in this case energy conservation) are equally likely to be populated. Specifically, in the non-dispersive phonon limit where

$$\omega = v(\hat{k})|k|$$

the density of states as a function of energy scales as

$$n(E) \propto \frac{1}{v^3}$$

where v is equal to the phase velocity of a given phonon. After averaging over all directions, one finds the polarization probabilities of [54.1%(ST), 36.3%(FT),9.6%(L)] for a diffusing phonon [91].

With this information we can then probabilistically weight the group velocities for the various polarizations to estimate an average propagation speed for a diffusive phonon of $3550\frac{m}{s}$ which can then be used along with $\Gamma_{isotope\,Ge}$ to calculate the average scattering length as a function of energy shown in Fig. 6.3 (right).

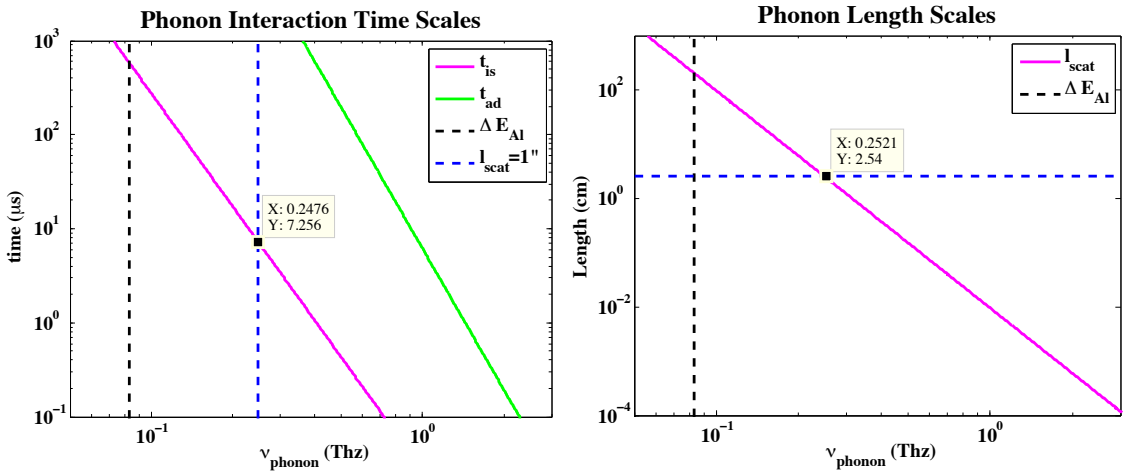

Figure 6.3: Left: Isotopic Scattering (magenta) and polarization averaged anharmonic decay (green) rates for phonons as a function of frequency. The threshold for Al quasi-particle production (black) and the frequency for which the scattering length is 1"(blue) are highlighted
Right: Isotopic scattering lengths for phonons as a function of frequency.

Roughly, we can split the phonons into 3 broad regions. Phonons with $E_p < 80$Ghz, are energetically unable to break an Al cooper pair and thus their energy can not be collected and condensed in our TES sensing elements through the Al collection fins. In principle, they can be directly absorbed by the W TES itself but this is highly suppressed largely due to the greater than 2 order of magnitude difference in the Al and W surface coverage. Furthermore, W has an anomalously small electron-phonon coupling coefficient and thus it's even further suppressed (For us this is a bonus ...remember we want a smaller G for better sensor/absorption bandwidth matching.) Secondly, there is range of phonons with 80Ghz $< E_p \lesssim$ 250Ghz, that have completely ballistic propagation. Finally, high energy phonons are transported diffusively in the crystal body. To set the scale on the high side, phonon energies at the edge of the Brillouin zone are $\sim$ [2.4Thz(ST),3.7Thz (FT),6.2Thz(L)] (We are

concerned with pretty small energy phonons).

Since isotope scattering is elastic, it's a very poor thermalizer and thus other interactions must dominate the thermalization process. For diffusive phonons near the crystal surface, interactions with metal films or even down conversion interactions with the bare Ge surface could dominate. In the bulk, Tamura [93] estimated anharmonic decay rates from experimentally measured second and 3rd order elastic coefficients in an isotropic framework and found that FT $\rightarrow$ ST+ST and ST $\rightarrow$ ST+ST processes are forbidden due to 4 momentum conservation and minimal polarization coupling. However, both L $\rightarrow$ T +T and L $\rightarrow$ L +T transitions are feasible and were estimated to have a rate of

$$\Gamma_{\mathrm{L\,AD\,Ge}} = \mathrm{B_L}\nu^5 = 1.62\mathrm{x}10^{-54}\frac{1}{\mathrm{s\,hz}^5}\nu^5 \tag{6.2}$$

when using Ge higher order elastic constants measured at 3K [94] (Fig. 6.3). One issue with this elastic constant measurement is that the 300K values measured with the same apparatus and experimental technique aren't consistent with those of other groups with seemingly higher sensitivity [95]. In particular, there is disagreement between measured $C_{123}(300K)$ values at an order of magnitude (and many σ) scale. If we simply plug in these high temperature coefficients instead, the expected anharmonic decay rate is suppressed by a factor of $\sim$x3 ($B_L = 6.43x10^{-55}\frac{1}{s\,hz^5}$ [93]).

For simulations and analytical theories which don't directly track the polarization state of a phonon, it makes sense to define a polarization averaged anharmonic decay rate,$\Gamma_{avg\,AD\,Ge}$, which weights $\Gamma_{L\,AD\,Ge}$ by the probability that a diffusive phonon is in a longitudinally polarized state which we know from earlier to be 10%, and thus our best estimate of $B_{avg} = 1.62x10^{-55}\frac{1}{s\,hz^5}$ [21].

The combination of energy conserving isotopic scattering and thermalizing anharmonic decay in phonon dynamics has been called 'quasi-diffusive propagation' in the literature. Basically, a high energy phonon diffuses with a very small diffusion constant until it anharmonically down converts into 2 phonons, each with approximately

1/2 the energy but with ∼x16 larger diffusive constant. This cascade continues until the phonons are fully ballistic. Though seemingly quite complex and very sensitive to energy sharing distributions between the two daughter phonons in the anharmonic decay, both simulations and simplistic analytical models [96] show a ballistic phonon production rate from a diffusive phonon source that has a simple decaying exponential pulse shape for time scales much larger than the ballistic time,$t_{ballistic}$, as shown in Fig. 6.4. In the simple analytic models, this characteristic time constant,t_o, is estimated to be

$$t_o = \frac{4}{9}\left(\frac{15}{4\pi^2}\right)^{\frac{5}{9}} \frac{A^{\frac{5}{9}}}{B_{avg}^{\frac{4}{9}}} t_{ballistic}^{\frac{10}{9}} \tag{6.3}$$

To study these higher frequency phonon dynamics, Msall and Wolfe excited bare Si and Ge semiconductor surfaces with a diffuse laser and then measured the phonon flux hitting the opposite crystal surface with an Al bolometer. All crystal surfaces except for the excitation surface were placed in direct contact with liquid He in the hope that ballistic phonons which bounced off multiple surfaces would minimally obscure the quasi-diffusive transport signal. In both Si and Ge, the ballistic phonon production rate was found to have a simple exponential pulse shape. Furthermore, in Si, the measured t_o were consistent with theoretical expectations and found to scale almost linearly with crystal size as expected.

For germanium, however, the measurements of t_o were x2 faster than expected (Fig. 6.4). The dominate experimental systematic discussed in the paper is the possibility of non-opacity of Ge/He surfaces. However, this would tend to systematically slow the measured t_o not quicken the response. One possibility is that the calculated anharmonic decay rate underestimates the true value because of its isotropic nature (in a non-isotropic framework FT $\rightarrow$ ST + ST interactions could be possible). Another possibility is that the bare Ge surface significantly dominated the thermalization process either intrinsically or due to slight amounts of liquid He contamination.

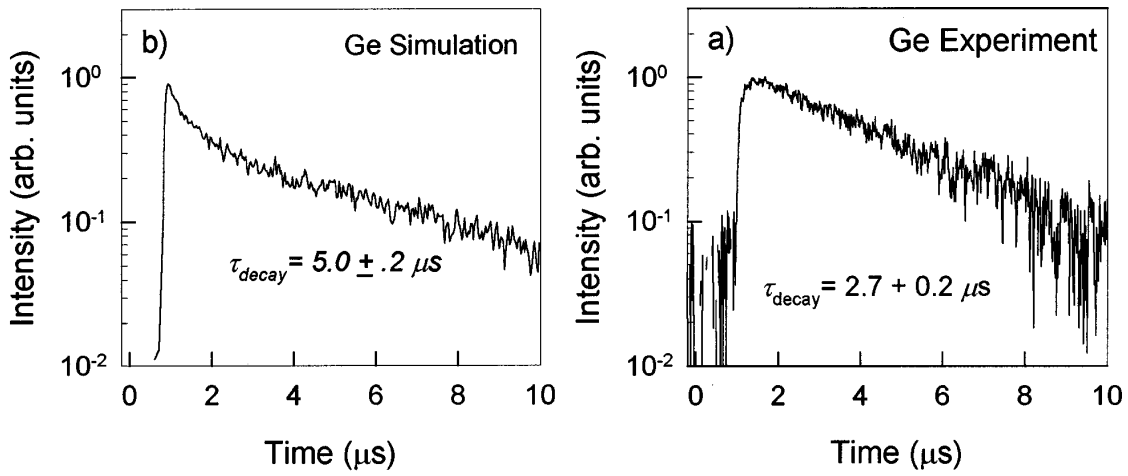

Figure 6.4: Simulated (left) and experimental measurements (right) by Msall and Wolfe [21] of ballistic phonon production from highly diffusive phonons as a function of time in Ge.

6.2 Position sensitivity and initial phonon distributions

To collect position information from a ballistic phonon is exceedingly difficult. Basically one needs to collect the phonon in an Al QET fin during it's first surface interaction. If this does not occur, then this phonon will reflect in an arbitrary direction and it could end up absorbed by a QET on the other side of the crystal 15μs later. Thus, to have any hope of having position sensitivity with ballistic phonons one needs a large percentage of Al fin coverage! By contrast, position sensitivity with diffusive phonons is much more forgiving! A 500Ghz phonon will have a scattering length of $\sim$ 1mm and a $\sim$100μs anharmonic decay time. Thus, if it reflects off a bare Ge surface on it's first attempt, don't worry. It will interact with that same local surface many more times. Consequently, reasonable position sensitivity may be possible for diffusive phonons with smaller Al coverage (though more coverage is still better). With this in mind, when describing the phonon distributions created during an event interaction, we should pay careful attention to the frequency distribution.

6.2.1 Recoil Phonons

Following the narrative presented in Klein [43], an electronic recoil produces a single highly energetic e^-/h^+ which then starts an electronic cascade (it almost exclusively interacts by exciting another e^-/h^+ pair). This process continues until further e^-/h^+ production is kinematically forbidden: until all the excited e^- and h^+ have less than a bandgap of kinetic energy. At this point, the excitations start to shed phonons and thermalize. To set a rough scale on the energy of the phonons produced one needs only realize that the 250Ghz ballistic/diffusive boundary corresponds to ∼1meV in energy units and the Brillouin zone edges correspond to [10meV, 15meV, 26meV] all of which are << the kinetic energy of the electron Thus, pretty much the entire acoustic phonon spectrum is kinematically accessible to the non thermalized electronic excitations and on phase space arguments we can say that the vast majority of recoil phonons produced will initially be diffusive.

For nuclear recoils unfortunately, one can't just invoke cascade theory since here we have a single nucleus flying across the crystal continually shedding phonons (only very rarely would it rutherford scatter and give a large amount of energy to another nuclei). To get a rough idea of the energy distribution of the generated phonons, let's follow the principles laid out by Blas in internal notes and published by Gensheng [97] and calculate what phonon energies are kinematically allowed in a 3 body interaction for a nuclear recoil with say 1keV of kinetic energy, or a velocity of 5x10^4m/s. This velocity is an order of magnitude larger than the speed of sound in the Ge crystal and thus collinear acoustic phonon production is absolutely impossible. To see this just note that $\frac{\partial E}{\partial P} = \frac{\partial \omega}{\partial k} = v$. Consequently, if I conserve p in a collinear interaction that produces a single phonon, I will have a huge amount of unused extra energy laying just laying around. To solve this, acoustic phonons can only be created in a 'cherenkov' cone where the phonon momentum is almost at right angles with respect to nucleus momentum and thus the 4 momentum conserving phase space is quite small. After accounting for this constraint, since the density of states goes $\sim |k|^2$ we expect that larger phonons would be phase space preferred. A second possible process is the creation of very low momentum optical phonons ($\omega(k = 0) \neq 0$). Any

optical phonon production though would decay into diffusive acoustic phonons.

Thus, it's reasonable for us to expect all recoil phonons to be largely diffusive and consequently we expect that recoil phonons should give us position sensitivity in [x,y,z].

6.2.2 Luke Phonons

In a CDMS detector, charge excitations created by a particle interaction are drifted across the crystal by an external voltage bias to electrodes which are instrumented with high impedance charge amplifiers for measurement (chapter 1). Due to significant, electron-phonon interactions, the vast majority of the work done on the carriers by the external electronic potential is immediately released as Luke-Neganov phonons and consequently the phonon energy released scales directly with the E-field strength.

Energy distributions for these phonons have been estimated as a function of E-field for both e^- and h^+ analytically with isotropic simplifications by Blas/Gensheng [97] and computationally by Kyle [98]. As shown in Fig. 6.5, as one increases the magnitude of the E-field, the average kinetic energy of the carriers is greater and thus larger energy phonons are accessible and even preferred (phase space arguments).

For the iZIP E-field configuration, we roughly have 2 distinct regions. For our standard Ge running condition with the electrode bias lines at $\pm$2V, the E-field in the bulk of the detector is planar and has a magnitude of $\sim$ 0.5 V/cm. Consequently, we expect that the vast majority of the 'bulk Luke phonons' to be ballistic (E_p <250Ghz). Due to the large voltage drop between the interleaved conductors on the surface (2V across $\sim$1mm), "surface Luke phonons" have significantly larger energy distributions, so much so that we expect h^+ produced surface Luke phonons to be almost entirely diffusive. Using the Cabrera/Wang calculation, e^- produced surface Luke phonons almost perfectly straddle the diffusive/ballistic boundary.

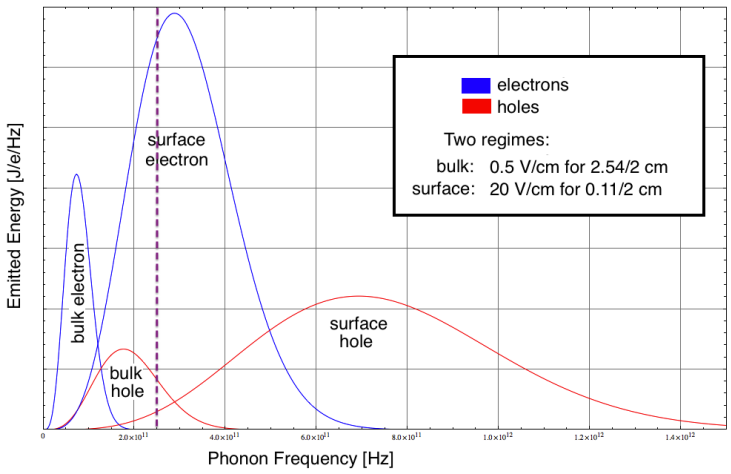

Figure 6.5: Luke phonon distributions from the Cabrera/Wang isotropic model for e^- propagation (blue) and h^+ propagation (red) with the ballistic / diffusive boundary for 1" Ge shown in purple. (created by Scott Hertel)

An event interaction in the bulk which produces a symmetric charge signal, will first produce a column of bulk Luke phonons with roughly 1/3 of the total Luke phonon energy which is nominally localized in [x,y] but not z (they're all ballistic so even this [x,y] position sensitivity is marginal). Secondly, these carriers will travel through the surface E-fields on both sides of the detector and produce a significant percentage of surface Luke phonons which again carry only [x,y] information but these will be mostly diffusive and thus have lots of position dependence.

For a surface event by contrast, no charges traverse the crystal. Consequently, all the Luke phonon production is near the surface and localized in [x,y,z]! Basically, the surface/bulk charge transport signal is also imprinted upon the Luke phonon signal. As a historical aside, realizing that the bulk /surface charge discrimination was imprinted upon the position dependent phonon signal was one of the primary reasons why we allocated resources to a second generation interdigitated detector design (the other impetus being the charge fiducial volume success that the Edelweiss collaboration had with their interdigitated device).

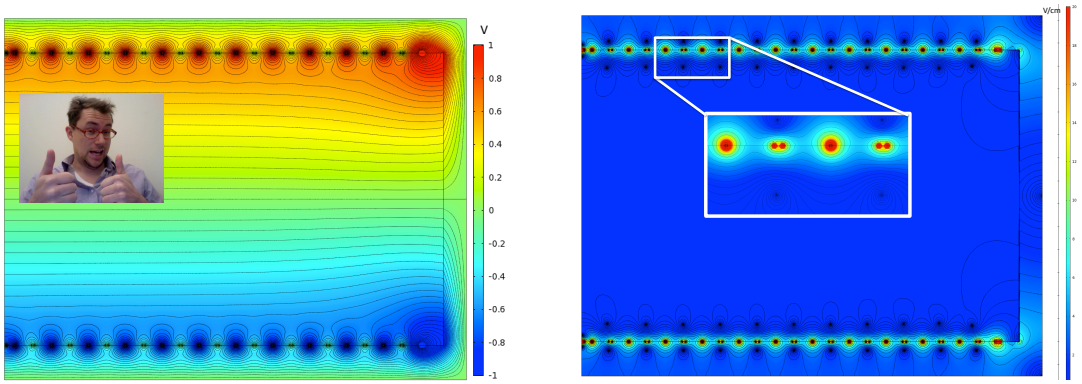

Figure 6.6: Voltage (left) and E-field (right) Contours for the iZIP SuperCDMS detector. Created by Scott Hertel (left inset)

6.2.3 Relaxation Phonons

If the transported electronic excitations are not trapped at the Ge/Al interface, but instead are absorbed into the Al electrodes, then their potential energy (crystal semiconductor bandgap), will be converted into lower energy excitations. A first guess at the resulting phonon energy distributions can be gleaned from looking at the ballistic phonon transport experiments [20] where a laser was shined onto a metal surface and copious amounts of ballistic phonons were created thus suggesting dominate ballistic phonon production.

However, we should look at these thermalization cascades in a little more depth since the vast majority of the metal films on the surface of our detector are Al at 40mK, a completely frozen out superconductor, and thus the electronic density of states around E_f are completely different from those in a normal metal system. Estimates of the interaction rates involved in superconducting metal thermal processes were estimated by Kaplan et al [99] for all T/T_c. Paul Brink [19] and Kozorezov [22], though, have significantly helped in quantifying which processes dominate at different energy scales.

Following Kozorezov's nomenclature, we can split up superconductive thermalization

into 4 different energy scales:

- $E > E_1$:

  When the energy of the phonon or quasiparticle exciation, E, is much much larger than the superconducting bandgap, then we can disregard all of the superconducting subtleties and look at the relative interaction rates in a normal metal for an excited electron to directly scatter with another electron (breaking a cooper pair in the process), $\Gamma_{ee\to ee}$, and the phonon production process by which an excited quasiparticle creates an acoustic or ballistic phonon, $\Gamma_{e\to ep}$. As shown in Fig. 6.7, $\Gamma_{ee\to ee} \propto E^2$ for all pertinent E (dotted line), where $\Gamma_{e\to ep} \propto E^3$ for $E < \Omega_D$, the debeye frequency, but constant for energies above this Ω_D (solid line).

  Thus, for all excitation energies greater than the crossover energy, E_1, where $\Gamma_{ee\to ee}(E_1) = \Gamma_{e\to ep}(E_1)$, a standard electron cascade with relatively equitable energy splitting between the two daughters occurs. For Ge, $E_1 \sim 2.5$eV or $67\Omega_D$.

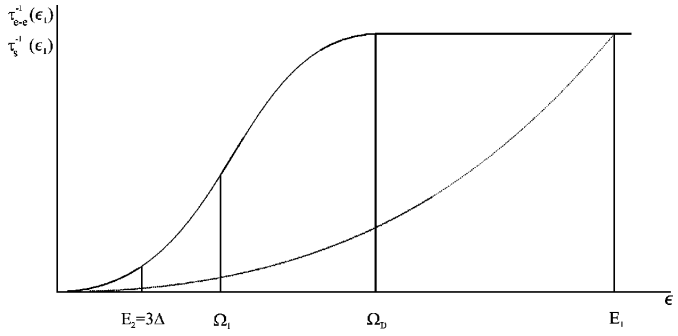

Figure 6.7: $\Gamma_{ee\to ee}$(dotted) and $\Gamma_{e\to ep}$ (solid) as a function of quasiparticle excitation energy. Created by [22]

- $\Omega_D < E < E_1$:

  Once $E < E_1$, each electron starts to primarily shed acoustic and optical phonons. In Ge, all of the electronic excitations reach an energy scale of Ω_D in ∼500fs. The phonons produced are roughly static on these time scales since

both anharmonic down conversion and destruction of the phonon through quasi-particle scattering,$\Gamma_{p\rightarrow qq}$, occur on much longer time scales (4-200ps). Consequently, at the end of this thermalization stage, almost all of the excitation energy is found in the phonon system.

- $\Omega_1 < E < \Omega_D$:

  Since $\Gamma_{p\rightarrow qq} = \frac{1}{\pi\tau_{ph}}\frac{E}{\Delta E_{gap}}$, the E^3 dependence of $\Gamma_{e\rightarrow ep}$ means that phonon shedding will dominate for all E above some crossover point Ω_1($\sim$440Ghz in Ge). In this energy range, as soon as an interaction which destroys a phonon and creates two quasi-particles occurs the residual kinetic energy of the two quasi-particles will be almost immediately reshed as phonons. Thus, there will be significant increases in both the number of phonon and electron excitations, but the vast majority of the excitation energy will reside in the phonon sector. For Ge, the actual value of τ_{ph} has a bit of uncertainty. Kaplan and Kozerzov use a theoretical estimate of 242ps while Paul uses a $\tau_{ph} = 134ps$ from experimental STJ measurements. It goes without saying that we will assume greater accuracy in the experimental value just out of experimental solidarity!

- $2\Delta E_{gap} < E < \Omega_1$:

  In the final thermalization stage, the change in the relative magnitude of $\Gamma_{e\rightarrow ep}$ and $\Gamma_{p\rightarrow qq}$ means that the extra excitation energy should start to be dominately stored as electronic kinetic energy and potential energy of broken cooper pairs. It is here that we must also take into account the differences in the electronic density of states caused due to Al being in a completely frozen out superconducting state. The differences can be seen in Fig. 6.8. Because of the huge increase in the density of states right near the superconducting bandgap edge, both the $p \rightarrow qq$ and $q \rightarrow qp$ interactions preferentially populate quasiparticles very near the band edge. The consequences of this don't significantly effect the quality of the phonon population, but due lead to both a small fano factor of ~ 0.2 for the cascade as well as an average energy per quasiparticle produced of $1.7\Delta E_{gap}$, which is definitely smaller than $\sim$x3 bandgap multiples found for

semiconductor excitations [19].

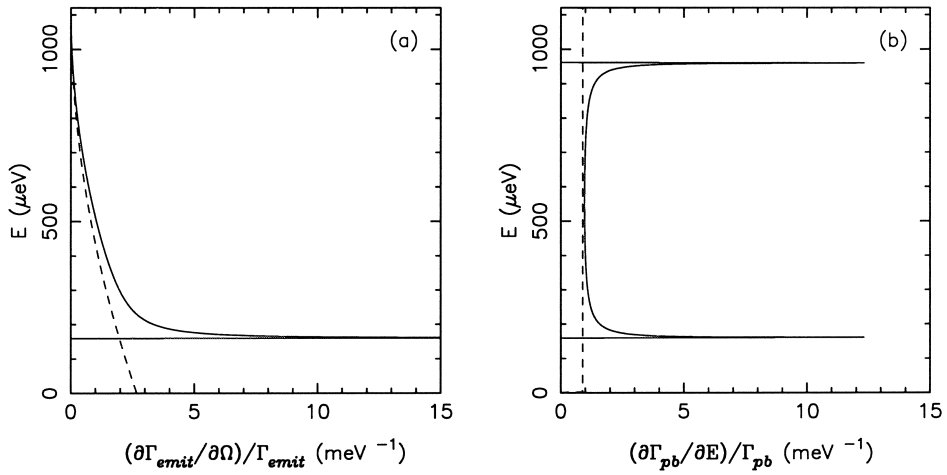

Figure 6.8: (left) Distribution of residual kinetic energy of the quasiparticle after an $q \rightarrow qp$ interaction for a quasiparticle with ∼1meV initial energy in both a metal (dotted) and a completely frozen out superconductor (solid) . (Right) Distribution of quasi particle energies after a $p \rightarrow qq$ interaction. Created by Paul [19]

If this final thermalization stage goes to completion, then not only are the residual phonons ballistic but they are also subgap. So our original question was totally moot. However, this final thermalization stage can be bypassed or at least significantly delayed by phonons leaking into the semiconductor substrate before they interact with a cooper pair. To set the frequency scale for which substrate leakage is possible, let's equate the average length over which a phonon travels,$v_{p\,Al}/\Gamma_{p\rightarrow qq}$, to the nominal thickness of our Al films, 350nm (where we've used the exeperimental τ_{ph}). With this we find a characteristic leakage frequency, ν_{leak}, of 320Ghz, which suggests that both ballistic and diffusive relaxation phonons could end up rattling around in the substrate. Equivalently, we could invert this question and ask what is the characteristic interaction length for a phonon on the ballistic/diffusive boundary,$l_{p\,Al}$, for which we find 450nm. (This is Steve Leman's preferred method of scaling the leakage issue [90]). Of course, the amount and frequency of phonon leakage depends significantly on the reflectivity of the Ge/Al interface and the Al film

quality, either of which could significantly increase the average amount of time a phonon spends in the Al and thus could significantly decrease ν_{leak}.

As a side note, for bulk events in the iZIP where all charges are collected by the high impedance charge electrodes, none of the quasi-particles produced in the charge carrier relaxation process will be measured by our QET sensors, and thus the total athermal phonon energy will be reduced. The upper bound on the magnitude of the systematic comes under the assumption of total metal thermalization ($\nu_{leak} < 2\Delta E_{gap}$) where all of the semiconductor electronic potential energy ($\sim 25\%$ of the total recoil energy for electron recoils) is converted into subgap phonons to which our athermal phonon sensors are insensitive and quasiparticles located on the charge electrodes. This suggests two things. First, our yield measurements for nuclear recoils can be systematically biased. Secondly, surface events which have significant charge collection on the grounded phonon sensor will be directly sensitive to the semiconductor excitation potential energy and thus relative to bulk events we would expect a systematic overestimate of the total phonon energy, or an underestimate in the true yield. The magnitude of this systematic depends not only on the efficiency of superconducting metal thermalization, but also on the voltage polarity (i.e. which carrier is carrying the electronic potential energy).

Though the thermalization process discussed above was motivated by trying to understand the phonon spectrum emanating from an e^-/h^+ pair relaxation process, the last stage is fully applicable to understanding how athermal phonons from the substrate create quasiparticle excitations. Even the concerns about ν_{leak} are identical. Ideally, we would like a $4\Delta E_{gap}$ phonon to travel into the Al and interact to produce 4 quasiparticles rather than 2 quasiparticles, a high energy phonon and a low energy phonon both of which leak back into the semiconductor.

6.3 Experimental Phonon Pulse Shapes and Position Sensitivity

Now that we have developed an entire theoretical narrative let's map it onto to some real characteristic pulse shapes from the iZIP (G48) and see if the story as laid out is consistent with our pulse shapes. Ideally, we would like to go a little further and ask if the pulse shapes can be used to precisely measure parameters in the above phonon narrative (ν_{leak}, B, A) and remove from consideration any other potential pulse shape narratives, that have been discussed over the years by the CDMS collaboration.

Fig. 6.9 displays characteristic charge symmetric and charge asymmetric pulses for the Ge iZIP, G48, taken at the UCB test facility. By far, the most striking feature shared by these pulses and all pulses regardless of interaction location is the $740 \pm 20\mu$s long single exponential decay for which absolutely no position dependence is seen. Like all iZIPs so far measured, G48 TES sensors are phase separated and thus their $\frac{\partial I}{\partial P}$ has some uncertainty. However, with absolute certainty (chapter 3) we can say that the long sensor falltime is $< 40\mu$s, and thus this absolutely isn't caused by bizarre phase separated TES physics. Secondly, we can completely disregard any and all theories which hypothesize slow time constants in either the Al quasiparticle dynamics or the TES dynamics by realizing that both of these hypotheses would require position dependence in the falling edge amplitudes which is **absolutely** not seen experimentally.

Per the discussion above, we know that high energy diffusive phonons will pretty much always carry significant position dependence, and thus the only way to get such long position independent tails is to have ballistic phonons rattle around in the detector and bounce off of multiple surfaces before they are finally collected. To gain some appreciation as to how many bounces we're talking about, the time it takes for a ballistic phonon to travel 1" is 7.2μs, so this suggests on the order of 100 bounces before the total ballistic phonon energy is collected. Since only 6.2% of the crystal surface is covered with Al, this suggests $\sim$6 impotent interactions with Al where

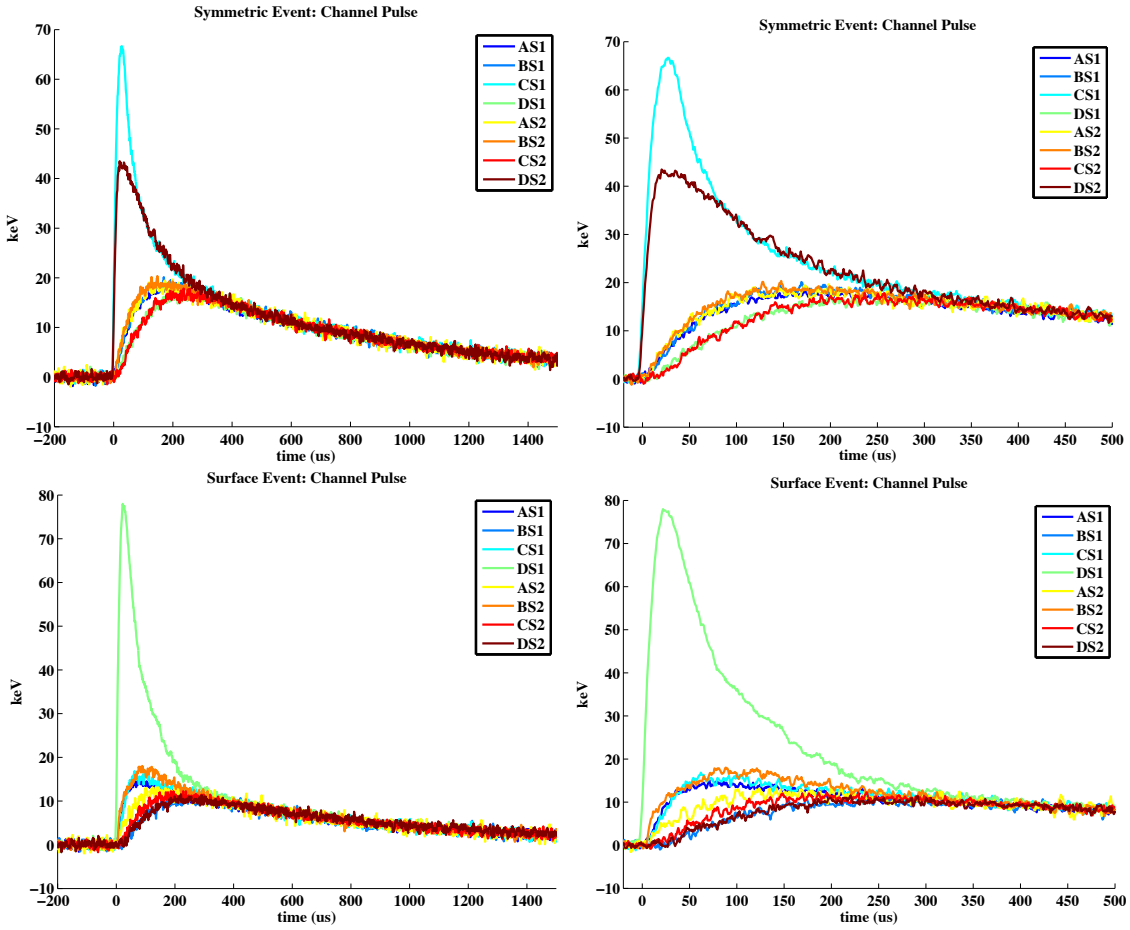

Figure 6.9: Representative pulse shapes for symmetric (top) and asymmetric (bottom) events from G48 testing at UCB. On the right, x axis has been rescaled to better emphasize position dependence.

the phonon either bounced off the Al/Ge interface or the phonon travelled through the Al either without interacting or interacting only partially so that a phonon with $E > 2\Delta E_{gap}$ leaked back into the Al (ν_{leak} is pretty high). Assuming no reflection at the Ge/Al interface and an energy averaged $\Gamma_{p\to qq}$, Steve, Kevin and the Monte Carlo group have calculated that to match the measured falltimes requires a reflectivity coefficient for phonons transporting from the Ge to the Al of 2/3.

The simplest technique to somewhat directly measure $l_{p\,Al}$ (equivalently ν_{leak}), is to look at the phonon energy absorption falltimes for multiple Al film thicknesses. If

the long falltime decreases and the percentage of phonons which exhibit position dependence increases as one increases the film thickness, then low energy phonons are leaking out of the Al. By contrast, if the falltime remains invariant, then Ge/Al surface reflectivity is the dominate cause for the slow falltimes.

At early time scales ($t < 300\mu$s), there are also quite a few general position dependent pulse shape features which should be highlighted. First, all bulk/symmetric charge events show a spiked primary channel response on both sides (CS1 and DS2 in Fig. 6.9)while all surface/asymmetric charge events only show a spiked primary channel on one side. This suggests that the surface Luke phonons are primarily diffusive phonons for both e^- and h^+ production. It's reasonable to hope that this experimental fact could be used to constrain our understanding of e^- Luke phonon production at high fields (our pulse shapes may be in disagreement with the Cabrera/Wang [97] isotropic calculations).

Secondly, it may be possible for one to use the rising edge pulse shape of the side 2 primary channel (red Fig. 6.10) for surface events on side 1 to directly estimate limits upon the anharmonic decay magnitude, B. To estimate the expected single exponential risetime for a given anharmonic decay scaling coefficient, B, one must only realize that the iZIP is precisely the opposite experimental setup to that used by Msall and Wolfe [21]. As mentioned earlier, they purposely surrounded their crystal by liquid He so as to immediately absorb all ballistic phonons which did not hit their small bolometer on the first bounce, and thus their pulse shape features directly correspond to the rate of ballistic phonon creation, t_o. By contrast, in our detector we are purposely sensitive to ballistic phonons even after many bounces. Consequently, the expected pulse shape on the side 2 primary channel is the ballistic phonon source function (measured by Msall) convoluted with the ballistic phonon absorption function for our sensor geometry (roughly a simple single exponential with 740 μs falltime) and the $\frac{\partial I}{\partial P}$ for the TES sensor. Assuming that the pole for $\frac{\partial I}{\partial P}$is much higher than for the ballistic phonon source function (a big systematic), the rising edge time scale will be precisely the ballistic phonon source falltime! Surprisingly, the fitted rising edge falltime of $\sim 45\mu$s is a very close to what one expects from

using the bottleneck approximation, 38μs, or by scaling Msalls Ge montecarlo by $(25.4\text{mm}/3\text{mm})^{10/9}$ (Fig. 6.4) and thus it is seemingly in agreement with theory but disagreement with their previous measurement at the x2 scale. To have confidence on this measurement though, one must account for the numerous systematics. A finite sensor bandwidth ($\frac{\partial I}{\partial P}$) would mean that $\sim 45\mu$s is an overestimate of the ballistic phonon creation timescale. On the otherhand, the possibility that the e^- generated surface Luke phonons are at least partially ballistic at origination would suggest that 45μs is an underestimate of the bulk phonon creation time scale. A possible measure on this systematic would be to also match the opposite side summed pulse shape response (green). Finally, the fact that much of this anharmonic down conversion is occurring near a Ge surface with 6% Al coverage suggests that superconducting metal downconversion could significantly speed up the measured t_o from its bulk value (the same systematic that may have affected Msall). So, careful accounting of each of these systematics is required before we will have confidence in our measurement of the phonon down conversion time constant.

Interestingly, varying the characteristic phonon leakage frequency, ν_{leak}, doesn't significantly effect the measured t_o. If the athermal phonon thermalizes completely in the Al, then the high energy phonon density is rapidly decreasing and the t_o will be shorter. Likewise, if there is significant ballistic phonon leakage from the superconductor, then the ballistic phonon density will increase quite quickly; t_o will be shorter. Flipping this around, measurement of the percentage of phonon energy which carries position dependence is quite sensitive to ν_{leak}, and thus the combined measurement of the ballistic phonon absorption time scale, opposite side risetimes for surface events (t_o), and side summed partition quantities for surface events, can split the degeneracies between ν_{leak}, B, and Ge/Al surface reflectivity.

As was first attempted by Steve and Kevin [21], one should also be able to use non-primary channel pulse shapes (channels far from any surface Luke phonon creation) to split these degeneracies as well. This initial study was unfortunately systematically limited by the lack of correct superconducting metal thermalization cascades and most importantly poor $\frac{\partial I}{\partial P}$ control. Finally, this study additionally requires the added hassle

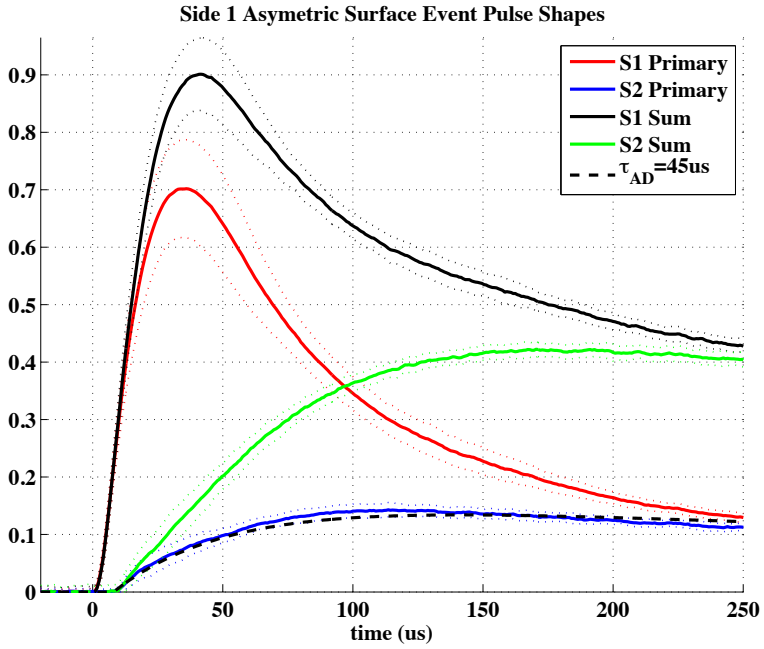

Figure 6.10: Averaged side summed and primary channel pulses for events with asymmetric charge collection. $\pm 1\sigma$ position dependent bands shown as dotted lines. Black dashed line is the best fit of the opposite side primary channel to a simple exponential rise time.

of a source montecarlo (one must know the event interaction z depth distribution for a collimated source or the full [x,y,z] event position distribution for a non-collimated source).

6.4 CDMS II: Understanding surface event yield and pulse shape rejection

With such excellent qualitative correspondence between the iZIP pulse shapes and the theoretical pulse shape narrative, it makes sense to go back and try to make sense of some empirical CDMS results.

- Surface event yield assymetry:

Charge electrode surface events are roughly x5 less likely to leak into the nuclear recoil band than phonon side surface events [100]. Many hypotheses have been floated by the CDMS collaboration. The most widely held hypothesis for this asymmetry, is that ion-implantation of the surface on the phonon side for T_c suppression drastically increases the number of atomic dislocations in the surface region which effectively p dopes the substrate. This hypothesis received significant circumstantial support when ion-implanting the first iZIPII detector (G3D) drastically decreased the breakdown voltage. Another reasonable hypothesis (first put forward by Nader), is that the increased Al surface coverage on the phonon side leads to greater ground plane attraction (i.e. method of images) and thus back diffusion is enhanced on the phonon side relative to the charge side.

A whole realm of hypotheses in which the yield asymmetry is at least partially caused by systematics in the phonon collection have not been strongly publicized. In particular, we naturally expect that charge side surface events will have significant diffusive phonon down conversion within the Al charge electrode. By definition, this means that there will be sizeable quasi-particle production which is not seen by the Al QETs on the other surface and thus our phonon collection should be systematically suppressed leading to larger yields. On the otherhand, phonon side surface events will have not only have higher quasi-particle production efficiency, but the interaction of the diffusive phonons with the phonon sensors at short times will lead to very fast risetimes (larger phonon absorption collection bandwidth), which through our imperfect optimum filter routines will lead to systematically overestimated phonon energy estimators.

- Surface event timing asymmetry:

  Z Surface fiducial volume pulse shape cuts tend to be significantly more powerful on the phonon side than the charge side [100]. So much so infact, that our total surface event leakage after timing cuts (after pulse shape fiducial volume cuts) in CDMS II has always been dominated by charge side leakage. This is a natural

corollary to the yield asymmetry discussion, above. The phonon side surface events have enormous position sensitivity (i.e sharp risetimes) because diffusive phonons are immediately interacting with Al QETs. By contrast, for a charge side surface event, one is only sensitive to ballistic phonons which leak out the Al on the charge electrode which is only a portion of the total thermalized energy. Furthermore, this portion is not as quickly absorbed as near surface diffusive phonons by the QETs. Basically, charge side surface events arent so much fast compared to the bulk electron recoils as nuclear recoils are slow compared to bulk electron recoils.

6.5 Optimizing Position Sensitivity

The simple scaling laws created for position sensitivity produced in the QET design chapter assumed a ballistic only phonon model. In this chapter though, we have significantly increased the complexity of the ideas behind position sensitivity by introducing the idea that position sensitivity varies significantly with phonon frequency, and thus we should ask if the scaling laws are still valid.

The crux of scaling argument which may have to be modified was the idea that the magnitude of the position dependent signal (magenta Fig. 6.11) varied linearly with the Al coverage percentage while the shape of the position dependent signal was invariant. This though is only true in the limit that only a small percentage of phonons undergo metal downconversion before they become ballistic. Diffusive bulk recoil phonons will certainly satisfy this property, since to even get to the surface requires that the phonon had anharmonically downcoverted in the bulk of the crystal many times but diffusive phonons that originate near the surface may not. If this is not true, then the position dependent bandwidth with increase linearly (as long as it is not cut off by $\frac{\partial I}{\partial P}$) but the DC magnitude will remain fixed at $\sim 10\%$(naively, a bit scary). We though shouldn't get too concerned about this. For us to have a DC position dependent magnitude of only 10% would require that $\nu_{leak} \sim 20\Delta E_{gap}$, which

is ∼x3 larger than the highest possible value (i.e. no phonon reflection at the Al/Ge surface helping to keep the phonons in the Al film for longer periods of time).

Finally, even if partially true this is actually exciting! It opens up another path through which we can improve our detectors: we could just increase the Al film thickness until ν_{leak} stabilizes.

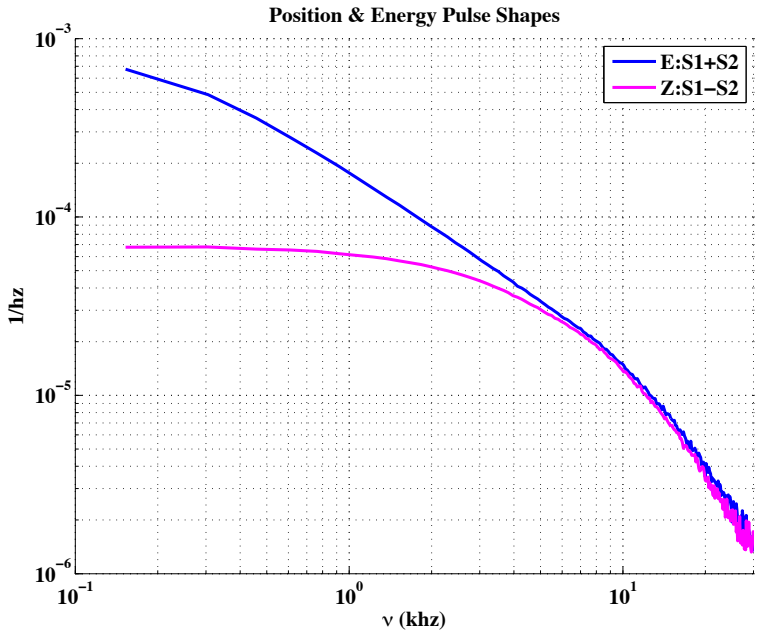

Figure 6.11: Total phonon signal pulse shape (blue) and z position signal (magenta) as a function of frequency for a Ge iZIP4 detector (G48). The total phonon signal is the direct sum of all channel traces on both sides of the detector, while the z position dependent signal corresponds to the difference in side 1 and side 2 trace sums.

6.6 Summary

- High frequency diffusive phonons encode position information on times scales large with respect to the ballistic transport time.
- Charge transport behavior is imprinted upon the phonon signal through high frequency surface Luke phonons.

- Without accounting for potentially dangerous systematics, rising edges for far side primary channel pulses match theoretical expectation for quasi-diffusive phonon propagation.

6.7 Future Studies

- Continue to improve detector monte carlo.

Chapter 7

iZIP Detector Performance

With our qualitative understanding of both how a CDMS detector works and ways we can design better detectors in the future, it's time for us return to the quantitative present and precisely estimate our ability to distinguish between nuclear recoils and electron recoils as a function of energy, and experimentally estimate the sensitivity of our energy scales. In the process of meeting these goals, we'll highlight the ways in which this 2 sided detector analysis differs from the now obsolete single sided CDMS II analysis techniques, explore the disadvantages and inherent systematics involved in estimating nuclear/electron recoil discrimination at a ground level test facility in general and finally emphasize some of the special quirks of the UCB test facility that had confused us for many years.

Of course, as with any analysis of a relatively complex system (we have an enormous number of independent estimators compared with the average detector), we'll also spend significant word count on discussing how the methods used here could be improved.

7.1 Charge Estimators

To create relatively simplistic radial fiducial volume estimators, the interleaved charge electrodes have been split into two sections on both faces of the detector with the approximate collection areas quite reminiscent of those in single sided CDMS II detectors diagrammed in Fig. 7.1 (the outer 2 bias rails compose the outer electrode).

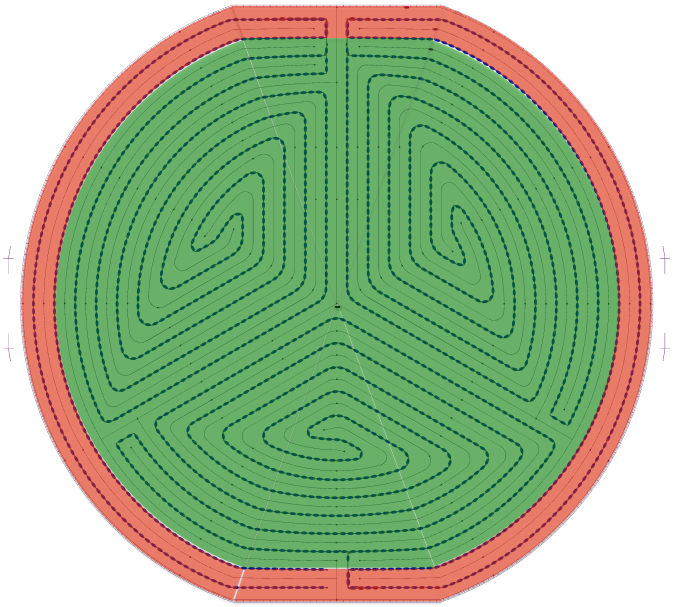

Figure 7.1: iZIP4 side 1 surface design colored to indicate the inner/outer electrode collection areas

Unlike in CDMS II though, this is true for both faces and thus with our 4 separately instrumented charge electrodes we measure this radial position independently with both e^-s and h^+s. Even more importantly, as discussed in Ch. 2, this two sided interleaved electrode geometry allows us to also fiducialize in z by measuring the assymetry in the number of carriers collected on the two sides. Finally, the measurement of both carriers means that for bulk events we in principle have 2 independent measurements of the number of e^-/h^+ pairs,$n_{e/h}$, created during the interaction.

The representative trace displayed in Fig. 7.2 left, illustrates these principles. Charge sharing between the inner and outer electrodes on both sides suggests that this event

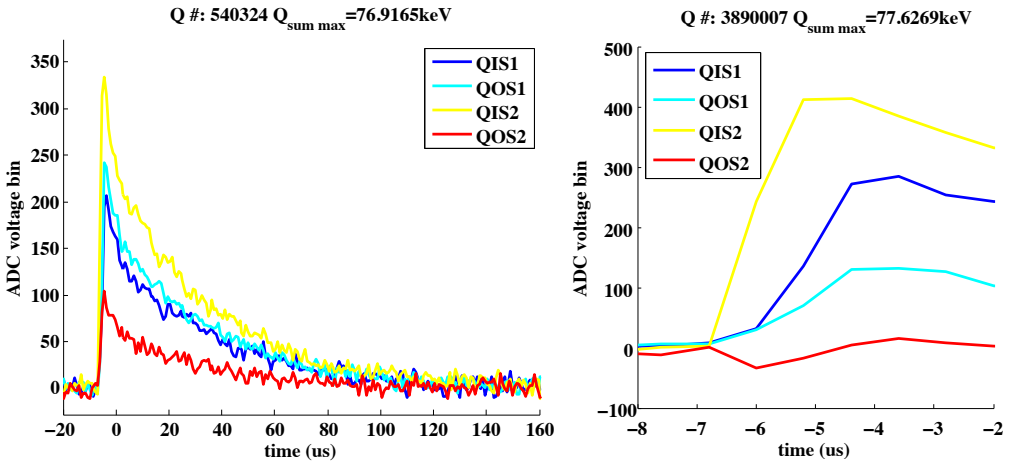

Figure 7.2: (left) Charge trace for a symmetric event at relatively high radius for the iZIP4 detector, G48, tested at the UCB surface facility.
(right) Rising edge of a symmetric low radius charge trace.

occurred at high radius, and it's roughly symmetric nature suggests that it's a bulk event (height of QIS1 (blue) + QOS1 (cyan) $\sim$ QIS2 (yellow)+QOS2(red)). These traces also show that the pulse shape itself is almost completely identical for all events. This is because the pulse falltime is determined by the feedback circuit in the charge preamp, not by any detector physics. In principle, the risetimes of the events are determined by carrier drifting speeds and thus vary with z event location. This effect though is quite suppressed due to the interleaved phonon electrodes. Due to their much larger width ($\sim$ 300μm for phonon ground rails versus 40μm biased charge electrodes), while carriers are drifting in the bulk region of the detector the majority of the image charge travels onto the non charge sensitive phonon rails. It's only when the charges transport into the surface region that the majority of the image charge quickly transfers to a charge line. This is a poor man's version of the shielding plane in TPCs.

Consequently, the majority of the z dependence is seen in the pulse start time difference between the two sides as shown in Fig. 7.2 right. On the brightside, this is conceptually one more estimate of z which we shouldn't disregard. With S/N of $\sim$ 2 for events with 100keV$< E_r <$200keV it's not currently worth too much effort (Fig.

7.3) though. Conceptually, we could improve the shown performance in the future (if wanted) by increasing both the digitization rate to say 0.25μs from 0.8μs (easy) and the readout electronics bandwidth (harder) [98].

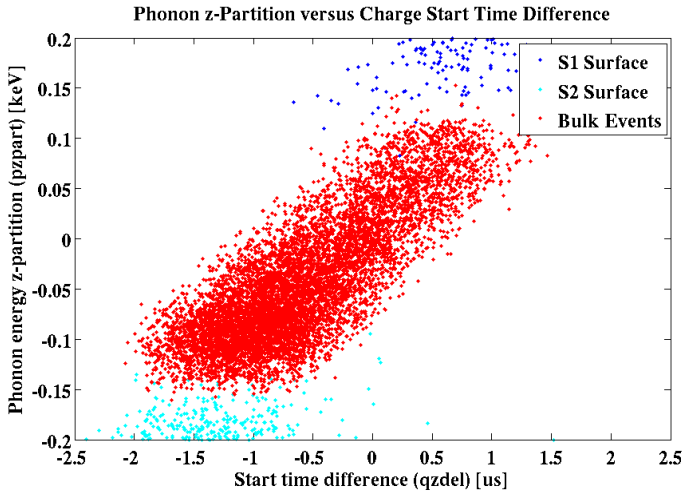

Figure 7.3: Correlation between qzdelOF (Δt between side summed OF best fit start times)and pzpartOF (currently our best z metric from phonons)

This physical time delay between the pulses on the two sides also affects our choice of Optimum Filter (OF). A traditional 1D Optimum Filter (OF-1D) is precisely designed to optimally fit a fixed shape template to a trace with stationary noise by varying only the start time and the amplitude [2]. This is already pretty close to ideal! We could just OF-1D fit each charge electrode independently of the others and end up with 4 independent amplitude estimators (qi1OF, qo1OF, qi2OF, qo2OF) and 4 independent start time estimators. We though can do better than this. We know that the noiseless charge traces for the inner and outer electrodes on the same side must have the same start time. Thus, a better estimator would have only two start time estimators. Generalizing, we would really like to design an Optimum Filter for n comingled traces with n amplitude degrees of freedom (DOF) and a single start time (OF-nD) that we could apply to each face separately. This has now been designed and implemented in the G48 analysis. The reason for it's tardiness was algorithmic difficulties. Best fitting a time shift is a non-linear phenomena and thus it's computationally quite intensive ($\propto n^2$ where n is the number of digitization bins)!

The secret to OF algorithms in general is that time shifting is done naturally through an FFT and thus they are relatively quite quick ($\propto n\log(n)$) compared to all other methods and it simply took a bit of time and effort to generalize OF-1D but keep it's excellent computational performance.

The advantage to limiting the number of time degrees of freedom, can be visually seen in Fig. 7.4 which scatter plots the best fit charge amplitudes (qi1OF, qo1OF) for random noise traces. To understand this plot, note that a single OF-1D algorithm will always tend to estimate a non-zero value for the mean charge pulse amplitude. The reason is that the template will shift around in time until it finds the largest positive or negative random noise fluctuation to cancel out. So running 2 independent OF-1D algorithms on the inner and outer charge traces will tend to give 4 random noise blobs at the corner of square. By contrast, the OF-2D algorithm creates a noise donut: it's quite unlikely for a large stochastic fluctuation to exist for both the inner and outer traces at the same time and thus the average distance of a noise event from the origin is suppressed by a laudable $\sqrt{2}$, over the simple 0F-1D algorithm.

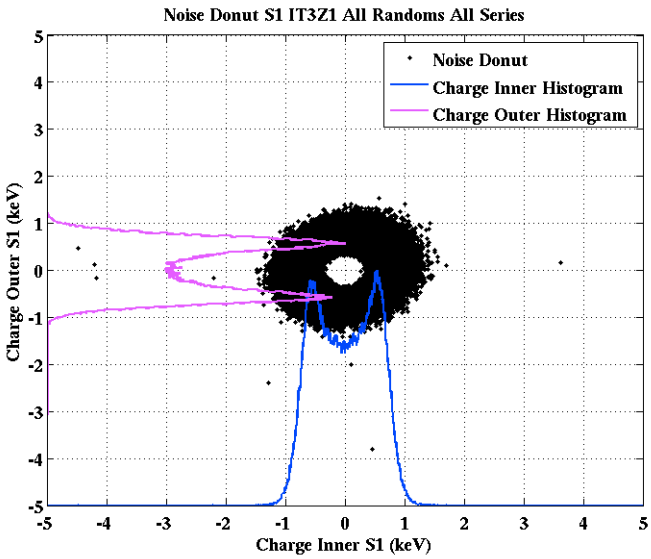

Figure 7.4: qi1OF vs qo1OF scatter plot for randomly selected noise events for iT3Z1 (G48) at Soudan in R133 (created by Brad Welliver [23]).

In principle, we could continue down this path and remove the time degree of freedom

between the two sides, qzdelOF, by using a single 4D optimum filter, OF-4D, on all traces. Once again following the argument above we would expect a decrease in the total noise offset of $\sqrt{2}$. Unfortunately though, this algorithm is untenable at high energies because the true physical time delay between the two sides of 2μs leads to a significantly larger fit χ^2 and a charge amplitude systematic that limits the precision of the calibration. For R133, we plan to combine the best of both worlds by using a newly designed 4D Optimum Filter algorithm which allows constrained time delay freedom between the two sides up to 2μs which precisely matches the true physical detector constraints. Unfortunately, as of this moment, the algorithm is still in development and has not yet been tested.

7.1.1 Charge OF Baseline Resolution

Another technique to minimize the charge noise offsets from zero is to constrain the total time shifting degree of freedom for all charge traces to a window around the physical phonon trigger. For CDMS II data, this window has traditionally been set to the rather large range of [-100μs,10μs] [2]. This rather huge range was chosen because the physical phonon trigger varies in time with both event position and event data. Potentially, for future analyses, this time shifting range could be significantly decreased in size by basing it instead on best fit OF phonon trace start times. Scientifically, these slight algorithmic changes would be most visible in next generation searches for low mass WIMPs [101].

To easily characterize the quality of our charge sensitivity without worrying about the time degrees of freedom, CDMS has traditionally used Optimum Filter resolutions in which all time degrees of freedom are fixed ([qi1OF0, qo1OFO,qi2OF0,qo2OF0]) on random noise events whose histograms are shown in Fig. 7.5 left for G48 UCB data. With time fixing, we expect these histograms to be gaussians strictly centered about 0. As is clearly seen, this is not the case! Eventually, the cause of these unexpected and unwanted offsets was found to be nonstationary/time dependent noise which correlates with the electronic trigger pulse (Fig. 7.5 right). Hopefully,

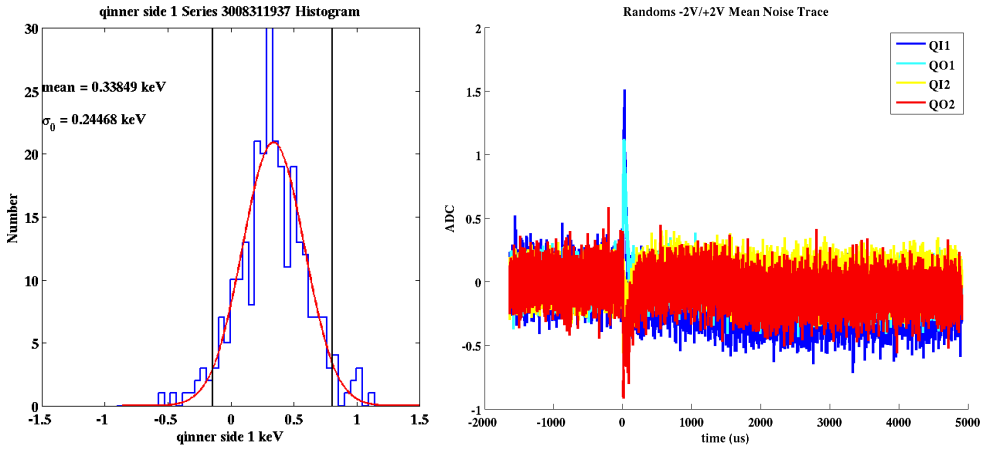

Figure 7.5: (left) Optimum filter best fit amplitude charge noise histograms for side 1 inner electrode with no time shifting freedom (qis1OF0) and (right) temporal average of 1000 noise traces which displays phase coherent noise correlated with the trigger.

future SuperCDMS warm electronics will not display this issue.

The measured charge resolutions, σ_q for G48 at UCB are [260,140,215,180]eV$_{ee}$±10% (sys) for [qi1OF0, qo1OFO,qi2OF0,qo2OF0] [102] where the systematics are dominated by long timescale temporal variations (i.e. noise variation with series). This temporal variation in resolution along with the fact that nominally identical charge channels (qi1OF0 vs. qi2OF0 for example) exhibit ∼20% variation suggests that non-intrinsic environmental noise is unfortunately the dominate noise currently. The almost 40% variation in sensitivity between inner and outer electrodes definitely is indicative of the expected $\sqrt{C}$ resolution dependence but with all the environmental noise floating around this conclusion is prone to systematics.

Taking a step backwards, the charge noise PSDs sourced to the preamp output for the G48 run are shown in Fig. 7.6 left. The rolloff of the FET noise at 1/40μs (black dotted line) is clearly visible, unlike at Soudan where environmental noise completely dominates our low frequency performance. Unfortunately, low frequency noise begins to dominate the noise plateau at ∼1khz. The rate of rise seen is quite impressive! Remember, the FET noise itself is rolling off with 1/f due to feedback below the black dotted line and thus if we posit this is intrinsic low frequency noise

of our IF4500 JFET then we need to have significantly degraded performance from that shown in Fig. 7.6 right, where the noise doesn't seem to have $> 1/f$ dependence until <20hz.

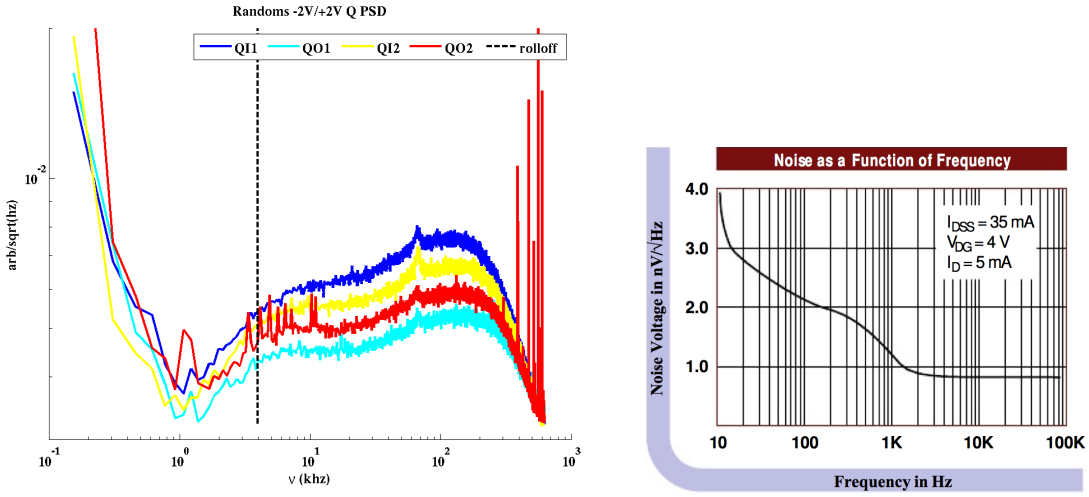

Figure 7.6: Charge Noise Power Spectrums for G48 at UCB (left) and for the JFET IF4500 at room temperature (right) [24]

As an aside, these n trace, n amplitude OF routines were generalized further to allow for cross talk between the 4 signals/ traces (i.e. charge collected on the inner electrode also creates a signal on the outer electrode). This was a required algorithmic improvement for CDMS II detectors which display crosstalk on the order of $\sim 10\%$. This large crosstalk in the CDMS II design is due to 2 reasons. First, while the charges are drifting within the bulk of the detector, image charge is moving on and off all electrodes, not just the electrode on which the charges are eventually collected. As discussed above, this physical cross-talk is substantially suppressed in the iZIP design do to the wide interleaved phonon electrodes. Secondly, any direct capacitive coupling between the 2 instrumented electrodes,C_{io}, will lead to charge sharing. To estimate the magnitude of this effect one only needs to compare the capacitive coupling between the electrodes to the coupling capacitor, C_c, in the charge preamplifier circuit. For a 1cm CDMS II device, C_{io} has been estimated to be 21.0 ± 0.1pf [103] while C_c was chosen to be 300pf [104] and thus we expect $\sim 7\%$ charge coupling between the two channels. Here again, the interleaved phonon lines of the iZIP design drastically

suppress the cross talk since the inner channel capacitance is <2pf as shown in the estimated 2D capacitance matrix (Tab. 7.1) [105]. As an even further aside, the obvious question to ask is "why don't we just bump up C_c to suppress the cross-talk?". I asked this question to Dennis myself, and the answer is that for the footprint budgeted in the original board layout, any capacitors with larger size tend to be easily destroyed by static electricity buildup and/or larger voltage differentials, and thus the 300pf C_c is the largest 'robust' option.

	V_{1G}(pf)	V_{1I}(pf)	V_{1O}(pf)	V_{2G}(pf)	V_{2I}(pf)	V_{2O}(pf)	$V_{chassis}$ (pf)
Q_{1G}	?	-87.7	-20.6	?	-3.2	-1.0	?
Q_{1I}	-87.7	100.0	-2.0	-3.2	-1.2	-0.3	-6.2
Q_{1O}	-20.6	-2.0	28.4	-1.0	-0.3	-0.2	-4.4
Q_{2G}	?	-3.2	-1.0	?	-87.7	-20.6	?
Q_{2I}	-3.2	-1.2	-0.3	-87.7	100	-2.0	-6.2
Q_{2O}	-1.0	-0.3	-0.2	-20.6	-2.0	28.4	-4.4
$Q_{chassis}$	?	-6.2	-4.4	?	-6.2	-4.4	?

Table 7.1: Estimated Electrode Capacitance Matrix for the iZIP4 detector. Matrix elements between 2 elements kept at 0V bias in standard running mode were not estimated.

7.1.2 Charge OF Calibration

The OF best fit amplitudes were calibrated using the 356keV line from a ^{133}Ba source as is standard in CDMS (the 356keV line is near ideal for an external source since it's roughly the lowest energy γ which can punch through the various thermal shielding layers and still produce a decent peak). In Fig. 7.7, the resultant after calibration scatter plots of qi2OF vs qo2OF are shown for both voltage bias polarities. Of immediate interest is that for h^+ collection (-2V bias on the charge collection electrode for the side being biased) higher density structure along the 356keV diagonal is readily apparent which physically corresponds to events in which the full energy of the 356keV γ is collected and all of the charge excitations are shared between the inner and outer electrodes.

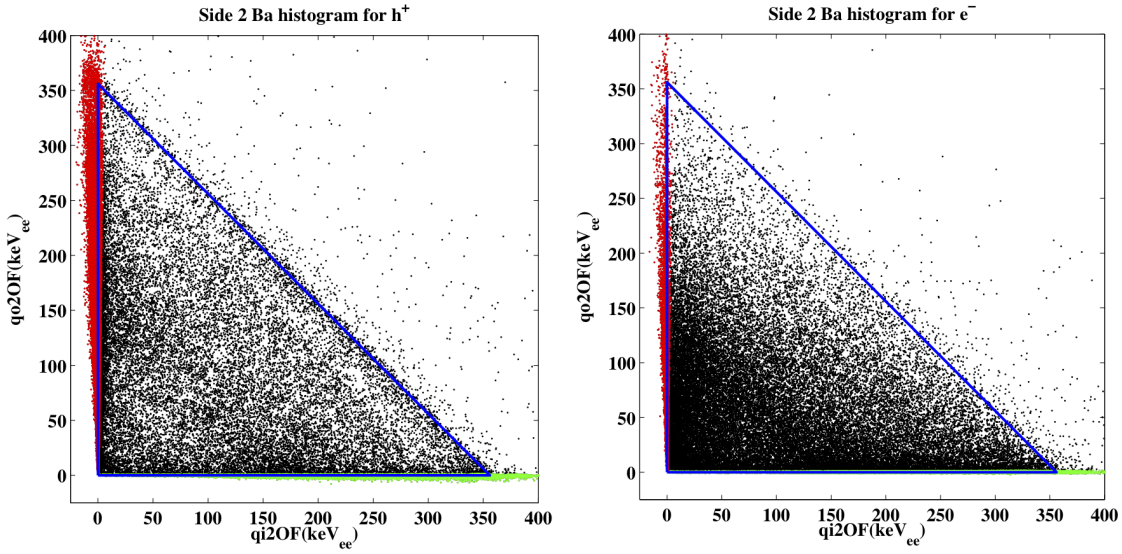

Figure 7.7: h^+ (left) and e^- (right) collection optimal filter estimators for side 1 inner and outer electrodes for symmetric events from a ^{356}Ba

By contrast, for e^- collection, the structure is much less visible. This same effect can be seen by cutting on events which are approximately fully collected in only a single electrode using the cuts cQin2tight_g48 (green) and cQout2_g48 (red) and then histogramming the results as seen in Fig. 7.8. The h^+ collection electrodes (solid) display a quite prominent 356keV line while any peak for e^- collection electrode is marginal to non-existent. Now, I've only shown this data for side 2 of G48 for UCB test facility data, but every viable Ge detector yet tested as UCB shows qualitatively similar behavior; e^- peaks are always less sharp than hole peaks. Due to these features, we chose to calibrate the charge signals using only h^+ collection data: side 1 charge signals were calibrated with Ba data taken with -2V bias on side 1 and +2V bias on side 2, while side 2 charge signals were calibrated with the opposite polarity.

These histograms also show that even for h^+ collection, the peak on the outer electrode (red solid) is significantly suppressed and broadened. This suggests that the detector volume for which the outer electrode fully collects all charge is quite small. Roughly, the event is either too close to the outer cylindrical face and the carriers get stuck on

the side wall (bad!), or the event occurs at a lower radius where a percentage of the carriers are collected on the inner electrode. The later certainly isn't a big deal from a larger detector performance issue (we are after all fully collecting all the carriers), but it does make calibration a bit difficult. We can't simply fit the q-outer peak to a gaussian. Instead, we should really χ^2 optimize for the outer electrode calibration coefficient by using the shared event 356keV sample.

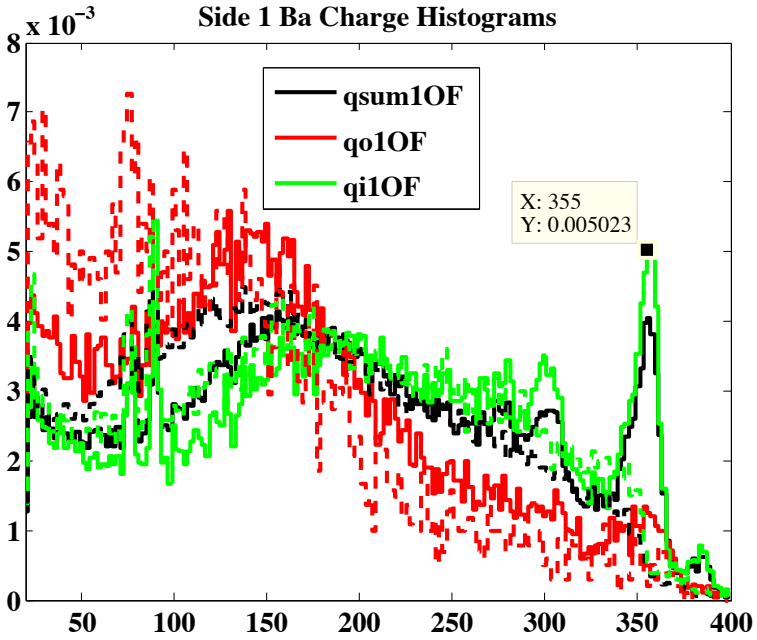

Figure 7.8: iZIP4 side 1 surface design colored to indicate the inner/outer electrode collection areas

7.1.3 Qualitative Carrier Transport Features

The e^- broadening is also quite visible in scatter plots of the total charge collected on side 1(qsum1OF) vs. total charge collected on side 2 (qsum2OF) as seen in Fig. 7.9, and in this plot it's more nefarious implications are quite clear: our ability to distinguish bulk events in which the excited carriers drift across the detector giving us symmetric charge signals on the two surfaces from assymetric surface events in

which carrier transport occurs only between the phonon and charge rails on a single surface is degraded.

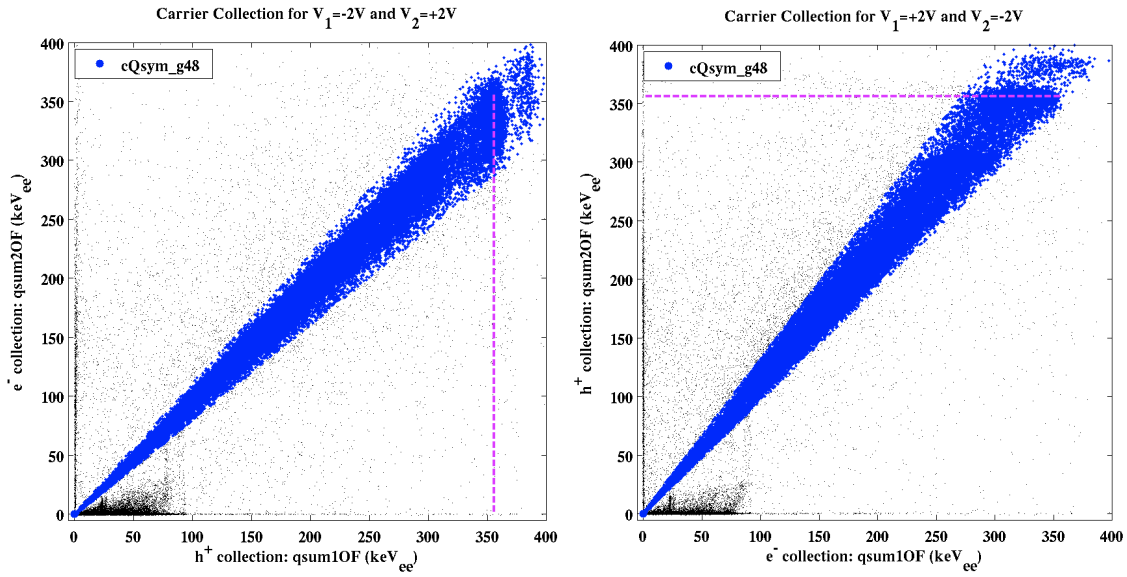

Figure 7.9: side1 vs. side 2 carrier collection for a ^{356}Ba Source. Blue events pass the charge symmetry cut, cQsym_g48

The physical mechanism underlying these features is almost certainly e^- trapping in the bulk of the crystal since the length over which e^- drift and consequently the bulk trapping probability varies as a function of position [106]. For events which interact near the -2V surface, almost all carrier transport is through e^- and thus the probability for trapping will be on the high side. By contrast, for events near the +2V surface, h^+ drifting is dominate and thus the e^- trapping probability would be low. We can even go a step further, and estimate that an e^- trapping length of 25cm would approximately match the trapping experimentally seen.

The most compelling evidence for this theory comes from the location of the 88keV γ line from the ^{109}Cd internal source which shined onto side 1 for all of the UCB test facility runs. Due to it's low energy, the interaction length in Ge is only $\sim$ 2.6mm, and thus all of the 88keV events are localized very near the side 1 surface (by contrast the 356keV events are much more evenly distributed). By flipping the bias polarity, we can thus alternate between e^- and h^+ carrier transport and we see in Fig. 7.10

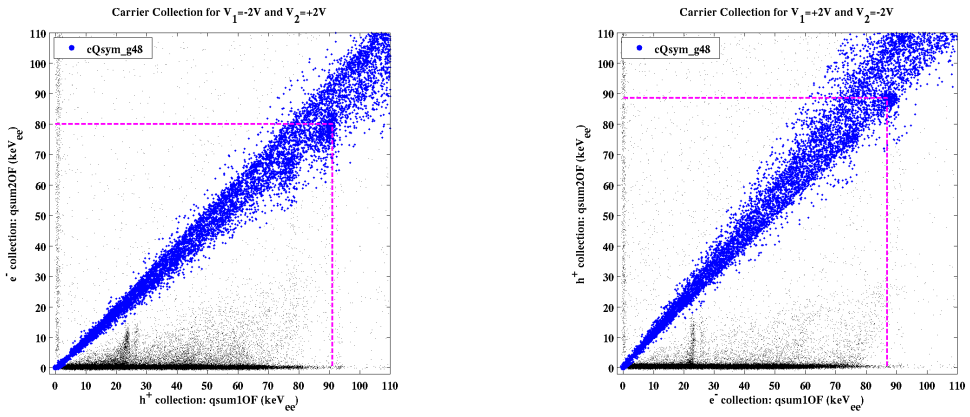

Figure 7.10: side1 vs. side 2 carrier collection highlighting the ^{109}Cd 88keV line

that e^- drifting decreases the total charge collection on the side 2 electrode by ∼10% over h^+ drift. We can generalize the 88keV line evidence to all of the medium energy Ba data (100keV< E_r <160keV) by looking for a correlation between the fractional charge collection difference between the 2 sides, called internally 'z charge partition' or qzpartOF (defined in Tab. 7.2), and our best z phonon estimator which is seen quite strongly in Fig. 7.11.

Due to bulk e^- trapping and, even more importantly, the fact that surface events have collection on only one instrumented electrode, our best estimator for the total number of charge excitations produced during an interaction is the maximum of qsum1OF and qsum2OF, qsummaxOF. The largest negative consequence of this choice, is its systematic bias towards positive values which from previous discussions we know limits our electron recoil/ nuclear recoil rejection capability. Thus for low mass WIMP searches in the future, it may make sense to revert back to the naive mean(qsum1OF, qsum2OF) near threshold if phonon only fiducial volume leakage can be easily held below ∼ 1/100.

e^- and h^+ transport differ qualitatively in others ways as well. Electrodes which collect e^- tend to have more charge sharing between the outer and inner electrodes than those who collect holes as shown in Fig. 7.12 using the radial metrics for the two faces, qrpart1OF and qrpart2OF (Tab. 7.2) [107]. Of great importance to this

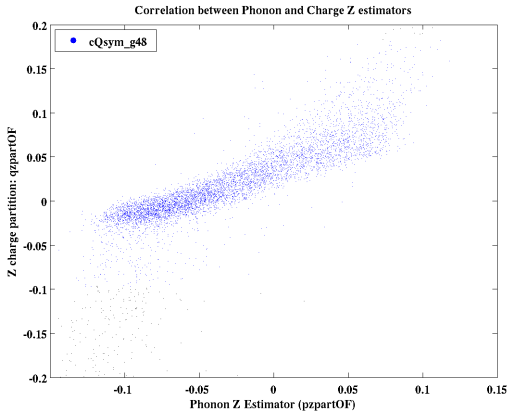

Figure 7.11: Correlation in the bulk region of z phonon metrics and qzpart illustrating that e^- trapping varies as a function of z

conclusion, is that this effect is seen for both polarities and thus this can't simply be z dependence in the source interaction location. Blas was the first to recognize that this increased lateral diffusive transport for e^- is a natural consequence of anisotropic propagation in the e^- [90].

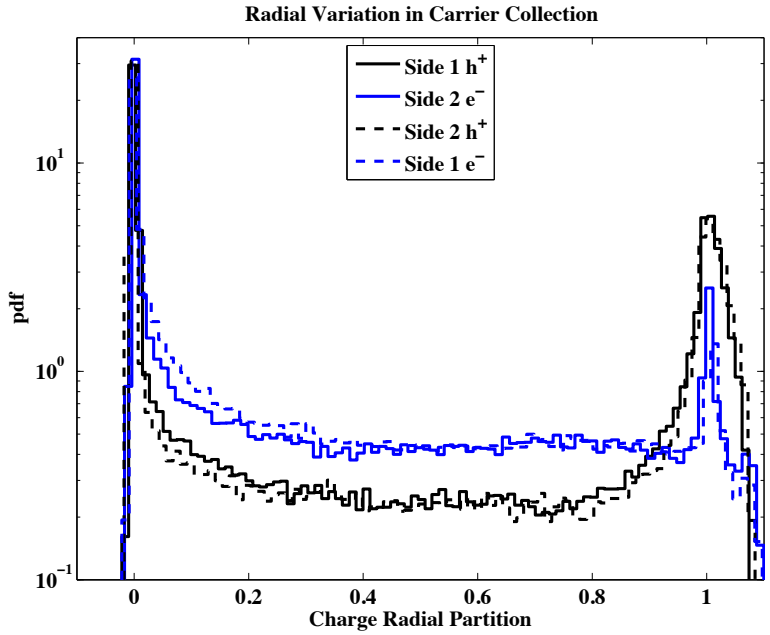

Figure 7.12: Charge Radial Partitions separated by carrier polarity (h^+: black / e^-: blue) and side (1: solid / 2: dashed)

As a quick aside, the events shown in Fig. 7.12 pass all quality cuts (discussed in detail later) and a charge amplitude cut of 30keV< Q <400keV. On the high side, the energy cut edge was chosen so as to remove events corresponding to muon showers which could have large multiplicities. There are such a small number of these events though, that removal of this cut won't qualitatively change the histogram. By contrast, the charge threshold cut is very important. qrpart1OF ($\frac{qo1OF-qi1OF}{qsum1OF}$) and more generally all partition estimators have distributions whose width increases rapidly as the signal to noise of the component estimators decreases. Thus, if one wants to study energy independent behavior, energy threshold cuts are required to make certain that stochastic noise is well below signal scales. With this in mind, 30keV seems pretty natural; it sets the stochastic noise at $\sim 1\%$.

7.2 Phonon Estimators

In the previous chapter, we discussed in great depth the physical mechanisms which lead to position dependence in both the amplitudes and pulse shape for our phonon signals (Fig. 7.13). We even introduced the long term dream of using the detector monte carlo to optimally calculate the time, position, energy and recoil type (electronic/nuclear), for each and every event. To quantify this dream just a bit more concretely, please note that conditional on the event being a single scatter, there are 5 continuous DOF and one binary recoil type parameter. Allowance for both single and double internal scatters substantially increases the number of continuous DOF to 9 and binary parameters to 2, electron recoil/nuclear recoil and multiple/single scatter discrimination). The point of being so explicit in counting the true degrees of freedom, is so that we can gain intuition into how far our current analysis techniques are from ideal. If we introduce intermediate estimators based upon pulse fits that aren't eventually used to generate these final estimators, then we have just degraded our resolution.

qi1OF qo1OF qi2OF qo2OF		OF charge amplitude estimates with temporal shifting
qi1OF0 qo1OF0 qi2OF0 qo2OF0		OF charge amplitude in which all temporal shifting is fixed
qzdelOF	QS1OFdelay- QS2OFdelay	Difference in best fit charge OF time shifts for the two sides which is our best direct estimator for event z from charge drift time (μs). **Should be changed in R133**
qsum1OF qsum2OF	qi1OF+qo1OF qi2OF+qo2OF	Side Summed OF Estimators (keV$_{ee}$)
qsummaxOF	max(qsum1OF,qsum2OF)	Our best estimate of the total number of e^-/h^+ pairs produced in an interaction estimated by Optimum Filter (keV$_{ee}$)
qzstartOF	qsum1OF > qsum2OF: QS1OFdelay qsum2OF > qsum2OF: QS2OFdelay	Charge OF best fit start time with respect to trigger(μs) **Should be changed in R133**
qzpartOF	$\frac{\text{qsum1OF}-\text{qsum2OF}}{\text{qsum1OF}+\text{qsum2OF}}$	Fractional difference in carrier collection for side1 and side 2 using OF estimators
qrpart1OF qrpart2OF	qo1OF/ qsum1OF qo2OF/ qsum2OF	Side specific fractional difference in carrier collection between inner and outer electrodes using OF estimators
plukeqOF	(| qsum1OF |+| qsum2OF |) $\|V_{q\,bias}\|/\epsilon$ -|qsum1OF-qsum2OF|V_p/ϵ	best estimate of luke phonon production from charge measurement
pgqOF	qsummaxOF + plukeqOF	best estimate of total phonon production solely from charge measurements

Table 7.2: Calibrated Charge Estimators (RRQs)

7.2.1 Standard Optimum Filter Quantities

Due to our great comfort with Optimum Filters from our work with charge pulses, our first inclination as a collaboration is to always toss each individual phonon trace through an OF-1D, after which we end up with 8 channel amplitudes, [pa1OF, pb1OF, pc1OF, pd1OF, pa2OF, pb2OF, pc2OF, pd2OF], plus 8 independent OF best fit time shift estimates (which currently aren't used). Due to the huge pulse shape dependence

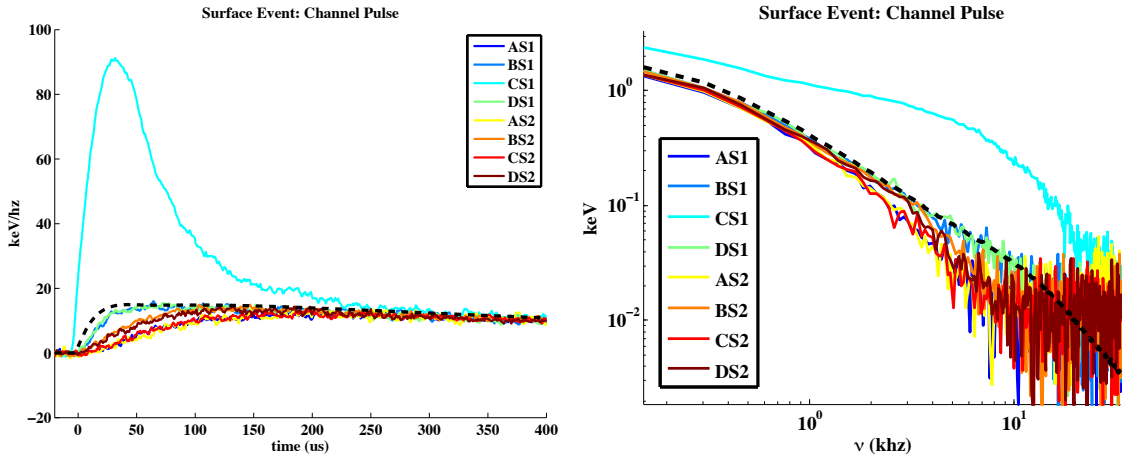

Figure 7.13: Representative phonon trace as a function of time (left) and frequency (right)

though, no single fixed pulse shape template will even remotely fit all channels and thus we are left with the slightly unpalatable requirement of choosing a template which is 'least bad'. For G48 iZIP analysis, we've chosen to use the mean direct trace sum of all channels which is shown in dashed black in Fig. 7.13. Being that this is the mean over all channel traces, this is the obvious compromise candidate (albeit perhaps not the ideal one).

The lack of high frequency signal in non-primary channels compared to the total trace templates, means that the high frequencies push down the best fit amplitude relative to the true DC value while for primary channel events the opposite is true. For the assymetric surface event shown, the difference in the integrated phonon energy absorbed in the CS1 and CS2 channels is only 70% where the difference in best fit OF-1D amplitude values for the two channels is much larger, 220%. On the downside, this sensitivity suggests that the sum of all OF-1D best fit amplitudes, psumOF, will not be the perfect estimator for the total amount of phonon energy collected in the TES. On the upside, this accentuated position dependence means that we can define 7 independent fractional/ partition estimators between the channels, [pxpart1OF, pypart1OF, pxpart2OF, pypart2OF, prpart1OF, prpart2OF, pzpartOF] (Tab. 7.3), which should be pretty good position estimators.

p[j][k]OF		OF-1D best fit amplitude quantities for each channel with time shifting
p[j][k]OF0		No time shifting best fit OF-1D parameters for use in resolution estimates
psumOF	$\sum_{jk}$ p[j][k]OF	Total phonon estimator for OF-1D quantities
psum[k]OF	$\sum_{j}$ p[j][k]OF	OF-1D estimator for the total phonon energy collected on side [k]
pxpart[k]OF	$\frac{\sum_{\mathrm{j}} \mathrm{p[j][k]OF} \tilde{\mathrm{r}_{\mathrm{jk}}} \cdot \hat{\mathrm{x}}}{\mathrm{psum[k]OF}}$	OF-1D estimator of the event location in the x dimension from side [k]
pypart[k]OF	$\frac{\sum_{\mathrm{j}} \mathrm{p[j][k]OF} \tilde{\mathrm{r}_{\mathrm{jk}}} \cdot \hat{\mathrm{y}}}{\mathrm{psum[k]OF}}$	OF-1D estimator of the event location in the y dimension from side [k]
pxpartOF	$\frac{\sum_{\mathrm{jk}} \mathrm{p[j][k]OF} \tilde{\mathrm{r}_{\mathrm{jk}}} \cdot \hat{\mathrm{x}}}{\mathrm{psum[k]OF}}$	OF-1D estimator of the event location in the x dimension using inner channels from both sides
pypartOF	$\frac{\sum_{\mathrm{jk}} \mathrm{p[j][k]OF} \tilde{\mathrm{r}_{\mathrm{jk}}} \cdot \hat{\mathrm{x}}}{\mathrm{psum[k]OF}}$	OF-1D estimator of the event location in the y dimension using inner channels from both sides
prxypart[k]OF	$\sqrt{\mathrm{prxpart[k]OF}^2 + \mathrm{prypart[k]OF}^2}$	OF-1D radial estimate from inner 3 channels of side [k] channels only
phiOF	$\tan^{-1}$(prxpartOF, prypartOF)	azimuthal estimator form all inner channels
prxypartOF	$\sqrt{\mathrm{prxpartOF}^2 + \mathrm{prypartOF}^2}$	OF-1D radial estimate from the inner 6 channels
pzsumpartOF	$\frac{psum1OF - psum2OF}{psum1OF + psum2OF}$	OF-1D estimator of the z location of event from channel traces
prpart[k]OF	$\frac{pa[k]OF}{psum[k]OF}$	radial event location using the OF-1D estimators of the outer circular channel (A) for a single side
prpartOF	$\frac{pa1OF + pa2OF}{psumOF}$	radial event location combining information from both sides
ps[k]OF		OF-1D best fit amplitude on face summed trace.
pzpartOF	$\frac{ps1OF - ps2OF}{ps1OF + ps2OF}$	OF-1D estimator of the z location of event from face summed estimators
ptOF		OF-1D estimator of the total phonon energy from the total summed pulse

Table 7.3: Calibrated Phonon Estimators (RRQs). In the definitions, the channel index,j, runs over a,b,c, and d while the side index, k, runs over 1 and 2

The scatter plots for the [x,y] OF position estimators shown in Fig. 7.14 left strongly display a triangular shape even though the detector itself has circular symmetry which suggests a nonsimplistic mapping between the true event coordinates and those of

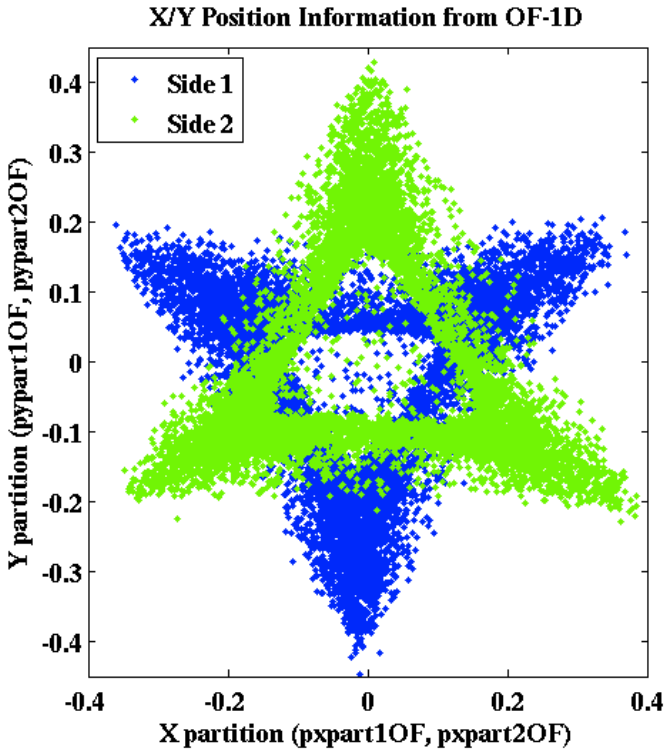

Figure 7.14: OF-1D [x,y] event location estimators. Right: detector geometry colored by phonon channel.

the OF partitions. This deformation is a natural consequence of sub-pixel position interpolation [108]. To limit the number of sensor channels to 8, we are forced to read out QETs massively in parallel (485 per channel) and as a consequence we lose sub channel position information. To see this most clearly, let's imagine an event which only dissipates power into QETs within the white circle labeled 2 in Fig. 7.15 left. For this event, the only channel which receives any energy is B, and thus our best estimator of the excitation energy is the vector to the center of B, $\vec{r_B}$. Event 1, on the other hand fortuitously ended up evenly straddling channels B and D, and thus, following the position estimator definitions in Tab. 7.3, our position estimate for event 1 is

$$\vec{r_1} = \frac{\frac{E_1}{2}\vec{r_B} + \frac{E_1}{2}\vec{r_D}}{E_1} = \frac{|r_B|}{2}\hat{y}$$

So, even though event 1 actually occurs at a higher radius than event 2, on the partition manifold it's mapped to a location with much smaller radius. If one continues this thought experiment by adding more events with different fractions of sharing, then one ends up with a triangular map which is highly degenerate at the vertices (all events which are fully collected by a single channel have no subpixel position information). This last fact suggests that even with perfect reconstruction, the position sensitivity of CDMS detector will vary as a function of position. Events which occur near a boundary will have significantly greater position sensitivity than events that occur far from a phonon boundary [45]. It's for this qualitative reason, that we rotated the channel geometries by 60^o between the two faces as shown in Fig. 7.15 right; we simply get better azimuthal sensitivity.

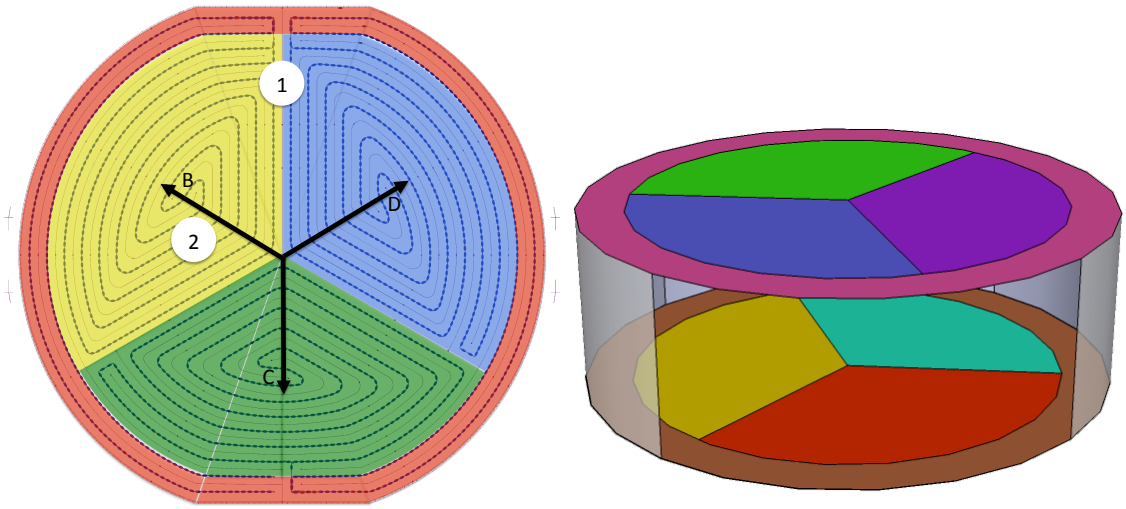

Figure 7.15: Left: detector geometry colored by phonon channel for side 1. Right: 3-D phonon channel diagram

A second deformation of the partition manifold that was a significant problem for CDMS II [3] and still exists today is the concept of radial foldback of the partition manifold seen in fig. 7.16. At low radius, as an event location moves differentially to higher radius along the $\hat{b}$ direction, more energy will be absorbed in B, and less phonon energy will be absorbed in the C and D channels. Consequently, prxypartOF will increase. For events that occur near the inner/outer phonon channel boundary (i.e. higher radius), a differential movement to higher radius results in a smaller prxypart,

since the A channel will receive a larger percentage of the position dependent signal. The non-monotonic mapping between prxypart and true r, means that additional parameters are needed to split this degeneracy and come up with a reasonable estimate of true r.

Prpart1OF and Prpart2OF, which are phonon partition estimators that measure the ratio of energy absorbed in inner(BCD) and outer phonon channels (A), also display radial foldback but to a much smaller extent (7.16). Here, the physical mechanism is some combination of phonon interactions with the side wall and the fact that for fabrication reasons the outer 2mm of the crystal face are not instrumented and thus in this region there is greater likelihood that a phonon will become ballistic and be equally likely to be absorbed by all channels. Of the greatest import is that prxypartOF and prpartOF have estimator maximums at different radial locations and thus the combination of the two estimators allows for non-degenerate true r estimate as shown in the Fig. 7.16. This plot also shows that the intrinsic width of the 8 dimensional partition manifold is largely caused by z dependence since surface events selected by cQsurf_g48 (blue) are clearly separable from bulk events selected by cQsym_g48 (green). The fact that the surface/bulk event discrimination is so good along manifold dimensions that were constructed to be nominally z independent is quite exciting! It means that there is a lot of information for fiducial volume information in lots of different variables

The final partition quantity, which deserves special mention, is the fractional difference in energy collection between the two sides of the detector, pzpartOF (Figs. 7.3 and 7.12). As shown in Fig. 7.17, the total side estimators from which this estimator is created, psum1OF and psum2OF, show an amazing amount of position dependence. They can easily discriminate between bulk and surface events as selected by cQsym_g48 and cQsurf_g48. What's even more interesting is that this phonon surface/bulk discrimination seems better than our charge discrimination ability since the blue and red distributions start to have substantial overlap below psum1OF = 6keV, where in this phonon plot the true distributions seem to be differentiable down to $\sim$ 3keV. Please note, that we are being a bit unfair towards the charge sensitivity

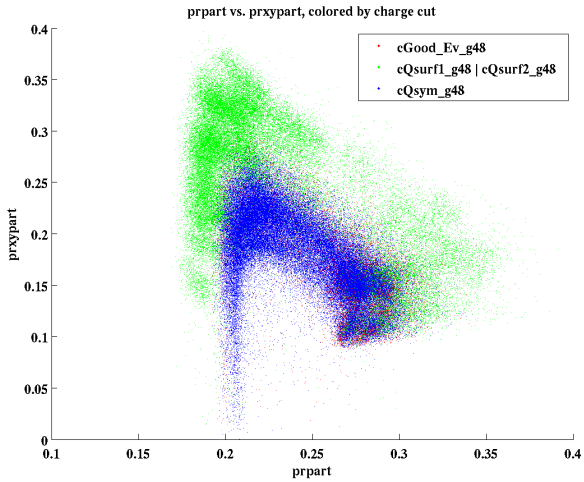

Figure 7.16: Scatter plots of prxypartOF versus prpartOF for a single azimuthal slice of data which show radial degeneracy splitting using both parameters (created by Scott Hertel) [25]

with the above statement, since we have already recognized 2 ways to improve the charge sensitivity near threshold that haven't been implemented in these plots (time constraining the two sides together, decreasing the trigger window size). At the same time, these OF estimators also aren't optimized for the identical reasons. We allow complete time shifting freedom between the 8 channels even though this isn't the case. Furthermore, from earlier chapters we recognize that we can lower the T_c's of the TES in future sensors and drastically increase the sensitivity of the device. Just using the T_c^3 resolution law we developed, a iZIP5 device with T_c around 45mK would have have surface to bulk discrimination down to ~0.4keV with this exact analysis and with the current noisy UCB test facility setup.

One final note: the precise definition used for these 7 independent partition estimators is by no means unique. One could easily define other estimators that, with psumOF, also completely span the 8D OF-1D amplitude space and thus in principle contain identical information. For example, center of energy estimates which combine information from both sides like pxpartOF and pypartOF, naturally have less z dependence. Likewise, position estimators metrics which linearly combine inner and

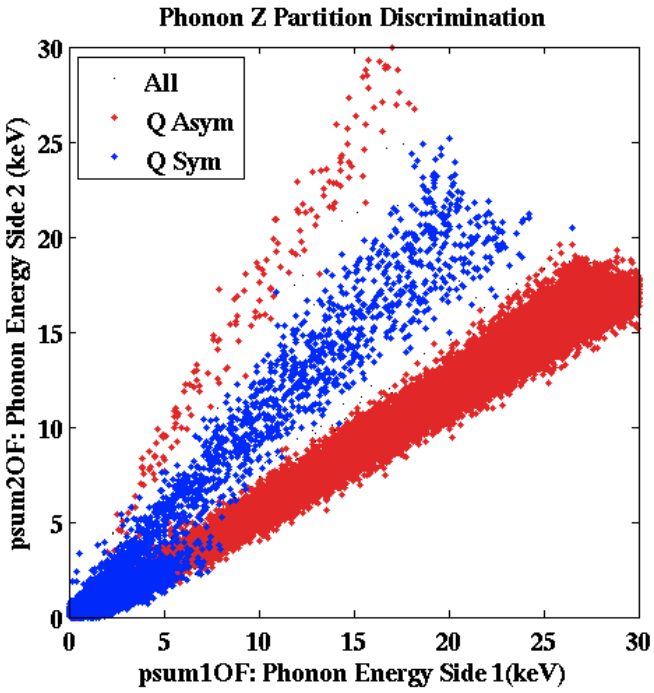

Figure 7.17: Scatter plots of psum1OF vs. psum2OF showing discrimination between asymmetric surface events (red) and symmetric bulk events (blue)

outer channel information together can better remove the radial degeneracies. The real benefit in going down this research path in the future is that a subspace of estimators (say 4D rather than 8D) could contain all the information and yet be easier to handle statistically: the difficulty of characterizing non-gaussian outlier tails goes up with the number of dimensions.

We've now shown that a simple OF-1D analysis of our phonon quantities retains lots of position and energy information, even if it may not be the most ideal analysis. We should now highlight the large systematic uncertainties that this algorithm also give us. Above, we discussed how the vast intrinsic pulse shape variation means that the low frequency and high frequency signals are always in direct competition with each other for choosing the best fit amplitude. This competition is refereed within the OF by the noise PSD and thus changes in noise will significantly effect the value of the partition parameters. An almost perfect example of this effect can be found in

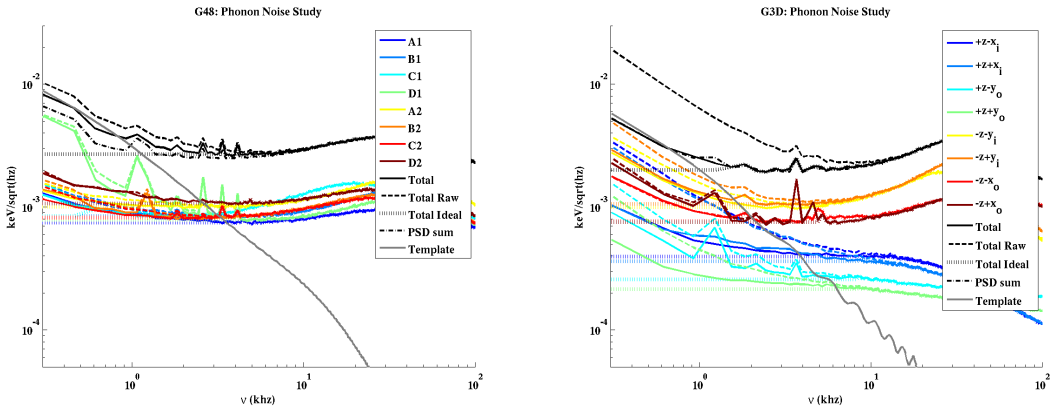

Figure 7.18: Noise power spectrums for G3D (iZIP2 series) and G48 (iZIP4 series) at UCB referenced to keV/$\sqrt{hz}$

G48 test facility data [26] shown in Fig. 7.18, where channel D1(lime green) had an enormous amount of environmental noise at low frequencies. If the true experimental PSD for D1 is used, then low frequencies will have suppressed weighting and thus the detector will seem to have greater position dependence (the triangle gets skewed!) as seen in Fig. 7.19. By contrast, if the OF-1D estimators use a noise spectrum from B1 for the D1 calculations, the position dependence returns to being symmetric.

If noise is constant throughout the run, then this abnormal position dependence can be easily removed through calibration. The real problem comes when the noise has temporal dependence. In this case the change in noise couples to a change in the phonon gain which is difficult to account for and thus one picks up a systematic jitter in all OF metrics. It's uncertain, if this systematic was limiting in CDMS II analysis since it would look for all intents and purposes like a long tail outlier. The only ways to remove these problems is very strict cut on noise uniformity between series. We expect this to be a significant problem for the Soudan R133 analysis due to significant temporal dependence of the environmental noise as a function of time.

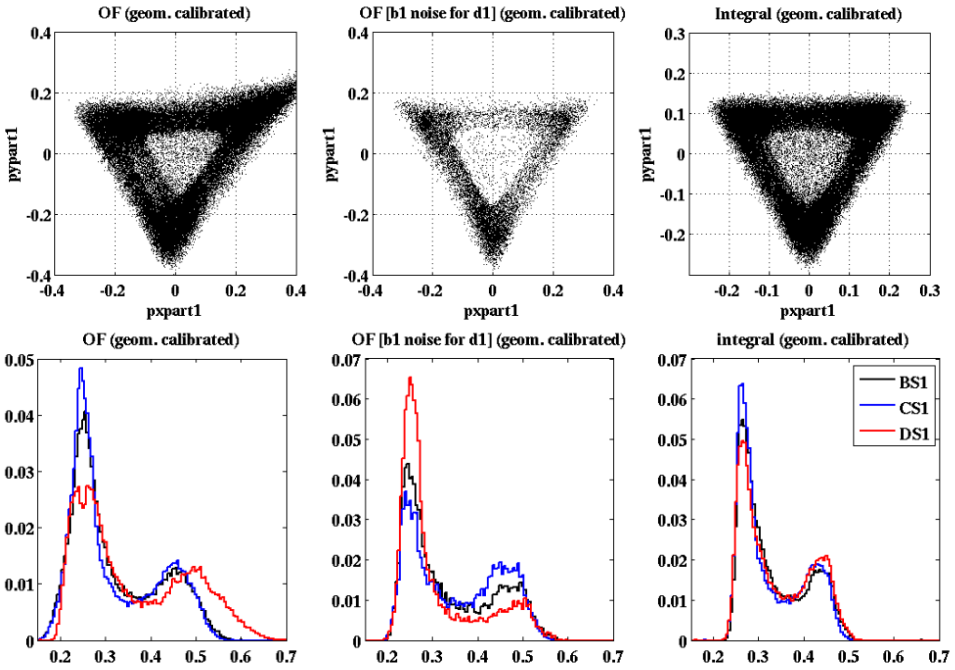

Figure 7.19: Top: [X,Y] Partition plots for pd1OF calculated with the true abnormally large experimental noise (top left), with B1's noise spectrum (top center), and with pure integrals. Bottom: pd1OF/psumOF for the same 3 estimators (produced by Scott Hertel [26])

7.2.2 Resolution and Irreducible surface facility issues

Since we've introduced the experimental noise power spectrums at UCB, it only makes to look at them critically in other ways. Unlike FETs, HEMTs and most other semiconductor sensing techniques, both TES and Squids are known to have almost negligible amounts of 1/f noise. A perfect example of this impressive low frequency performance can be seen in the noise PSDs for the TES based CMB experiment Spider (Fig. 7.20 [27]),which is dear to many of my collaborators. The 1/f noise finally peaks above the TFN plateau at 1/10hz!

For the UCB test facility this clearly isn't the case! Low frequency noise begins to dominate in both the G3D and G48 noise spectrums around ∼1khz! This is quite depressing. First and foremost, this means that the OF resolution estimates made

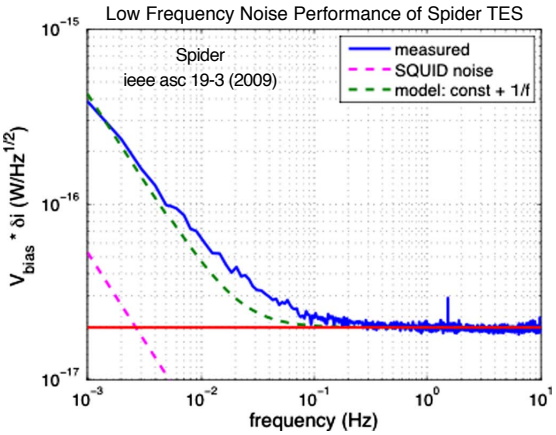

Figure 7.20: Characteristic noise PSDs for the SPIDER experiment [27]

in chapter 1 are overly optimistic (with a phonon absorption bandwidth,ν_{pulse}, of ∼210hz, the majority of our total phonon signal is below this low frequency noise turn on). This statement is made explicit in the second line of Tab. 7.4 for G48 where the best measured resolution is 65eV on C1. Behaving as if all channels had C1's resolution and their was no noise correlations between channels, the the total noise on psumOF would be $\sqrt{8}$ 65eV or 180eV, definitely a far cry from the best noise performance seen on the Si CDMS II T2Z2 of 62eV [109].

There are definitely some abnormalities in these raw noise power spectrums which are quite suggestive. First, the low frequency noise seems to be phase coherent across all channels (the noise on the direct sum trace is much larger than the quadrature sum). Secondly, the estimated OF-1D resolutions are very different from the measured OF-1D resolutions. This suggests that the noise also has phase correlations across frequencies as well. In the hopes of understanding this noise in greater depth, we started to look at long time scale traces in the time domain, and the results seen in Fig. 7.21 are quite telling.

When DC electronically coupled, all events seem to display a second pulse shape with ∼200ms time constant which we assume to be the thermal signal [110]. Now this signal is many orders of magnitude smaller than the athermal signal and thus for most events it's hidden well within the noise. At the surface though, μ's directly

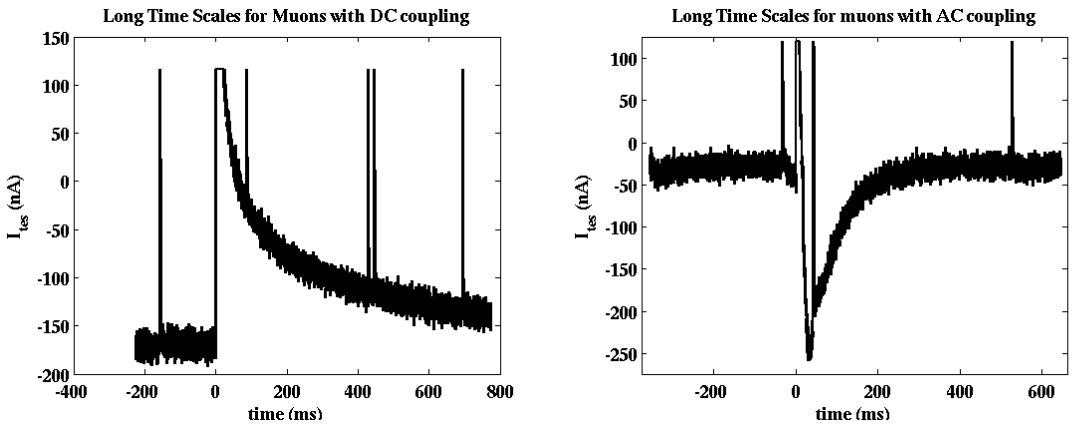

Figure 7.21: Long time scale phonon traces showing a ∼200ms thermal muon tail when electronics are DC coupled (left), and a huge amount of overshoot after a muon event when the electronics are AC coupled(right).

interact with our detectors at ~ 0.5hz and they leave ∼18MeV of phonon energy in our detector which is large enough that the thermal tail is much larger than all other noise sources at low frequencies. When AC coupled (our usual operating condition), the mechanism is different but the result is quite similar(Fig. 7.21 right): our quite poorly designed auto-zero circuit (not enough damping) substantially overshoots whenever a μ hits the detector leading to a long negative muon tail that dominates all noise sources at low frequencies.

Since this is only a surface test facility issue (the μ rate is suppressed by many orders of magnitude underground at both Soudan and SNOLAB), our original inclination was to just let it slide and recognize that detector performance will be drastically improved by running underground at Soudan/SNOLAB. Recently though, a subset of the CDMS collaboration has been considering running highly sensitive athermal phonon detectors at nuclear reactors near the surface to look for evidence of sterile ν and non-standard ν interactions through coherent ν scattering, where the μ pileup problem becomes a critical issue affecting performance. With this in mind, we'll need to develop algorithms that can subtract off this long exponential signal and that hopefully don't significantly increase the necessary processing time (i.e. continue to use FFT's for time shifting minimization). This was accomplished [111]. The

key point was to recognize that the long exponential tail background signals don't require any time shifting DOF and thus there remains only a single nonlinear degree of freedom. An example trace with the background subtracting Optimum Filter (OF-mBnS) can be seen in Fig. 7.22.

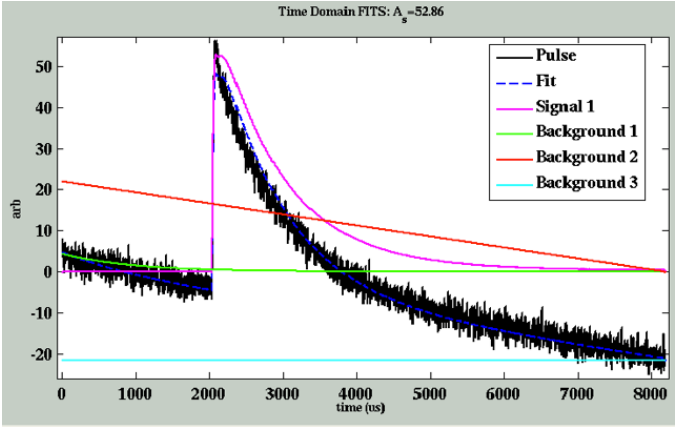

Figure 7.22: Implementation of the background subtracting OF on G48 trace

Noise PSDs can now be remade from the random noise traces in which the OF-mBnS best fit μ exponential tail has been subtracted (solid lines in Fig. 7.18) and for G3D the low frequency noise magnitude was reduced by a $\sim$x2. G48 on the otherhand showed only a 20% decrease in the total low frequency noise. This somewhat makes sense. The Tc's on side 1 of G3D are somewhere in the range of 45-60mK which is much lower than our standard 80-110mK and thus our TES TFN noise and TES Johnson noise are suppressed significantly($\propto T_c^3$). Furthermore, since $\frac{\partial I}{\partial P} \sim -1/V_o$ and V_o scales as $T_c^{5/2}$, all low frequency downstream noise sources (squid, environmental noise) are also significantly suppressed when referenced to power. So for G48, the muon tail signal could be of secondary importance while for G3D side 1 it could completely dominate all other noise sources. With these background subtracted noise spectrums, we can now reestimate our best fit OF resolution for both G48 and G3D.

Interestingly, the measured improvement in resolution through background subtraction is only 15-30% for side 1 G3D (line 4 Tab. 7.5) rather than x2. Most likely this is due to the fact that even for the non-background subtracting case, phase coherence

of the μ tail means it's easily distinguishable from an athermal pulse. Note, that the difference in estimated resolution for the two OFs (lines 1 and 3) is much closer to expectation.

G48	A1	B1	C1	D1	A2	B2	C2	D2	Total
Estimated OF-1D σ_P (eV)	75	76	76	116	82	79	75	99	377
Measured OF-1D σ_P (eV)	66	67	65	100	77	70	69	92	293
Estimated OF-nSmB σ_P (eV)	59	61	70	102	74	65	59	91	264
Measured OF-nSmB σ_P (eV)	60	62	62	101	71	64	59	86	275
Idealized OF σ_P (eV)	33	37	40	35	45	36	37	47	120
Measured T_c (mK)	88	91	91	91	109	101	101	101	

Table 7.4: Estimated and measured baseline optimum filter resolutions for G48

G3D	-Xi1	+Xi1	-Yo1	+Yo1	-Yi	+Yi2	-Xo2	+Xi2	Total
Estimated OF-1D σ_P (eV)	70	68	40	30	112	129	65	80	394
Measured OF-1D σ_P (eV)	62	58	34	24	78	108	53	70	316
Estimated OF-nSmB σ_P (eV)	38	40	30	19	71	86	53	72	184
Measured OF-nSmB σ_P (eV)	43	45	31	20	66	85	52	69	196
Idealized OF σ_P (eV)	16	14	10	8	38	41	29	29	79
Measured T_c (mK)	40-70	40-70	40-70	40-70	105	105	105	105	

Table 7.5: Estimated and measured baseline optimum filter resolutions for G3D

The remaining low frequency noise after background subtraction is pretty problematic. If we could magically remove it (Fig. 7.18 dotted curves), our estimated OF resolution improves to 33-47eV per channel (line 5) for G48 or roughly 120eV in total. After accounting for the fact that G48 has such high T_cs, this doesn't seem that bad. G3D looks even better with the additional low frequency noise removed. The large central channels on side 1 have ∼15eV resolution, which means that we would expect nominally expect $\sqrt{5}$ 15eV or 33eV total energy resolution which would make this our most sensitive device ever. Of course, to rationalize this subtraction, we should really have some understanding of this noise source and how to remove it in the future. As of this moment, we can only say that preliminary studies at UCB suggest the noise is coming in down stream of the FEB (front-end board) and thus somewhat easily removeable. In fact, this problem may very well be solved with the new DCRC boards.

7.2.3 Trace Summed Phonon Quantities

One way to remove position dependence that Blas has always championed is the idea of direct trace summation. On length scales > 1mm, the Al coverage of the iZIP is quite homogenous which suggests that if we remove the artificially imposed channel differentiation through direct summation of the channel traces on a given side, then we should end up with a pulse, whose shape and magnitude depend only upon z and energy. Of course, this isn't entirely accurate. First, a T_c gradient across the crystal will mean that the sensor bandwidth will change as function of (x,y) and thus high frequency pulse shape information could have some residual dependence. Secondly, the outermost 2mm of the crystal have no Al coverage because of fabrication constraints (photolithography starts to have a huge number of defects in this region so we choose not to pattern QETs out there). Consequently, there will be some residual r dependence at high radius. As an aside, in the iZIP6 design, we have a higher density of QETs in the outermost rail to roughly compensate for this effect and also naturally increase our position sensitivity at high radius.

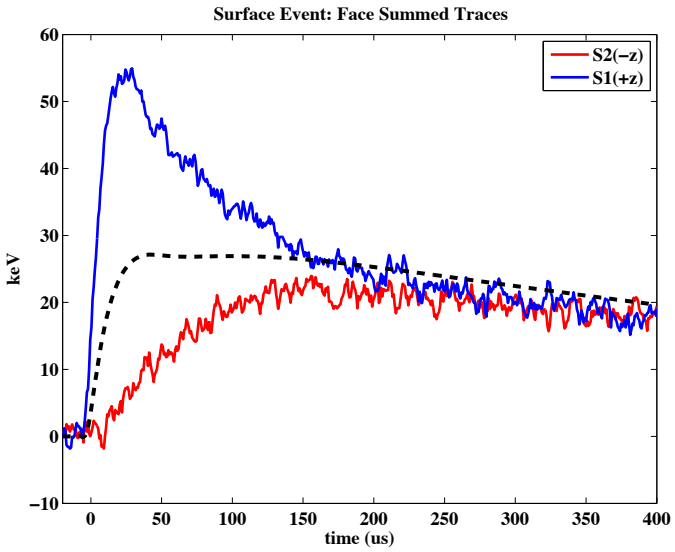

Figure 7.23: Characteristic face summed traces for an asymmetric charge surface event. OF-1D total template in dashed black

Example face summed traces for a characteristic asymmetric charge event can be seen

in Fig. 7.23. With the suppression of [x,y] position dependence the enormous amount of z dependence in our pulse shapes is now even more explicit and conceptually we can use the same non-ideal OF-1D algorithms used on the channel traces to distill this z only position information into 2 best fit amplitudes, ps1OF and ps2OF, and their z partition derivative, pzpartOF.

With all the advantages of naturally separating [x,y] dependence from z comes some disadvantages. First, the majority of the z position information is in the primary channel only, and consequently by summing the 4 channels on a single side together, we are, at minimum, decreasing our z sensitivity by x2. Even worse, if the noise frequency spectrum varies significantly between channels, as seen for example in the G48 test facility data where D1 has such poor low frequency performance (Fig. 7.18), then the OF-1D will choose different frequency weightings for the different channels. By directly summing the traces, we lose this optimization freedom, and thus our z sensitivity could be suppressed even further.

We can take this idea of channel summing to remove independence one step further and sum the two sides together. If one thinks of the z dependence of the pulse shapes as being taylor expanded in z, then this sum should remove all odd power z dependence leaving us with only the even powered remnants. The resultant total sum traces are found to be quite position independent. The maximum variation has been suppressed from almost 100% to roughly 20%. Furthermore, the time scale of over which variation occurs has been suppressed by x3 to just the first $\sim 80\mu$s after the interaction time (Fig. 7.24).

We can again apply the simple OF-1D algorithm, and with the suppressed position dependence we fully expect that this total phonon energy estimator, ptOF, should have significantly less position systematics than psumOF. Surprisingly, this isn't seen in Fig. 7.25 left. Looking into the total OF-1D estimators in more depth, we find that position sensitivity is quite sensitive to the noise spectrum used. Using the actual raw noise spectrum for G3D, we found that ptOF varied from the DC integral value by 15% (black Fig. 7.25 right). If instead we use a non-physical flat/white noise

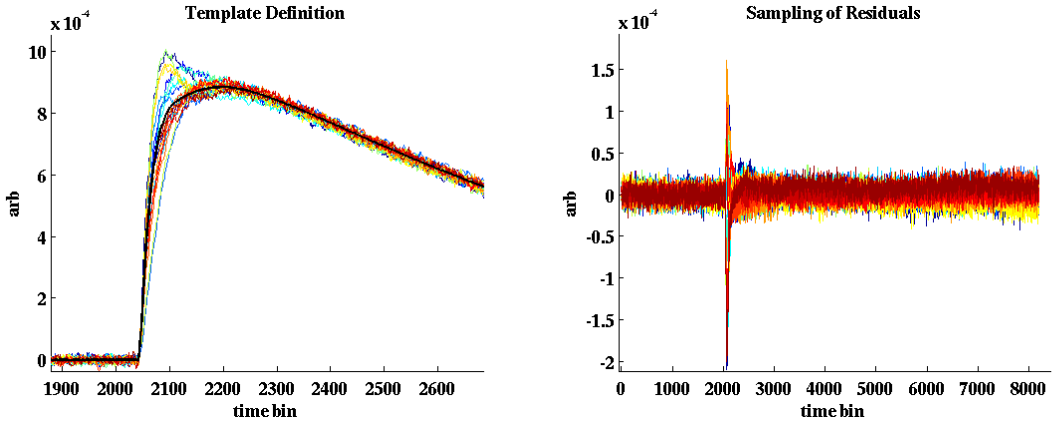

Figure 7.24: All channel trace sums for 10 pulses highlighting the residual position dependence (left). Residuals after best fit pulse subtraction (right).

spectrum we can decrease the position dependence by x3. This fact though, doesn't explain why psumOF isn't always worse than ptOF, no matter what noise spectrum is used. We can only hypothesize that the [x,y] position dependence naturally cancels out in psumOF even though there is no mathematical reason to expect this.

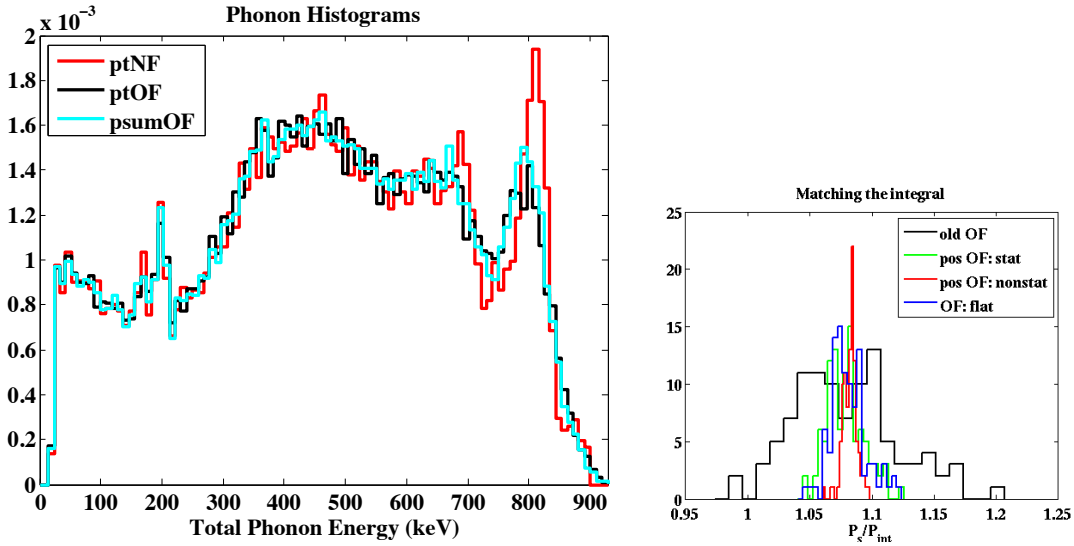

Figure 7.25: Right: Total Phonon Histograms for G48 with an external Ba source. Left: Histogram of the ratio of OF-1D to DC integral values for total phonon pulses for G3D using raw total noise spectrum (black), a non-physical flat/white noise spectrum (blue), and non-stationary Optimum Filter algorithm (red).

Non-Stationary Optimum Filters

To create simple position free total phonon estimators, we've played one more trick. Rather than think of the residual position dependence seen in the total trace sum as signal, we can think of it as non-stationary (phase correlated) noise which scales linearly with the total best fit pulse energy and which is time correlated with the best fit start time. These two ideas can be integrated into a least-squares optimizer for amplitude and time shift that is unfortunately quite computational intensive but shares some features of an OF, and thus we call it a non-stationary Optimum Filter [112] [113]. Results for this estimator (Fig. 7.25 left) are quite impressive. The FWHM on the 356keV line is 7% which is quite comparable to the FWHM of 4% on the hole charge histogram. Furthermore, position dependencies in the charge transport are transferred to the phonon system through both luke phonon and relaxation phonon production and thus the FWHM of 7% is the upper bound on the true phonon position systematic.

It's also interesting to think about why direct trace summing was never found to be useful in CDMSII analysis. First, it's clear that as a position independent total phonon estimator, a 1-sided trace sum still has a lot of z-dependence and thus a z position correction or implementation of a non-stationary Optimum Filter algorithm is needed. Unfortunately, use of the first means that one might as well just correct out [x,y] dependence at the same time one corrects out z and the second wasn't created until 2010. On the other hand, We should have been able to compose lots of z-only estimators that would be pretty great for fiducial volume definition. Unfortunately, this was never successful. My guess of the culprit is poor relative calibrations between channels. In the iZIP, the long 730μs homogenous phonon tail allows us to trivially and quite precisely, relatively calibrate the phonon channels with respect to each other by minimizing differences between channels at long time scales. Effectively, every single pulse contains information on the correct relative calibration. By contrast, in CDMS II, the larger Al coverage and smaller crystal thickness meant that the ballistic phonon collection time was of the same time scale as phonon quasi-diffusion, and thus all pulses displayed position dependence on all time scales: there simply wasn't

a position insensitive tail from which to create a relative calibration and thus we were forced to match edges on fractional phonon histograms from OF-1D quantities like those shown in Fig. 7.19 which we have already proven are incredibly sensitive to noise and a moments thought will also convince you that they are also sensitive to source position and TES sensor bandwidth.

7.2.4 Phonon Recoil and Yield Estimators

Estimating the true phonon recoil energy can get enormously messy, enormously quickly because all of the different phonon populations (recoil, luke, relaxation) can have slightly different energy collection efficiencies. Even worse, these collection efficiencies can vary with event location. If charge transport is dominated by h^+ the produced luke phonon frequency spectrum will be different than if e^- dominate the transport. Likewise, a symmetric bulk event will have relaxation phonons generated in the charge bias lines while an asymmetric surface event will have a portion of the relaxation phonons generated within a phonon sensor rail which will lead to higher phonon sensor collection efficiencies. In the long term having an understanding of these subtle variations would be nice but our standard practice as of this moment though is to make an empirical bulk electron recoil calibration and then through an assumption that all efficiency factors for all phonons are identical, we automatically generate a nuclear recoil energy scale, which can be tested and tweaked using an empirical neutron calibration (difficult but not impossible) [114].

So with this collection efficiency assumption firmly in place, let's first discuss how we account for the Luke-Neganov phonon production from drifting excitations in an idealized detector; a detector in which there is no trapping either on a surface or in the bulk of the crystal. Equivalently, all carriers end up on an electrode and relax to the Al fermi level. With this additional assumption (which we know to be simplistic in the extreme), we can calculate luke phonon production solely from the measured

charge signals on the FET instrumented bias electrodes:

$$\begin{aligned} P_{luke} &= \min(N_h, N_e)e|2V_{q\,bias}| + |N_h - N_e|e(|V_{q\,bias} - V_p|) \\ &= (N_h + N_e)e|V_{q\,bias}| - |N_h - N_e|eV_p \end{aligned} \tag{7.1}$$

where $\pm V_{q\,bias}$ is the voltage bias of the FET instrumented charge electrodes on the 2 faces and $\pm V_p$ is the voltage bias of the phonon lines on the two sides (we've largely run the phonon lines at ground even though this isn't required). Basically, what we've done here is split up our charge signal into a symmetric and asymmetric signal. The symmetric excitations travel between the voltage bias lines on the two sides and thus each carrier produces $e2|V_{q\,bias}|$ of luke phonon energy. An asymmetric recoil, by contrast, only travels between the phonon and bias line on the same side and consequently it produces only $e|V_{q\,bias} - V_p|$ of luke phonon energy. Luckily, this simplifies substantially in the second line of Eq. 7.1. Plugging in the electron recoil calibrated OF quantities, qsum1OF and qsum2OF, and dividing by the average electron recoil energy per e^-/h^+ pair,ϵ_{eh}, allows us to create the OF based luke phonon estimator, plukeqOF (Tab. 7.2). Recoil energy estimators (precoiltNF,precoiltOF,precoilsumOF) can now be created by simply subtracting plukeqOF from the total phonon estimators that we've already discussed (Tab. 7.6).

Now that we've created estimators for both the recoil energy as well for the amount of ionization created, the obvious next step is to ratio the two quantities to create an event by event measure ionization yield which can then be used to discriminate between nuclear and electron recoils:

$$ytNF = \frac{qsummaxOF}{precoiltNF} = \frac{qsummaxOF}{ptNF - plukeqOF} \tag{7.2}$$

To obtain a qualitative feel for the energy scale at which we lose yield based electron-recoil discrimination, let's taylor expand ytNF to first order

$$\delta_Y = \frac{\partial Y}{\partial Pt}\delta_{Pt} + \frac{\partial Y}{\partial Q}\delta_Q$$

and then let's make the further assumption that our phonon and charge noise in non-correlated and thus

$$\sigma_Y^2 = \frac{\partial Y}{\partial Pt}^2 \sigma_{Pt}^2 + \frac{\partial Y}{\partial Q}^2 \sigma_Q^2$$

(this later assumption is a bit sketchy since we are currently dominated by environmental noise in much of the signal region at both UCB and Soudan). Finally, just to keep the math absurdly simply let's restrict ourselves to regions of the detector with symmetric charge collection ($N_h \sim N_e$) and thus

$$\frac{\sigma_Y}{Y} = \frac{1}{E_r}\sqrt{\sigma_{Pt}^2 + \left(\frac{1}{Y} + \frac{2eV_b}{\epsilon_{eh}}\right)^2 \sigma_Q^2} \tag{7.3}$$

As expected for all ratio/ partition estimators, the inverse scaling with recoil energy is clearly manifest! Somewhat unexpectedly though, the scaling coefficients for the charge and phonon differ significantly due to the fact that the charge estimator is used for two purposes. First to measure the number of charge carriers produced (numerator) and secondly, to measure the amount of luke phonon energy which must be subtracted from the total phonon energy (denominator). Plugging in our standard Ge iZIP running condition of $V_b = \pm$ 2V, we find that our charge noise is scaled by 7/3 for electron recoils, and consequently the ionization yield performance is completely dominated by charge noise for G48 at UCB, even including all of the extra noise that we have painstakingly documented! Since we fully expect to have vast improvement in phonon performance in next generation devices, we fully expect that we will always be dominated by charge noise for our yield discriminators.

The linear dependence of the scaling ratio with V_b also indicates that we should run at the absolute lowest V_b for which we have adequate charge carrier transport. As an

aside, it's interesting that Edelweiss doesn't follow this guideline as strictly as we do. Clearly, they are willing to accept a higher discrimination threshold in exchange for more stable performance.

Though not shown, it's trivially obvious that the recoil estimators so far derived (precoilsumOF, precoiltOF, precoiltNF) all have their sensitivity degraded by both charge and phonon noise, and consequently we would also like to have phonon only recoil energy estimators, particularly in future generation detectors where we can expect an order of magnitude difference in the phonon and charge resolutions. A second reason why these estimators are so useful is that yield discrimination can be calculated in a charge - phonon only recoil energy plane where there is minimal correlation in the noise of the two quantities and where there is no deviation from gaussianity which occurs naturally for ratio quantities whenever the signal in the denominator is roughly the same size as it's resolution. This later advantage is practical only. It's simply easier to use gaussian discriminators. The underlying discrimination is invariant and will always scale with V_b no matter how we define it.

So, following in the footsteps of CDMS II [101], we'll define two recoil energy estimators which are conditional upon the recoil type. The idea is to write P_{luke} as function of recoil energy and a pre-measured ionization yield, $Y^{meas}_{ER/NR}(E_r)$, which depends upon both the recoil energy and the particle type and **assumes that the event occurred within the symmetric region of the detector and was fully collected:**

$$\begin{aligned} P_t &= E_r + P_{luke} \\ &= E_r + \frac{2|V_{q\,bias}|}{\epsilon_{eh}} Q \\ &= E_r\big(1 + \frac{2|V_{q\,bias}|}{\epsilon_{eh}} Y_{ER/NR}(E_r)\big) \end{aligned} \tag{7.4}$$

This later constraint is new for the iZIP, and thus a high quality phonon only fiducial volume is required so as to not have surface events which have systematically underestimated recoil energies. For electron recoils, the ionization yield is flat down to quite low energies (∼10eV) due to cascade physics [43] and thus

$$\mathrm{precoiltNFg} = \mathrm{PtNF}/\left(1 + \frac{2\mathrm{V_{q\,bias}}}{\epsilon_{\mathrm{eh}}}\right)$$

while the nuclear recoil ionization yield,Y_{NR}^{meas}, has been seen to roughly follow lindhard's ionization rule and thus

$$\mathrm{precoiltNFn} = \mathrm{PtNF}/\left(1 + \frac{2\mathrm{V_{q\,bias}}}{\epsilon_{\mathrm{eh}}}\mathrm{Y_{NR}^{meas}}(\mathrm{P_r})\right)$$

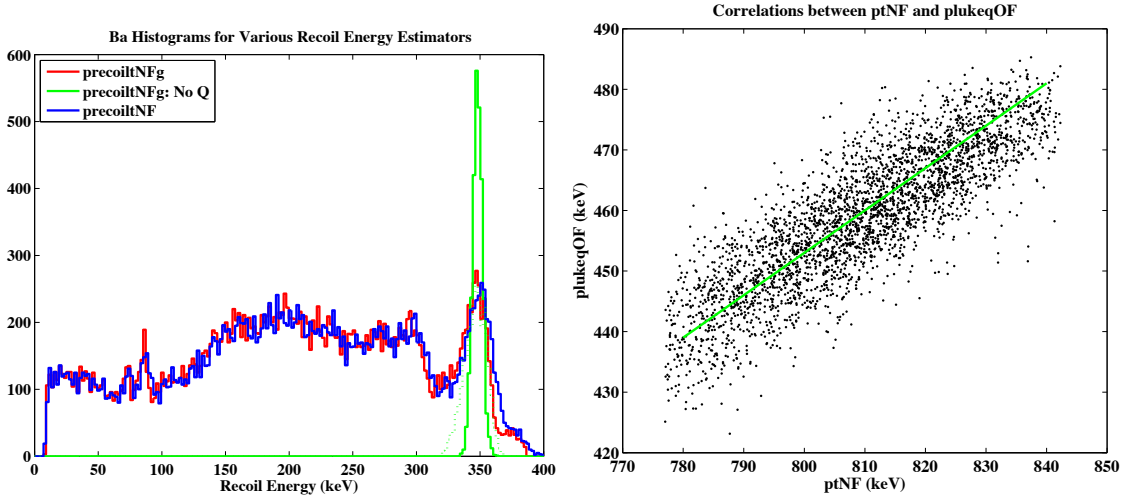

Figure 7.26: Right: Recoil energy estimators for G48 with an external Ba source. Left: correlation between charge based luke phonon estimate (plukeqOF) and ptNF for events in the 356Ba line.

The position dependence of the various recoil estimators can be seen in Fig. 7.26 left for G48 with a Ba source. The 7% FWHM resolution of precoiltNFg (red) is identical to that of ptNF as expected, since both the signal and the position dependence are scaled by the same factor. The performance of precoiltNF (blue) though, is at first glance horribly disappointing. We had hoped that the width of ptNF Ba 356 line

was primarily caused by physical fluctuations in the total phonon production due to bulk e^- trapping, and under this scenario the luke phonon subtraction in the precoil quantities should have been helped reduce the fractional error.

To be a bit more explicit, let's estimate the total phonon energy loss due to an e^- being trapped. First, the relaxation phonon energy deficit will be

$$\Delta P_{relax} = -f_{gap\,e^-} eV_{gap} f_{relax} \tag{7.5}$$

where V_{gap} is the semiconductor band gap, $f_{gap\,e^-}$ is the fractional amount of the total bandgap energy released by the e^- (unlike standard equilibrium situations where this is obviously known through fermi level matching, our crystal is in a non-equilibrium state and thus this answer is not immediately obvious [98]), and f_{relax} is the relative collection efficiency for bulk relaxation phonons. The luke phonon deficit through trapping can be split into surface and bulk luke phonon deficits per our qualitative discussion in the previous phonon physics chapter. If we quite reasonably assume that all e^- trapping occurs in the low E-field bulk region, then no luke phonons will be generated in the near surface region on the $+V_{q\,bias}$ and thus we'll have a surface luke phonon deficit of

$$\Delta P_{luke\,surface} = -2/3eV_{q\,bias} \tag{7.6}$$

The bulk luke phonon deficit for charge trapping is more complex since it depends precisely on the location of the e^- trapping. As diagrammed in Fig. 7.27, we can estimate the total suppression in bulk luke phonon production due to trapping as the integral over trapped charges multiplied by the voltage difference between the edge

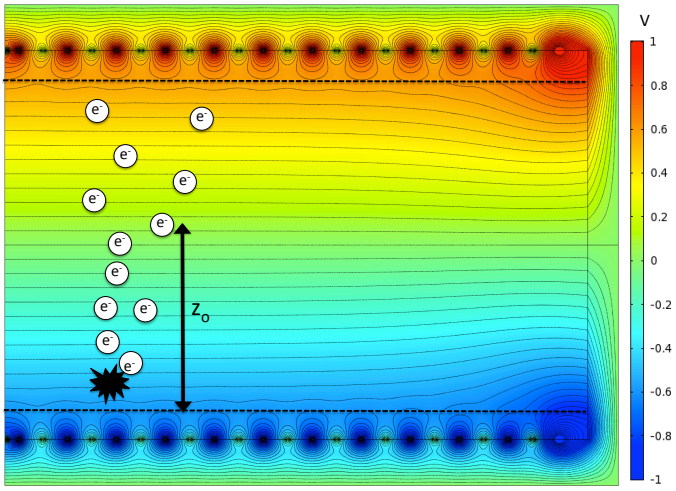

Figure 7.27: Diagram displaying bulk luke phonon suppression due to e^- trapping. Dotted black lines indicate the rough boundaries of the bulk region. Please note that though the voltage color scale only goes from [-1V,1V], the voltage bias of the charge electrodes is ±2V. (Created by Scott Hertel)

of the bulk region, V_{edge}, and that of the trapping location, $V(z)$:

$$\begin{aligned}\Delta P_{lukebulk} &= -\int_{z_o}^{h} dz \frac{dn_{trap}}{dz} e(V_{edge} - V(z)) \\ &= -\int_{z_o}^{h} dz \frac{n_{trap}}{h - z_o} \frac{2eV_{q\,bias}}{3}(h - z) \\ &= -n_{trap} \frac{eV_{q\,bias}}{3}(1 - \frac{z_o}{h})\end{aligned} \tag{7.7}$$

The simplifications come from the fact that the density of traps is approximately constant because the e^- trapping length is x10 larger than the crystal dimensions, and from the fact that the E-field within the bulk region is roughly constant and can be approximated as $\frac{1}{3}\frac{2V_{q\,bias}}{h}$ where h is the height of the crystal. Consequently, the total phonon signal suppression per trapped charge is estimated to be

$$\Delta P_{total} = -eV_{gap} f_{gap\,e^-} f_{relax} - eV_{q\,bias}(1 - \frac{1}{3}\frac{z_o}{h}) \tag{7.8}$$

which we can bound as being -2.7eV $< \Delta P_{total} <$ -1.33eV for our standard operating biases.

Now even though plukeqOF and thus precoiltNF were explicitly derived with an assumption of no trapping, an e^- trapping in the bulk of the detector will cause a suppression of plukeqOF of -2eV (Eq. 7.1) which is fortuitously within the expected range and thus it was quite reasonable for us to expect a sharper precoiltNF linewidth (Fig. 7.26 blue) than we found. To help diagnose the problem, ptNF has been scatter plotted against qi1OF and qi2OF for the events in the Ba peak in Fig. 7.26 right and there's definitely a correlation with the amount of e^- trapping! Infact, the linear correlation coefficient, r, is 0.86 which suggests that an optimal linear least squares removal of the charge correlation will decrease the width to 51% ($\sqrt{1-r^2}$) of it's current value. This has been done and is shown in green on Fig. 7.26. The best fit slope of the correlation gives us a fitted value of ΔP_{total}=-2.77eV which is right on the hairy edge of what we consider physical possible.

Before redesigning all the recoil estimators to take into account these increased trapping losses, we should really think carefully about other physical mechanisms which mimic the observed correlation. One possibility is that we have either impact ionization or smaller than expected average recoil energy required per e^-/h^+ for electron recoils ,ϵ_{eh}, and therefore a larger percentage of the total phonon energy is attributable to luke phonons than naively expected.

A third possible explanation would be that some portion of the strong correlation between charge trapping and ptNF is actually caused by a difference in the relative collection efficiency between luke phonons created by e^- and h^+ drift. The idea here is that a longer drifting length for e^-s means both greater e^- trapping in the bulk and a larger percentage of bulk luke phonons created by e^-. To account for 1/3 of the visible correlation (the other 2/3 would be caused by the trapping itself), one only needs a difference in collection efficiency of 10%.

precoiltNF	ptNF - plukeqOF	Recoil Energy Estimator using non-stationary OF on the summed phonon trace and charge estimators
precoiltOF	ptOF-plukeqOF	Recoil Energy Estimator using OF-1D on the summed phonon trace and charge estimators
precoilsumOF	psumOF-plukeq	Recoil Energy Estimator using the OF-1D phonon channel estimators and charge estimators
precoiltNFg	$\mathrm{ptNF}/(1+2/3\mathrm{V_{qbias}}/\epsilon_{\mathrm{eh}})$	Phonon Only Energy Estimator which assumes bulk electron recoil interaction
precoiltNFn	precoiltNFn=$\frac{ptNF}{1+2/3V_{qbias}/\epsilon_{eh}Y_{nr}^{meas}}$	Phonon Only Energy Estimator which assumes bulk nuclear recoil interaction
YtNF	$\frac{\mathrm{qsummaxOF}}{\mathrm{PrecoiltNF}}$	Ratio of carrier creation to recoil energy for total non-stationary Optimum FIlter

Table 7.6: Recoil Energy and Yield Estimators (RRQs)

7.3 Quality Cuts

Due to their very small bandwidths, large mass thermal detectors (Cuore, Edelweiss, Generation 1 CDMS II) are almost impossible to characterize at a surface facility due to being continually saturated by muon events (at the surface, muon interactions occur every ∼2s). Since athermal phonon detection technology doesn't share this bandwidth limitation, one would hope that, in principle, each and every detector could be **completely** characterized at the surface, and to a large degree this hope isn't misplaced. In particular, all tests of the charge and phonon sensor sensitivity as well as studies of phonon and charged based fiducial volume estimators with electron recoils can be performed with minimal additional hassles due to surface operation. This is enormously beneficial for the collaboration since underground operation is staggeringly costly both from a financial and morale perspective for the collaboration.

Unfortunately, above ground operation does limit our ability in one respect. Without an anti-coincident muon veto, we have found that surface operation of our detectors leads to a neutron interaction rate, R_n, of 110 ± 30 evt/kg livehr (10-100keV$_r$) or approximately 1evt/min for our detectors [115]. Consequently, it's impossible for us

to define a sample of events which we are certain will be composed entirely of electron recoils and thus it's difficult for us to directly measure the very small electron recoil and surface event leakage past our fiducial volume and ionization yield discriminators. To be more quantitative, if we are estimating the fractional leakage of surface events with an internal source with rate R_{se}, then the best non-background subtracted limit (and thus the most systematically robust) we can hope for running at the surface is

$$\epsilon_{leak\,se} < \frac{R_n}{R_{se}}$$

The moral of the above equation is clear. If we want to characterize our discrimination to the greatest extent possible at the surface, then we need to use test sources with high rates! Unfortunately, high rates mean lots of event pileup and thus there is a balancing act. Specifically, let's assume that we can operate with only 25% of events being non-pileup. With a trace length of 6.6ms (8192x0.8μs), this means that we can run with a total event rate of 212hz or we can directly probe sensitivities at the 1.4e-4 level, which is within an order of magnitude of the requirements of the 100kg SuperCDMS SNOLAB experiment. Of course, running with a 75% pileup rate is certainly non-standard, and comes with an enormous number of data quality issues. Most importantly, our pileup discriminators need to be good enough that leakage of pileup events into the WIMP search region is negligible.

Secondly, if we are using an internal source that can not be removed during the neutron source calibration then we will need to apply these very same pileup and quality cuts to the nuclear recoil sample **before** estimating the fiducial volume cut passage efficiency. Specifically, our best estimates of the nuclear recoil passage fraction will be

$$\epsilon_{\text{pass WIMP UCB}} = \frac{\text{number of nuclear recoils which pass quality cuts and fiducial volume cuts}}{\text{number of nuclear recoils which pass quality cuts}}$$

By contrast, in all of our published standard WIMP search analyses at Soudan we are much more conservative and calculate our WIMP passage fractions as

$$\epsilon_{\text{pass WIMP Underground}} = \frac{\text{number of nuclear recoils which pass quality cuts and fiducial volume cuts}}{\text{number of nuclear recoils}}$$

Basically, we assume that all events which fail our quality cuts during WIMP search running (times when we are taking data without any radioactive sources) are good high quality events and thus we must also account for the fact that a hypothetical WIMP event interaction would be removed by the quality cuts with the same probability. This is definitely quite conservative, since many of the events which fail the quality cuts are due to sporadic electronic noise and other non-events, but we simply don't care since our total quality cut efficiency is usually >98%. If we used a similar assumption in analyses at the surface though, where 75% of our events are pileups, then we would be systematically underestimating the size of our fiducial volume by x3.

To keep from being systematically biased using the surface passage fraction definition, we need to require that all quality cuts have identical acceptance on all event samples [116]. Practically, this boils down to these cascading guidelines:

1. estimators used in the definition of quality cuts, should have no/minimal position or recoil type sensitivity.

2. quality cuts should be defined to minimize not only bad event leakage but also maximize good event passage whenever possible.

3. any good event efficiency losses should be found equally on all samples.

With this rule in my mind, we'll briefly discuss the most important quality cuts.

- cQChiSq_g48:

  Due to the very minimal pulse shape dependence on position (just barely in

cQChiSq_g48	General charge optimum filter fit quality metric
cPChiSq_g48	General phonon non-stationary optimum filter fit quality metric
cQpileup_g48	Charge based pileup cut based upon the best fit optimum filter amplitude of the residual charge pulse
cPTend_g48	Cut which removes events which occur during temporal periods where the noise background has a significant slope
cGlitch_g48	Cut which removes TES glitch events through a phonon pulse shape likelihood analysis
cGlitchBox_g48	Cut which removes square wave glitch events through a phonon pulse shape likelihood analysis
cGoodEv_g48	Total Quality Cut

Table 7.7: Notable Quality cuts used in the G48 UCB analysis

the rising edge), the optimum filter fit quality metric, χ^2_Q, has always been and will almost certainly always be the estimator upon which we base our primary quality cut. This cut removes the majority of pileups as well as periods with large amounts of temporal varying environmental noise on the charge channels.

- cQpileup_g48:

  When calculating the quantity χ^2_q, we are answering the very general question of "After removal of a signal with the the optimum filter, does the residual trace look like noise?". The generality of this question allows the cQChiSq_g48 to be sensitive to a wide variety of problems (pileup, environmental noise,...). Unfortunately, this generality also means that the cQChiSq_g48 is not incredibly sensitive to any specific background. In particular, we can significantly improve our sensitivity to pileups, like that shown on the left in Fig. 7.28 by asking the more specific question, "After removal of a signal with the the optimum filter, does the residual trace contain a pileup event?" Specifically, in cQpileup_g48, we run through the OF routine twice being careful to restrict the time shifting of the second OF (right), to areas which don't overlap with any residual position dependence from the first event (the high frequency blue spike), and then require that the amplitude of the residual pulse be consistent with noise. In this way, we can remove charge pileup pulses with amplitudes very near our sensitivity limit ($Q_{pileup} > 6\sigma_Q$).

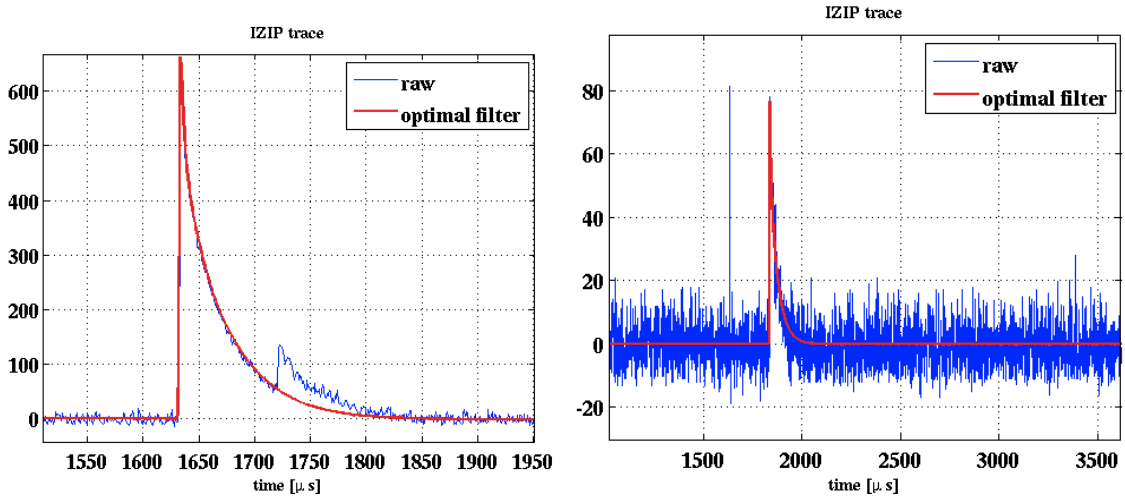

Figure 7.28: Left: Initial Optimum filter fit (red) to a pileup trace (blue). Right: Optimum filter fit to the residual charge trace. Created by Jeff Yen [28]

- cPChiSq_g48:

  Naturally, quality cuts based solely upon the charge signal performance miss periods of large environmental noise on the phonon channels. Furthermore, due to the large difference in total signal bandwidth between the charge and phonons there exists a set of pileup events (Fig. 7.29) in which the first event occurs during a period in which the DAQ is non active (i.e. dead time) and the charge pulse has decayed away before the DAQ becomes active while the phonon pulse has not. With this configuration, if a second event triggers the DAQ, then pileup will only be visible in the phonon channel and will thus pass all charge quality cuts.

  Before the introduction of the non-stationary optimum filter, residual position dependence of the phonon pulses meant that quality cuts on phonon quantities were largely ineffective at separating environmental noise and pileups from good pulses whenever the energy of the pulse was significant. As seen in Fig. 7.29 right, there is minimal energy dependence in χ^2_{PNF} (there is actually a slight negative correlation) and thus we can use the likelihood as a general phonon quality cut for the iZIPs [29]. This is a substantial improvement over all previous

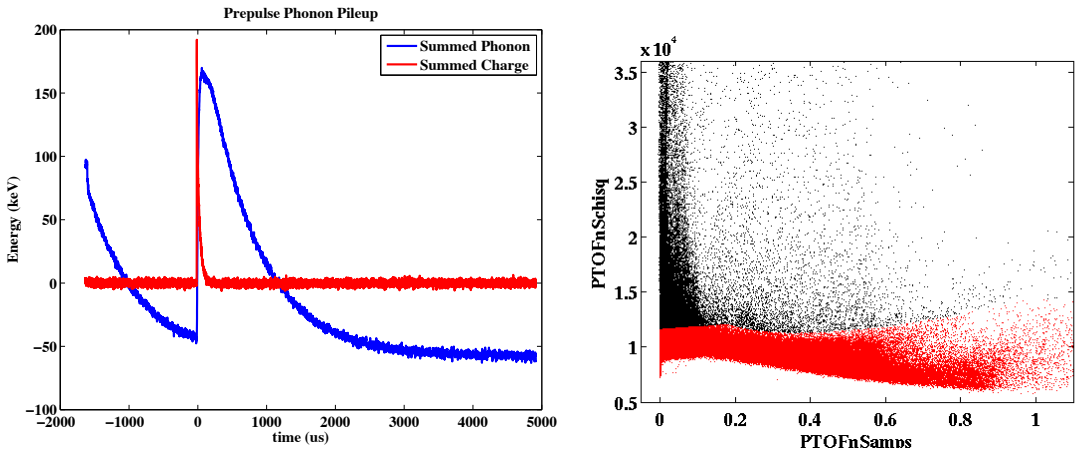

Figure 7.29: left: Prepulse Phonon Pileup right: Difference between the first 1000 and last 1000 bins of the total phonon trace for all events in red, and for those which pass cPTend_g48 in blue. Created by Brett Welliver [29]

analyses. We now have powerful event quality estimators for both phonons and charge. In fact, our confidence in the phonon quality estimators is so large, that for R133, the trace lengths and digitization rates for the phonon and charge signals were optimized independently.

As successfully shown with the charge estimator, more complex iterative Optimum Filter routines (or equivalently Optimum Filter routines with 2 time shifting DOF), can be implemented if improved phonon pileup rejection is wanted.

- cPTend_g48

  To remove events which have the largest low frequency baseline changes due to their temporal proximity to a muon event, a simple cut, cPTend_g48, was designed that looks at the difference between the average value of the first and last 1000 digitization bins [30]. The use of only temporal regions which are from any expected position dependence (digitization bins 2048-2500) suggests that this cut will be orthogonal to any fiducial volume discriminators. Thus belief is supported by the fact that width of it's distribution is independent of phonon energy (Fig. 7.30). This cut will eventually be superseded by the background subtracting OF which was developed for operation in a surface environment

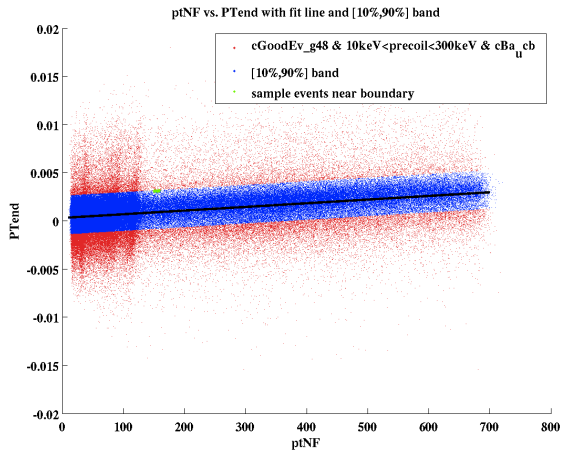

Figure 7.30: Difference between the first 1000 and last 1000 bins of the total phonon trace for all events in red, and for those which pass cPTend_g48 in blue as a function of energy. Created by Adam Anderson [30]

with significant muon tails.

- cGlitch_g48 and cGlitchBox_g48

  Two very common environmental electronic noise features which are only visible upon the phonon channels and thus mimic zero ionization yield events are shown in Fig. 7.31 (black/red) along with an actual event (blue). These events are a potential serious background for low mass WIMP searches because at low energies, discrimination between nuclear recoils and zero yield events is increasingly difficult. Luckily, we have empirically found that the vast majority of glitch events effect multiple detectors and thus at Soudan our primary glitch discriminator is a cut in which physical phonon triggers are required on 6 distinct detectors [117].

  Of course, as the amplitude of a glitch event becomes smaller and smaller, eventually any cut on the physical trigger will become ineffective and thus there has recently been discussion in our collaboration that modulation in the rate of glitches and/or their discrimination could systematically bias potentially both single and multiple scatter annual modulation signals at the lowest energies, and

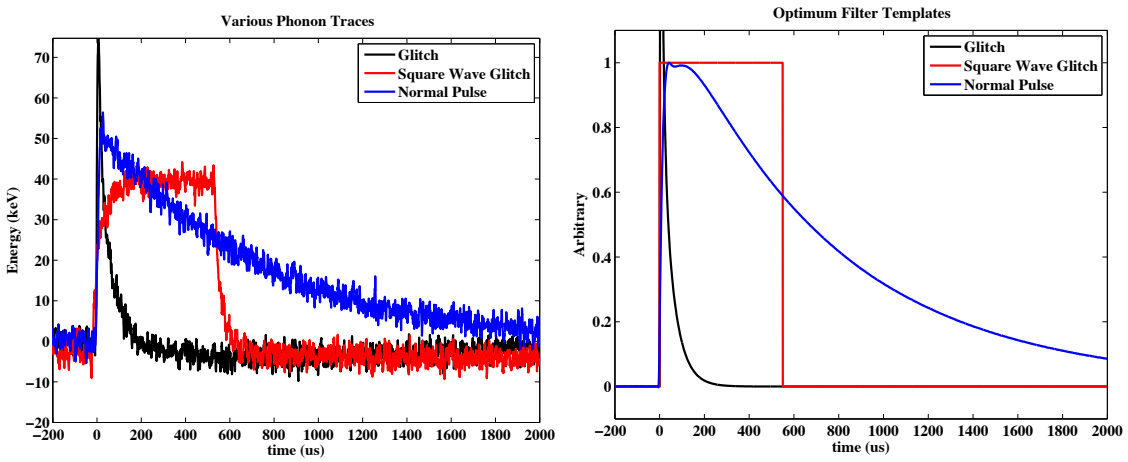

Figure 7.31: Left: Characteristic phonon traces for TES glitch events(black), square wave glitch events(red) and regular pulses (blue). Right: Optimum filter templates used for pulse shape likelihood analysis

consequently more sensitive glitch discriminators are required if we hope to extend our annual modulation studies significantly below our currently published threshold of 5keV$_{nr}$ [118].

Furthermore, at surface test facilities we do not yet have the capability to readout multiple iZIPs at once, and thus at high energies discrimination was originally accomplished by cPChiSq_g48. Near threshold, this general phonon quality cut was found to be insufficient and thus more specific discriminators were required.

Do to the invariance of the glitch event pulse shapes, proper likelihood pulse shape estimators were generated by looking at the difference in the Optimum Filter χ^2 for pulse and glitch templates (Fig. 7.32). Clear separation between glitch events (orange) and charge symmetric recoils (green) is found all the way down to 2keV$_t$, while separation between glitches and more spiky asymmetric events (red) is found down to 4keV$_t$. To limit any potential systematics, the cut threshold was set so as to pass the vast majority of asymmetric events. Square wave electronic glitches were removed in a similar fashion with similar sensitivity scales.

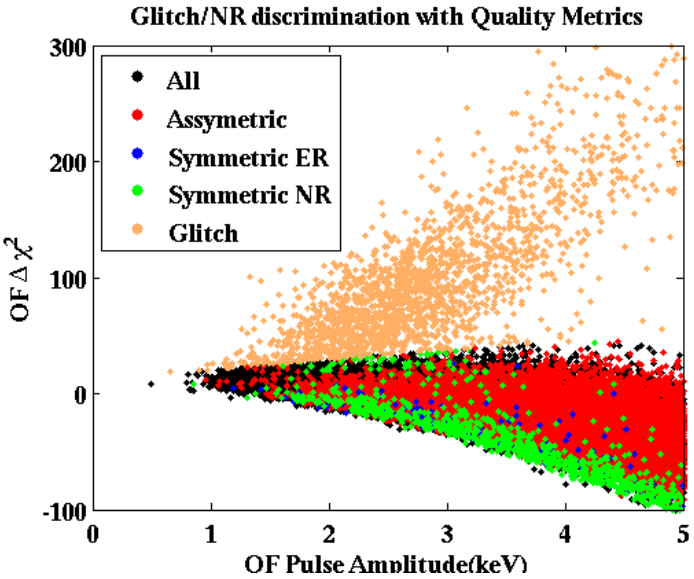

Figure 7.32: Optimum filter pulse shape discrimination between sharp TES electronic glitches (orange) and good pulses (red/blue/green) as a function of total phonon energy

With the expected improvements in low frequency noise as well as the ability to improve our phonon resolution dramatically by simply decreasing the TES T_c ($\sigma_{pt} \propto T_c^3$), the performance illustrated should be considered conservative compared to that expected for future devices.

- cGoodEv_g48

  Due to the fact that there exist events which have high quality charge traces but whose phonon traces exhibit pre-pulse pileup or whose phonon traces are degraded by time dependent environmental noise, it makes sense to define the total charge quality cut cGoodEvQ_g48, which removes all events with problematic charge traces / poor charge transport and separately cGoodEvP_g48, which removes those additional events with problematic phonon traces. When the overall quality cuts are designed in this manner, analyses which only involve charge quantities can use the higher statistics sample which passes cGoodEvQ_g48. Analyses involving phonon and charge estimators use the low statistics sample (cGoodEv_g48 = cGoodEvQ_g48 & cGoodEvP_g48).

7.4 Yield Discrimination and Fiducial Volume Estimators

Historically, CDMS has very rarely publicly showed showed yield discrimination plots without at least some fiducial volume selections already applied and the reason is readily apparent when looking at the ionization yield of all events which pass all quality cuts (black) with respect to the experimentally measured well collected $\pm 2\sigma$ yield bands for both electron recoils and nuclear recoils shown in yellow (Fig. 7.33). Basically, the fact that drifting charges readily trap on the surfaces of the detector means that electron recoils near the surface of the detector can mimic a well collected nuclear recoil since the amount of charge collected/measured on the instrumented bias electrodes is significantly suppressed with respect to the actual amount of charge created in the interaction.

So our task is to create fiducial volume estimators that **remove the vast majority of the physical region of the detector which produces yield suppressed electron recoils that mimic a nuclear recoil signal, while keeping the largest possible well collected volume**.

7.4.1 Charge Fiducial Volume Definition

When introducing the concept of the fiducial volume above, we emphasized it's physicality: the idea of defining a physical 3D inclusion volume within the detector. Though intuitive, this definition needs to be expanded and generalized. In particular, we must decide how the physical fiducial volume scales with energy/signal size. Do we decrease the physical size of the fiducial volume as we near threshold so that electron recoil leakage is kept constant as a function of energy? Do we allow the physical size to grow to that of the entire detector in the limit of zero signal? Or do we do something in between?

No matter what choice is made, it makes sense to expand the dimensionality of the

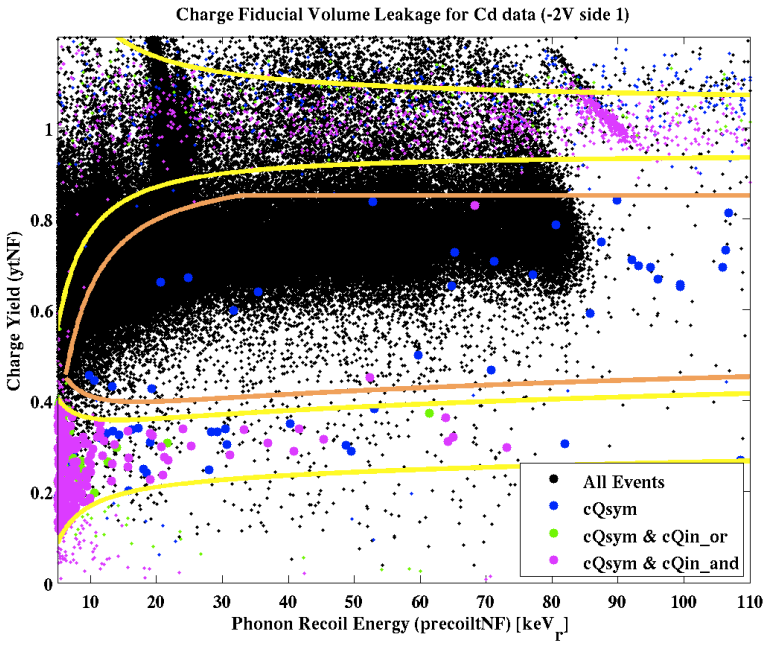

Figure 7.33: Ionization Yield vs Recoil Energy for an iZIP detector with an internal ^{109}Cd source illuminating side 1 (h^+ collection). With no charge fiducial volume cuts (black) a significant number of electron recoils leak into the nuclear recoil band (2 σ bands displayed in yellow). The requirement of symmetric charge signals (cQsym_g48: blue) plus charge radial fiducial volume cuts (green/magenta), decreases the leakage considerably.

fiducial volume space to include energy as well as position metrics. Also, since we haven't yet fully integrated the detector monte carlo into our analyses, it makes sense to map this physical energy-position space into that of the estimators which we plan on using. Specifically for the charge fiducial volume, we must define our acceptance volume in the space of [qi1OF,qo1OF, qi2OF, qo2OF] (energy is implicitly included in this space).

Since the interleaved electrode geometry was purposely designed to have asymmetric charge collection for events near the faces and symmetric charge collection for events in the bulk, it makes sense to define our primary fiducial volume cut in the subspace qsum1OF-qsum2OF as shown in Fig. 7.34. Unlike the traditional CDMS II radial fiducial cut (qoOF $< 2\sigma_{\mathrm{qoOF}}$), this linear function form was purposely chosen so that

the physical fiducial volume remains invariant in the high energy limit. A second reason for the inappropriateness of the CDMSII cut, is that the qsum1OF -qsum2OF distributions are physically defined by bulk electron trapping and thus are completely non-gaussian in shape. For low energies, the choice was made to be maximally accepting (90% of the noise ball is accepted). This is a particularly reasonable choice for the charge fiducial volume since phonon optimal filter fiducial volume estimators remain sensitive below the charge threshold. The upper and lower slope edges were chosen by eye so as to pass the vast majority of the symmetric high energy Ba events. For actual science analyses, this technique could potentially be automated and generalized.

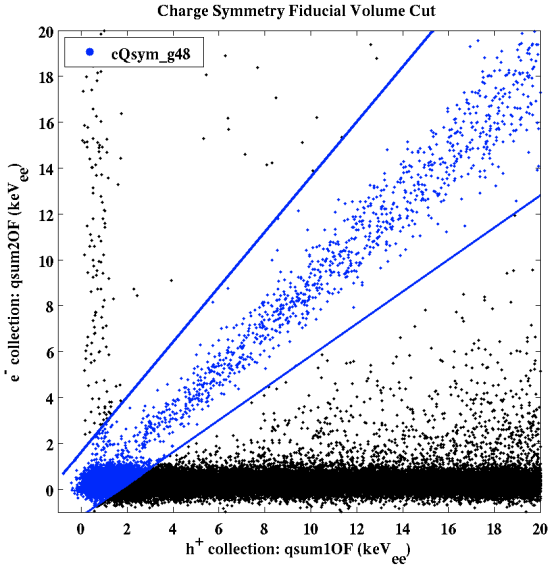

Figure 7.34: Charge collected on side 1 versus side 2 for all events in black and for those which pass the charge symmetry cut (cQsym_g48) in blue

Though this cut was chosen to specifically remove events near the faces, events near the outer radial sidewall will usually have different amounts of trapping for e^- and h^+ and thus the symmetric cut is surprisingly robust at defining the radial fiducial volume as well. This can be seen in Fig. 7.33 where very few events remain below Y<0.85 after the application of cQsym_g48 (blue).

In Fig. 7.35, leakage fractions for cQsym_g48 have been computed for runs with only a

^{109}Cd source (green) and ^{109}Cd + ^{133}Ba source runs (black) with different assumptions. On the left, fractional leakage is calculated assuming the source sample is all mid-yield events (basically e^- from the ^{109}Cd source) and under this assumption the leakage fractions for the two runs are completely inconsistent. On the right, we instead assume that the symmetric mid-yield events share the same source distribution as the symmetric fully collected electron recoils. Under this assumption, the rates for the two runs are fully consistent except at low energies suggesting that the vast majority of the mid yield leakage isn't from the ^{109}Cd source but rather the more uniformly distributed Ba source.

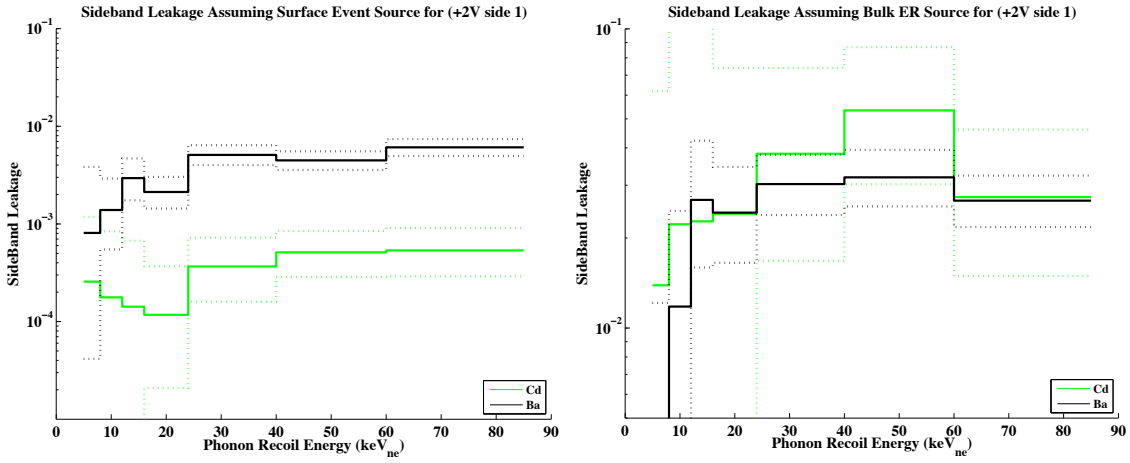

Figure 7.35: Estimates for the fraction of events which pass cQsym_g48 based fiducial volume and droop into the midyield region for runs with the ^{109}Cd source (blue) and^{109}Cd+ ^{133}Ba source (black) assuming a surface event source (left) and electron recoil source (right).

The origin story for these symmetric mid-yield events is further clarified by looking at their locations in the qi1OF-qo1OF and qi2OF-qo2OF spaces (Fig. 7.36) where it is clearly visible that the vast majority of these events occur at very high radius. Basically, there exists a small phase space in which side wall trapping will be similar for both carrier species. To remove these events, it makes sense to apply the additional radial based fiducial volume cuts, cQin1_g48 and cQin2_g48, shown in green. Again, the high energy performance was chosen to have a relatively constant fiducial volume at high energies, while the low energy performance was chosen to be maximally

inclusive.

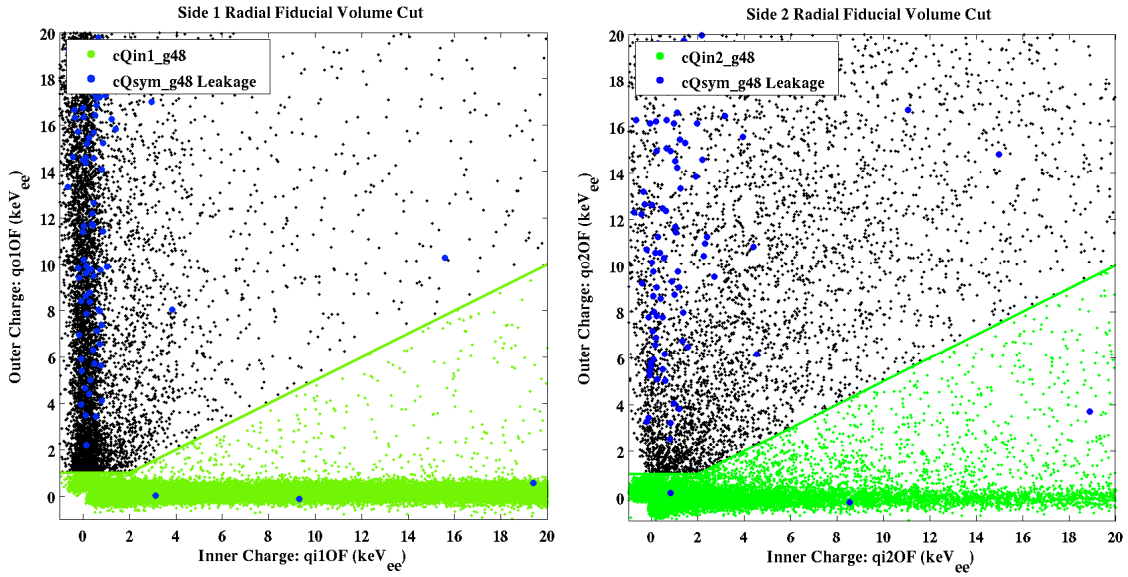

Figure 7.36: Additional radial fiducial volume cuts (blue) are defined in the qi1OF vs qo1OF (left) and qi2OF vs qo2OF(right) planes.

Beyond, the two degrees of freedom which define the slopes in the qi-qo planes, we must also choose between excluding those events which fail both cuts, cQin1_g48 | cQin2_g48 (cQin_or_g48), or instead keeping those events which pass both cuts, cQin1_g48 & cQin2_g48 (cQin_and_g48). Leakage past these additional radial cuts combined with cQsym_g48 are shown in green and magenta respectively in Fig. 7.33. In the mid-yield region between the electron recoil and nuclear recoil bands, both of these compound cuts remove the vast majority of events which pass cQsym_g48 alone, and thus we seem to have successfully defined a 3D fiducial volume. In particular, Fig. 7.37 right estimates the fractional leakage for mid-yield surface events past the various fiducial volume cuts as a function of recoil energy.

The blue cQsym_g48 line has events within every bin and thus isn't completely statistically limited. By contrast, the overlapping magenta and green lines are completely statistically limited for every bin. Consequently, it makes sense for us to increase statistics by rebinning the data into a single energy bin from 8keV$_r$-60keV$_r$ fully accepting the energy systematics that this choice entails. With this change, we find a

mid-yield fractional leakage rate of $< 2\text{x}10^{-5} \pm^{2.5\text{x}10^{-5}}_{2\text{x}10^{-5}}$ (90%CL). This is only a limit on the fractional leakage of surface electrons impinging past the fiducial volume cut because ^{133}Ba + ^{109}Cd source data has a similar rate of mid-yield leakage above the 88keV Q value as below it, suggesting that this residual leakage is also dominated by events sourced by the Ba.

Naively, we expect surface event leakage into the bulk WIMP signal region to be even further suppressed below these fiducial volume only leakage estimates since the vast majority of surface electrons populate a band within the yield range of 0.6-0.85. Specifically, we can set an enormously conservative estimate on the fractional leakage of surface e^- impinging on the face of the detector into the nuclear recoil yield band without any fiducial volume definition as $< 5\text{x}10^{-3} \pm 5\text{x}10^{-4}$90%CL (black Fig. 7.37 left) . This number is staggeringly conservative, since even with a partial fiducial volume cut, we were completely dominated by standard photonic interactions near the cylindrical sidewall.

Unfortunately, direct measurement of the combined yield and fiducial volume leakage is impossible at the surface due to cosmogenic nuclear recoil background (the measured super conservative limits with no background subtraction are displayed in Fig. 7.37 left and are consistent with our background expectation). Furthermore, our first attempt to measure this cumulative leakage at Soudan with an implanted ^{210}Pb source has led us to realize that our ionization performance near the faces is so high that ^{206}Pb recoils impinging on the outer surfaces will almost certainly be the dominate background of the large scale experiment [119], and thus the fiducial volume only leakage is more appropriate performance metric in any event.

To measure WIMP passage fractions as a function of energy for the various fiducial volume metrics, one would ideally have a homogeneously distributed single scatter nuclear recoil only source impinge on the detector with which one could measure the ratio of events pre/post the application of the fiducial volume. Unfortunately, we are non-ideal in two ways. First, a neutron source has a significant probability of multiple scattering and has a slightly position dependent event rate, both of which suggest

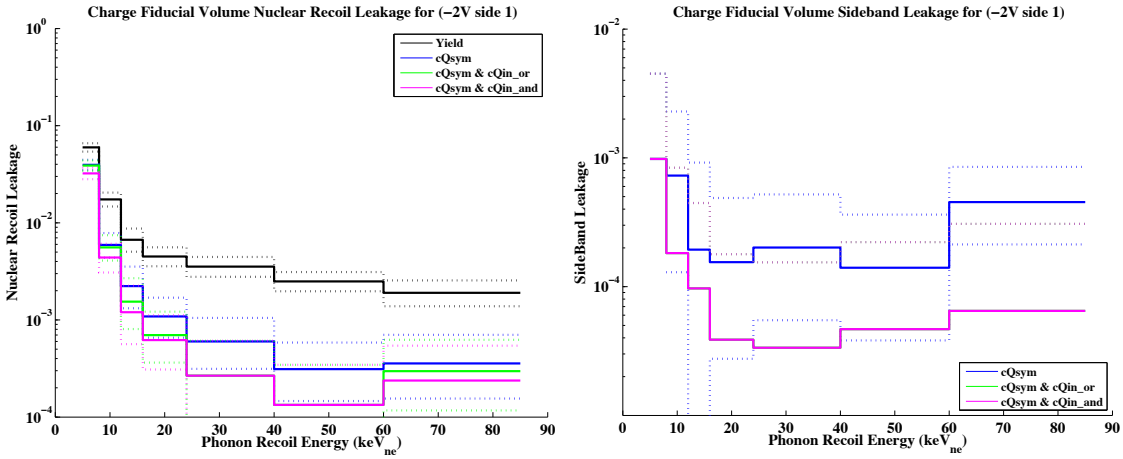

Figure 7.37: left: Estimate of surface event leakage into the nuclear recoil signal region as a function of energy **assuming that all events in the nuclear recoil band are surface events** for various charge based fiducial volumes. right: Estimate of surface event leakage past various charged based fiducial volume estimators in the mid-yield region. 90% CL shown as dotted lines.

that our neutron measured fiducial volume passage fraction will be systematically underestimated by ∼7.5% [120]. Secondly, the weakness of our ^{252}Cf source with respect to the ambient photon background at the surface of ∼7hz with the full Pb shield suggests that the nuclear recoil yield band pre-fiducial volume cut will be slightly contaminated by electron recoils occurring near the cylindrical sidewall again systematically suppressing our passage fraction estimate.

In CDMS II at Soudan, pre-fiducial volume electronic recoil leakage was also an issue, but for a different reason. At Soudan, shielding around the Cf source is unable to suppress the high energy photons from the same decay chain, and consequently our nuclear recoil source is infact a nuclear recoil+ high energy photon source. To remove this bias in CDMS II, we historically have extrapolated the electronic recoil leakage into the Cf nuclear recoil band by measuring the ratio in the number of q-outer nuclear recoil events to midyield events in Ba and then applying this ratio to the Cf data accepting all the systematics that this extrapolation entails [121].

Due to the fact that the photon source rate at the surface is environmental and not

correlated with the Cf nuclear recoil rate, we have the unique capability to directly measure the electronic leakage rate during runs without the Cf source and then background subtract from the Cf runs to get the true pre-fiducial nuclear rate. Far from the trigger threshold, this background subtraction should be virtually systematic free with the sole exception being precisely estimating the total experimental good event live time for each configuration. Rather than calculating directly, we chose to match the number of asymmetric yield surface events which pass cGoodEv_g48 and cQin1_g48 within the range of 20keV$_r$-90keV$_r$ (i.e. the number of events collected from the Cd). This direct measurement over standard daq estimates of lifetime has the added benefit of naturally taking into account any temporal variation in the quality cut passage fraction as well as any variation in the trigger threshold (i.e. a change in the percentage of events which are noise triggered).

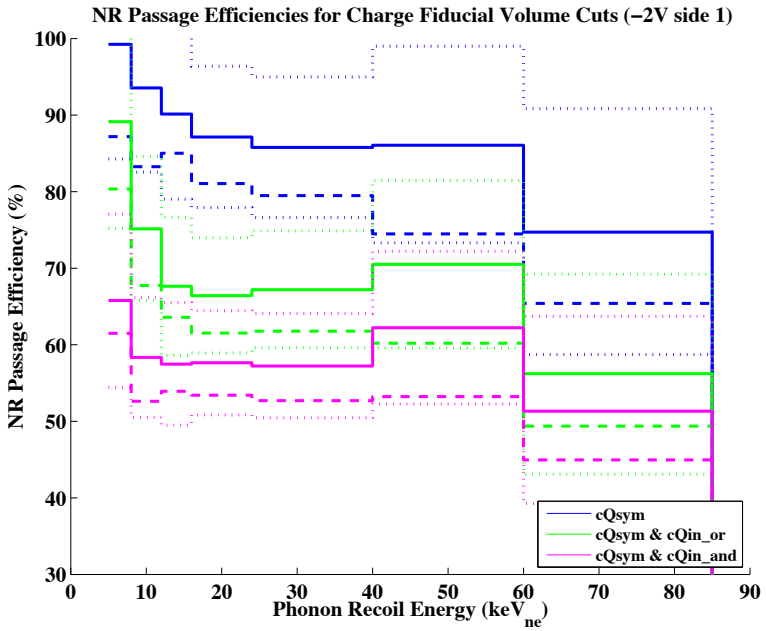

Figure 7.38: Background subtracted nuclear recoil passage fractions as a function of recoil energy for various charge based fiducial volume selections. 90% CL shown as dotted lines.

This background subtracted neutron nuclear recoil passage fraction is displayed as a function of energy in Fig. 7.38 (solid) with the 90% confidence limits on the

background subtracted passage fraction estimates dotted. To set the scale on the importance of the background subtraction, the negatively biased non-background subtracted estimates are shown as dashed lines and seem to be ∼7% lower.

The shape and relative sizes of three fiducial volume cuts seem to match expectation. Due to our choice of inclusiveness at low energies, all fiducial volumes tend to rapidly increase in size at lower energies. Secondly, the passage fractions are consistent with flat /scale invariant behavior at high energies. Finally, the more constraining fiducial volumes have smaller neutron passage fractions, and thus for this test facility analysis we will choose cQsym_g48 & (cQin1_g48 | cQin2_g48) as our primary charge fiducial volume selection (cQ3D_g48) since the mid-yield leakage is quite similar to that of the more restrictive cut while the neutron passage fraction is 10% higher at 69% ± 5% (90%CL) over the 8keV$_r$-60keV$_r$ energy range. After accounting for WIMP/neutron distributions difference, this fiducial volume metric selection should pass 75% of potential WIMPs.

In preliminary R133 underground studies with the ^{210}Pb source, Scott chose the more strict cQsym_133 & cQin1_133 & cQin2_133 charge fiducial volume definition since T3Z3 seemed to have temporal variation in charge transport / surface trapping at high radius, which was preliminarily found to be easier to remove with the strict fiducial volume cut [**?**]. Understanding and minimizing both the temporal and detector-to-detector variability in carrier transport will certainly be a dominate research task in the upcoming years. One potential long term solution to these problems is to follow in Edelweiss' footsteps [122] and add additional electrode bias rails on the outer surface, which would drastically limit the ability of built up space charge to change carrier transport on long length scales leading to much more stable behavior.

7.4.2 Low Energy Phonon Fiducial Volume Definition

The most unfortunate side effect of the suppressed nuclear recoil yield in semi conductors that we use to our enormous benefit in discriminating between recoil type,

cQsym_g48	Symmetric charge collection cut (Fig. 7.34 left)
cQin1_g48	Charge based side1 radial cut (Fig. 7.36 left)
cQin2_g48	Charge based side 2 radial cut (Fig. 7.36 right)
cQ3D_g48	Charge based fiducial volume:cQsym_g48&(cQin1_g48|cQin2_g48)
cNR_uncorr_g48	$\pm 2\sigma$ non-stationary Optimum Filter nuclear recoil yield bands
cER_uncorr_g48	$\pm 2\sigma$ non-stationary Optimum Filter electric recoil yield bands

Table 7.8: Ionization yield and charge fiducial volume cuts for G48 at UCB test facility

is that fiducialization through charge is significantly more difficult for nuclear recoils since for a given recoil energy, the ionization signal is so much smaller. To internalize this a bit more precisely, just recognize that a 9keV$_r$ nuclear recoil produces 3keV$_{ee}$ of ionization (the ionization yield is ~ 0.3) or for a baseline σ_{qsumOF} of $\sim$ 300eV$_{ee}$, we have a signal to noise ratio of 10. The situation is exactly reversed for phonon sensors. Due to luke phonon creation, a 10keV$_r$ nuclear recoil will have a boosted total phonon energy of $\sim$14keV or a signal to noise of 47 ($\sigma_{pt} \sim$ 300eV$_t$)!

This huge difference in signal to noise for nuclear recoils suggests that as long as the position dependent signal is O(1) with respect to the position independent signal (when optimally summed over all frequencies), than we should expect that defining a fiducial volume through phonons will always lead to better fiducialization than charge. This belief is put to the test in Fig. 7.39 left, where we've separated events into asymmetric (orange) and symmetric (blue overlaid by cyan and green) samples using cQsym_g48, and plotted them on in the psum1OF- psum2OF plane. At high energies, these two samples are quite well separated strongly suggesting that these simple 1D-OF estimators could be used for fiducial volume definition. Even more interesting, if we look down at low energies (psum1OF $<$ 6keV), events which pass cQsym_g48 are seen to populate a phase space region which is indicative of phonon signal asymmetry which strongly suggests that our ability to fiducialize using phonon information remains at energies below those at which we lose charge fiducialization.

Using the symmetric and asymmetric samples as defined through the charge fiducial volume as a guide, we can design phonon fiducial volume cuts in the psum1OF-psum2OF (Fig. 7.39: cPsym_g48), pa1OF-psum1OF (Fig. 7.41 left: cPin1_g48),

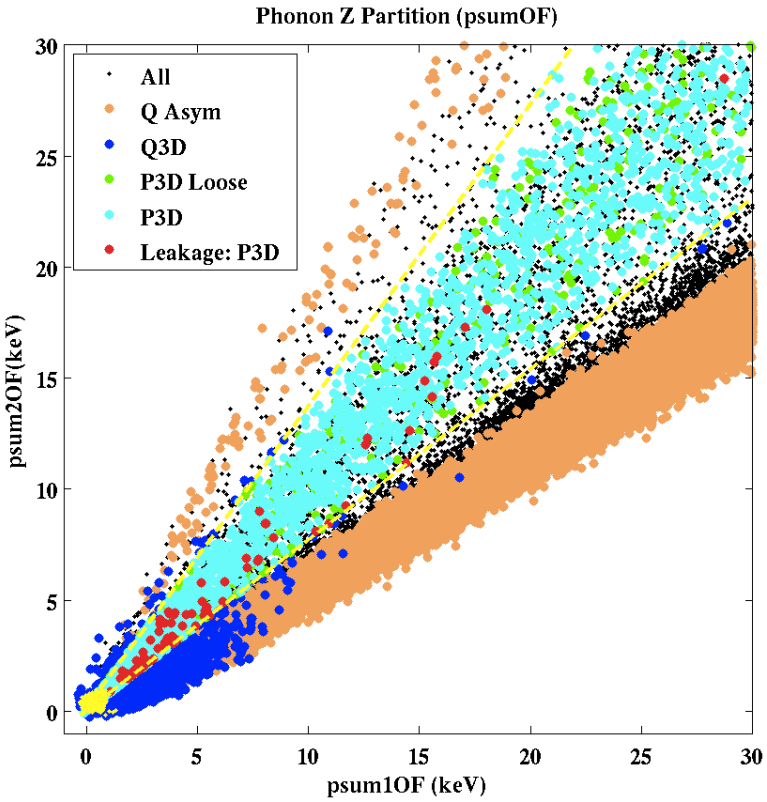

Figure 7.39: Optimum Filter estimates of phonon signal for side1 (x-axis) and side 2 (y-axis) separate asymmetric charge events (orange) from symmetric nuclear and electron recoils (blue, cyan, green). cPsym_g48 cut edges are shown in yellow while events which pass the loose phonon fiducial volume (cPsym_g48 & cPin1_g48 & cPin2_g48) and strict phonon fiducial volume are shown in green and cyan repsectively. Mid-yield events which fail cQ3D_g48 but leak pass cP3D_g48 are shown in red, and randoms are shown in yellow.

pa2-psum2OF (Fig. 7.41 right: cPin2_g48), and pa1OF+pa2OF-psumOF (Fig. 7.40: cPin12OF) spaces which are shown in yellow that roughly match the high energy behavior of the charge fiducial volume and are constrained at low energy by requiring a random noise passage fraction of 56±4% (95% CL) Notice the change in cut setting philosophy with respect to that used for the charge fiducial volume where we were fully inclusive[123].

The resulting phonon fiducial volume performance can be seen in Fig. 7.42. The vast

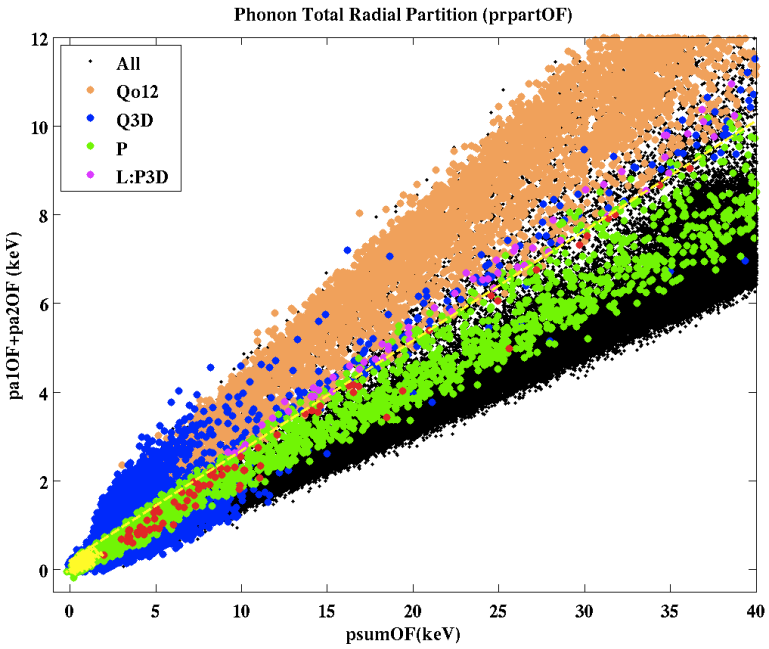

Figure 7.40: The relative amplitude of the outer phonon signals (y-axis) compared to the total phonon energy collected (x-axis) separates events with significant charge collection on the outer electrodes of both faces (orange) from events which pass charge fiducial volume at high energy (blue) and those which pass the loose phonon cut (green). cPin12_g48 cut boundary shown in yellow.

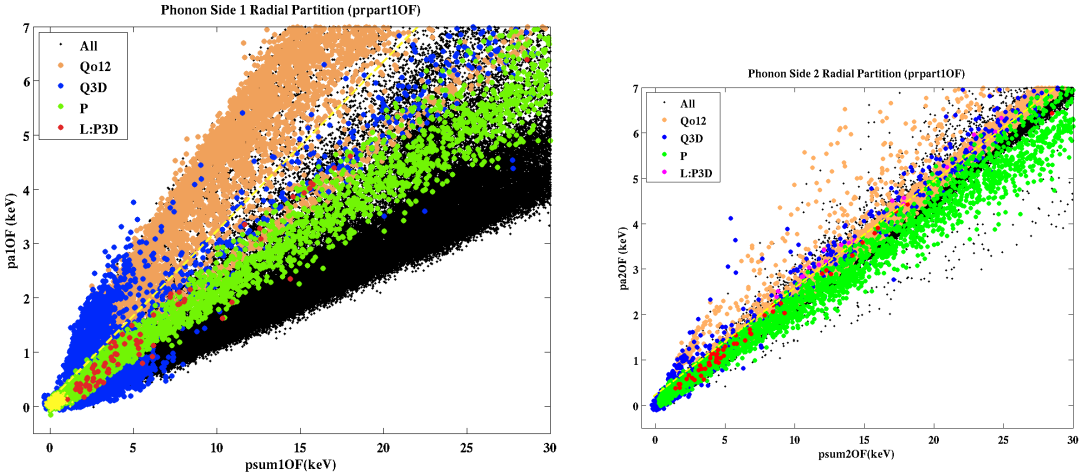

Figure 7.41: Outer phonon amplitude versus faced summed quantities for side 1 (left) and side 2 (right) with identical color scheme as that used in Fig. 7.39

majority of the ^{109}Cd surface events in the mid-yield region (and the 22keV$_r$ photon line) are removed (black) while the majority of the bulk Ba events in the electron recoil band are kept (green). Degradation in the charge fiducial volume cut at low energies is also clearly visible (blue). The most interesting events are those at relatively high energies which fail cQ3D_g48 but pass cP3D_g48 (red). Looking carefully at both the charge and phonon traces (Fig. 7.43), all of these events have significant charge collection on the outer electrodes and thus fail cQ3D_g48, but the expected high frequency position dependent signal is relatively muted in the outer phonon channels. Most likely, these are events which occur near the detector center line at very high radius and thus by the time the diffusive recoil phonon ball has expanded to a size of >10mm to start interacting with the Al QET fins on the faces of the detector it has also expanded into the crystal by >10mm leading to a position dependent phonon signal which is shared between inner and outer phonon channels.

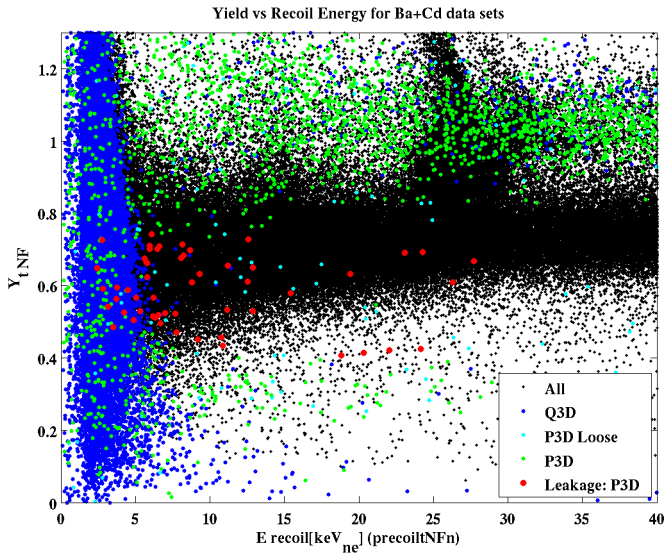

Figure 7.42: Ionization Yield versus recoil energy for ^{133}Ba and ^{109}Cd source runs for charge symmetric recoils as defined charge (cQ3D_g48) in blue as well as by phonons (cP3D_g48) in green. Events which fail cQ3D_g48 but pass cP3D_g48 are shown in red.

In future designs, greater pixelation of the phonon sensors and increased phonon

sensor Al coverage at high radius should lead to better radial fiducial volume performance. Furthermore, improvement in phonon signal to noise by reducing T_c and removing all sources of non-intrinsic environmental noise can't help but improve the phonon only fiducialization at low energies. Finally, the use of OF-1D quantities which use the mean summed phonon pulse template, suggests that we are not optimally sensitive to high frequency position dependent signals in this analysis and thus implementation of a multidimensional Optimum Filter algorithms could lead to significant fiducialization improvement at low energies.

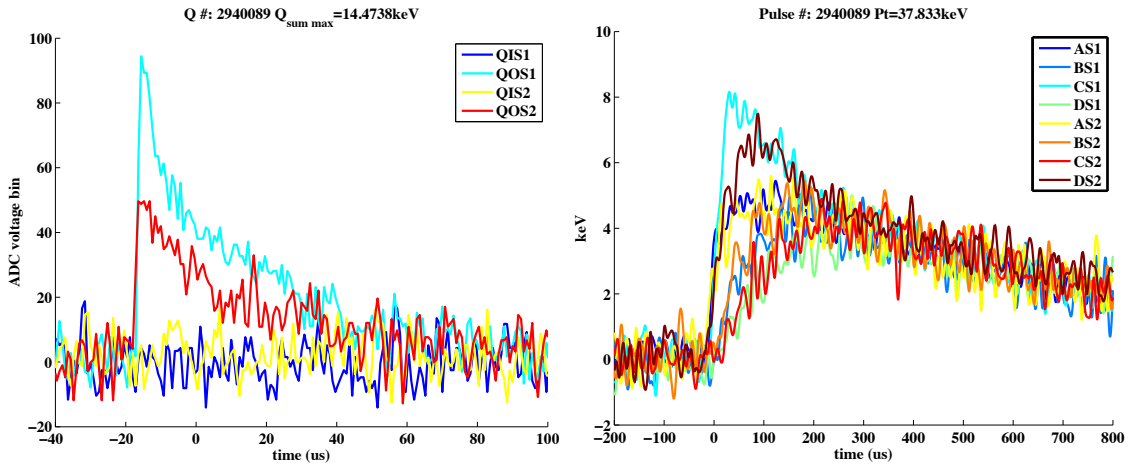

Figure 7.43: Charge (left) and phonon (right) traces for a characteristic event which fails cQ3D_g48 but passes cP3D_g48

Surface event leakage and neutron passage fractions can be estimated for low energy phonon fiducial volume cuts in an identical manner as that used for the charge fiducial volume. The emphasis on very low energy / near trigger threshold performance of these phonon fiducial volume estimators, means we do pick up additional systematics, unfortunately. In particular, the degradation in yield estimators at low energies means that well collected bulk electron recoils will leak into the mid-yield region, limiting our ability to measure surface event leakage (the leakage estimates should be even more conservative). Secondly, when motivating the background subtraction technique for the nuclear recoil passage estimate, we assumed that events had an energy much larger than the trigger threshold and thus temporal variations in the percentage of noise triggered events would not change our passage fraction estimates. At these low

energies, this constraint is not satisfied and consequently we need to carefully reassess the reliability of these presented low energy passage fractions.

The energy functional form (y=mx+b) chosen for our phonon fiducial volume cuts is very helpful in this regard. Specifically, in the limit that our sensors are manifestly linear, the passage fraction for a cut with a linear threshold should be monotonic. Consequently, though it is very difficult to constrain temporal trigger systematics, we know that this systematic can be largely disregarded because the passage fraction for random noise is quite similar to that found in the high energy limit for good nuclear recoils.

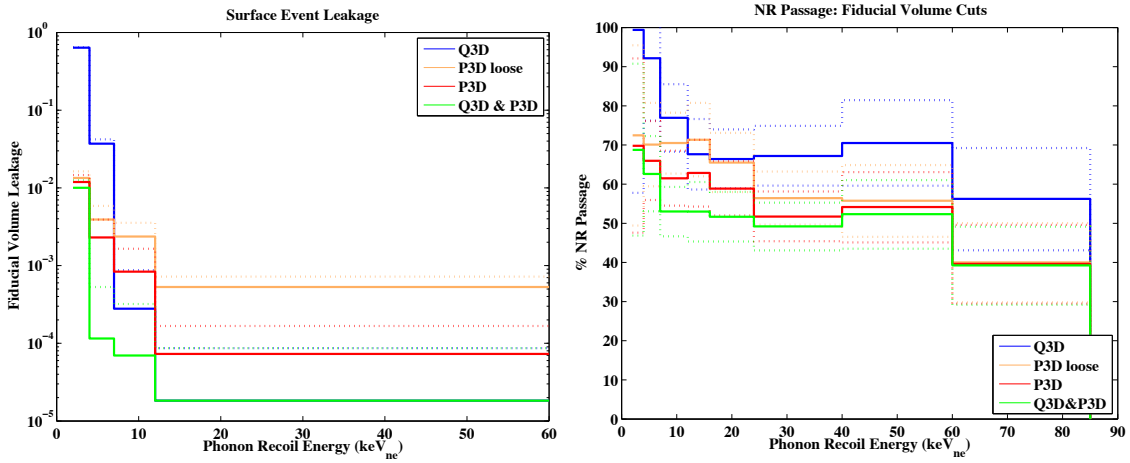

Figure 7.44: Surface event leakage fraction (left) and background subtracted nuclear recoil passage fraction (right) for various charge and phonon fiducial volumes as a function of energy with 90% CL dotted.

Since the ionization yield discrimination between electron recoils and nuclear recoils degrades only slightly below that of the charge fiducial volume definition, it's reasonable to ask if significant analysis resources should be used to produce these phonon only fiducial volume definitions (we could afterall, use this money to build more detectors and increase our mass). The most compelling reason to go down this path is that the claimed CoGENT/CRESST 8GeV WIMP signal largely would lie in this signal region and thus the factor of 2 improvement in fiducialization energy scale is enormously important to strongly test these other experiments. Secondly, searches for

exotic dark matter candidates with masses in the MeV-GeV range requires sensitivity to single e^-/h^+ production. The easiest way to achieve this sensitivity in massive semiconductor devices at the present moment is to put a large voltage bias across the detector and measure the luke phonons produced rather than the recoil phonons (Luke-Neganov phonon gain). Use of this technique requires that all carriers travel across the entire voltage drop, and consequently these techniques require a phonon only fiducial volume definition.

7.4.3 High Energy Phonon Fiducial Volume Effectiveness and Pulse Shape Ionization Yield

At higher energies where the charge based fiducial volume is fully effective, the phonon only fiducial volume cut is effective only insofar as he offers a quasi-independent cross check of the charge fiducial volume effectiveness. Specifically, there may exist pathological classes of electron recoil events (with an occurrence probability well below the current leakage fraction limits) which could be removed with phonon based rejection that passes all possible charge based cuts. The most studied event class of this type is the 'MISS' or Multiple Internal Surface Scatter event which is diagrammed in Fig. 7.45 left. A very small fraction of photon interactions will meet these criteria:

1. the photon compton scatters very near the surface of the detector ($\sim 10\mu$m) so that ionized carriers travel laterally along the surface and have significant charge trapping.

2. the residual photon compton scatters on the other side anywhere in the lateral transport area ($\sim$ 1mm) with roughly the same recoil energy as in the first scatter.

3. the residual photon does not interact with another detector.

This is truly a very small fraction of electron recoils. Our/Kevin McCarthy's best estimate currently is that $6\text{x}10^{-8}$ of electron recoils will produce recoils which satisfy

these constraints [31] which means that this background should always be subdominant to neutron recoils from U/Th contamination in our refrigerator and shielding. With this said, we believe that phonon pulse shape could potentially be used to remove these events. The key is to recognize that MISS events have all of their phonon energy released very near the instrumented faces of the detector and as such the pulse shapes for these events should have rising edges which are much faster than that of the average nuclear recoil. This is shown in Fig. 7.45 right, where we have taken traces from actual asymmetric electron recoil surface events which occurred on the top and bottom of the detector and directly summed the traces, producing simulated MISS events [124] which are clearly seen to have rise times that are inconsistent with standard electron recoils.

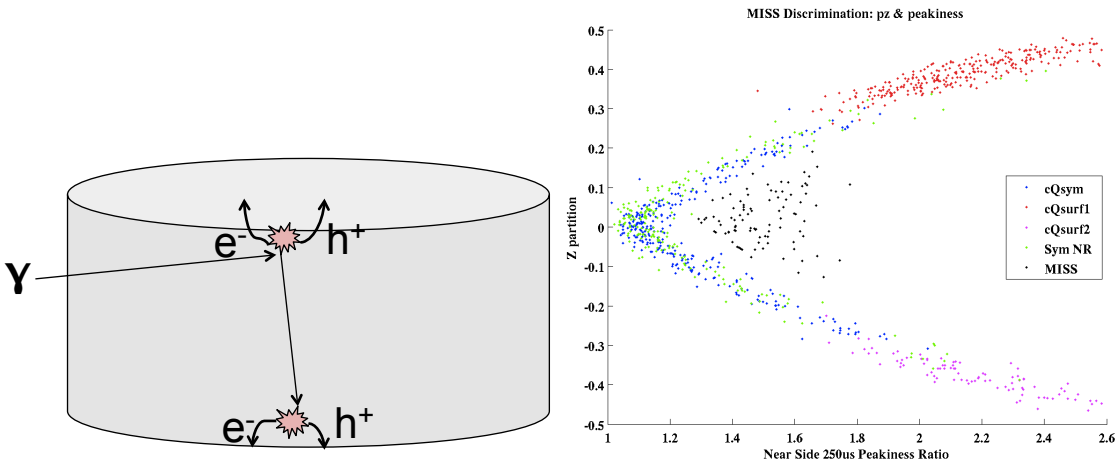

Figure 7.45: left: A diagram of a MISS event (produced by Kevin McCarthy [31]) right: MISS event discrimination based upon the peakiness of the total phonon pulse shape

As a complete aside, if the phonon sensor rails on one side are converted to an instrumented high impedance charge readout rather than a low impedance TES/SQUID readout, MISS events can be directly removed by measuring significant amount of charge on this 'veto' channel. Furthermore, though we've removed over 1/2 the phonon channels (for a fabrication cost benefit of say 30% per detector) we haven't significantly decreased the phonon energy performance since the loss in phonon absorption bandwidth should be largely compensated for by almost equal suppression

of the electron-phonon thermal conductance, G. The biggest fear originally was that this device would have significant residual position dependence in the energy which would hurt the ionization yield performance, but with the non-stationary Optimum Filter algorithm, the Queen's group has proven that this fear was unfounded [125]. Every indication is that this 'half iZIP' or hiZIP concept is a valid second generation high mass dark matter detector, and should thus be studied in parallel with minimal resources as we continue R&D on our primary symmetric detector design.

Since other, yet to be understood, non-gaussian leakage background tails could exist at levels which limit our future WIMP sensitivity, it makes sense to further develop and optimize phonon fiducial volumes in the high signal to noise regime. Specifically, let's expand low energy phonon only fiducial volume which was composed of the 8 OF-1D best fit phonon amplitudes, to include 14 quite noisy additional pulse shape and relative phonon channel delay metrics (for a total fiducial volume dimensionality of 22!). Since the actual dimensionality of the manifold is 4D for single scatters and 8D for a multiple compton scatter within a single detector, this manifold is enormously constrained. Basically, it's the 22D analogue to a pancake in 3D space which has 1 dimension that is much smaller than the other 2. Here, though, we have 18 dimensions which are much smaller than the other 4.

Now using the position correction algorithms that were developed extensively for CDMS II analysis [3], events were compared against symmetric nuclear recoil, symmetric electron recoil, and asymmetric surface event manifolds that were generated for event samples defined by yield and charge fiducial volume cuts, and distance from these manifolds was converted to an event likelihood by calculating the local covariance matrix for each manifold and assuming gaussianity.

Most interestingly, these phonon pulse shape manifolds contain information with which one can separate electron recoils and nuclear recoils with the same energy and position with marginal loss of nuclear recoil passage efficiency for nuclear recoils which pass the charge fiducial volume cuts (Fig. 7.46). Qualitatively this discrimination ability comes from the fact that events with larger ionization yield have a larger

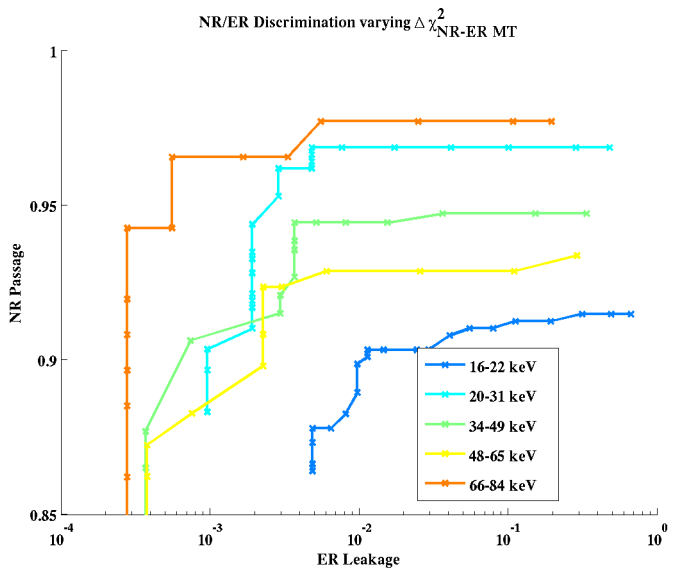

Figure 7.46: Discrimination between electron recoils and nuclear recoil using phonon pulse shape alone

fraction of their total phonon energy in diffusive surface luke phonons which are absorbed quite quickly by the Al fins producing sharp rise times.

At present, the recoil type discrimination is inferior to ionization yield discrimination (particularly at low energies), but in the future we expect to design devices with $> x2$ the Al coverage as well as with significantly lowered Tc's and consequently one is not being wildly optimistic by considering the scenario in which pulse shape rejection is our dominate recoil discrimination for low energies.

The combination of pulse shape recoil discrimination and muon induced neutron contamination of our nuclear recoil band in all data taken at the surface, means that an apples to apples comparison of the phonon and charge fiducial volume performance is almost impossible. For the charge fiducial volume alone, our best estimate of leakage came from looking at the number of symmetric events in the midyield side band. When looking at the $\Delta\chi^2$ between the nuclear recoil and surface event manifolds (Fig. 7.47), these charge leakage events are removed, but this doesn't necessarily mean that a phonon fiducial volume is superior. Rather, it very likely means that

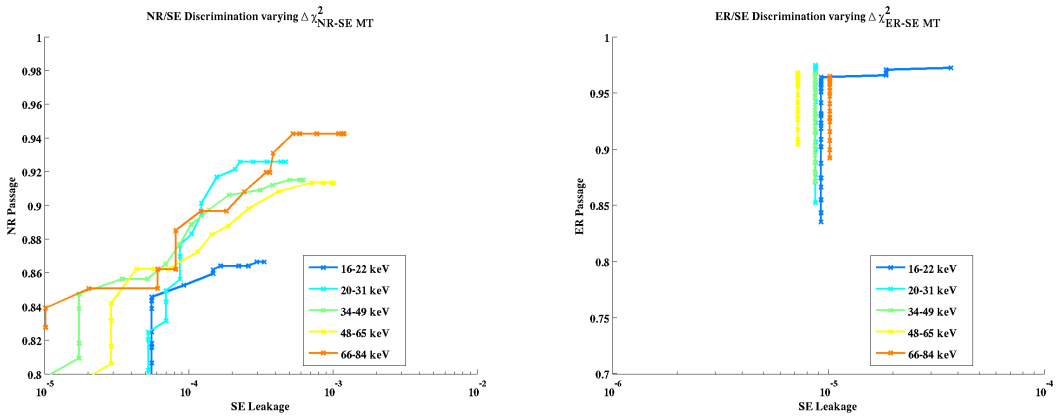

Figure 7.47: left: Nuclear recoil passage fraction (after charge fiducial volume cuts) as a function of mid-yield surface event leakage for various energies based upon the difference in the manifold likelihoods for the different event types ($\Delta\chi^2$). right: the improved performance in manifold discrimination between electron recoils and surface events suggests that the nuclear recoil manifold performance could be limited by poor statistics.

these symmetric mid-yield leakage events are just mid-yield. So, to really test this combined phonon recoil type/ fiducial volume rejection, we need electron recoil data with absolutely no nuclear recoil contamination. We need underground calibration data.

7.5 Potential Future Studies

1. Low Frequency Charge and Phonon noise: Both our charge and phonon sensitivities are suppressed due to low frequency environmental noise by $> x2$ for experimental setups at both Soudan and UCB. If solved, our experimental thresholds and thus our sensitivity, in particular to low mass WIMPs could be substantially improved. Sterile neutrino searches through the coherent neutrino-nucleus scattering channel also require this excellent phonon resolution performance.

2. Time constrained optimum filter for charge amplitude estimation: Physically, charge pulse start times between the two sides of the iZIP are constrained to

within $\sim 2\mu s$ of each other and consequently, the time shifting offset found in our current charge optimum filters can be decreased by $\sqrt{2}$ without any loss if this constraint is placed into the current algorithm.

3. Tying charge trigger window to phonon pulse start time: Charge start times are physically constrained to be within $\sim 20\mu$s before the phonon pulse start time. Consequently, tying the charge optimum filter start window to the phonon pulse start time instead of the physical trigger, could significantly decrease the time shifting offset.

4. More complex charge fiducial volume definitions: For transparency, cuts were defined within the qsum1OF-qsum2OF, qi1OF-qo1OF, qi2OF-qo2OF subspaces of [qi1OF, qo1OF, qi2OF, qo2OF] charge amplitude space. Potentially, more complex functional form shapes could increase the fiducial volume without increasing leakage.

5. Charge transport temporal stability and space charge buildup: Though discussed only very briefly, temporal variability in charge transport has been found to be a significant hassle for iZIP style detectors at Soudan. Understanding why the temporal variability varies between detectors and developing fabrication and sourcing procedures which minimize this effect are very important for the long term success of the iZIP design as a dark matter detector.

6. Multi-dimensional linear optimum filter fits for low energy phonon fiducial volume definition: The use of the mean channel summed phonon pulse as the template for the 1-D optimum filter means that the high frequency position dependent information is naturally suppressed, and thus superior fiducial volume estimators could potentially be created by using multidimensional linear optimum filters which don't unnaturally constrain pulse shape position dependence.

7. Non-linear phonon pulse shape fitting: Non-linear pulse fitting algorithms which accurately span the entire good pulse shape space but do not include any non-physical degrees of freedom would significantly improve our high energy phonon

fiducial volume estimators as well as our pulse shape yield discrimination.

8. Better implementation of non-linear likelihood techniques: Phonon manifold definition through position correction potentially has a significant systematic (i.e. discrimination outlier tails) when the density of events within the estimator space varies significantly. Consequently, better non-linear likelihood techniques (boosted decision trees, ...) should be tried.

9. Detector Monte Carlo: A detector monte carlo which qualitatively and quantitatively matches detector performance will help us develop improved fiducial volume estimators particular at high energy.

Bibliography

[1] S. Golwala, "Exclusion limits on the wimp-nucleon elastic-scattering cross section from the cryogenic dark matter search," Ph.D. dissertation, University of California Berkeley, 2000.

[2] J. Filippinni, "A search for wimp dark matter using the first five-tower run of the cryogenic dark matter search," Ph.D. dissertation, University of California Berkeley, 2008.

[3] Z. Ahmed, "A dark-matter search using the final cdms ii dataset and a novel detector of surface radiocontamination," Ph.D. dissertation, California Institute of Technology, 2012.

[4] D. Brandt and et al, "Monte carlo simumlation of massive absorbers for cryogenic calorimeters," *Journal of Low Temperature Physics (LTD 14)*, vol. 167, pp. 485–490, 2012. [Online]. Available: http://www.springerlink.com/content/p2638426121438j3/

[5] S. Leman, K. McCarthy, and et al, "Monte carlo comparisons to a cryogenic dark matter search detector with low transition-edge-sensor transition temperature," *Journal of Applied Physics*, vol. 110, no. 9, p. 094515, 2011.

[6] Y. Sofue and V. Rubin, "Rotation curves of spiral galaxies," *Annual Review of Astronomy and Astrophysics*, vol. 39, no. 1, pp. 137–174, 2001. [Online]. Available: http://www.annualreviews.org/doi/abs/10.1146/annurev.astro.39.1.137

[7] K. Nakamura and P. D. Group, "Review of particle physics," *Journal of Physics G: Nuclear and Particle Physics*, vol. 37, no. 7A, p. 070521, 2010. [Online]. Available: http://iopscience.iop.org/0954-3899/37/7A/075021

[8] E. Komatsu and et al, "Seven-year wilkinson microwave anisotropy probe (wmap) observations: cosmological interpretation," *The Astrophysical Journal Supplement Series*, vol. 192, no. 2, pp. 18–234, 2011. [Online]. Available: http://iopscience.iop.org/0067-0049/192/2/18/

[9] E. Kolb and M. Turner, *The Early Universe*. Westview Press, 1994.

[10] E. Aprile and et al (Xenon 100), "Dark matter results from 100 live days of xenon100 data," *Physical Review Letters*, vol. 107, no. 13, p. 131302, 2011. [Online]. Available: http://prl.aps.org/abstract/PRL/v107/i13/e131302

[11] Z. Ahmed and et al (CDMS II), "Dark matter search results from the cdms ii experiment," *Science*, vol. 327, no. 5973, pp. 1619–1621, 2010. [Online]. Available: http://www.sciencemag.org/content/327/5973/1619.full

[12] E. Armengaud and et al (EDELWEISS II), "Final results of the edelweiss-ii wimp search using a 4-kg array of cryogenic germanium detectors with interleaved electrodes," *Physical Letters B*, vol. 702, no. 5, pp. 329–335, 2011. [Online]. Available: http://www.sciencedirect.com/science/article/pii/S037026931100824O0

[13] P. Benetti and et al (WARP), "First results from a dark matter search with liquid argon at 87 k in the gran sasso underground laboratory," *Astroparticle Physics*, vol. 28, no. 6, pp. 495–507, 2008. [Online]. Available: http://www.sciencedirect.com/science/article/pii/S0927650507001016

[14] C.E.Aalseth, P.S.Barbeau, and et al (CoGENT), "Results from a search for light-mass dark matter with a p-type point contact germanium detector," *Physical Review Letters*, vol. 106, p. 131301, 2011. [Online]. Available: http://prl.aps.org/abstract/PRL/v106/i13/e131301

[15] C. Savage, G. Gelmini, P. Gondolo, and K. Freese, "Compatibility of dama/libra dark matter detection with other searches," *Journal of Cosmology and Astroparticle Physics*, vol. 4, no. 10, 2009. [Online]. Available: http://iopscience.iop.org/1475-7516/2009/04/010/

[16] J. Ellis, K. A. Olive, Y. Santoso, and V. C. Spanos, "Update on the direct detection of supersymmetric dark matter," *Physical Review D*, vol. 71, no. 9, p. 095007, 2005. [Online]. Available: http://prd.aps.org/abstract/PRD/v71/i9/e095007

[17] L. Roszkowski, R. Ruiz de Astri, and R. Trotta, "Implications for the constrained mssm from a new prediction for $b \to s\gamma$," *Journal of High Energy Physics*, vol. 07, no. 75, 2007. [Online]. Available: http://iopscience.iop.org/1126-6708/2007/07/075/

[18] C. I. Webpage, "Cold hardware thermal layout." [Online]. Available: http://cdms.berkeley.edu/cdms_restricted/coldhardware/Overview/PhononChannelDiagram.pdf

[19] P. Brink, "Non-equilibrium superconductivity induced by x-ray photons," Ph.D. dissertation, Magdalen College, Oxford University, 1995.

[20] G. A. Northrop and J. P. Wolfe, "Ballistic phonon imaging in solids- a new look at phonon focusing," *Physical Review Letters*, vol. 43, no. 19, pp. 1424–1427, 1979. [Online]. Available: http://prl.aps.org/abstract/PRL/v43/i19/p1424_1

[21] M. E. Msall and J. P. Wolfe, "Phonon production in weakly photoexcited semiconductors:?quasidiffusion in ge, gaas, and si," *Physical Review B*, vol. 56, no. 15, pp. 9557–9564, 1997. [Online]. Available: http://prb.aps.org/abstract/PRB/v56/i15/p9557_1

[22] A. G. Kozorezov, A. Volkov, and J. Wigmore, "Quasiparticle-phonon downconversion in nonequilibrium superconductors," *Physical Review B*, vol. 61, no. 17, p. 11807, 2000.

[23] B. Welliver, "R133 charge of noise donuts from low bg using optimal filter quantities," in *Internal CDMS electronic note*, 2012. [Online]. Available: http://titus.stanford.edu/cdms_restricted/Soudan/R133/ebook/120423_q/120423_q.html

[24] I. corporation. [Online]. Available: http://www.scribd.com/doc/65684420/FETs-Databook#outer_page_157

[25] A. Anderson and S. Hertel, "Basic plots of g48 data for position correction," in *Internal CDMS electronic note*, 2010. [Online]. Available: http://titus.stanford.edu/cdms_restricted/detector_physics/iZIP/ebook/101007/PhononManifoldPlots.html

[26] S. Hertel, M. Pyle, and B. Serfass, "Thinking about optimal filtering in g48," in *Internal CDMS electronic note*, 2010. [Online]. Available: http://titus.stanford.edu/cdms_restricted/hertel/ebooks/g48optimalfiltering/part1.html

[27] J. Bonetti, P. Day, and et al, "Characterization of antenna-coupled tes bolometers for the spider experiment," *Applied Superconductivity*, vol. 19, no. 3, pp. 520 – 523, 2009. [Online]. Available: http://dx.doi.org/10.1109/TASC.2009.2019297

[28] J.Yen, M. Pyle, and B. Serfass, "Charge pile-up study on g48 ucb run 400," in *Internal CDMS electronic note*, 2010. [Online]. Available: http://titus.stanford.edu/cdms_restricted/detector_physics/iZIP/ebook/101118/Qpileup.html

[29] B. Welliver, "Phonon χ^2 cut from non-stationary of," in *Internal CDMS electronic note*, 2010. [Online]. Available: http://titus.stanford.edu/cdms_restricted/detector_physics/iZIP/ebook/100930/ptnsofchisq.html

[30] A. Anderson and S. Hertel, "Quality cut to eliminate phonon traces with rising baseline in g48," in *Internal CDMS electronic note*, 2010. [Online]. Available: http://titus.stanford.edu/cdms_restricted/detector_physics/iZIP/ebook/101015/TraceBaselineQualityCut.html

[31] K. McCarthy, "Miss paper meeting," in *Internal CDMS electronic note*, 2012. [Online]. Available: http://titus.stanford.edu/cdms_restricted/kevmc/20120424_MISSpaper/20120424_MISSpaper.html

[32] M. Loewenstein and R. E. W. III, "Prevalence and properties of dark matter in elliptical galaxies," *The Astrophysical Journal*, vol. 518, no. 1, pp. 50–63, 1999. [Online]. Available: http://iopscience.iop.org/0004-637X/518/1/50

[33] F. Zwicky, "On the masses of nebulae and of clusters of nebulae," *The Astrophysical Journal*, vol. 86, pp. 217–246, 1937.

[34] J. P. Kneib and et al, "Dynamics of abell 2218 from optical and near-ir imagery of arc(let)s and the rosat/hri x-ray map," *Astron. Astrophys*, vol. 303, pp. 27–40, 1995.

[35] R. H. Cyburt, B. D. Fields, and K. A. Olive, "Primordial nucleosynthesis in light of wmap," *Phys. Lett. B*, vol. 567, pp. 227–234, 2003.

[36] A. R. Liddle and D. H. Lyth, *Cosmological inflation and large-scale structure*. Cambridge University Press, 2000.

[37] J. Preskill, M. B. Wise, and F. Wilczek, "Cosmology of the invisible axion," *Phys. Lett. B*, vol. 120, pp. 127–132, 1983.

[38] J. L. Feng, A. Rajaraman, and F. Takayama, "Superweakly-interacting massive particles," *Phys. Rev. Lett.*, vol. 91, p. 011302, 2003.

[39] D. J. H. Chung, E. W. Kolb, and A. Riotto, "Nonthermal supermassive dark matter," *Phys. Rev. Lett.*, vol. 81, pp. 4048–4051, 1998.

[40] A. Kusenko and M. E. Shaposhnikov, "Supersymmetric q-balls as dark matter," *Phys. Lett. B*, vol. 418, pp. 46–54, 1998.

[41] G. Jungman, M. Kamionkowski, and K. Griest, "Supersymmetric dark matter," *Phys. Rept.*, vol. 267, pp. 195–373, 1996.

[42] A. Kurylov and M. Kamionkowski, "Generalized analysis of the direct weakly interacting massive particle searches," *Physical Review D*, vol. 69, no. 6, p. 063503, 2004. [Online]. Available: http://prd.aps.org/abstract/PRD/v69/i6/e063503

[43] C. A. Klein, "Bandgap dependence and related features of radiation ionization energies in semiconductors," *Journal of Applied Physics*, vol. 39, no. 4, p. 2029, 1967. [Online]. Available: http://jap.aip.org/resource/1/japiau/v39/i4/p2029_s1

[44] J. Lindhard, V. Nielsen, M. Schraff, and P. Thomsen, "Integral equations governing radiation effects," *Mat. Fys. Medd. Dan. Vid. Selsk.*, vol. 33, no. 10, pp. 1–42, 1963. [Online]. Available: http://cdms.berkeley.edu/cdms_restricted/cdmsnotes/0710/1963_Lindhard33_10.pdf

[45] R. W. Ogburn, "A search for particle dark matter using cryogenic germanium and silicon detectors in the one- and two- tower runs of cdms ii at soudan," Ph.D. dissertation, Stanford University, 2008.

[46] P. N. Luke, "Single polarity charge sensing in ionization detectors using coplanar electrodes," *Applied Physics Letters*, vol. 65, no. 22, pp. 2884–2886, 1994. [Online]. Available: http://apl.aip.org/resource/1/applab/v65/i22/p2884_s1

[47] P. L. Brink and et al, "First test runs of a dark-matter detector with interleaved ionization electrodes and phonon sensors for surface-event rejection," *Nuclear Instruments and Methods A*, vol. 559, no. 2, pp. 414–416, 2006. [Online]. Available: http://www.sciencedirect.com/science/article/pii/S0168900205024162

[48] K. Irwin and G. Hilton, "Transition-edge sensors," *Topics in Applied Physics*, vol. 99, 2005. [Online]. Available: http://www.springerlink.com.ezproxy.stanford.edu/content/2chgqa70h5yd1pw5/

[49] K. Irwin, "An application of electrothermal feedback for high resolution cryogenic particle detection," *Appl. Phys. Lett.*, vol. 66, no. 15, 1995.

[50] B. A. Young and et al, "Effect of implanted metal impurities on superconducting tungsten films," *Journal Applied Physics*, vol. 91, no. 10, p. 6516, 2002. [Online]. Available: http://jap.aip.org/resource/1/japiau/v91/i10/p6516_s1

[51] S. J. Hart, M. Pyle, and et al, "Phase separation in tnugsten transition edge sensors," in *THE THIRTEENTH INTERNATIONAL WORKSHOP ON LOW TEMPERATURE DETECTORSLTD13*, A. C. Proceedings, Ed., vol. 1185, 2009, pp. 215–218. [Online]. Available: http://proceedings.aip.org/resource/2/apcpcs/1185/1/215_1

[52] M. Sisti and et al, "Performance of cresst detectors and status of the experiment," in *7th International Workshop on Low-Temperature DetectorsLTD7*, 2007, pp. 232–236.

[53] C. I. Webpage, "Useful coldhardware parameters." [Online]. Available: http://cdms.berkeley.edu/wiki/doku.php?id=coldhardware:table_of_useful_parameters

[54] T. Saab, "Search for weakly interacting massive particles with the cryogenic dark matter search experiment," Ph.D. dissertation, Stanford University, 2002.

[55] A. J. Miller, "Development of a broadband optical spectrophotometer using superconducting transition-edge sensors," Ph.D. dissertation, Stanford University, 2001.

[56] T. Saab, S. R. Bandler, and et al, "Determination of complex microcalorimeter parameters with impedance measurements," *Nuclear Instruments and Methods A*, vol. 559, no. 2, pp. 712–714, 2006. [Online]. Available: http://www.sciencedirect.com/science/article/pii/S0168900205025489

[57] M. A. Lindeman, S. Bandler, and et al, "Impedance measurements and modeling of a transition-edge-sensor calorimeter," *Review of Scientific*

Instruments, vol. 75, no. 5, p. 1283, 2004. [Online]. Available: http://rsi.aip.org/resource/1/rsinak/v75/i5/p1283_s1

[58] N. Iyomoto, S. Bandler, and et al, "Modeling of tes x-ray microcalorimeters with a novel absorber design," *Journal of Low Temperature Physics*, vol. 151, no. 1-2, pp. 406–412, 2008. [Online]. Available: http://www.springerlink.com/content/f3358533v6765134/

[59] B. Hines, K. M. Sundqvist, and et al, "Flux-coupled direct feedback in a squid amplifier," *Applied SuperConductivity*, vol. 21, no. 3, pp. 262–266, 2011. [Online]. Available: http://ieeexplore.ieee.org/xpls/abs_all.jsp?arnumber=5672549&tag=1

[60] M. A. Lindeman, B. Dirks, and et al, "Relationships between complex impedance, thermal response, and noise in tes calorimeters and bolometers," *Applied Superconductivity*, vol. 21, no. 3, p. 254, 2011. [Online]. Available: http://ieeexplore.ieee.org/xpls/abs_all.jsp?arnumber=5680947&tag=1

[61] R. F. Voss and J. Clarke, "Flicker (1/f) noise: Equilibrium temperature and resistance fluctuations," *Phys. Rev. B*, vol. 13, no. 2, p. 556, 1976.

[62] W. S. Boyle and K. R. Jr., "Performancs characteristics of a new low-temperature bolometer," *Journal of the Optical Society of America*, vol. 49, no. 1, p. 1125, 1959.

[63] McCammon, "Thermal equilbrium calorimeters- an introduction," *Topics in Applied Physics*, vol. 99, 2005. [Online]. Available: http://www.springerlink.com.ezproxy.stanford.edu/content/7vdtfkrhlvj91j0b/

[64] J. C. Mather, "Bolometer noise: non equilibrium theory," *Appl. Optics*, vol. 21, no. 6, p. 66, 1982.

[65] B. Hines, K. M. Sundqvist, and et al, *Izv. VUZ Radiofizika*, vol. 13, p. 1512, 1970.

[66] R. Stratonovich, *Nonlinear Nonequilibrium Thermodynamics I: Linear and Nonlinear Fluctuation-Dissipation Theorems*. Springer-Verlag, 1992.

[67] J. Angle, E. Aprile, and et al (Xenon 10), "Search for light dark matter in xenon10 data," *Physical Review Letters*, vol. 107, p. 051301, 2011. [Online]. Available: http://prl.aps.org/abstract/PRL/v107/i5/e051301

[68] L. Cryogenics, "2 mw, 5mk cryogen-freedilution rfrigerator for the cuore experiment." [Online]. Available: http://www.leidencryogenics.com/news.php?id=7

[69] E. Figueroa-Feliciano, "Theory and development of position-sensitive quantum calorimeters," Ph.D. dissertation, Stanford University, 2001.

[70] H. F. C. Hoevers and et al, "Thermal fluctuation noise in a voltage biased superconducting transition edge thermometer," *Applied Physics Letters*, vol. 77, no. 26, p. 4422, 2000.

[71] N. Iyomoto, S. Bandler, and et al, "Close-packed arrays of transition-edge x-ray microcalorimeters with high spectral resolution at 5.9?kev," *Applied Physics Letters*, vol. 92, no. 1, p. 013508, 2008. [Online]. Available: http://apl.aip.org/resource/1/applab/v92/i1/p013508_s1

[72] K. Sundqvist, "Some thoughts about the tes transfer function," in *Internal CDMS electronic note*, 2007. [Online]. Available: http://titus.stanford.edu/cdms_restricted/Soudan/R125-128/ebook/070821/tes.html

[73] A. Luukanen and et al, "Fluctuation-limited noise in a superconducting transistion-edge sensor," *Physical Review Letters*, vol. 90, p. 238306, 2003. [Online]. Available: http://prl.aps.org/abstract/PRL/v90/i23/e238306

[74] B. Cabrera, "Design considerations for tes and qet sensors," *NIM A*, vol. 44, no. 1, p. 304, 2000.

[75] T. Saab, R. Clarke, and et al, "Design of qet phonon sensors for the cdms zip

detectors," *Nuclear Instruments and Methods A*, vol. 444, no. 1-2, pp. 300–303, 2000. [Online]. Available: http://www.sciencedirect.com/science/article/pii/S0168900299014011

[76] S. W. Leman, "Development of phonon-mediate transition-edge-sensor x-ray detectors for use in astronomy," Ph.D. dissertation, Stanford University, 2006.

[77] M. Pyle, P. L. Brink, and et al, "Quasiparticle propagation in al fins and w tes dynamics in the cdms zip detector," *Nuclear Instruments and Methods A*, vol. 559, p. 405, 2006.

[78] J. P. Filippini and M. Pyle, "Tes transfer functions and the hummingbird plot," in *Internal CDMS electronic note*, 2007. [Online]. Available: http://titus.stanford.edu/cdms_restricted/Soudan/R125-128/ebook/070819/TEStransfer.html

[79] J. Burney, "Transition-edge sensor imaging arrays for astrophysics applications," Ph.D. dissertation, Stanford University, 2006.

[80] A. Anderson, "Square wave tes response," in *Internal CDMS electronic note*, 2007. [Online]. Available: http://space.mit.edu/figueroagroup/cdms/model/20110415SquareWaveResponse/index.html

[81] K. D. Irwin and et al, "A quasiparticle?trap?assisted transition?edge sensor for phonon?mediated particle detection," *Review of Scientific Instruments*, vol. 66, no. 11, p. 5322, 1995. [Online]. Available: http://rsi.aip.org/resource/1/rsinak/v66/i11/p5322_s1

[82] M. Kurakado, "Possibility of high resolution detectors using superconducting tunnel junctions," *Nuclear Instruments and Methods*, vol. 196, no. 1, pp. 275–277, 1982. [Online]. Available: http://www.sciencedirect.com/science/article/pii/0029554X82906541

[83] M. Loidl and et al, "Quasiparticle diffusion over several mm in cryogenic detectors," *Nuclear Instruments and Methods A*, vol. 465, no. 2-3, pp. 440–446,

2001. [Online]. Available: http://www.sciencedirect.com/science/article/pii/S0168900201006210

[84] D. Moore and et al, "Quasiparticle trapping in microwave kinetic inductance strip detectors," *AIP Conference Proceedings*, vol. 1185, pp. 168–171, 2009. [Online]. Available: http://proceedings.aip.org/resource/2/apcpcs/1185/1/168_1

[85] R. Barends and et al, "Enhancement of quasiparticle recombination in ta and al superconductors by implantation of magnetic and non-magnetic atoms," *Physical Review B*, vol. 79, p. 020509, 2009.

[86] H. Chagani and M. Pyle, "Absolute phonon calibration of g48 (izip4) from ucb run 400," in *Internal CDMS electronic note*, 2010. [Online]. Available: http://titus.stanford.edu/cdms_restricted/chagani/ebooks/101005/absPCalib_ucbR400G48.html

[87] R. W. Ogburn, "Absolute phonon calibration," in *Internal CDMS electronic note*, 2007. [Online]. Available: http://titus.stanford.edu/cdms_restricted/Soudan/r118r119/ebook/070223_2/

[88] K. McCarthy, S. Leman, and M. Pyle, "Phonon collection in g9f," in *Internal CDMS electronic note*, 2009. [Online]. Available: http://titus.stanford.edu/cdms_restricted/Soudan/r118r119/ebook/070223_2/

[89] M. Pyle, K. McCarthy, and B. Serfass, "izip absolute phonon calibration," in *Internal CDMS electronic note*, 2009. [Online]. Available: http://titus.stanford.edu/cdms_restricted/mpyle1/ebooks/IZIP2/abs_phononcal/Pcal_abs.html/

[90] S. W. Leman, "Review article: Physics and monte carlo techniques as relevant to cryogenic, phonon and ionization readout of cdms radiation-detectors," *arXiV:1109.1193*, 2012. [Online]. Available: http://arxiv.org/abs/1109.1193

[91] S. Tamura, "Isotope scattering of dispersive phonons in ge," *Physical*

Review B, vol. 27, no. 2, pp. 858–866, 1983. [Online]. Available: http://prb.aps.org/abstract/PRB/v27/i2/p858_1

[92] ——, "Quasidiffusive propagation of phonons in silicon: Monte carlo calculations," *Physical Review B*, vol. 48, no. 18, pp. 13 502–13 507, 1993. [Online]. Available: http://prb.aps.org/abstract/PRB/v48/i18/p13502_1

[93] ——, "Spontaneous decay rates of la phonons in quasi-isotropic solid," *Physical Review B*, vol. 31, no. 4, pp. 2574–2577, 1985. [Online]. Available: http://prb.aps.org/abstract/PRB/v31/i4/p2574_1

[94] J. Philip and M. A. Breazeale, "Third?order elastic constants and grneisen parameters of silicon and germanium between 3 and 300?k," *Journal of Applied Physics*, vol. 54, no. 2, p. 752, 1983. [Online]. Available: http://jap.aip.org/resource/1/japiau/v54/i2/p752_s1

[95] H. J. McSkimin and P. Andreatch, "Measurement of third?order moduli of silicon and germanium," *Journal of Applied Physics*, vol. 35, no. 11, p. 3312, 1964. [Online]. Available: http://jap.aip.org/resource/1/japiau/v35/i11/p3312_s1

[96] S. Tamura, "Numerical evidence for the bottleneck frequency of quasidiffusive acoustic phonons," *Physical Review B*, vol. 56, no. 21, p. 13630, 1997. [Online]. Available: http://prb.aps.org/abstract/PRB/v56/i21/p13630_1

[97] G. Wang, "Phonon emission in germanium and silicon by electrons and holes in applied electric field at low temperature," *Journal of Applied Physics*, vol. 107, p. 094504, 2010. [Online]. Available: http://jap.aip.org/resource/1/japiau/v107/i9/p094504_s1

[98] K. Sundqvist, "Carrier transport and related effects in detectors of the cryogenic dark matter search," Ph.D. dissertation, University of California Berkeley, 2012.

[99] S. Kaplan, C. Chi, D. Langenber, J. Chang, S. Jafarey, and D. Scalapino, "Quasiparticle and phonon lifetimes in superconductors," *Physical Review*

B, vol. 14, no. 11, pp. 4854–4873, 1976. [Online]. Available: http://prb.aps.org/abstract/PRB/v14/i11/p4854_1

[100] D. Moore, "Systematic differences between ba and low background beta distributions," in *Internal CDMS electronic note*, 2009. [Online]. Available: http://titus.stanford.edu/cdms_restricted/Soudan/R125-128/ebook/090720_2/

[101] Z. Ahmed and et al (CDMS), "Results from a low-energy analysis of the cdms ii germanium data," *Physical Review Letters*, vol. 106, p. 131302, 2011. [Online]. Available: http://arxiv.org/abs/1011.2482v3

[102] B. Welliver, "Charge baseline noise sigmas in g48 run 400," in *Internal CDMS electronic note*, 2010. [Online]. Available: http://titus.stanford.edu/cdms_restricted/detector_physics/iZIP/ebook/r400g48qsigmas/qbaselinesigma.html

[103] A. Phipps, "The cdms ionization readout capacitance budget," Undergraduate Honors Thesis, University of California at Berkeley, 2008.

[104] D. Seitz, "Typical charge channel connections," in *Internal CDMS electronic note*. [Online]. Available: http://cdms.berkeley.edu/cdms_restricted/coldhardware/Overview/ChargeChannelDiagram.pdf

[105] M. Pyle, "The next izip," in *Internal CDMS electronic note*, 2009. [Online]. Available: http://titus.stanford.edu/cdms_restricted/mpyle1/ebooks/IZIP2/intro/IZIP2_intro.html

[106] B. Serfass and M. Pyle, "Charge collection study," in *Internal CDMS electronic note*, 2009. [Online]. Available: http://titus.stanford.edu/cdms_restricted/serfass/ebooks/IZIP2/charge_study/charge_collection.shtml

[107] M. Pyle, B. Serfass, and K. Sundqvist, "Qi/qo studies on the izip," in *Internal CDMS electronic note*, 2009. [Online]. Available: http://titus.stanford.edu/cdms_restricted/mpyle1/ebooks/IZIP2/qiqo_issues/IZIP2_qiqo.html

[108] M. Pyle and R. W. Ogburn, "Subpixel position systematics: Why are

box plots boxy?" in *Internal CDMS electronic note*, 2010. [Online]. Available: http://titus.stanford.edu/cdms_restricted/detector_physics/iZIP/ebook/101031/BoxPlts.html

[109] M. Pyle, "Resolution and linearity at low energies," in *Internal CDMS electronic note*, 2010. [Online]. Available: http://titus.stanford.edu/cdms_restricted/Soudan/R125-128/ebook/100426/

[110] D. Seitz, M. Pyle, and et al, "Understanding test facility low frequency phonon noise," in *Internal CDMS electronic note*, 2010. [Online]. Available: http://titus.stanford.edu/cdms_restricted/detector_physics/iZIP/ebook/101119/UCB_LF_Pnoise.html

[111] M. Pyle, "Further understanding of low frequency phonon noise at tf's and optimum filter mitigation strategies," in *Internal CDMS electronic note*, 2011. [Online]. Available: http://titus.stanford.edu/cdms_restricted/detector_physics/iZIP/ebook/110912/Pnoise_lowfreq.html

[112] ——, "Initial attempts to create high quality pt estimators without position correction," in *Internal CDMS electronic note*, 2010. [Online]. Available: http://titus.stanford.edu/cdms_restricted/mpyle1/ebooks/IZIP2/YPt_poscor_free/Ypt_pcfree.html

[113] R. Basu Thakur, "Notes on optimal filter theory," in *Internal CDMS electronic note*, 2011. [Online]. Available: http://cdms.berkeley.edu/wiki/lib/exe/fetch.php?media=software:cdmsbats_batroot_user_guide:ofnotes.pdf

[114] S. Fallows, "Soudan 5-tower nuclear recoil energy scale - data & monte carlo," in *Internal CDMS electronic note*, 2010. [Online]. Available: http://www.hep.umn.edu/cdms/cdms_restricted/misc/100830/

[115] B. Serfass, "Private communication," 2010.

[116] M. Pyle, "G48 quality cut summary," in *Internal CDMS electronic*

note, 2011. [Online]. Available: http://titus.stanford.edu/cdms_restricted/detector_physics/iZIP/ebook/110421/QualCuts_G48.html

[117] K. Koch, "Low energy glitch cut for c58," in *Internal CDMS electronic note*, 2010. [Online]. Available: http://titus.stanford.edu/cdms_restricted/Soudan/R125-128/ebook/100727/

[118] Z. Ahmed and et al (CDMS), "Search for annual modulation in low-energy cdms-ii data," *arXiV*, vol. 1203.1309, 2012. [Online]. Available: http://arxiv.org/abs/1203.1309

[119] S. Hertel, "Very preliminary look at r133 low-background data, with an eye towards beta rejection," in *Internal CDMS electronic note*, 2012. [Online]. Available: http://titus.stanford.edu/cdms_restricted/Soudan/R133/ebook/120403_1/betarejection.html

[120] O. Kamaev, "Extrapolation of cdms-ii neutron-wimp fiducial correction to izip," in *Internal CDMS electronic note*, 2012. [Online]. Available: http://titus.stanford.edu/cdms_restricted/backgrounds/ebook/120410/

[121] Allan, "Detailed study of cqin_c58 efficiency," in *Internal CDMS electronic note*, 2009. [Online]. Available: http://titus.stanford.edu/cdms_restricted/Soudan/R125-128/ebook/090730/CQinC58/DetailedCQinC58EfficiencyStudy.phpl

[122] S. Henry, "Conference slides: The edelweiss dark matter search: Latest results and future plan," 2012. [Online]. Available: http://www.ep.ph.bham.ac.uk/general/seminars/slides/Sam-Henry-2012.pdf

[123] M. Pyle, "Low energy phonon only fiducial volume," in *Internal CDMS electronic note*, 2012. [Online]. Available: http://titus.stanford.edu/cdms_restricted/detector_physics/iZIP/ebook/120418/PFVle_G48.html

[124] ——, "Miss discrimination: Potential discrimination techniques," in *Internal CDMS electronic note*, 2010. [Online]. Available: http://titus.stanford.edu/cdms_restricted/detector_physics/iZIP/ebook/101022/MISSdiscrim.html

[125] Y. Ricci, C. Crewdson, and O. Kamaev, "New hizip studies with non stationary optimum filter quantities and comparison with previous studies on psum-based quantities," in *Internal CDMS electronic note*, 2011. [Online]. Available: http://titus.stanford.edu/cdms_restricted/detector_physics/iZIP/ebook/111130_hiZIP_reproc/note.html

Matt Christopher Pyle

I certify that I have read this dissertation and that, in my opinion, it is fully adequate in scope and quality as a dissertation for the degree of Doctor of Philosophy.

(Blas Cabrera) Principal Adviser

I certify that I have read this dissertation and that, in my opinion, it is fully adequate in scope and quality as a dissertation for the degree of Doctor of Philosophy.

(Giorgio Gratta)

I certify that I have read this dissertation and that, in my opinion, it is fully adequate in scope and quality as a dissertation for the degree of Doctor of Philosophy.

(Chao-Lin Kuo)

Approved for the University Committee on Graduate Studies